

**ASSESSMENT OF TENSILE AND CREEP BEHAVIOUR OF 316LN
STAINLESS STEEL USING AUTOMATED BALL INDENTATION
AND SMALL PUNCH CREEP TESTING TECHNIQUES**

By
GANESH KUMAR J
ENGG02201104001

IGCAR, Kalpakkam

A thesis submitted to the
Board of Studies in Engineering Sciences
In partial fulfillment of requirements
for the Degree of
DOCTOR OF PHILOSOPHY
of
HOMI BHABHA NATIONAL INSTITUTE



November, 2016

Homi Bhabha National Institute

Recommendations of the Viva Voce Committee

As members of the Viva Voce Committee, we certify that we have read the dissertation prepared by **GANESH KUMAR J** entitled "Assessment of tensile and creep behaviour of 316LN stainless steel using Automated Ball Indentation and Small Punch Creep testing techniques" and recommend that it may be accepted as fulfilling the thesis requirement for the award of Degree of Doctor of Philosophy.

Chairman – Dr. K. VELUSAMY




Date: 27/03/2017

Guide / Convener – Dr. K. LAHA



Date: 27/03/2017

Examiner – Prof. RABINDRA NATH GHOSH



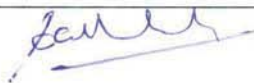
Date: 27/03/2017

Member 1- Dr. B.P.C. RAO



Date: 27/03/2017

Member 2- Dr. G. SASIKALA



Date: 27/03/2017

Final approval and acceptance of this thesis is contingent upon the candidate's submission of the final copies of the thesis to HBNI.

I hereby certify that I have read this thesis prepared under my direction and recommend that it may be accepted as fulfilling the thesis requirement.

Date: 27/03/2017

Place: Kalpakkam



27.3.2017.

Dr. K. LAHA

(Guide)

STATEMENT BY AUTHOR

This dissertation has been submitted in partial fulfillment of requirements for an advanced degree at Homi Bhabha National Institute (HBNI) and is deposited in the Library to be made available to borrowers under rules of the HBNI.

Brief quotations from this dissertation are allowable without special permission, provided that accurate acknowledgement of source is made. Requests for permission for extended quotation from or reproduction of this manuscript in whole or in part may be granted by the Competent Authority of HBNI when in his or her judgment the proposed use of the material is in the interests of scholarship. In all other instances, however, permission must be obtained from the author.



GANESH KUMAR J

DECLARATION

I, hereby, declare that the investigation presented in the thesis has been carried out by me.
The work is original and has not been submitted earlier as a whole or in part for a degree /
diploma at this or any other Institution / University.

A handwritten signature in blue ink, appearing to read 'Ganesh', with a stylized flourish extending from the end.

GANESH KUMAR J

List of Publications arising from the thesis

Journals

1. "Analyses of transient and tertiary small punch creep deformation of 316L(N) stainless steel", J. Ganesh Kumar, V. Ganesan and K. Laha, Metall. Mater. Trans. A, 2016, 47, 4484-4493.
2. "Small punch creep deformation and rupture behaviour of 316L(N) stainless steel", J. Ganesh Kumar and K. Laha, Mater. Sci. Eng. A, 2015, 641, 315-322.
3. "Evaluation of variation of tensile strength across 316LN SS weld joint using automated ball indentation technique", J. Ganesh Kumar, V.D. Vijayanand, M. Nandagopal and K. Laha, Mater. High Temp., 2015, 32, 621-628.
4. "Ball indentation studies on the effect of nitrogen content on the tensile properties of 316LN SS", M.D. Mathew, J. Ganesh Kumar, V. Ganesan and K. Laha, High Temp. Mater. Proc., 2015, 34, 827-832.
5. "Small punch creep studies for optimisation of nitrogen content in 316LN SS for enhanced creep resistance", M.D. Mathew, J. Ganesh Kumar, V. Ganesan and K. Laha, Metall. Mater. Trans. A, 2014, 45, 731-737.

Conferences

1. "Small punch creep studies on 316L(N) stainless steel", J. Ganesh Kumar and K. Laha, in: *Proc. Seventh Intl. Conf. on creep, fatigue and creep-fatigue interaction*, Jan 19-21, 2016, Kalpakkam.
2. "Small punch creep studies for remnant life assessment", J. Ganesh Kumar, K. Laha and M. D. Mathew, in: *Applied Mech. Mater.*, 592 (2014) 739-743, *Intl. Mech. Engg. Congress*, Jun 13-15, NIT, Tiruchirapalli.



GANESH KUMAR J

The thesis is dedicated to

Department of Atomic Energy, India

ACKNOWLEDGEMENTS

I would like to express my sincere gratitude to my guide, Dr. K. Laha for providing me continuous support through his patience, motivation and immense knowledge. His deep and enthusiastic involvement has rendered a systematic progress of this research work. I also thank him for all his contributions to improve the quality of this thesis.

I am grateful to my former guide Dr. M.D. Mathew for emphasizing me to pursue PhD in the present topic, by providing a broad outline of this work and educating me the basics of the techniques studied in this thesis. I am greatly obliged to my doctoral committee members Dr. S. Velusamy, Dr. S. Venugopal, Dr. B.P.C Rao, and Dr. G. Sasikala for steering my research work in the right direction. Their insightful suggestions helped me to overcome the shortcomings and widen the scope of research.

I sincerely thank Dr. A.K. Bhaduri, Director, IGCAR for encouraging me throughout this research work. I thank Dr. G. Amarendra, scientist-in-charge, UGC-DAE-CSR lab, Kalpakkam node for his kind support in maintaining the lab. I thank Dr. T. Jayakumar, Dr. M. Saiababa, Dr. G. Sasikala and HBNI professors who conducted my course work, for making my Ph.D. course at HBNI fruitful and enjoyable.

I thank Mr. N.S. Thampi for all his supports during operation and maintenance of testing facilities. I thank Dr. S. Ravi, V.D. Vijayanand, V. Ganesan, J. Christopher, Dr. Sunil Goyal and other colleagues of Mechanical Metallurgy Division for offering technical support and useful discussions. I thank Dr. N.L. Parthasarathi, Dr. R.G. Joshi for their help while availing the characterisation equipments. I thank my colleagues in central workshop division for doing various machining works.

I wish to highlight the cheering company of my wife, Lalithasri and loving daughter, Hansithasri who vitalised me during difficult days. I feel happy over the good wishes from my parents Mr. M. Jayakumar and Mrs. J. Kalarani, brother, sister-in-law and my teachers.

CONTENTS

	Page No.
SYNOPSIS	i
LIST OF FIGURES	xi
LIST OF TABLES	xv
NOMENCLATURE	xvi
1 INTRODUCTION	
1.1 Small Specimen Testing Techniques	1
1.2 Automated Ball Indentation Technique	4
1.3 Small Punch Creep Technique	13
1.4 Materials Under Investigation	24
1.5 Motivation	33
1.6 Organisation and scope of thesis	35
2 EXPERIMENTAL DETAILS	
2.1 Materials under investigation	37
2.2 Automated Ball Indentation test	40
2.3 Small Punch Creep test	46
2.4 Imaging and other characterisation techniques	50
2.5 Finite Element Analysis (FEA)	52
3 TENSILE PROPERTIES OF 316L(N) SS USING ABI TECHNIQUE	
3.1 ABI analyses	56
3.2 Influence of test parameters	64
3.3 High Temperature Tensile properties of 316L(N) SS	75

3.4	SEM EBSD analysis	86
3.5	FEA results	88
4	SMALL PUNCH CREEP BEHAVIOUR OF 316L(N) SS	
4.1	SPC results	100
4.2	Analysis of SPC deformation	110
4.3	SPC mechanism	126
4.4	Correlation with uniaxial creep results	131
4.5	Finite Element Analysis	139
5	APPLICATION I – EFFECT OF NITROGEN ON TENSILE AND CREEP BEHAVIOUR OF 316LN SS	
5.1	Effect of nitrogen on tensile behaviour of 316LN SS using ABI technique	145
5.2	Effect of nitrogen on creep behaviour of 316LN SS using SPC technique	153
6	APPLICATION II – LOCALISED CHARACTERISATION OF 316LN SS WELD JOINT	
6.1	Tensile strength variation across weld joint using ABI technique	173
6.2	Creep strength variation across weld joint using SPC technique	183
7	CONCLUSIONS AND FUTURE WORK	
7.1	Conclusions	190
7.2	Scope for future work	193
	REFERENCES	194

SYNOPSIS OF Ph. D. THESIS

Small specimen testing techniques are utilized whenever sufficient material is not available for making specimens to carry out conventional uniaxial tensile or creep tests. Requirement of small specimen testing arises in situations such as (i) residual life assessment of components in high temperature service (ii) localized characterisation of narrow heterogeneous regions of weld joint (iii) development of heat resistant alloys (iv) failure analysis, etc.

Automated Ball Indentation (ABI) technique is a promising technique used for evaluating tensile behaviour of materials by testing a small volume of material. It involves strain controlled, multiple indentation cycles at a single penetration location on the polished metal surface by a spherical indenter, with each cycle comprising loading and partial unloading. The load-depth of indentation data measured from ABI tests are analyzed to obtain tensile properties.

Small Punch Creep (SPC) technique is another small specimen testing technique used for evaluating the creep properties of a material and is capable of producing reliable creep deformation and rupture data. In SPC testing, a thin disc specimen of square cross-section 10 mm x 10 mm and 0.5 mm thickness is held between upper and lower dies. A silicon nitride spherical indenter of diameter 2.38 mm is used to apply load to the specimen at high temperature, till the specimen ruptures. SPC test is conducted under load controlled mode and the central deflection is measured as a function of time. An interesting feature in SPC test is that the measured curve appears similar to the conventional creep curve.

Austenitic stainless steel (SS) of type 316L(N) containing 0.02-0.03 wt.% carbon and 0.06-0.08 wt.% nitrogen is used as the major structural material for out-of-core reactor

assembly components in sodium cooled fast reactors. With an objective to increase the efficiency and plant life of future fast reactors, extensive studies are being carried out to achieve superior high temperature mechanical properties of 316LN SS, by increasing the nitrogen content beyond 0.08 wt.%. Type 316N SS containing 0.045-0.055 wt.% carbon and 0.06-0.10 wt.% nitrogen is widely chosen as the electrode for fabrication of 316LN SS weld joints. Though the tensile and creep properties of 316LN SS have been evaluated in various dimensions using conventional tests, detailed studies using ABI and SPC techniques are scarcely available for this material in the literature. The studies on 316LN SS using ABI and SPC techniques are essential to provide baseline data for the future structural integrity assessment of service components.

Life extension activities on nuclear components can result in huge cost savings as well as defer the issues associated with the disposal of nuclear components after decommissioning. However, at present, small specimen testing techniques such as ABI and SPC are not in the position to be deployed in such activities, as these techniques are still evolving. It is, therefore, essential to validate the applicability of these small specimen techniques to assess mechanical behaviour of reactor materials by means of elaborate studies, involving analysis and interpretation of data, resulting in deep understanding of the techniques. The use of ABI and SPC techniques for research in nuclear industry can also support the critical activities including post irradiation examination of irradiated materials, irradiation embrittlement of reactor pressure vessel steel, degradation of piping and other service components, etc.

This thesis focuses on use and applications of SPC and ABI testing techniques in assessing tensile and creep behaviour of 316LN SS, its nitrogen enhanced variants and across its weld joint. In this thesis, chapters 1 and 2 provide introduction and experimental details. The overall views of the chapters 3-6 are presented in the following four sections. The thesis is completed with conclusions and directions for future work.

A. Tensile behaviour of 316L(N) SS using ABI technique

ABI test involves various parameters such as surface finish of test specimen, maximum depth of indentation, number of cycles and indenter material. As ABI testing is yet to be standardized, initially, the influence of above parameters on ABI results has been studied by conducting tests on 316LN SS containing 0.07 wt.% nitrogen at 298 K. It was found that by increasing the maximum depth of indentation (in the range 12% to 50% of indenter radius), number of cycles (in the range 5 to 12 cycles) and surface finish of test specimen (average roughness (R_a) in the range 2-4 microns) to higher values, at the cost of time and efforts, ABI results were not altered significantly. For the same depth of indentation, the applied load decreased when silicon nitride indenter was used in place of tungsten carbide indenter, which is an indication of the extent of elastic deformation of silicon nitride indenter relative to tungsten carbide indenter. The indenter material must be selected judiciously. Due to chances of oxidation at higher temperature, use of tungsten carbide indenter is restricted upto 673 K. At high temperatures (> 673 K), relatively stable silicon nitride indenter is used.

The high temperature tensile properties of 316L(N) SS were evaluated using ABI technique over the temperature range 298-973 K. The test temperature was maintained within ± 2 K.

The load-depth of indentation data measured on 316L(N) SS at various temperatures were analysed using semi-empirical relationships to determine various tensile properties such as yield stress, ultimate tensile strength, strength coefficient and strain hardening exponent. Generally, it was observed that the true stress-true plastic strain values determined from ABI tests lie closer to corresponding uniaxial flow curves. The decreasing trend of yield stress, strength coefficient, yield ratio and the increasing trend of strain hardening exponent with temperature were obtained. The plot between tensile strength (normalized with Young's modulus) and temperature showed three regimes, with a peak value at around 823 K. The results obtained can serve as a part of database for future high temperature studies involving damage assessment.

Finite element analysis (FEA) was carried out to investigate the stress distribution inside the region of specimen subjected to compressive load under the indenter. An axisymmetric model of the indenter and specimen was developed for this purpose. The load-depth of indentation curves that were obtained from FEA and ABI test were found to overlap closely, which established the validation of finite element model and the procedures adopted in the analysis. The evolution of plastic zone with increasing depth of indentation was investigated using Von Mises yield criterion. When the maximum depth of indentation was 24% of indenter radius, the region immediately below the indenter upto the depth approximately equal to the indenter diameter, showed higher level of plastic deformation. The material pile-up phenomenon occurring over specimen surface on indentation was studied. It is generally known that the applied load in ABI specimen is converted into equivalent uniaxial stress using semi-empirical relationships. Such calculated equivalent stress was found to occur in the portion of specimen that was away from the center of the indenter tip at a distance approximately equal to the depth of indentation at that cycle.

B. Small Punch Creep (SPC) behaviour of 316L(N) SS

SPC tests were carried out on 316LN SS at various loads in the range 300-1000 N at 923 K, with a temperature accuracy of ± 2 K. The SPC deflection curves clearly exhibited distinct primary, secondary and tertiary stages of creep deformation. Though the state of stress developed in SPC test specimen is biaxial, the uniaxial creep relationships were found to be analogously applicable to SPC data. It was observed that dependence of steady state deflection rate ($\dot{\delta}_s$) on applied load (F) obeyed Norton's power law. Monkman-Grant relationship was established between steady state deflection rate and SPC rupture life. An expression analogous to Dobes and Cadek equation for uniaxial creep strain curve^[1] has been proposed for SPC deflection (δ) as,

$$\delta = \delta_0 + \delta_T (1 - e^{-\kappa t}) + \dot{\delta}_s t + \delta_3 e^{\varphi(t-t_r)} \quad (1)$$

where, ‘ δ_0 ’ is instantaneous deflection on loading, ‘ δ_T ’ is limiting transient creep deflection, ‘ κ ’ is the rate of exhaustion of transient creep, ‘ φ ’ is rate of acceleration of tertiary creep, ‘ δ_3 ’ represents tertiary creep deflection and ‘ t_r ’ is SPC rupture life. The rate of exhaustion of transient creep has been calculated by rearranging Eqn. (1) on ignoring tertiary creep term and taking natural logarithm as,

$$\kappa = -\frac{1}{t} \ln \left(1 - \frac{(\delta - \delta_0 - \dot{\delta}_s t)}{\delta_T} \right) = -\frac{1}{t} \ln \left(1 - \frac{\Delta_1}{\delta_T} \right) \quad (2)$$

where, $\Delta_1 = \delta - \delta_0 - \dot{\delta}_s t$, is the transient creep deflection component.

The rate of acceleration of tertiary creep (φ) has been calculated by rearranging Eqn. (1) and taking natural logarithm as,

$$\varphi = -\frac{1}{(t - t_r)} \ln \left(\frac{\delta - \delta_0 - \delta_T - \dot{\delta}_s t}{\delta_3} \right) = -\frac{1}{(t - t_r)} \ln \left(\frac{\Delta_3}{\delta_3} \right) \quad (3)$$

where, $\Delta_3 = \delta - \delta_0 - \delta_T - \dot{\delta}_s t$, is the tertiary creep deflection component. The linear relationships of ‘ κ ’ with $\dot{\delta}_s$ and time to attain steady state deflection rate and the relationship between initial creep deflection rate ($\dot{\delta}_i = \kappa \delta_T + \dot{\delta}_s$) and $\dot{\delta}_s$, implied that transient SPC deformation of 316LN SS was governed by first order kinetic reaction rate theory. Similarly, the relationships of ‘ φ ’ with $\dot{\delta}_s$ and tertiary life and the linear relationship between final creep deflection rate ($\dot{\delta}_f = \varphi \delta_3 + \dot{\delta}_s$) and $\dot{\delta}_s$, revealed that tertiary SPC deformation obeyed first order kinetic reaction rate theory. The above relationships implied that transient, secondary and tertiary creep parameters were interrelated. The values of κ , $\dot{\delta}_s$ and φ were found to follow similar decreasing trend with rupture life and increasing trend with applied load.

In order to estimate the activation energy of SPC deformation (Q_{spc}), SPC results obtained over the temperature range of 898-973 K at 400 N were used. An Arrhenius form of equation has been used to express the load (F) and temperature (T) dependence of steady state

deflection rate as, $\dot{\delta}_s = B F^{n_{SPC}} \exp\left(-\frac{Q_{SPC}}{RT}\right)$, where, 'B' is a constant, 'n_{SPC}' is load exponent of steady state deflection rate and 'R' is the universal gas constant. From the determined values of 'n_{SPC}' and apparent activation energy for creep deformation, it is concluded that dislocation creep mechanism governed SPC deformation under the investigated conditions. The stress distribution in thin disc specimen subjected to compressive load under spherical indenter was obtained through finite element analysis.

The existing procedures for design of high temperature components are based on the data generated from uniaxial creep tests. It is necessary to translate the results implied from SPC test in terms of conventional creep test. According to CEN (European committee for standardization) code of practice, the equivalent uniaxial stress for SPC load is determined as,

$$F/\sigma = 3.33 K_{SP} R_h^{-0.2} r^{1.2} h, \quad (4)$$

where, 'R_h' is the radius of receiving hole, 'r' is radius of indenter, 'h' is thickness of specimen and 'K_{SP}' is ductility constant. The equivalent stresses for SPC loads obtained using Eqn. (4) were correlated well with corresponding uniaxial creep stresses ^[2], for the same rupture life. The comparison of SPC and uniaxial creep results have largely been dealt with rupture life and steady state deflection rate. It has been attempted to correlate the deformation behaviour of SPC with uniaxial creep tests. The master curves obtained for transient creep deformation from both SPC and uniaxial creep tests were found to be in good agreement with one another.

The studies pertaining to ABI and SPC testing provide confidence that these testing techniques can be used to evaluate mechanical properties of 316LN SS and their results could be correlated with conventional test results. Further, the testing techniques are applied to optimize nitrogen content in 316LN SS and to evaluate the heterogeneity in mechanical properties across 316LN SS weld joint.

C. Application-I: Optimisation of nitrogen content in 316LN SS

The effect of nitrogen content on the tensile properties of 316LN SS has been estimated by ABI technique. ABI tests were conducted at several temperatures in the range 298-973 K on four heats of 316LN SS containing 0.07, 0.11, 0.14 and 0.22 wt.% nitrogen (designated respectively as 7N, 11N, 14N and 22N for discussion purposes). The load required to cause the same depth of indentation increased with increase in nitrogen content. For the same plastic strain, the true stress for 316LN SS increased with addition of nitrogen content. The increase in strength coefficient and decrease in strain hardening exponent with increase in nitrogen content implied the corresponding decrease in rate of work hardening of 316LN SS with increase in nitrogen content. The yield stress (YS) and ultimate tensile strength (UTS) values increased with increase in nitrogen content as observed similarly from uniaxial tensile tests. In general, ABI values were found closer to tensile test results at all temperatures. All ABI values were found to fall almost within 10% scatter limits on tensile test values.

SPC technique has been used to estimate the influence of nitrogen content on the creep deformation and rupture behaviour of 316LN SS. SPC tests were carried out on 7N, 11N, 14N and 22N steels at 923 K at various loads in the range 300-550 N. The rupture life increased with increase in nitrogen content upto 0.14 wt.%. The 22N steel which showed the highest creep strength among the investigated steels during uniaxial creep test, behaved differently under biaxial state of stress in SPC test. From the multiaxial creep studies (on notched specimens), it was observed similar to SPC results that creep rupture strength of 22N steel was lower than that of 14N steel ^[3]. Thus ABI and SPC studies performed under multiaxial state of stress are necessary to understand the complete deformation behaviour of the material.

Transient and tertiary creep deformation behaviour of 316LN SS with different nitrogen content have been analysed according to Eqn. (1). The relationships of κ with steady state deflection rate and time to attain steady state deflection rate and those of ϕ with tertiary life

and steady state deflection rate were found to be similar for all nitrogen content. The first order reaction rate theory was found to govern transient as well as tertiary creep deformation of all the four heats. A master curve for transient creep was constructed for the four heats. By increasing the nitrogen content in 316LN SS from 0.07 to 0.14 wt.%, the parameters κ , $\dot{\epsilon}_s$ and ϕ decrease for the same applied load, consequently resulting in higher rupture life.

D. Application-II: Characterisation of 316LN SS weld joint

The variation of tensile strength across the various regions of 316LN SS weld joint such as base metal, heat affected zone (HAZ) and weld metal was determined using ABI technique. ABI tests were conducted across various zones of 316LN SS weld joint at 298 K, 523 K and 923 K. For the same depth of indentation, the applied load was higher at HAZ as compared to other regions of the weld joint, at all investigated temperatures. The flow curves obtained for weld metal and base metal were consistent with corresponding tensile test results. Though the flow curve for HAZ was lower than that for weld metal initially, the increase in stress with strain was more in HAZ relative to weld metal. The highest YS value was observed in the weld metal region whereas the highest UTS was found in HAZ region, at all temperatures. A better interpretation of YS and UTS trend curves was achieved by UTS/YS ratio that represents the work hardening of the material. The UTS/YS ratio increased with increase in temperature for the base metal and HAZ whereas it remained almost the same for weld metal. In order to obtain the variation in creep deformation and rupture strength across 316LN SS weld joint, SPC tests were carried out on specimens sliced out from weld metal, HAZ and base metal regions of the weld joint at 923 K at various loads in the range 300-550 N. It was observed that the weld metal showed highest creep rupture strength among the three regions of 316LN SS weld joint. The rupture strength of HAZ was significantly higher than that of base metal. The values of κ , $\dot{\epsilon}_s$ and ϕ calculated for the same conditions exhibited increasing

trend across the weld joint from weld metal to base metal. A master transient creep curve for the different constituents of the weld joint has been developed.

Conclusions

Automated Ball Indentation (ABI) technique has been used to assess high temperature tensile properties of 316L(N) SS in the temperature range 298-973 K. These results highlighted the capability of ABI tests to grasp the degradation of the strength of materials on exposure to high temperature. Finite element analysis aids to understand the plastic deformation in the region of specimen beneath the indenter.

Small Punch Creep (SPC) technique has been used to evaluate the creep behaviour of 316L(N) SS at various loads and at several temperatures in the range 898-973 K. The dislocation creep mechanism was found to govern SPC deformation in the investigated range of temperature. The transient and tertiary SPC deformation behaviour have been analysed according to the equation proposed for SPC deflection, $\delta = \delta_0 + \delta_T (1 - e^{-\kappa t}) + \dot{\delta}_s t + \delta_3 e^{[\phi(t-t_r)]}$ on the basis of Dobes and Cadek equation for uniaxial creep strain. SPC results were correlated well with corresponding uniaxial creep results. Master curves representing transient creep deformation have been derived from both SPC and uniaxial creep tests and their near coincidence brings unique equivalence between both the test techniques.

ABI and SPC techniques have been respectively used to investigate the effect of nitrogen content on tensile and creep properties of 316LN SS. The yield stress and ultimate tensile strength increased with increase in nitrogen content at all the investigated temperatures. These results are consistent with the corresponding uniaxial tensile test results. The SPC rupture life increased and steady state deflection rate decreased with increase in nitrogen content of 316LN SS from 0.07 to 0.14 wt.%, then the trends reversed at 0.22 wt.%. Increase in nitrogen content lowers the transient, secondary and tertiary creep parameters (i.e., κ , $\dot{\delta}_s$ and ϕ), for the

same load, resulting in higher rupture life. Thus ABI and SPC techniques can be considered to be quick and reliable to study heat to heat variations of tensile and creep strength.

The variations of tensile and creep properties across 316LN SS fusion welded joint, comprising base metal, heat affected zone (HAZ) and weld metal, were evaluated respectively using ABI and SPC techniques. It is emphasized that ABI and SPC techniques can be effectively utilised in the study of weld joints used in high temperature applications.

This thesis also discusses the scope for future research including application of ABI and SPC techniques to other fast reactor materials, damage assessment of service components, etc.

References

- 1) F. Dobes and J. Cadek, Kovove Mater. Vol. 19 (1981), pp. 31-40.
- 2) M.D. Mathew, K. Laha and V. Ganesan, Mater. Sci. Eng. A. Vol. 535 (2012), pp. 76-83.
- 3) V. Ganesan, J. Ganesh Kumar, K. Laha and M.D. Mathew, Nucl. Eng. Des. Vol. 254 (2013), pp. 179-184.

LIST OF FIGURES

Fig. No.	Title	Page No.
1.1	Various zones formed during indentation	6
1.2	Johnson's expanding cavity model	7
1.3	Pile-up and sink-in phenomenon	10
1.4	Deformation of SP specimen	14
1.5	Radius of contact area varying with central deflection	15
1.6	Volume of material required for evaluating creep strength	22
2.1	Microhardness profile obtained across 316LN SS/ 316N weld joint	39
2.2	ABI experimental setup	41
2.3	(a) Details of specimen fixture assembly (b) Φ 0.76 mm indenter	42
2.4	Weld joint specimen used in ABI test	45
2.5	SPC testing facility	46
2.6	(a) Furnace (b) Specimen mounting assembly	47
2.7	Schematic of SPC testing facility	47
2.8	Fabrication of SPC specimens for weld joint studies	49
2.9	Axisymmetric FE model of spherical indenter and specimen	53
2.10	Axisymmetric FE model of indenter and SPC specimen held between upper and lower die	54
3.1	ABI load-depth of indentation curve measured at 298 K	56
3.2	Linear regression of first loading cycle, to estimate the depth of indentation corresponding to preload	58
3.3	Determination of plastic depth from total depth of indentation	58
3.4	Indentation profile during ABI test	59
3.5	Calculation of yield parameter (A) shown typically at 298 K	62
3.6	Relationship between yield parameter and uniaxial yield stress	63
3.7	Influence of indenter material on applied load for the same depth of indentation	67
3.8	Comparison of flow curves obtained using tungsten carbide and silicon nitride indenters	67
3.9	Effect of surface finish of test specimen on measured data	69
3.10	Effect of surface finish of test specimen on flow curves of 316LN SS	70
3.11	Optical micrographs of indentations obtained by setting maximum depth of indentation as (a) 12% (b) 24% (c) 36% (d) 42% and (e) 50%	71
3.12	Load-depth of indentation curves obtained by varying maximum depth of indentation	72
3.13	Flow curves obtained by varying maximum depth of indentation	73
3.14	Load-indentation depth curves measured by setting various number of test cycles	74
3.15	Flow curves obtained for 316LN SS by setting various number of test cycles	74
3.16	ABI specimen tested at 298 K	75
3.17	Optical micrograph of ABI specimen tested at 298 K	76
3.18	Differences in microstructure subjected to indentation	76
3.19	Load-depth of indentation curves measured at various temperatures	77

Fig. No.	Title	Page No.
3.20	Yield stress values plotted as a function of temperature	78
3.21	Flow curves obtained for 316L(N) SS at various temperatures using ABI technique	78
3.22	Comparison of flow curves obtained from ABI and uniaxial tests	79
3.23	Influence of temperature on strength coefficient and strain hardening exponent	80
3.24	Ultimate tensile strength plotted as function of temperature	81
3.25	Variation of ultimate tensile strength/E with temperature	82
3.26	Effect of temperature on yield ratio	83
3.27	Estimation of uniform ductility from ABI test conducted at 298 K	84
3.28	Uniform ductility plotted as function of temperature	85
3.29	ABI hardness obtained as function of temperature	85
3.30	SEM EBSD micrograph showing the orientation due to indentation load	86
3.31	Strain distribution in ABI specimen tested at 298 K	87
3.32	Strain distribution obtained through KANM approach	87
3.33	Comparison of load-depth of indentation curves obtained from FEA and test	89
3.34	Contact pressure at the surface of contact between specimen and indenter	89
3.35	(a) Axial stress and (b) radial stress developed below the indenter during each cycle	90
3.36	Von-Mises stress developed under indenter during eighth cycle	91
3.37	Variations of Von-Mises stress along the axis of symmetry	92
3.38	Development of plastic zone relative to elastic zone	92
3.39	Plastic strain accumulation at the end of the test	93
3.40	Triaxial state of stress expressed by (a) hydrostatic stress and (b) Triaxiality factor	94
3.41	Direction and magnitude of maximum principal stress during eighth cycle	96
3.42	Direction and magnitude of minimum principal stress during eighth cycle	96
3.43	Pictorial representation of pileup on increasing depth of indentation, using vector symbol plot of resultant displacement	97
3.44	CSLM 3D profile images of indentation in ABI specimen tested at 298 K (a) lateral view and (b) isometric view	98
3.45	Region of occurrence of calculated stress in eighth cycle	99
4.1	Examination of repeatability of SPC test results	101
4.2	Total deflection measured from SPC tests on 316L(N) SS at 923 K	101
4.3	Creep deflection curves for 316L(N) SS at 923 K	102
4.4	Rate of deflection curves for 316L(N) SS at 923 K	103
4.5	Rate of deflection curves for 316L(N) SS plotted against normalised time at 923 K	103
4.6	Isothermal rupture curve obtained for 316L(N) SS at 923 K	104
4.7	Ruptured SPC specimen tested at 923 K at (a) 300 N along with indenter and (b) 480 N (lateral view)	105
4.8	(a) SEM fractograph of SPC specimen tested at 923 K at 720 N (b) Higher magnification image of same surface	105

Fig. No.	Title	Page No.
4.9	Geometry of deformation of SPC test specimen	107
4.10	Relationship derived between measured SPC deflection and strain	108
4.11	Maximum strain curves derived from SPC deflection for 316L(N) SS	109
4.12	Schematic illustration of analyses of transient and tertiary creep deflection	112
4.13	Norton power law relationship shown for 316L(N) SS	113
4.14	Monkman-Grant relationship established for 316L(N) SS at 923 K	114
4.15	Relationship between rate of exhaustion of transient creep and steady state deflection rate	115
4.16	Relationship between rate of exhaustion of transient creep and time to attain steady state deflection rate	116
4.17	Relationship between initial creep deflection rate and steady state creep deflection rate	117
4.18	Master curve obtained for transient SPC deflection	118
4.19	Relationship between ϕ and steady state deflection rate	120
4.20	Dependence of time spent in tertiary stage on rate of acceleration of tertiary creep	121
4.21	Relationship between final creep deflection rate and steady state deflection rate	122
4.22	Master curve obtained for tertiary SPC deflection	123
4.23	Trends of variation of rate of exhaustion of transient creep, steady state deflection rate and rate of acceleration of tertiary creep with rupture life	124
4.24	Dependence of transient, secondary and tertiary creep parameters on applied load	125
4.25	Optical micrograph of sectioned SPC specimen tested at 923 K at 400 N and interrupted at (a) secondary stage – 35h (b) tertiary stage 65 h and (c) just before rupture 74 h (rupture life at same load is around 75 h)	127
4.26	Influence of temperature on SPC deformation at 400 N	128
4.27	Determination of SPC activation energy; Temperature range: 898-973 K	129
4.28	Dependence of SPC rupture life on temperature. Temperature range: 898-973 K	130
4.29	Monkman-Grant relationship established over SPC data in the temperature range 898-973 K	131
4.30	Comparison of SPC loads with conventional creep stress, taking rupture life as common in abscissa	132
4.31	Correlation of SPC equivalent stress with uniaxial creep stress	133
4.32	Comparison of variations of SPC steady state deflection rate and conventional creep steady state creep rate with rupture life	134
4.33	Comparison of steady state creep rate values determined using derived strain curves with conventional test results	134
4.34	Relationship between rate of exhaustion of transient creep and steady state creep rate calculated from uniaxial creep tests	136
4.35	Variation of rate of exhaustion of transient creep with time to attain steady state creep rate	136
4.36	Variation of rate of exhaustion of transient creep with rupture life, as obtained from uniaxial creep and SPC tests	137
4.37	Variation of rate of exhaustion of transient creep with rupture life, as obtained from uniaxial creep and SPC tests on multiplying 'κ' value by empirical factor 1.8	138

Fig. No.	Title	Page No.
4.38	Master curves for transient creep deformation as estimated from SPC and uniaxial creep tests	138
4.39	Comparison of FEA predicted curves with test results	141
4.40	Von-Mises stress developed in SPC specimen	142
4.41	Damage accumulation in the deformed specimen	143
4.42	Symbol plot of Maximum principal stress	144
5.1	Effect of nitrogen on load-depth of indentation curves for 316LN SS at 723 K	146
5.2	Flow curves obtained for (a) 11N (b) 14N and (c) 22N steels	147
5.3	Typical comparison of flow curves obtained for various heats at 973 K	148
5.4	Strain hardening exponent at various temperatures as function of nitrogen content	149
5.5	Strength coefficient at various temperatures as function of nitrogen content	149
5.6	Influence of nitrogen content on yield stress at different temperatures	150
5.7	Influence of nitrogen content on UTS at different temperatures	151
5.8	YS and UTS plotted as a function of nitrogen content at (a) 298 K (b) 523 K (c) 623 K (d) 723 K (e) 823 K (f) 923 K and (g) 973 K	153
5.9	SPC curves obtained for 11N steel at 923 K	154
5.10	SPC curves obtained for 14N steel at 923 K	154
5.11	SPC curves obtained for 22N steel at 923 K	155
5.12	Influence of nitrogen content on SPC curves for 316LN SS at (a) 550 N (b) 450 N (c) 400 N and (d) 300 N	156
5.13	Isothermal rupture life curves determined for various nitrogen content	157
5.14	Dependence of steady state deflection rate on applied load shown for various nitrogen content	158
5.15	Rupture lives plotted as function of nitrogen content	158
5.16	Steady state deflection rate plotted as function of nitrogen content	159
5.17	SEM fractograph of SPC specimen of 11N steel tested at 923 K taken at (a) lower and (b) higher magnification	160
5.18	Fractured surface of 14N steel specimen tested at 923 K	160
5.19	Relationship between rate of exhaustion of transient creep and steady state deflection rate for the four heats	162
5.20	Relationship between rate of exhaustion of transient creep and time to attain steady state deflection rate, for the four heats	163
5.21	Relationship between initial creep deflection rate and steady state deflection rate for the four heats	164
5.22	Master curve for transient creep deflection determined for four heats	165
5.23	Estimation of rupture life based on rate of exhaustion of transient creep	165
5.24	Dependence of rate of exhaustion of transient creep on applied load	166
5.25	Rate of exhaustion of transient creep plotted as function of nitrogen content	167
5.26	Relationship between rate of acceleration of tertiary creep and steady state deflection rate	168
5.27	Relationship between rate of acceleration of tertiary creep and tertiary life	168

Fig. No.	Title	Page No.
5.28	Relationship between final creep deflection rate and steady state deflection rate	169
5.29	Master curves for tertiary creep deflection	170
5.30	Variation of rate of acceleration of tertiary creep with rupture life	170
5.31	Dependence of rate of acceleration of tertiary creep on applied load	171
6.1	Microstructural heterogeneity across 316LN SS weld joint	174
6.2	Load-depth of indentation curves obtained across 316LN SS weld joint at 923 K	174
6.3	Correlation of results from ABI and uniaxial tensile tests on weld joint	175
6.4	Flow curves for various zones of 316LN SS weld joint	176
6.5	Flow curves obtained on HAZ of weld joint at various temperatures	177
6.6	Optical micrograph of indentations across 316LN SS weld joint at 298 K	178
6.7	Optical micrograph of indentation at 298 K on (a) HAZ (b) base metal (c) weld metal	179
6.8	Evaluation of yield stress across 316LN SS weld joint	180
6.9	Evaluation of ultimate tensile strength across 316LN SS weld joint	181
6.10	Estimation of UTS/YS ratio across 316LN SS weld joint	181
6.11	Variation of strength at several passes of 316LN SS weld joint at 298 K	182
6.12	SPC curves obtained for weld metal at 923 K	183
6.13	SPC curves obtained for HAZ at 923 K	183
6.14	Rupture curves obtained from various regions of 316LN SS weld joint	184
6.15	Steady state deflection rate obtained from various regions of 316LN SS weld joint	185
6.16	SEM fractograph of SPC specimen sliced out of HAZ region and tested at 923 K	186
6.17	SEM fractograph of weld metal specimen tested at 923 K	186
6.18	Variation of creep strength across various zones of 316LN SS weld joint	187
6.19	Variations of κ , $\dot{\delta}_s$ and ϕ across the weld joint	188
6.20	Master curves for transient creep deflection for various zones across 316LN SS weld joint	188

LIST OF TABLES

Table No.	Title	Page No.
2.1	Chemical composition of 316LN SS [wt.%]	37
2.2	Chemical composition of four heats of 316LN SS [wt.%]	38
2.3	Chemical composition of 316LN SS weld joint [wt.%]	39
3.1	Surface roughness achieved after each level of polishing	69
4.1	Parameters used for defining creep model	141

NOMENCLATURE

a	radius of hemispherical hydrostatic core under ABI indenter	r_c	outer radius of plastic zone developed under ABI indenter
a_c	radius of arc of contact in ABI test	t	time
d	chordal diameter of indentation	t_{ot}	time to onset of tertiary creep
d_p	plastic diameter of indentation	t_r	SPC rupture life
d_t	total diameter of indentation	t_{r-uc}	uniaxial creep rupture life
h	thickness of SPC specimen	t_s	time to attain steady state deflection rate
h_o	initial thickness of SPC specimen	v_i	indenter velocity
h_e	elastic depth of indentation	A	yield parameter
h_p	plastic depth of indentation	B	yield offset constant
h_t	total depth of indentation	D	Diameter of ABI indenter
m	Meyer's coefficient or index	E	Young's modulus of indented material
n	strain hardening exponent	E_{ind}	Young's modulus of ABI indenter
n_r	load exponent of SPC rupture life	E_{spec}	Young's modulus of ABI specimen
n_{spc}	load exponent of steady state deflection rate	F	SPC load
n_{uc}	stress exponent of steady state creep rate	H	Indentation hardness
p	rate of acceleration of uniaxial tertiary creep	K	strength coefficient
r'	rate of exhaustion of uniaxial transient creep	P	load applied in ABI test
r	radius of SPC spherical indenter	Q	Activation energy
r_a	radius of contact area (SPC)	Q_f	Activation energy for fracture
		R	Universal gas constant
		R_h	Radius of receiving hole in SPC setup
		R_i	Radius of ABI indenter

T	Temperature	θ	angle made by the normal to surface of SPC specimen with the vertical axis
α	effective area parameter	θ_0	value of θ at the contact boundary
α_m	material parameter in ABI analysis	κ	rate of exhaustion of transient creep in SPC analysis
β	material yield slope	μ	Poisson's ratio of indented material
δ	SPC deflection	μ_{ind}	Poisson's ratio of ABI indenter
δ_o	instantaneous SPC deflection on loading	μ_{spec}	Poisson's ratio of ABI specimen
δ_3	tertiary creep deflection	σ	uniaxial stress
δ_c	constraint factor	σ_1	maximum principal stress
δ_r	rupture SPC deflection	σ_2	mid principal stress
δ_T	limiting transient creep deflection	σ_3	minimum principal stress
$\dot{\delta}_i$	initial creep deflection rate	σ_{eq}	Von Mises equivalent stress
$\dot{\delta}_f$	final creep deflection rate	σ_H	hydrostatic stress
$\dot{\delta}_s$	steady state deflection rate	σ_t	true stress
ε	strain	σ_{uts}	True ultimate tensile strength
ε_o	instantaneous strain on loading	S_{uts}	Engineering ultimate tensile strength
ε_{cont}	strain at the contact boundary	σ_y	yield stress
ε_p	true plastic strain	Φ	dimensionless parameter used in ABI analysis
ε_T	limiting transient creep strain	φ	rate of acceleration of tertiary creep in SPC analysis
ε_u	uniform strain	ω	scalar damage variable
ε_3	tertiary creep strain		
$\dot{\varepsilon}$	ABI strain rate in each cycle		
$\dot{\varepsilon}$	creep rate		
$\dot{\varepsilon}_s$	steady state creep rate		

CHAPTER 1

Introduction

The tensile and creep properties of a material are conventionally evaluated by conducting uniaxial tensile and creep tests on specimens of sizes specified as per the ASTM standards E-8^[1] and E-139^[2], respectively. But sufficient material may not be available for carrying out the conventional tests in some practical situations such as: (i) Residual life assessment of components in service in high temperature applications, where removal of bulk material from the component for testing purpose would itself lead to its impairment. (ii) Study of weld joint requires localised characterisation of narrow microstructural regions across the weld joint. The conventional tests can be used to evaluate tensile or creep properties of the weld joint as a whole and not the individual constituents. In an ideal situation, the weld zones can be formed in the material by applying heat treatment that simulates the thermal conditions experienced by the various regions in the weld joint during welding. Even then, the simulated specimens may not truly represent the weld joint. (iii) The development of new alloys for high temperature applications usually involves detailed tensile and creep testing, thus demanding large quantity of heat to be produced. Also, the heat lot tested may not be the final one and the alloy development programme generally requires multiple iterations before optimising the chemical composition. For each iteration, production of a new lot of material involves huge cost, efforts, wastage and time. Therefore, alternative testing methodologies involving limited volume of material are to be looked upon in such situations, where conventional testing method may not be helpful.

1.1 Small specimen testing techniques

One way to tackle the issue of testing volume is miniaturisation of specimen, which is proportionately scaling down the size of test specimen and loading such sub-size uniaxial

specimen in conventional testing machines. As testing sub-size specimen is not standardised, different sizes of specimens are used, the smallest one found in literature being the specimen with length 3.1 mm and thickness 0.2 mm ^[3]. Miniature flat specimens of length 25.4-44.45 mm and thickness 0.25-0.76 mm were developed for irradiation damage studies after irradiation in experimental reactor ^[4]. The advantage of such tests is that the uniaxial flow behaviour is obtained directly. Alternatively, there are several innovative, non-invasive small specimen testing methodologies evolving for determining tensile and creep properties of a material.

Shear punch test is a small specimen testing technique used for evaluation of tensile properties of the material, by forcing a flat end cylindrical punch into a disc specimen clamped between the set of dies and then analysing the measured load-displacement curve ^[5, 6]. It is basically a slow blanking process in which the test specimen is ruptured through shear deformation taking place along the annular clearance zone between the flat punch and the die. In an impression creep test, a cylindrical indenter (of typical size $\Phi 1$ mm) is penetrated into the specimen (of typical size 10x10x2.5 mm) till the steady state creep stage is obtained ^[7]. As the area of contact with the specimen is fixed, constant stress can be maintained during the test. Impression creep tests were carried out to evaluate the creep behaviour of 316LN stainless steel ^[8]. The limitation of this technique is that the tertiary stage observed in uniaxial creep test is absent and the rupture data cannot be obtained. The material of indenter should have enough creep strength; say two or three orders of magnitude higher than the creep strength of the testing material, to cause required impression on the test surface.

Small ring creep test ^[9] is carried out by diametrically loading a circular or elliptical ring (radius ~ 3 -10 mm, ring thickness ~ 1 -2 mm) and measuring the load line deformation of specimen. Conversion factors are used to establish relationship between applied load and equivalent uniaxial stress. Since the deformation measured during the test is large, the test is

relatively insensitive to experimental noise and hence testing can be done at low equivalent stress. But the test is capable of producing only primary and secondary creep data of materials. Another drawback is the specimen geometry required for the test, as the fabrication of such geometry is complicated, especially from small regions such as narrow weld joints.

The small pin-loaded one-bar specimen (OBS) and two bar specimen (TBS) creep test are recently invented to obtain the creep properties ^[10, 11]. The OBS test involves four loading pins, two of them are used to constrain the specimen and another two pins are used to apply tensile load to the specimen. In case of TBS test, the specimen is loaded using two loading pins, one to constrain the specimen and another one to apply tensile load. The specimen deformation is recorded till the rupture of the specimen.

A new creep test method called small cantilever beam test is proposed to evaluate creep properties by subjecting a cantilever beam to concentrated load and converting the load into equivalent uniaxial stress using analytical equations ^[12]. The data conversion method is based only on small deformation and is not suitable for all stress levels.

Automated Ball Indentation (ABI) technique is a miniature specimen testing technique used for evaluating tensile and fracture properties of materials by carrying out indentation on the test surface. Small Punch Creep (SPC) testing is another promising testing technique used to evaluate the creep properties by testing small volume of material in the form of a thin disc specimen. Hyde et al. ^[13] reviewed several small specimen creep test techniques and observed that SPC technique is capable of providing reliable creep rupture data.

This thesis focuses on the use of ABI and SPC testing techniques for evaluation of tensile and creep properties and takes advantage of their applications. The ABI and SPC techniques are described in detail in the following sections.

1.2 Automated Ball Indentation technique

Indentation tests have been used for several decades to determine hardness and other mechanical properties. Subsequently instrumented indentation tests are developed to record and control the load and displacement signals from the indentation tests. Nano-indentation tests have been carried out on the same principles but at a very small length scale. With the advancement of digital technology, the Automated Ball Indentation technique fully automates the measurement and analysis of data from spherical indentation tests.

Automated Ball Indentation (ABI) technique employs strain-controlled multiple indentation cycles at single penetration location on the polished metal surface by a spherical indenter, with each cycle comprising loading and partial unloading ^[14,15]. It is used for evaluating tensile and fracture properties of materials such as yield stress, ultimate tensile strength, strain hardening exponent, fracture toughness, etc.

In case of indenters of conical or pyramidal shape, the indentation shape is invariant with depth of indentation and hence only a single stress-strain data point (at about 8% strain) can be obtained ^[16]. Multiple stress-strain data points can be obtained with the use of spherical indenter. The applied load - depth of indentation data measured during ABI test are analyzed to obtain the tensile properties of a material, by making use of elasticity and plasticity theories and semi-empirical relationships that govern the material behaviour under indentation loading ^[17].

1.2.1 Theory of indentation

The contact stresses are developed once the spherical indenter comes into contact with the specimen surface. The test surface deforms elastically according to Hertzian theory for normal contact between elastic solids. When a flat surface is deformed elastically by a spherical indenter, the region of contact is an arc of radius (a_c) ^[18],

$$a_c = \left[\frac{3}{8} PD \left(\frac{1 - \mu_{ind}^2}{E_{ind}} + \frac{1 - \mu_{spec}^2}{E_{spec}} \right) \right]^{\frac{1}{3}} \quad (1.1)$$

where, P is applied load, D is diameter of indenter, E_{ind} and E_{spec} are Young's modulus of indenter and specimen, μ_{ind} and μ_{spec} are Poisson's ratio of indenter and specimen respectively. The maximum pressure occurs at the centre of the indentation circle and becomes zero at the periphery of the indenter. The pressure (Pr_x) at any point at a distance x from the centre of indentation is,

$$Pr_x = Pr_0 \sqrt{1 - \left(\frac{x}{a_c} \right)^2} \quad (1.2)$$

where, Pr_0 is the maximum pressure at the centre of indentation and is equal to 1.5 times the mean pressure over the region of contact. As the applied load increases, the distribution of pressure (normal stress) becomes flatter.

The contact circle grows with increasing load in three mechanically distinct stages such as (1) elastic (2) elastic-plastic transition and (3) fully developed plastic regimes ^[19]. In the elastic regime, the deformation is reversible. As the depth of indentation increases with higher applied load, the material undergoes plastic deformation which in turn is confined by an elastic region surrounding the plastic zone (Fig. 1.1). The transition regime shows the nucleation of plastic zone. With further increase in load, plastic zone beneath the indenter progressively expands till the whole material around indentation is in a plastic state and a fully developed plastic zone is formed. The stress state in the plastic zone comprises of hydrostatic compressive stress and shear. The shear component alone is responsible for plastic flow. The maximum shear stress in the specimen occurs at a depth of 0.285 times the total diameter of indentation below the test surface. Its magnitude on the axis of indenter is 0.47 times the mean pressure. The initial yielding of the material takes place at this point. The

plastic strain is maximum at the centre of indenter tip and decreases with radial distance from the axis of symmetry and becomes maximum 0.2 at the contact edge.

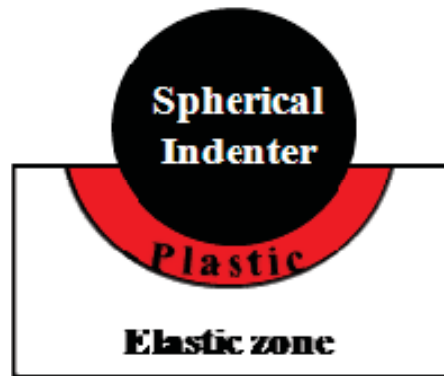


Fig. 1.1 Various zones formed during indentation.

Tabor ^[18] was the first to correlate indentation hardness (H) measured using spherical indenter with equivalent uniaxial stress (σ) as, $H=3\sigma$. Those correlations work on the following assumptions (i) monotonic true stress - true plastic strain curves obtained from tension and compression testing are reasonably similar, which is valid upto ultimate tensile strength since there is no necking instability in compressive loading; (ii) indentation strain correlates with true plastic strain in uniaxial tensile test; and (iii) mean ball indentation pressure correlates with true flow stress in uniaxial tensile test. The plastic flow in the region under the indenter is constrained by a large volume of elastic region enveloping the plastic zone. Due to such confinement of plastic zone within elastic zone, the increase in resistance to plastic flow under indentation conditions is higher than corresponding uniaxial flow stress. Several expanding cavity models (ECMs) have been developed to describe the indentation process, on the basis of Hill's solution for quasi-static expansion of an internally pressurised spherical shell of elastic-perfectly plastic materials. Johnson's ECM ^[20] describes the indentation as being encapsulated by a hemispherical hydrostatic core of radius a , surrounded by an incompressible hemispherical plastic zone of outer radius r_c which in turn is

constrained by the elastic region (Fig. 1.2). The volume of material displaced by an indenter of radius R_i is assumed to be accommodated by the radial expansion of the hemispherical core.

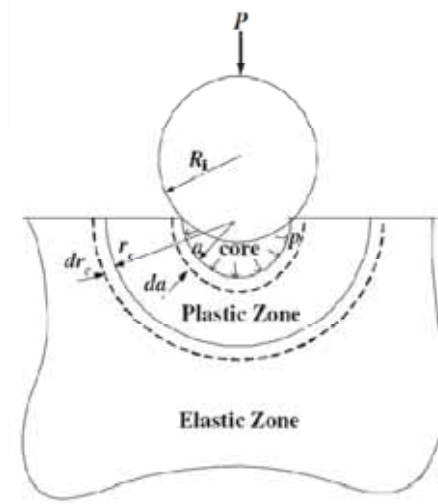


Fig. 1.2 Johnson's expanding cavity model.

The indentation hardness (H) is defined as the ratio of applied load to projected area of indentation measured in indentation test. Johnson's ECM related indentation hardness and yield stress (σ_y) as a function of both material properties and geometry of indenter as,

$$\frac{H}{\sigma_y} = \frac{2}{3} \left(1 + \ln \frac{E}{3\sigma_y} \frac{a}{R_i} \right) \quad (1.3)$$

Where, E is Young's modulus of indented material. Gao ^[21] developed ECM for elastic power law hardening materials subjected to spherical indentation based on solutions for internally pressurized thick-walled spherical shells of strain hardening material as,

$$\frac{H}{\sigma} = \frac{2}{3} \left\{ \left(1 - \frac{1}{n} \right) + \left(\frac{3}{4} + \frac{1}{n} \right) \left(\frac{1}{4} \frac{E}{\sigma_y} \frac{a}{R_i} \right)^n \right\} \quad (1.4)$$

where, n is the strain hardening exponent. This model can be reduced to Johnson's model if strain hardening exponent is not considered. This ECM was further improved by Gao to include the effect of indentation size ^[22].

An important parameter called constraint factor (δ_c) is used to correlate the mean pressure obtained from ABI tests with uniaxial flow stress, by considering the constraint effect over plastic deformation. The constraint factor is defined as the ratio of resistance to plastic flow under indentation conditions to the equivalent uniaxial flow stress. The value of constraint factor is based on the three stages of development of plastic zone and is specified by a dimensionless parameter Φ . The parameter Φ can be understood as the ratio of strain imposed by the indenter to the maximum strain that can be accommodated by the material before yielding. Johnson ^[20] observed on the basis of detailed indentation studies that the constraint factor is a linear function of $\ln(\Phi)$ in the elastic-plastic transition regime. During fully developed plastic zone, the parameter Φ attains the value around 28-30 and the ratio of mean pressure developed in indentation test to uniaxial flow stress remains nearly constant. Francis ^[19] improved the values of parameters through analysis over a large variety of materials available in the literature and provided the value of constraint factor as,

$$\begin{aligned} \delta_c = & \quad 8\Phi/3\pi (1-\mu^2) & \quad \Phi \leq 1.15 & \quad \text{(Elastic)} \\ & 1.11 + 0.534 \ln\Phi & \quad 1.15 \leq \Phi \leq 27.3 & \quad \text{(Transition)} \\ & 2.87 & \quad \Phi \geq 27.3 & \quad \text{(Fully developed plastic)} \end{aligned} \quad (1.5)$$

The parameter Φ is defined as $\Phi = (\epsilon_p E / 0.43\sigma_t)$ and at $\Phi > 27$, the fully plastic regime occurs. Tirupataiah et al. ^[23] compared Meyer hardness-strain curve with tensile test stress strain curve and estimated constraint factor as a function of strain, by dividing hardness by flow stress in the same range of strain. The ratio of Young's modulus to yield stress is interpreted as a measure of material accommodated in plastic zone during indentation ^[24]. The lower value of this ratio is marked by elastic dominated deformation offering lower constraint than with a higher ratio.

Meyer's law expresses the relationship between load (P) and size of indentation and is stated for a given indenter size as ^[18],

$$P = k d^m \quad (1.6)$$

where, d is the chordal diameter of indentation, k is material constant and m is called Meyer index whose value usually lies between 2 and 2.5. The value of 'k' is numerically equal to 'P' at d=1. The value of m is closer to 2 for fully work hardened materials and is near 2.5 for fully annealed materials ^[18]. Meyer found experimentally that index m was almost independent of the indenter size but 'k' decreased with increasing diameter of indenter. If D₁, D₂, D₃,... are the diameters of indenters that produces indentations of chordal diameters d₁, d₂, d₃,... respectively, 'k' varies such a way that ^[18],

$$A = k_1 D_1^{m-2} = k_2 D_2^{m-2} = k_3 D_3^{m-2} \dots, \quad (1.7)$$

where 'A' is a constant. The general relationship among load, indenter diameter and chordal diameter of indentation can then be obtained by combining Eqns. (1.6) and (1.7) as,

$$P = \frac{A d_1^m}{D_1^{m-2}} = \frac{A d_2^m}{D_2^{m-2}} = \frac{A d_3^m}{D_3^{m-2}} = \dots, \text{ which is rewritten as,}$$

$$\frac{P}{d^2} = A \left(\frac{d}{D} \right)^{m-2} \quad (1.8)$$

The triaxial stresses acting heavily on small plastic zone beneath the indenter force the material to flow upwards or downwards along the loading direction with respect to the surface of the indentation (Fig. 1.3). The upward flow of material towards the surface is called material pile-up which happens usually with highly work hardened materials whose Meyer index is near 2. In case of annealed metals, another phenomenon called sink-in is generally observed, where the deformed material is found depressed around the indentation. The extent of pile-up depends on the yield ratio and strain hardening exponent of the material tested.

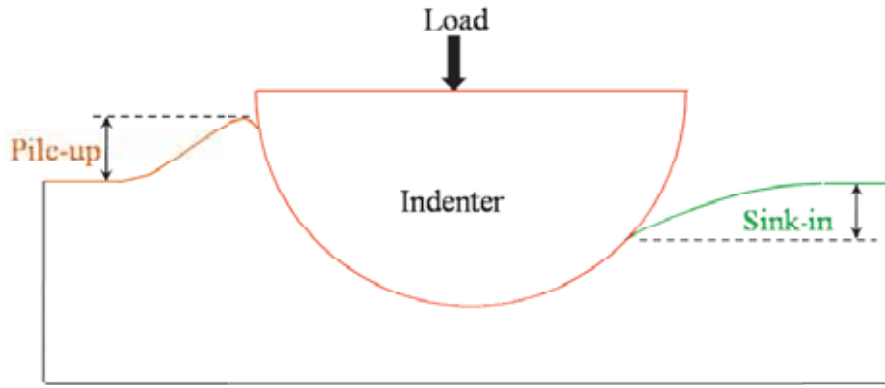


Fig. 1.3 Pile-up and sink-in phenomenon.

1.2.2 Advantages and applications

ABI technique is almost non-destructive as it leaves behind only a small impression on the tested surface at the end of the test. The spherical indentation has no sharp edges and hence there is no possibility of formation of stress concentration sites on tested surface. The residual stresses produced are compressive in nature which can retard crack initiation. Therefore, in-situ non-destructive structural integrity assessment of components operating in high temperature applications such as nuclear, chemical, aerospace, defence, etc. is feasible with ABI testing. The applications of ABI technique generally include estimation of degradation of strength of material on service exposure, weld joint characterization, etc.

ABI technique has been widely used for characterisation of materials used in nuclear industry. It is possible to study irradiation embrittlement of reactor pressure vessel steel, degradation of piping, etc., using ABI technique. The stress-strain curves obtained for A533 steel under various conditions such as unirradiated, embrittled neutron irradiated and post-irradiated thermally-annealed conditions were compared to quantify the degree of embrittlement as well as recovery due to thermal annealing ^[25]. The response to neutron irradiation (fast neutron fluence of $\sim 1 \times 10^{18} \text{ cm}^{-2}$) of mock-up A508 class 2 base plate and weld bead was investigated using ball indentation (BI) technique ^[26]. ABI technique was used

to measure the through-the-thickness variations of mechanical properties in SA508 Grade 3 forging steel (used in heavy section components of nuclear power plants) ^[27]. The highest gradient in variation in mechanical properties was reported in the near-surface region that was caused due to cooling rate gradient during heat treatment. ABI tests were conducted to study the effect of cold working in the range 0 to 12% on tensile and fracture properties of low alloy ferritic A36 steel (containing 0.29 wt.% C, 0.8-1.2 wt.% Mn, 0.15-0.3 wt.% Si) used for pressure vessel internals and support structures in light water reactors ^[28]. High strength ASTM grade SA-533B steels are commonly used for primary pressure vessels for pressurized water reactors. The gradients in tensile and fracture properties across SA-533B steel welds were studied using ABI technique ^[29]. The average flow stress and plastic strain were deduced from spherical indentation tests on a mechanically anisotropic Zr-2.5% Nb CANDU pressure tube material ^[30]. An in-house developed in-situ ball indentation system was used to measure mechanical properties inside an irradiated pressure tube removed from Kakrapar Atomic Power Station-2, after 12.76 full power years of operation ^[31].

ABI technique has also been used to study the effect of microstructural variables such as heat treatment, ageing, chemical composition, etc. on the tensile properties of materials. ABI tests were conducted on nickel base alloy 625 that was aged at various temperatures in the range 873-1173 K and the peak in strength observed at 973 K was attributed to precipitation of γ'' precipitate and fall in strength afterwards was due to the growth of δ -phase precipitates ^[32]. Mathew et al. ^[33] reported the effect of low temperature ageing on the tensile and fracture properties of cast CF-8 SS which is used for several components such as pump and valve casings, primary coolant pipes, etc., in pressurized water reactors. BI tests on 316L SS cold rolled to 7%, 15%, 24% and 40% of initial thickness revealed that with increase in percentage of cold rolling on 316L SS, tensile strength increased and strain hardening exponent decreased ^[34]. The degradation in mechanical properties due to thermal ageing of modified

9Cr-1Mo steel (upto 20,000 h) was quantified ^[35]. For the same material, a considerable reduction in creep strength of stressed gauge portion of the creep tested specimen was found in comparison with unstressed head (only thermally exposed portion) ^[36]. The variations in mechanical properties due to various heat treatments on En24 steel and Inconel 718 alloy were evaluated using BI tests ^[37, 38]. It was observed that the tensile strength decreased whereas strain hardening exponent increased due to softening of material with increase in tempering temperature. Similarly, the effect of tempering temperature on tensile properties of P92 steel (normalised at 1353 K) was investigated and the tensile properties such as yield stress, tensile strength and strength coefficient were found to decrease with increase in tempering temperature ^[39]. It was also found that there was no significant change in tensile properties due to change in normalizing temperature in the range 1313-1353 K ^[40]. ABI technique has also been used to characterize a variety of other materials such as molybdenum ^[41], high- manganese twinning induced plasticity steel ^[42], etc.

ABI technique has been used to evaluate the fracture properties ^[43-45] even though no fracture actually occurs. The fracture behaviour is evaluated from ABI by assuming that the indentation generates triaxial stress fields near and ahead of contact of indenter with test surface, which is similar to concentrated stress field triaxiality observed in front of a crack tip. A new parameter called indentation energy to fracture (IEF) was developed to determine the fracture energy by integrating the indentation deformation energy from the beginning of the test upto a critical indentation depth ^[46].

ABI technique was used to characterise the gradient in mechanical properties of HY-100 weld joint ^[47]. The gradient in strength of base metal, weld metal and different positions of heat affected zone of SA-533B steel weld shown by ABI results was consistent with changes in the microstructure ^[29]. The optimum value of heat input required for metal inert gas welding 316L SS plates that provided maximum strength and hardness value was obtained

using ABI technique ^[48]. BI tests conducted on two weld pools of cast stainless steel showed that weld pool having higher chromium content had higher strength but with lower fracture toughness, which was attributed to presence of higher amount of ferrite in it ^[49].

1.2.3 Limitations

The ABI testing has some limitations such as,

- The area of contact between the indenter and specimen keeps changing during the test, which makes it complicated to estimate the stress at any instant and also to maintain a constant strain rate.
- Assumptions and approximations are involved in ABI analysis as there is no actual necking or crack visible in this test.
- The ABI testing is not yet standardized.

In spite of such limitations, ABI technique is evolving as a potential tool for various applications because of its simplicity in completing the test and data analysis. It may be established as a reliable tool for use in nuclear industry with the aid of continuous and detailed studies over reactor materials.

1.3 Small Punch Creep technique

1.3.1 Small Punch test

In Small Punch (SP) testing, a disc specimen held between upper and lower die is loaded using a spherical ball indenter, usually of ceramic material, till the specimen ruptures (Fig. 1.4). The SP test was originally developed for evaluation of post irradiation mechanical properties, giving consideration to space limitation in reactor for irradiation, difficulty in handling irradiated material, neutron irradiation costs scaling up with specimen volume, etc. ^[50-52].

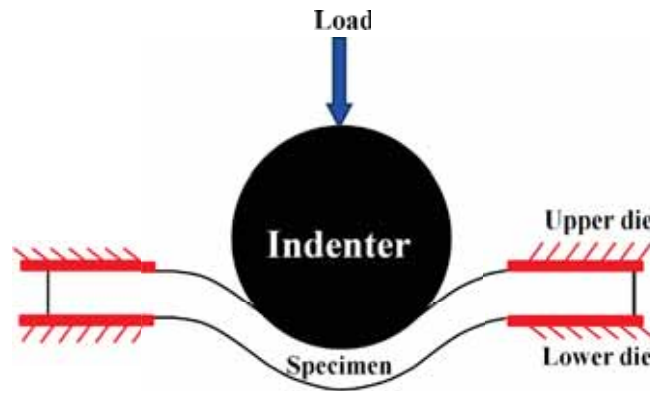


Fig. 1.4 Deformation of SP specimen.

The deformation behaviour of the SP disc specimen is divided into five regions such as, elastic bending, yield, plastic bending, membrane stretching and necking to failure ^[53]. The specimen undergoes elastic bending, as the ball initially comes in contact with the disc specimen. The bending action eventually produces enough stress to cause yield in the highest stressed region. When the thickness of SP specimen is increased, the effective stiffness of disc specimen is increased, thereby the load required to cause critical deformation is increased. Therefore, the load required to produce initial yielding increased with specimen thickness. Similarly, either by increasing the indenter diameter or decreasing the radius of receiving hole, the bending moment of the specimen tends to decrease resulting in increased yield load and maximum load.

Yielding subsequently produces plastic deformation leading to strain hardening. Plastic bending continues after yield, increasing the amount of plastic strain in the yielded sections with corresponding increase in flow stress. This results in the transfer of the load to adjacent non-yielded sections within the disc specimen, causing expansion of the yield front. This process continues until the yield front spreads completely through the specimen thickness. In addition, the yield front also spreads radially outwards. If the thickness of specimen increases, the yield front has to travel further and the plastic zone has to spread over larger

volume causing a higher level of deformation, which in turn demands higher load to be applied. This is followed by membrane stretching wherein the yield front extends beyond the region of contact between the punch and the disc. Deformation by membrane stretching places in the large annular section of specimen in tension which demands each section to contract laterally which in turn is resisted by development of lateral stresses in addition to longitudinal stress and this is a case of biaxial stress state of deformation. The membrane stretching leads to increase in load bearing capacity due to the combined effect of work hardening of the material as well as increase in contact area between the punch and the disc with increasing deformation.

The load required to produce certain deformation not only depends on thickness but also on the area of contact between the indenter and the specimen, because the increase in contact area naturally increases the amount of material undergoing deformation. Figure 1.5 shows schematically how the contact area between spherical indenter and specimen increases with increase in the central deflection of the specimen. Two distinct regions resulting from bending and membrane stretching modes of deformation can be seen.

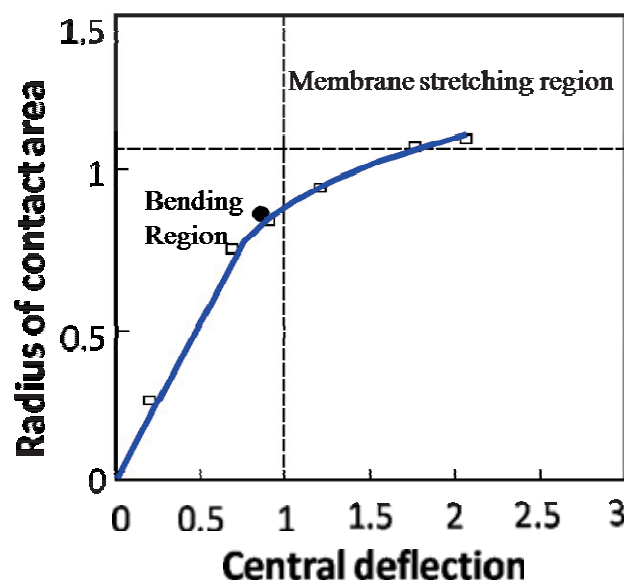


Fig. 1.5 Radius of contact area varying with central deflection ^[54].

The bending region is characterized by rapid increase of contact area with increase in central deflection. During plastic bending, the contact area is controlled by bending deformation. The bending region undergoes transition to a membrane stretching region where the contact area is controlled by reduction in thickness of the specimen ^[54]. Regardless of the punch diameter, the amount of contact between the punch and the disc is small and approximately the same at yield. The energy corresponding to the surface under load-displacement curve increases with increase in thickness of the specimen ^[55].

Actually, there is no clear boundary between the different stages and the deformation mode simply becomes predominant compared to another one. The stretching deformation exists at the beginning of the test but becomes predominant only during the membrane stretching stage. The deformation continues till the ductility is exhausted and specimen develops a neck due to thinning and finally leads to failure. The procedures for standard punch test of sheet metals described in ASTM standard E643-84 contain recommendations that can be applied to the SP specimen ^[56].

The SP test can be carried out in either load controlled mode or strain controlled mode, based on which the following two basic types of SP tests are extensively performed till the rupture of the disc.

(i) Constant deflection rate (CDR) test:

SP test carried out under strain controlled mode is equivalent to uniaxial tensile test on bulk specimens under constant strain rate. The ball punch penetrates through the disc at a given constant rate of deflection and the necessary force is measured. To a certain degree, the force-deflection curve obtained from SP test is similar to stress-strain curve of tensile tests. Fleury and Ha ^[57] calculated the stress under the indenter during plastic bending regime from the expression, $\sigma = CF_e / (4\pi r_a h_o / 3)$, where 'C' is a constant for the distributed load, F_e is the

load determined from the elastic calculation, r_a is the radius of contact area and h_o is the initial thickness. Milicka et al. ^[58] related the maximum force obtained from SP tests (F_{max}) on P91 steel with ultimate strength obtained from conventional uniaxial tensile tests (σ_{uts}) as, $F_{max}/\sigma_{uts}=7.26h - 0.63$, where 'h' is the thickness of the specimen. The SP technique is also used for evaluating the fracture toughness ^[53,59,60] and ductile to brittle transition temperature (DBTT) ^[52]. A remote controlled SP machine for post irradiation examination in the hot cell was developed to study the DBTT shift after irradiation on 2.25Cr-1Mo steel ^[61]. Apart from metals, SP testing is also used to measure the tensile properties of polymers such as ultra-high-molecular-weight-polyethylene used in total orthopaedic joint replacements ^[62]. The plastic deformation of martensitic T91 steel was studied in liquid lead bismuth eutectic using SP test and SP test seemed to be more sensitive to liquid metal embrittlement than conventional tensile test ^[63].

(ii) Constant force (CF) test:

SP test is also carried out under constant force and time dependence of the central deflection of the specimen is measured. This test is similar to conventional creep tests and has been described in detail in the following section.

1.3.2 Small Punch Creep test

The small punch test conducted in load controlled mode is known as Small Punch Creep (SPC) test which is used to obtain the creep properties of materials employed for applications at elevated temperatures. An interesting feature in SPC test is that the measured curve appears similar to conventional creep curve. It has attracted the attention of several researchers as an innovative tool to evaluate creep properties and their contributions over the years aided SPC technique to evolve as an effective technique.

Initially, the spherical indenter imparts a point load to disc specimen developing localised stresses around the little contact area, causing local plasticity and accumulation of large amount of plastic strain in short time. Ule and Sustar ^[64] used flat specimens as well as sombrero-shaped specimens whose contours were shaped before SPC test to fit the shape of the punch. It was found that the rupture life of flat disc specimens were one order of magnitude shorter than that of sombrero shaped specimens. This is because the initial rapid and hot plastic deformation accelerated the dynamic recovery process in flat disc specimen, due to increased strain energy density. However, a good consistency was observed between the activation energies obtained from conventional creep test and SPC test with flat disc specimens, thus emphasizing flat disc specimens for valid creep measurement using SPC test. Zhou et al. ^[65] analysed the effect of indenter diameter using finite element method and concluded that decrease in indenter diameter causes significant reduction in the rupture time of specimen. Standard uniaxial creep specimens are machined such that the axis of cylindrical specimen is parallel to the direction of rolling. In case of SPC tests, square or circular disc specimens are subjected to biaxial state of stress. The tensile stresses act with radial symmetry in the plane of SPC specimen during bending as well as membrane stretching modes of deformation. The specimen is therefore cut such that the plane of specimen is parallel to the rolling direction. The specimen whose plane is cut normal to the rolling direction represents the transverse direction. SPC technique was used to characterise the anisotropic effect on creep properties in 14Cr ODS steel ^[66]. The test results revealed that the rupture lives were reduced to several orders of magnitude when loaded in transverse direction (plane of specimen normal to direction of extrusion) compared to other direction. There are several relationships and equations that govern the uniaxial creep deformation behaviour. Though the state of stress developed in SPC test specimen is biaxial, the uniaxial creep relationships have been found to be analogously applicable to SPC data. Parker et al. ^[67]

described SPC rupture life (t_r) as a function of load (F) and temperature (T), similar to stress and temperature dependence of rupture life in uniaxial creep test as, $\frac{1}{t_r} = B_1 F^{n_r} \exp\left(\frac{-Q}{RT}\right)$, where, B_1 is a constant, n_r is the load exponent of rupture life, R is universal gas constant and obtained the value of activation energy (Q) closer to that calculated from uniaxial creep tests. Tettamanti and Crudeli ^[68] calculated the values of Larson-Miller parameter, Monkman-Grant indicator and activation energy of ASTM A335 P12 steel. Dobes and Milicka ^[69] used an equation analogous to Monkman-Grant relationship to relate minimum creep deflection rate and time to rupture in SPC tests on chromium steel and low alloy steel. Several methods available for extrapolating uniaxial creep data were applied to SPC data. SPC test results obtained for P91 steel were analyzed using various parametric approaches such as Larson-Miller, Fisher-Dorn, Goldhoff-Sherby, Manson-Haferd, Manson-Succop and Sud-Aviation and the best description was achieved with Sud-Aviation parameter, thus validating the possibility to extrapolate SPC data towards longer creep exposure times ^[70]. Stratford ^[71] indicated that as both conventional creep and SPC similarly follow Monkman-Grant relationship, the damage mechanisms operating during SPC test may be similar to conventional creep test. Dorn equation has been applied to analyze SPC test results of 1.25Cr 0.5Mo pearlitic steels by using minimum creep deflection rate in place of minimum creep rate and load in place of stress ^[72]. Larson-Miller and Orr-Sherby-Dorn parametric methods were applied to predict rupture life by SPC test on AZ31 magnesium alloy and the master curves obtained were similar to conventional creep results ^[73]. However, the uncertainties existing with such extrapolation methods may be equally applicable to SPC tests data.

Though an international standard is still sometime away, a common code of practice (CoP) for SPC testing has been evolved by European Committee for Standardization (CEN) ^[74]. The CEN CoP mainly deals with the testing equipment, testing procedures, specimen size and procedures for data analysis, etc. The CoP was achieved by taking input from the results of

small punch round robin programme in which several members of European Pressure Equipment Research Council (EPERC) participated for the harmonisation of test procedures [75-77].

1.3.3 Correlation with uniaxial creep results

The existing procedures for design of high temperature components are based on the data generated from uniaxial creep tests. The challenge is to obtain a valid relationship to translate the results implied from SPC test in terms of conventional creep test. This is imperative for acceptance of SPC tests as an alternative for conventional creep tests. However, the state of stress in SPC test is biaxial whereas it is uniaxial in conventional creep test. In a conventional creep test, the important test parameter is stress (load/area of cross-section of specimen) whereas it is only load in SPC test. The mode of deformation in conventional creep test is tensile whereas the mode of deformation in SPC test is a combination of bending and membrane stretching.

Taking such issues into account, various methodologies are adopted to correlate SPC results with uniaxial creep results, although there is no universally adopted method for converting SPC load into its equivalent uniaxial stress. The correlation relationships containing several material and geometrical parameters are proposed. Some of them are purely empirical while some are based on membrane stretching theory. The value of SPC load (F) that give the same creep life as a uniaxial stress (σ) was achieved from the balance of forces as,

$$\frac{F}{\sigma} = \left[2\pi h \left(r + \frac{h}{2} \right) \sin \theta_0 \right] \sin \theta_0, \text{ where, } r \text{ is the radius of spherical indenter, } h \text{ is thickness of SPC}$$

specimen and $\sin \theta_0$ was obtained empirically from comparison among uniaxial and SPC tests [68]. Dobes and Milicka [78] suggested a method for the approximate correlation of the force in small punch test with the stress in conventional creep tests of same duration. The applied force in a small punch creep test of low alloy steel normalised by square of the

specimen thickness was about nine times the stress for the conventional creep test under constant stress and about ten times the initial stress for the creep test under constant load of the same duration. The ratio F/σ was determined to be about 1, by comparing the plot of load of SPC test versus Larson Miller Parameter (LMP) with the plot of uniaxial stress versus LMP^[79]. An empirical relationship which is obeyed by several engineering materials is given by $F/\sigma = K_1 r h^2/R_h D_f$, where, K_1 is a geometrical constant, r is the radius of the spherical indenter, h is the thickness of the specimen, R_h is the radius of receiving hole and D_f is the ductility factor for the material in the test temperature and load range^[80].

According to CEN CoP, the equivalent uniaxial stress for SPC load can be determined as^[81,82],

$$F/\sigma = 3.33 K_{SP} R_h^{-0.2} r^{1.2} h \quad (1.9)$$

where ' K_{SP} ' is a constant related to the ductility of the material. The value of K_{SP} is usually obtained for a given class of materials by comparing SPC loads and uniaxial creep stresses which result in the same rupture life. If ' K_{SP} ' value is not available for the investigated material, it is initially assumed as 1 and then corrected based on further tests. Taking into account the material and geometrical parameters, Eqn. 1.9 can be simplified to the form of ratio of SPC load to equivalent stress as, $F/\sigma = \alpha$, where α is called the effective area parameter (in mm²). The SPC test technique has been undergoing continuous evolution and standardization ever since its introduction.

1.3.4 Advantages and applications

There are various non-destructive methods available for integrity assessment of components in service such as, hardness testing, ultrasonic inspection, metallurgical replication, etc.; but these techniques do not evaluate the creep properties. SPC is a very attractive technique for evaluation of creep residual life and structural integrity assessment studies on components

operating in high temperature. Though SPC technique involves rupture of specimen, considering the amount of material to be scooped out from components in service for estimation of degradation of creep strength, it may still be considered as almost non-destructive. The size of its specimen makes it advantageous over conventional creep test as illustrated in Fig. 1.6. From the volume of raw material blank used for fabricating a conventional creep test specimen, roughly around 720 SPC specimens can be fabricated.

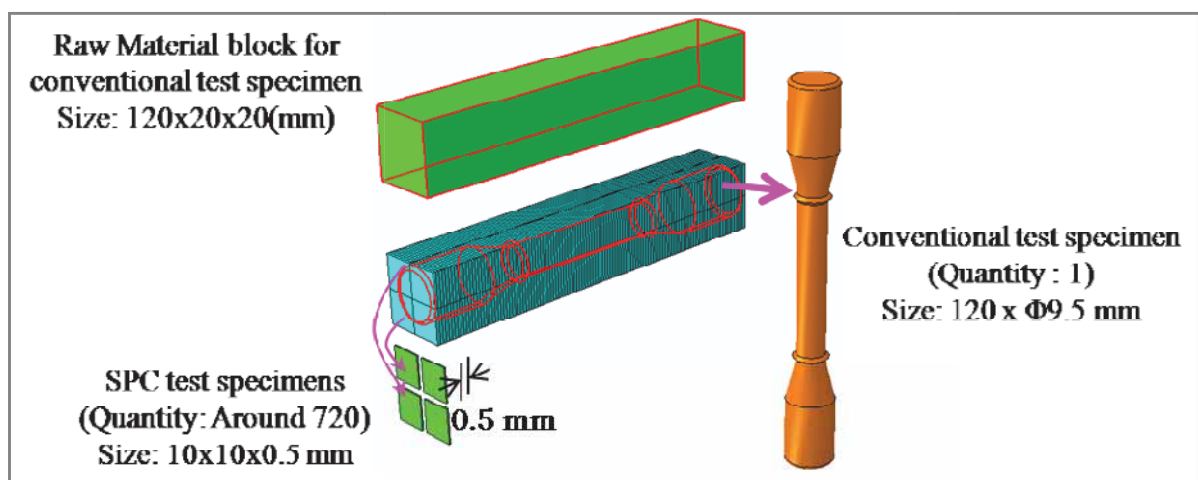


Fig. 1.6 Volume of material required for evaluating creep strength.

There are several applications of SPC technique in research and industry sector where conventional creep testing may not be suitable. It is essential to estimate the degradation in creep strength of components in long term service at elevated temperatures. Saucedo-Munoz et al. ^[79] applied SPC technique to estimate the change in creep properties of SUS 316 HTB stainless steel cut from secondary superheater tubes (exposed at 882 K for 100,600 hours) and found that the creep rupture strength of the unaged material was higher than that of the service-exposed materials. SPC tests were conducted on ASTM A335 P12 steel pipeline material of Italian ENEL power plant that was serviced for 227,000 hours at 813 K and forecasted the residual life upto 934,000 h ^[83]. An interlaboratory exercise was carried out in

different European countries to determine the residual creep life of service exposed components made of 14MoV 6 3 steel and X20CrMoV12 1 steel by employing SPC testing technique, showing good repeatability in the results ^[84]. SPC tests were carried out to measure the degradation of creep strength of tungsten alloyed 9% Cr ferritic steel due to thermal aging ^[85]. SPC technique was used for evaluating material deterioration due to ageing by applying it to aged low alloy steel (2¼- 1 Mo, V modified) in power generation and petrochemical plants ^[86]. Izaki et al. ^[87] tested virgin material, pre-crept (~50% of life fraction) and service aged (~20 years) material of 2.25Cr-1Mo steel boiler pipes and confirmed the decrease in creep strength of service exposed material. In all cases, the SPC test results indicated a clear reduction in creep life associated with enhancement of damage.

Localised characterisation of creep properties of weld joint comprising narrow, distinct and heterogeneous microstructural regions can be examined by SPC technique. SPC tests were conducted on various microstructural regions of P92 steel weld such as coarse grain heat affected zone (HAZ), fine grain HAZ, intercritical HAZ, weld metal and base metal at 873 K and intercritical HAZ was reported as the weakest part of weldment ^[88]. SPC tests were carried out following CEN CoP procedures on various regions of martensitic alloy P91 weldment and fine grained HAZ was identified as the weakest zone ^[89,90]. SPC technique was also used to estimate degradation of strength of weld joint in service. Komazaki et al. ^[91] evaluated damage of various zones of weld joint of a boiler header (1 Cr -0.3 Mo steel) in service for around 250,000 hours and estimated the remaining lives of HAZ, weld metal and base metal. SPC technique has also been used to measure the creep properties across variety of other weld joints made of reduced activation ferritic steel ^[92], Inconel 617 alloy ^[93], P91 steel ^[94], etc.

1.3.5 Limitations

Though SPC technique is largely utilised for various applications, it has its own limitations listed as follows:

- i) The amount of material under the indenter undergoing elastic, plastic and creep deformation is not constant. Hence defining the state of stress and strain in such a non-linear process involves high complexity and requires the aid of numerical methods.
- ii) Since the test time is generally short, typically a few hundreds of hours, creep behaviour due to long time microstructural changes in engineering alloys cannot be evaluated.
- iii) SPC testing is yet to be standardized.
- iv) The correlation between SPC results and uniaxial creep results are empirical.

Nevertheless, SPC test is a very attractive technique to evaluate creep properties of nuclear materials and service exposed materials in relatively shorter time and with minimal material consumed. Further investigations on reactor materials under different conditions can make SPC test to evolve as a reliable methodology to provide life extension data for nuclear industry.

1.4 Materials under investigation

Stainless steels are iron-carbon alloys that contain a minimum of 11.5 wt.% chromium and show resistance to corrosion and rust by forming a passive layer of chromium oxide. A variety of stainless steels suitable in specific for any intended application are produced by modifying the chemical composition. Stainless steels are broadly classified into five major groups namely, ferritic, austenitic, martensitic, duplex and precipitation hardened stainless steels.

Austenitic stainless steels are produced by stabilizing the face centred cubic (FCC) austenite (γ) phase against transformation into ferrite or martensite phase even at room temperature, by

the addition of nickel and other austenite stabilisers. The relative strength of austenite stabilisers is given by Ni equivalent (wt.%)= (%Ni) + (%Co) + 0.5(%Mn) +0.3(%Cu) + 30(%C) +25 (%N). The formation of δ -ferrite may occur, which may be difficult to eliminate completely during thermo-mechanical processing.

Austenitic stainless steels are chosen as the major structural materials for the currently operating and planned fast breeder reactors all over the world due to their elevated temperature mechanical properties, compatibility with liquid sodium coolant, design codification with availability of necessary data to designers, etc. Austenitic stainless steels have better high temperature strength and corrosion resistance as compared to ferritic and martensitic stainless steels. These steels do not undergo ductile to brittle transition at low temperatures as in the case of ferritic steels. These are low stacking fault energy materials and are generally non-magnetic. These are easily formable and weldable. However, these steels have low thermal conductivity and high thermal expansion coefficient as compared to ferritic steels, giving rise to high thermal stresses during service. Austenitic stainless steels generally have low yield stress and can be hardened by cold working rather than by heat treatment.

Austenitic stainless steels are susceptible to intergranular corrosion (IGC) and intergranular stress corrosion cracking (IGSCC) in chloride and caustic environments in the sensitised condition. Theoretical and experimental studies have shown that $(\text{Fe,Cr})_{23}\text{C}_6$ precipitation at grain boundaries and the consequent chromium depletion near grain boundary is the primary cause of sensitisation. Sensitised stainless steels are susceptible to corrosion due to decrease in chromium concentration around grain boundary regions. The time-temperature-sensitisation (TTS) diagram is useful to determine the critical linear cooling rate above which there is no risk of sensitisation.

1.4.1 316LN stainless steel

Failures due to intergranular stress corrosion cracking occur generally in the heat affected zone (HAZ) of welds of austenitic SS of type 316 due to sensitisation and residual stresses introduced during welding. The problem of sensitisation has been overcome in type 316 SS by reducing its carbon content in the range 0.02-0.03 wt.%. A loss in strength due to reduction in carbon content has been compensated by the addition of nitrogen and the material is designated as 316LN SS. A weak affinity of nitrogen to grain boundaries and the resulting absence of nitrogen segregation explain high resistance to intergranular corrosion. Nitrogen has greater solid solubility than carbon thus decreasing the tendency for precipitation. The nitrogen addition also retards the sensitisation kinetics because nitrogen delays the formation of chromium-rich carbides. Lower limits for carbon and nitrogen have been specified to ensure retention of mechanical strength of 316 SS.

Type 316L(N) SS containing 0.02-0.03 wt.% carbon and 0.06-0.08 wt.% nitrogen is used as the major structural material for out-of-core reactor assembly components in sodium cooled fast reactors in view of its compatibility with liquid sodium and adequate weldability. The mechanical properties including tensile, creep, fatigue, etc., are very crucial in the selection of 316LN SS for reactor structural components, operating with a plant design life of around 40 years. Irradiation properties are not so important for out-of-core structural materials.

Indigenously developed nuclear grade 316LN SS material has been used for this investigation. “Nuclear grade” steel differs from conventional grade steel with respect to closely controlled chemical composition, lower levels of inclusion content and low limits of residual elements such as sulphur, phosphorus, boron and silicon. The composition limits of 316LN SS have been set to meet specific property requirements. Chromium, molybdenum, nickel and carbon contents have been specified based on intergranular corrosion resistance criteria developed from light water and fast reactor operating experience. Nitrogen is a strong

austenite stabiliser thereby reducing the amount of nickel required for stabilisation. The upper limit of nitrogen is set on considerations of minimising scatter in mechanical properties. Phosphorus, sulphur and silicon are treated as impurities due to their adverse effects on weldability. Due to issues during weldability, acceptable limits are imposed on titanium, niobium, copper and boron. A minimum level has been specified for manganese to improve weldability. Acceptable maximum limits are lowered to values that can be achieved in steel making practice. A limit has been specified on cobalt to reduce Co^{60} activity induced by neutron irradiation, to facilitate ease of eventual maintenance. In addition to more stringent composition limits, a specification for inclusions has been added keeping in view that sulphide inclusions are most detrimental especially from welding considerations and globular oxides are least harmful. For 316L(N) SS grade, the grain size number is specified as larger than ASTM No. 2 (i.e., a finer grain size), to achieve optimum high temperature mechanical properties and to permit meaningful ultrasonic examination.

During fabrication of components, materials are subjected to cold working to different levels. Cold working has detrimental effects on mechanical properties such as ductility, toughness and creep resistance depending on time and temperature of exposure. Further, corrosion resistance is also lowered by cold working. Acceptable limits on cold working are therefore required to be determined on fabricated components without resorting to heat treatments. It is suggested that components manufactured with 316L(N) SS be subjected to solution treatments for cold work levels exceeding 15%. Solution annealing heat treatment is done to recrystallise the work hardened grains and to take chromium carbides, at grain boundaries in sensitised steels, back into solution in the austenite.

Three phases such as M_{23}C_6 , Laves, and sigma phase were detected during the study of precipitation behaviour of initially solution annealed 316L(N) SS on creep testing at 823 K and 873 K upto 85000 h ^[95]. The M_{23}C_6 (M = Cr, Fe, Mo, Ni) carbide is normally the first

phase to form in austenitic stainless steels, especially at grain boundaries because of limited solubility of carbon and the fast diffusion of interstitial carbon atoms. Sigma phase is an intermetallic phase that causes loss of ductility, toughness and corrosion resistance by lowering Cr and Mo contents in the austenite matrix. Sigma phase precipitation in austenite has a very slow kinetics, as carbon and nitrogen are insoluble in the sigma phase and normally appears only after carbide, nitride or carbonitride precipitation has taken place. Delta ferrite, enriched in Cr and Mo exhibits a more pronounced tendency to sigma phase formation than the austenite. Precipitation of the Laves phase Fe_2Mo (η) was detected in delta ferrite and at grain boundaries^[95].

1.4.2 Nitrogen alloying

Nitrogen alloying is challenging as the solubility of nitrogen in liquid iron and iron based alloys is very low at atmospheric pressure (0.045 wt.% at 1873 K). However, nitrogen solubility in liquid ferrous alloys generally follows Sievert's law and is proportional to the square root of nitrogen gas pressure over the melt. Therefore, it is possible to obtain nitrogen levels above 1 wt.% through alloying additions and by increasing nitrogen gas pressure above melt through specialized high pressure melting techniques^[96]. Addition of chromium and manganese increases nitrogen solubility while nickel reduces it.

Steel is considered as high nitrogen steel if it contains more nitrogen than can be retained in the material by processing at atmospheric pressure. For ferritic materials this limit is about 0.08 wt.% N while for most austenitic materials, it is about 0.4 wt.%^[97]. The effectiveness of nitrogen as a good interstitial solid-solution strengthener leads to improvement in mechanical properties. The low temperature flow stress of a series of Fe-Ni-Cr-Mo alloys containing nitrogen between 0.04 and 0.36 wt.% was found to have increased with increase in nitrogen content in the temperature range 78-523 K^[98]. Based on investigations over 316LN SS with nitrogen content in the range 0.01 to 0.15 wt.%, it was found that high temperature tensile

strength, creep strength, fatigue life and creep-fatigue life increased with increasing nitrogen content ^[99]. Similar results were reported on 316LN SS containing 0.023 wt.% carbon and nitrogen content in the range 0.15 to 0.25 wt.% ^[100]. The addition of nitrogen from 0.04% to 0.10%, induced grain refinement decreasing the grain size from 100 μm to 47 μm which in turn resulted in increase in yield stress and tensile strength ^[101]. Too high nitrogen can cause nitride (Cr_2N) precipitation. Simmons ^[102] investigated high nitrogen steel containing 0.69 wt.% nitrogen aged at 973 K and 1173 K and reported that high nitrogen steels are susceptible to Cr_2N precipitation leading to reduced tensile ductility although there is no much effect on tensile strength. Intermetallic phases such as sigma, chi and η are generally observed in stainless steels after high temperature ageing. Nitrogen generally suppresses formation of intermetallic phases due to its non-solubility in intermetallic phases, increase in the free energy of formation of sigma phase and higher solubility of chromium in austenite in the presence of nitrogen.

1.4.3 316LN SS weld joint

316LN SS weld joints are extensively employed in large structural components operating at high temperatures. Fusion welding is widely used to fabricate the reactor vessel and piping due to its complexity and size involved. Creep behaviour of 316LN SS weldment prepared with 16-8-2 (Cr-16 wt.%, Ni-8 wt.%, Mo-2 wt.%) filler wire has been investigated in air and flowing sodium environments at 823 K ^[103]. Rupture lives of the weldment were higher in the sodium environment than those in air. Minimum creep rates were essentially the same for the weldment as well as for the base metal in both the environments, whereas rupture strain and rupture lives were usually lower for the weldment than that of the base metal.

Type 316N SS containing 0.045-0.055 wt.% carbon and 0.06-0.10 wt.% nitrogen is widely chosen as the electrode for fabrication of 316LN SS weld joints. Limits for Carbon (0.045-

0.055 wt.%) and nitrogen (0.06-0.1 wt.%) are specified to provide weld joints with improved creep strength and freedom from sensitisation in the as-welded state. Nitrogen in the specified range has no detrimental effect on weldability of 316L(N) stainless steel. Nitrogen content upto 0.16 wt.% showed good weldability in 18-8 type stainless steels with no porosity but when it was increased to 0.24 wt.%, pinholes and porosity due to nitrogen evolution were observed ^[104].

Hot cracking and sensitisation are major areas of concern in welding austenitic stainless steels and can be generally controlled by optimising the chemical composition of the welding consumables. Hot cracking in stainless steel welds is caused by low melting eutectics containing S, P, Ti, Nb, etc. In nitrogen enhanced steels (upto 0.20 wt.%), cracking depends upon the levels of impurity elements ^[105]. The hot cracking can be reduced by adjusting the chemical composition of the weld metal so that the primary mode of solidification is ferrite. Presence of δ -ferrite reduces the tendency of austenitic stainless steels to hot cracking during welding. Ferrite in the weld metal is specified to be between 3-7 ferrite number (FN) to promote ferritic solidification mode. By means of stabilising the austenite phase, nitrogen decreases primary delta ferrite phase. A minimum of 3 FN is specified to ensure freedom from hot cracking in the weld metal. At high temperatures, the duplex microstructure becomes unstable as δ -ferrite undergoes phase changes to carbides and brittle intermetallic phases (such as sigma) and therefore an upper limit of 7 FN is specified. Weld Research Centre (WRC)-1992 diagram for stainless steel welds ^[106] can be used to attain desired solidification mode during welding.

1.4.4 Conventional test results

The tensile properties of 316L(N) SS under investigation have been evaluated extensively in the temperature range 300-1123 K using conventional uniaxial tensile tests ^[107]. The tensile

behaviour of 316L(N) SS was investigated under multi-axial state of stress by introducing U-notches with various radii into conventional tensile test specimens ^[108]. It was found that the tensile strength increased with decrease in notch radius and the notch sensitivity was more pronounced at room temperature than at higher temperature.

The creep properties of 316LN SS have been studied exhaustively to reveal that the steady state creep rate decreased by an order of magnitude due to addition of nitrogen in 316L SS ^[109]. Improvement in creep properties has been attributed to precipitation strengthening due to fine intergranular and intragranular carbides as well as solid solution strengthening by nitrogen. The multi-axial creep behaviour of 316L(N) SS has been evaluated by introducing V-notch in conventional creep test specimen ^[110]. It was found that for the same nominal stress, the rupture life of notched specimen was higher than plain specimen, implying that 316L(N) SS exhibits notch strengthening behaviour.

With an objective to increase the efficiency and plant life of future SFRs, extensive studies have been carried out to achieve superior high temperature mechanical properties of 316LN SS, by increasing the nitrogen content beyond 0.08 wt.%. The conventional uniaxial creep test results indicated that the rupture life increased almost 10 times by increasing the nitrogen content from 0.07 to 0.22 wt.% ^[111]. On the other hand, rupture ductility decreased with increase in nitrogen content. The time independent and time dependent allowable stresses were presented for various grades of 316LN SS containing 0.07, 0.11, 0.14 and 0.22 wt.% nitrogen content based on RCC-MR code procedures ^[112]. The internal creep damage and surface damage decreased remarkably with increase in nitrogen content and the fracture mode was found to shift from intergranular to transgranular failure with increasing nitrogen content ^[113]. The increase in strength with nitrogen addition was attributed to various reasons including (i) solid solution strengthening, (ii) decrease in stacking fault energy,

(iii) precipitation strengthening, (iv) formation of interstitial-solute complexes and (vi) order strengthening.

Though the tensile and creep properties of 316LN SS have been evaluated in various dimensions using conventional tests, detailed studies using small specimen testing techniques is scarcely available for this material.

The heterogeneity in composition and structure across a weld joint poses a potential cause for failure under service condition. Therefore, the mechanical behaviour of 316LN SS weld joint has been evaluated with due attention. Conventional creep tests have been carried out on 316N SS weld metal at 873 K and 923 K ^[114] and the rupture strength of the nitrogen-bearing weld metal was found to be ~40% higher than that of the nitrogen-free weld metal. The presence of nitrogen delays the precipitation and coarsening of particles like sigma phase thus increasing the rupture life. The ductility of the weld metal is however found to be lower than that of nitrogen-free weld metal due to higher δ -ferrite content. The creep properties of base metal, weld metal and weld joint obtained at 873 K and 923 K were evaluated based on RCC-MR and ASME design codes ^[115]. All the weld joint specimens failed in the weld metal region. Generally, weld strength reduction factors (WSRFs) are provided for welded component to adjust its creep strength, taking into account the variations in the strength of the weld metal, weld quality, stress redistribution, etc. ASME code defines WSRF as the ratio of the uniaxial creep rupture strength of weld metal to that of base metal; whereas RCC-MR code defines WSRF as ratio of strength of weld joint to strength of base metal.

Higher rupture life of the weld joint as compared to the weld metal was supposed to be resulting from the formation of a metallurgical notch. The microstructure of weld metal in 316LN SS weld joint, fabricated by shielded metal arc welding process, is found highly inhomogeneous having different morphologies of δ -ferrite such as vermicular and globular

regions ^[116]. High dislocation density was observed in the weld interface region due to microstructural modification caused by the heat input from the successive weld passes.

As the materials discussed above are used in high temperature applications designed for very long life, it will be worth and interesting to carry out detailed investigation on such materials using ABI and SPC techniques, with a view of life extension of service exposed components.

1.5 Motivation

Nuclear power was introduced in India with the commissioning of the first plant in 1969. The nuclear power plants in India are generally designed for 40-50 years of operating life, which sounds the start of an era of decommissioning and hence the need for ageing management and life extension activities in the future. Extension of service of nuclear components can result in huge cost savings as well as check the problems associated with the disposal of nuclear components after decommissioning. By using small specimen testing techniques, a small volume of material can be scooped out from the component in service for testing purposes without impairing the strength of component. However, at present, small specimen testing techniques such as ABI and SPC are not in a position to be considered for employment in such activities. ABI and SPC techniques are still evolving and it is therefore essential to validate the applicability of these small specimen techniques to assess mechanical behaviour of reactor materials by means of elaborate studies, involving analysis and interpretation of data, thereby resulting in deep understanding of such techniques.

Use of ABI and SPC techniques for evaluation of tensile and creep properties especially in nuclear industry offer several advantages. Characterisation of reactor material generally involves irradiating the material in a confined space in a nuclear reactor, where the use of small specimen testing is highly beneficial. ABI and SPC techniques can support the critical

activities such as post irradiation examination of irradiated materials, irradiation embrittlement of reactor pressure vessel steels, etc.

From the literature, it can be realized that ABI and SPC techniques have great potential to evaluate tensile and creep properties of materials. However, there is hardly any report of investigation available for 316LN SS material using the above techniques. In order to achieve the confidence and establish the accuracy of SPC and ABI test techniques, it is necessary to build a strong database over 316LN SS with adequate amount of such tests.

SPC parameters such as rupture life and steady state deflection rate have been largely dealt in the literature; with less emphasis on detailed analysis over the whole SPC deformation curve. It is essential to pay attention on the deformation that occurs during SPC test in detail. The correlation of ABI and SPC results with corresponding uniaxial test results is till date largely empirical. Hence, numerical analysis by finite element method is essential to obtain a better understanding of the physical basis of deformation in both the techniques.

Apart from this research work, various other studies on the same weld joint are underway, which require finite element analysis (FEA). For carrying out FEA on a model of weld joint, it is required to define the mechanical properties for each zone of the weld joint. The base metal or all-weld metal data alone can be obtained by employing conventional tests. However, the tensile data of HAZ of a weld joint cannot be determined directly from conventional tests. This is due to limitation in volume of test material as demanded by conventional uniaxial tests. In such cases, ABI and SPC techniques can be used to determine the tensile and creep properties across various zones of the weld joint more meaningfully. This research work has also been intended to generate and supply tensile data for the various regions of weld joint for different FEA studies ^[117].

The influence of nitrogen content on conventional tensile and creep properties of 316LN SS were studied extensively using standard uniaxial tests. However, the volume of material and

efforts involved in such studies are enormous. The effect of alloying elements on the tensile and creep properties of a material can be evaluated with minimal volume of material using the ABI and SPC techniques, like a pilot scale project. The objective behind this study is to demonstrate the support rendered by ABI and SPC techniques in accelerated development of new alloys by modifying the chemical composition.

1.6 Organisation and scope of thesis

This thesis focuses on use and applications of SPC and ABI testing techniques in assessing the tensile and creep behaviour of 316LN SS, its nitrogen enhanced variants and their weld joints.

The thesis is organized in the following manner:

Chapter 1: Present chapter – Introduction to the thesis

Chapter 2: The details of ABI and SPC testing facilities, the imaging techniques and other characterisation techniques employed in this research work are discussed. The materials under investigation and the test conditions are explained. The procedures used for carrying out finite element analyses on SPC and ABI specimens are described.

Chapter 3: The tensile behaviour of 316L(N) SS has been evaluated using ABI technique at several temperatures in the range 298-973 K.

In this chapter, the influence of some test parameters on ABI results over 316L(N) SS is discussed. The results obtained on tensile properties of 316L(N) SS at various temperatures are presented. Finite element analyses have been performed to study the stress distribution in the region of specimen under the indenter.

Chapter 4: The SPC behaviour of 316L(N) SS has been evaluated at various loads (300-1000 N) and temperatures (823-923 K).

In this chapter, the SPC behaviour of 316L(N) SS is described with the support of transient and tertiary creep deformation analyses and finite element analysis. SPC results have been correlated with uniaxial creep results at 923 K.

Chapter 5: ABI and SPC techniques were applied for the estimation of effect of nitrogen content on tensile and creep behaviour of 316LN SS containing 0.07, 0.11, 0.14 and 0.22 wt.% nitrogen content. The ABI and SPC results comparing various nitrogen content are presented.

Chapter 6: ABI and SPC techniques were applied for localized characterisation of 316LN SS weld joint comprising base metal, heat affected zone and weld metal. The variations of creep and tensile strength across the various zones of 316LN SS weld joint are presented in this chapter.

Chapter 7: The various results obtained from the above investigation are summarized and concluded. The scope for further research in this area is mentioned.

CHAPTER 2

Experimental Details

This thesis deals with the application of ABI and SPC testing techniques to evaluate the tensile and creep behaviour of 316LN SS. In this chapter, the details of ABI and SPC test setup, specimen size and fabrication, data measurement, testing procedures and the materials investigated are discussed in detail. The various characterisation techniques used with ABI and SPC test specimens are described. Finally, the details of finite element analyses performed on SPC and ABI test specimens are presented.

2.1 Materials under investigation

Nuclear grade 316L(N) SS containing 0.07 wt.% nitrogen was produced through a double melting process. Primary melting of the steel was carried out in an air induction melting furnace of 2.5 tons capacity. The charge consisted of pure raw materials in order to achieve the nuclear grade quality. During primary melting, nitrided ferrochrome was used to control the required amount of nitrogen in the steel. Secondary melting was carried out by electro slag refining (ESR) process in order to achieve low inclusion content and to eliminate segregation of elements in the steels. The ESR ingots were hot forged into slabs and subsequently hot rolled into plates of 22 mm thickness and finally given a solution annealing treatment at 1373 K for one hour, followed by water quenching. Equiaxed grains which were free of carbide precipitates were observed with an average grain size of 78 μm . The chemical composition of 316L(N) SS material under investigation is given in Table 2.1.

Table 2.1 Chemical composition of 316L(N) SS [wt.%]

Element	N	C	Mn	Cr	Mo	Ni	Si	S	P	Fe
wt.%	0.07	0.027	1.7	17.53	2.49	12.2	0.22	0.0055	0.013	Bal.

In order to study the effect of nitrogen content on tensile and creep properties of 316LN SS, three more heats of 316LN SS with nitrogen contents in the range of 0.11-0.22 wt.% were produced through the same double melting processes as described above. The quantity of the steel produced in each heat was about 1100 Kg. The chemical compositions of the four heats of steel produced are given in Table 2.2. All the heats had identical manufacturing history and chemical composition for all the elements except for nitrogen. The carbon content was in the narrow range of 0.025-0.033 wt.%. The nitrogen contents in the different heats were 0.07, 0.11, 0.14 and 0.22 wt.%. Other major and minor elements were controlled almost to the same level in all the heats. For the purpose of discussion, the four heats of 316LN SS with 0.07, 0.11, 0.14 and 0.22 wt.% nitrogen are designated as 7N, 11N, 14N and 22N respectively, in Chapters 5 and 6.

Table 2.2 Chemical composition of four heats of 316LN SS [wt. %]

Designation	N	C	Mn	Cr	Mo	Ni	Si	S	P	Fe
7N	0.07	0.027	1.7	17.53	2.49	12.2	0.22	0.0055	0.013	Bal.
11N	0.11	0.033	1.78	17.62	2.51	12.27	0.21	0.0055	0.015	Bal.
14N	0.14	0.025	1.74	17.57	2.53	12.15	0.20	0.0041	0.017	Bal.
22N	0.22	0.028	1.70	17.57	2.54	12.36	0.20	0.0055	0.018	Bal.

The chemical composition of 316LN SS base metal and 316N SS deposited weld metal are given in Table 2.3. Base metal 316LN SS plates of 22 mm thickness and 316N SS welding electrodes of 4 mm diameter were used for making weld pad by employing Shielded Metal Arc Welding (SMAW) process. The 316LN SS weld pad of size 500 x 250 x 20 mm³ was fabricated using multi-pass SMAW process by depositing 316N SS consumable electrodes. The weld pad was qualified for any weld defect by X-ray radiographic examination and was

found acceptable. It was necessary to identify the boundaries of the various zones of the weld joint so as to (a) position the various zones under the indenter tip during ABI test and (b) slice out the material from various zones for fabrication of SPC specimens. The microhardness profile was obtained across the weld joint, as shown in Fig. 2.1. Based on the hardness profile, the HAZ region was roughly marked upon the weld joint specimen.

Table 2.3 Chemical composition of 316LN SS weld joint [wt.%]

Material	C	Ni	Cr	Mo	Mn	Si	S	P	N
316LN SS (Base metal)	0.025	12.15	17.57	2.53	1.74	0.20	0.004	0.017	0.14
316N SS (Electrode)	0.052	11.50	18.60	2.20	1.74	0.64	0.007	0.022	0.10

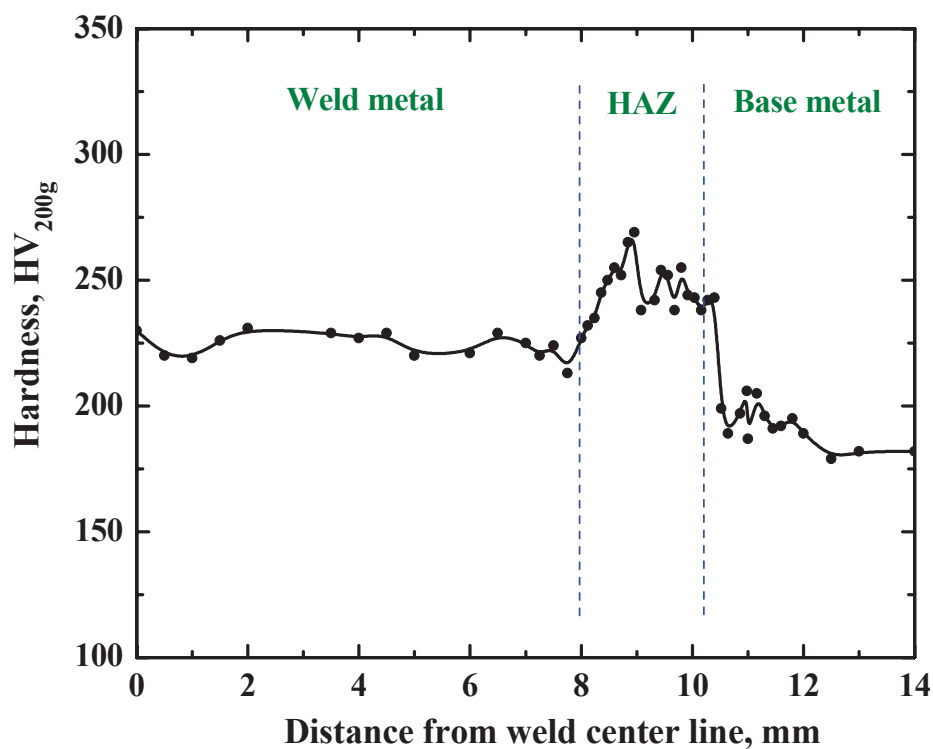


Fig. 2.1 Microhardness profile obtained across 316LN SS/ 316N weld joint.

2.2 Automated Ball Indentation test

The stress-strain microprobe (SSM) system based on ABI technique ^[118] has been employed to carry out ball indentation tests. Figure 2.2 shows SSM system with environmental chamber, loading fixture, XY positioning table and high resolution video camera. The environmental chamber is of split-box design and is mounted directly on the SSM load frame with stationary column mounts. The operating temperature range of the environmental chamber is 116 K to 1073 K. The temperature is monitored by standard K-type thermocouple which is connected to the temperature controller unit. The maximum loading capacity of the system is 17.8 kN. The ball screw actuator driven by stepper motor is used to apply compressive load upon the test specimen through spherical indenter. The loading fixture includes position adjustable crosshead, an indenter, load cell, spring-loaded linear variable differential transformer (LVDT). A 4452 N capacity compressive type load cell with resolution of 0.001 N is used to measure the applied load. The accuracy of the load cell is within $\pm 1\%$ of the full working range. The depth of indentation is measured using LVDT of range ± 0.5 mm and resolution of 0.1 microns. The non-linearity of LVDT is less than 0.20% of full output range and accuracy is $\pm 1\%$ of the full working range. The LVDT is calibrated using calibration instrument with high resolution digital micrometer. A signal conditioner is provided for all sensors and a shunt calibration switch is provided for the load cells.

The LVDT is placed close to the indenter during room temperature test. At high temperature tests, LVDT is placed outside the environmental chamber as shown in Fig. 2.2. In such cases, the correction for compliance of testing machine has been done as follows. The load-depth of indentation data are first collected by keeping LVDT close to the indenter. Then the same experiment on the same material and indenter is repeated by keeping LVDT outside the chamber in the required position. The difference in applied load obtained from these two

positions of LVDT is expressed as a function of depth and such compliance correction is applied on the load-depth of indentation curves when LVDT is kept outside the chamber.

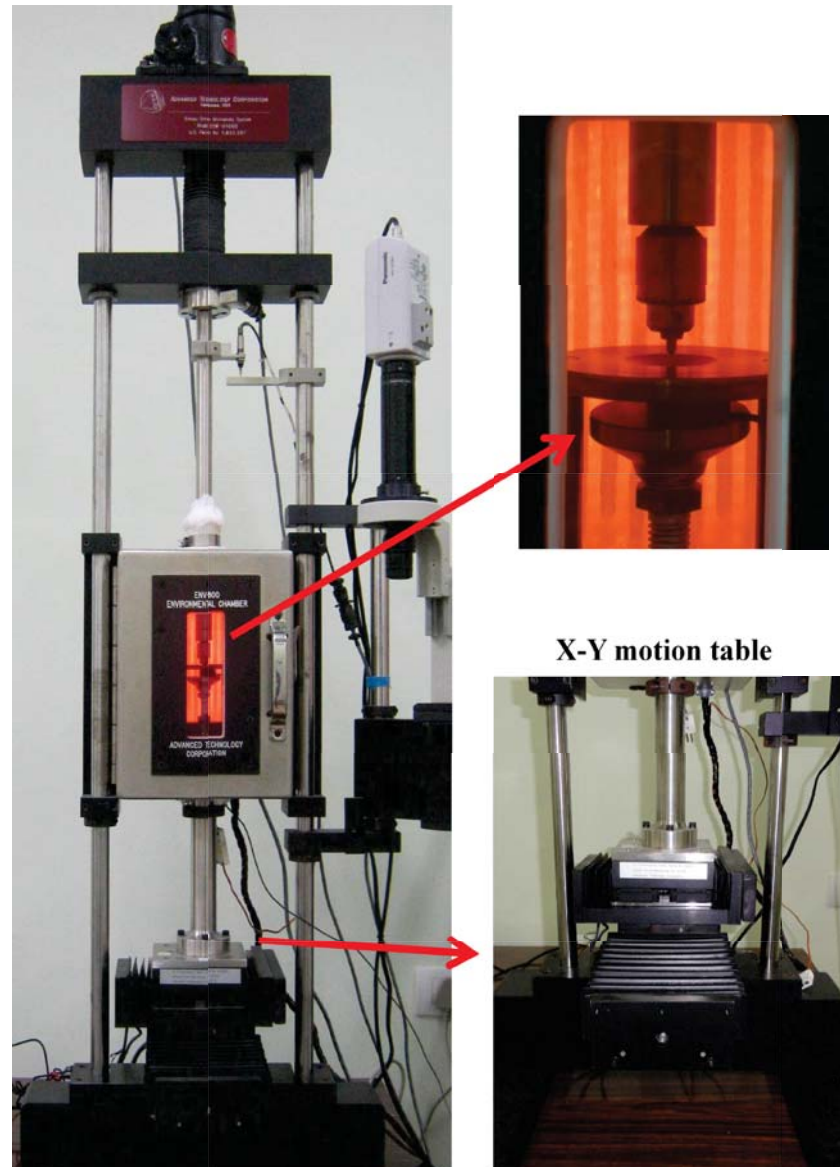


Fig. 2.2 ABI experimental setup.

The system operation is computer controlled and comprises of hardware and software to perform continuous loading and unloading cycles in an automated manner. The load and indentation depth data are continuously collected by a high resolution 16-bit 8-channels data acquisition system coupled with personal computer. The microprocessor based control for

stepper motor responds to the feedback signal from load and displacement sensors and accordingly apply load during the test. Thus SSM system operates under closed-loop control with continuous measurement and limits on both load and displacement signals and preventing possible damage to sensors during the test.

The indenter and specimen fixture assembly is shown in Fig. 2.3a. A 3-jaw geared chuck attached to the moving cross-head holds the indenter of appropriately-sized tip and ensures the perpendicularity of the indenter tip to the test surface. The indenter used has a spherical tip permanently attached to a cylindrical support stem of same material (Fig. 2.3b).

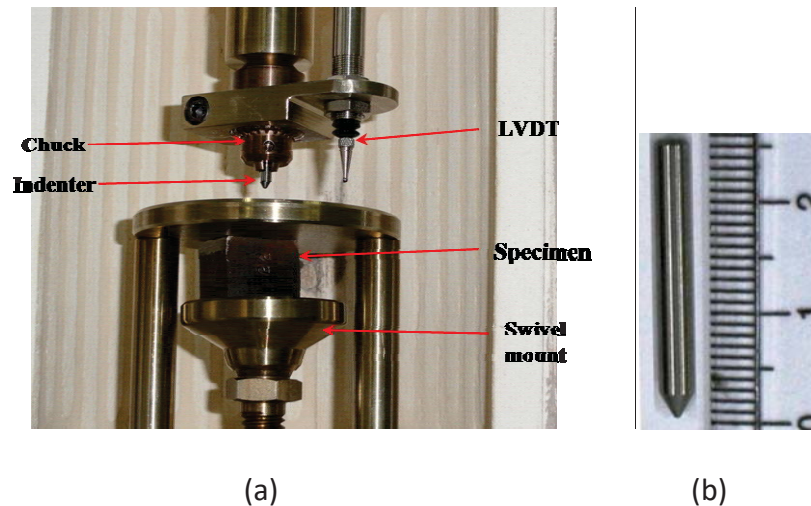


Fig. 2.3 (a) Details of specimen fixture assembly (b) Φ 0.76 mm indenter.

The indenters made of both tungsten carbide and silicon nitride were used depending on the temperature of the test. Spherical indenters of diameter 0.25 mm and 0.76 mm were used to conduct ABI tests. The selection of indenter size depends on the volume of material available for testing and the grain size of the test material. It is to be noted that the indentation produced by the minimum diameter of the indenter at the smallest practical strain covers at least three grains of the specimen. When the region of interest becomes narrow or the

material exhibit a sharp gradient in its tensile properties, the size of the indenter shall be reduced.

The test can be conducted on any metallic material with minimum thickness of 0.51 mm and cross-section having 0.76 mm square or diameter. The test specimen is mounted for loading by means of a swivel mount (Fig. 2.3a) that can take care of a small level of uniform taper present in the specimen surface to some extent. However, up and down deviations within the test surface cannot be adjusted and may cause large scatter in results. Therefore, the test specimens are manually polished progressively from 80 to 1200 grit paper followed by finer polishing using diamond paste to achieve surface finish of 2 microns. Care is taken so that the top and bottom surfaces of the specimen are made parallel and flat. In case, the specimen is irregular or very small, it can be mounted in bakelite. In this investigation, such a situation did not arise and the specimens of typical size 10mm x 10mm x 20 mm were used in all the tests.

The centre to centre spacing between indentations is maintained at least three times the indenter diameter. The planar spacing of indentation from the free edges is maintained atleast two times the diameter of the indenter. As it is generally required to maintain planar spacing between indentations, smaller the indenter radius, more the number of tests that can be conducted in the same volume. The test temperature is maintained within ± 2 K. The indenter is penetrated into the specimen at a desired speed which determines the strain rate of the test. The rate of displacement of indenter (v_i) during ABI test was held constant with a value of 0.008 mm s^{-1} .

The maximum depth of indentation in an ABI test is set in terms of percentage of radius of indenter used in the test. The maximum depth of indentation was kept the same as 24% of indenter radius in all the tests. It was taken care that the maximum depth of indentation did not exceed 10% of thickness of specimen used. The test is stopped automatically by

unloading the specimen once the specified depth of indentation is reached. A minimum of five cycles of loading and unloading is allowed in the system. The depth of indentation is distributed nearly equal in all the cycles so as to achieve the maximum depth of indentation in the specified number of cycles. A single cycle test can also be performed without partial unloading by continuous loading upto maximum depth of indentation and then fully unloading. Such test is considered suitable for very high temperature or high strain rate testing so as to avoid indentation creep and non-linear unloading slope respectively. However, plastic depth cannot be determined from single cycle test thus resulting in determination of only total true strain. In this work, 7 to 8 number of cycles with equal increments of depth were used. The unloading in any cycle is set as 50 % of the maximum load at the end of that cycle. At the end of loading of last cycle of the test, it is fully unloaded. An initial preload is required to overcome data scatter due to minor irregularities in the specimen surface as well as to calculate the zero indentation point at which the indenter starts to touch the test surface. The initial preload depends on the indenter size and should be less than 10% of the load corresponding to depth of indentation value of 30% of the indenter radius. In the present studies, the initial preload of 13 N and 44 N were applied when indenter diameters were 0.254 mm and 0.762 mm respectively. It was ensured that after initial preloading, sufficient depth should remain for completing the test till the maximum depth of indentation.

In order to assess the effect of test parameters such as indenter material, surface finish of test specimen, number of cycles of penetration and depth of indentation on ABI results, tests were conducted at 298 K, by varying one parameter while keeping others the same. To study the effect of indenter material on ABI data, tests were carried out using both silicon nitride and tungsten carbide indenters at 298 K, keeping other test parameters as the same. ABI tests were conducted on the four heats of 316LN SS containing 0.07, 0.11, 0.14 and 0.22 wt.%

nitrogen at several temperatures such as 298 K, 523 K, 623 K, 723 K, 823 K, 923 K and 973 K. The weld joint specimen used in ABI studies is shown in Fig. 2.4. The ABI test specimen was cut out from the weld joint in such a way so that it covered all the weld zones yet it was small enough to be mounted in the specimen fixture. ABI tests were conducted across the various zones of 316LN SS weld joint at 298 K, 523 K and 923 K. Smaller indenter (Φ 0.25 mm) was used to carry out ABI tests at several locations across the weld joint at 300 K and 523 K. Larger diameter (Φ 0.76 mm) was used to conduct ABI test at a location in each zone at higher temperature (923 K). In order to investigate the pass-to-pass variation of tensile strength that may occur during multi-pass welding, ABI tests were conducted over several passes of the weld metal region from the weld root to the crown of the weld joint.



Fig. 2.4 Weld joint specimen used in ABI test.

2.2.1 Uniaxial tensile test

The uniaxial tensile test specimens were fabricated out of the all-weld metal region in such a way that the gauge length is parallel to the welding direction. The uniaxial tensile tests were conducted on the all-weld metal region of the weld joint at 298 K and 923 K at a nominal strain rate of $3 \times 10^{-3} \text{ s}^{-1}$ as per ASTM standards E8 and E21 respectively ^[1,119].

2.3 Small Punch Creep test

SPC tests have been carried out using a dedicated testing facility of 2 KN load capacity under compression load, as shown in Fig. 2.5. The system comprises of a furnace (Fig. 2.6a), a specimen fixture (Fig. 2.6b), loading arrangement, argon flow control, vacuum pump and control unit. The maximum operating temperature is 973 K. The constant load is maintained through a linear actuator coupled with a servo motor, having an accuracy of $\pm 0.5\%$ on full scale. The displacement is measured using a pulse encoder with a resolution of 0.01 microns and measurement range of 0-5 mm in the output voltage range 0-10 volts. The temperature is measured using sheathed R-type thermocouple which is kept in contact with the upper die and very close to the specimen. The system is provided with various safety features such as furnace overheat limit alarm, specimen overheat limit alarm, indication for no flow of cooling water, over pressure alarm and overload.



Fig. 2.5 SPC testing facility.

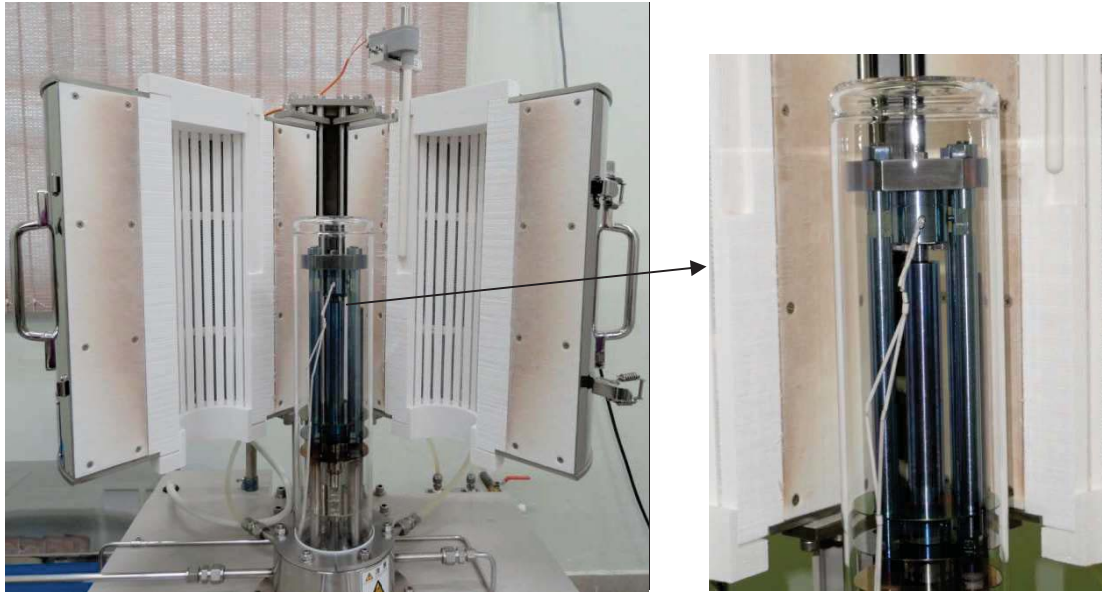


Fig. 2.6 (a) Furnace (b) Specimen mounting assembly.

The schematic of the SPC test setup is shown in Fig. 2.7. A square specimen of cross-section 10 mm x 10 mm (with tolerance of +50 microns on all edges) and thickness 0.5 mm (with tolerance of ± 5 microns) is used in SPC test. A silicon nitride spherical indenter of diameter 2.38 mm is used to apply load to the specimen under load controlled mode at high temperature, till the specimen ruptures.

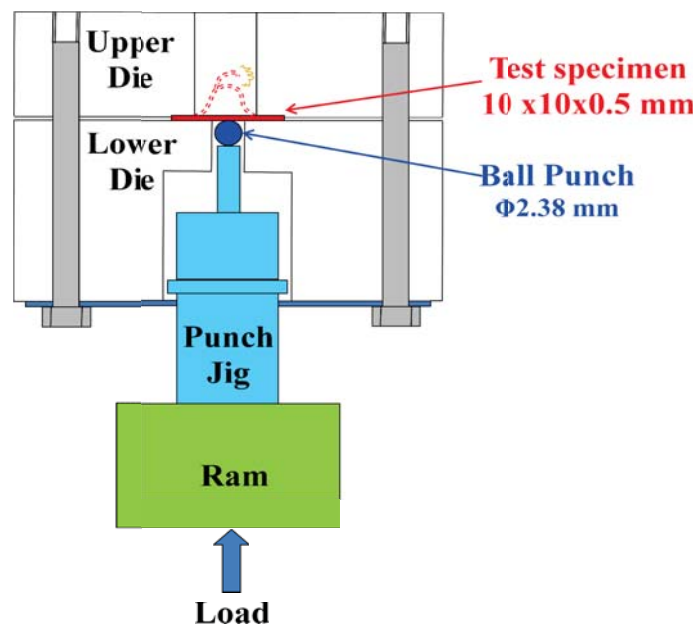


Fig. 2.7 Schematic of SPC testing facility.

The specimens are initially cut using Electrical Discharge Machining (EDM) by providing allowance in thickness for polishing. The disc specimens are manually polished progressively from 80 to 1200 grit paper followed by finer polishing using diamond paste to achieve surface finish of 2 microns and at the same time the required thickness is maintained. Since the investigated materials, do not have issue of anisotropic properties, the specimens can be cut and loaded in any random direction. The test specimen is held between upper and lower dies. The bore diameter of the upper die is designed to be greater than the sum of bore diameter of the lower die ($\Phi 2.5$ mm) and twice the original thickness of the specimen ^[54]. Consequently the deformation of SPC specimen is not subjected to frictional forces arising from the contact of the specimen with the inner wall of the upper die. The diameter of the receiving hole in upper die is kept as 4 mm. The specimen holder prevents the specimen from cupping upward during punching operation.

The displacement is measured as a function of time at constant load and data are acquired at the rate of 1 s to 30 s per data point, depending on expected duration of the test. Initially, the specimen chamber is evacuated upto -0.1 MPa and flushed with argon gas several times before heating the specimen to the test temperature. Argon atmosphere is then maintained by means of continuous flow of argon so as to prevent oxidation of specimen at high temperature. Out of the study on the influence of argon gas flow rate, it was observed that the influence of argon atmosphere was less or negligible in the primary stage but it was significant in the secondary and tertiary stages, thereby increasing the time to rupture significantly, when flow rate was increased from 0 to 0.3 litres per minute ^[65]. In the present investigation, a continuous flow of argon is ensured with flow rate of 0.5 litres per minute throughout the period of test.

The structural components in fast reactors are generally designed for temperature range 773-823 K. However, uniaxial creep properties are generally studied under accelerated

conditions, i.e., at higher stress or temperatures. Uniaxial creep test results are available for the investigated material at 923 K at various stress levels in the range 140-225 MPa. Since this work intends to correlate SPC results with uniaxial creep results, SPC tests have to be carried out at the same temperature. SPC tests were conducted on 316LN SS at various loads in the range 300-1000 N and at temperature 923 K with a temperature accuracy of ± 2 K. SPC tests were also carried out at a load of 400 N and at several temperatures in the range 898-973 K in steps of 25 K, to estimate the activation energy for creep deformation. SPC tests were carried out on four heats of 316LN SS containing 0.07, 0.11, 0.14 and 0.22 wt.% nitrogen at 923 K at various loads in the range 300-550 N to estimate the effect of nitrogen content on creep strength 316LN SS. In order to obtain creep strength profile across 316LN SS weld joint, specimens were sliced out from the various regions of weld joint using wire-cut electrical discharge machining, as shown in Fig. 2.8. The cut specimens were manually polished upto a surface finish of 2 microns. SPC tests were carried out on specimens of various zones at 923 K at various loads in the range 300-550 N. SPC tests were also carried out across 316LN SS weld joint at 923 K at 400 N.

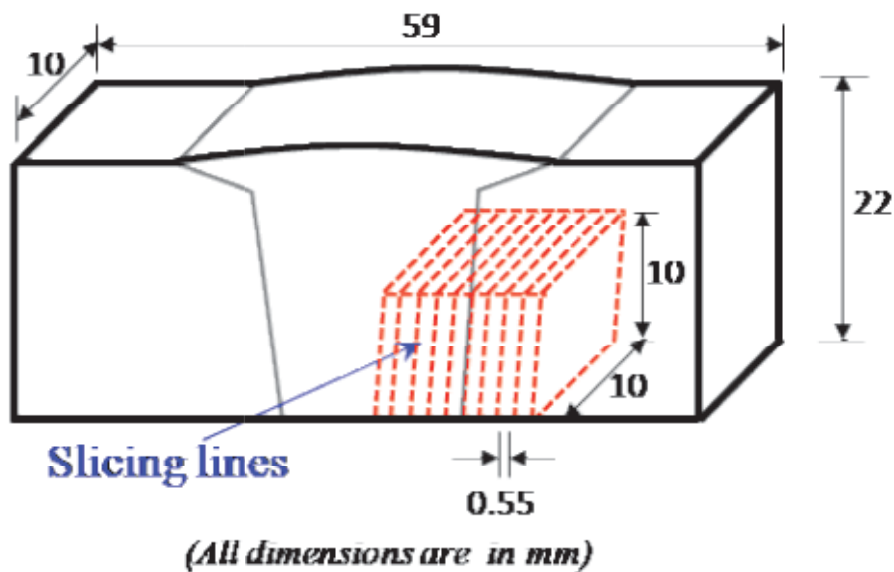


Fig. 2.8 Fabrication of SPC specimens for weld joint studies.

2.4 Imaging and other characterisation techniques

a) Optical microscopy

The surface of specimen to be visualized under optical microscope was polished using silicon carbide (SiC) polishing papers progressively from 80 grit to 1200 grit. The diamond suspension was used to further polish in two stages, first using 6 and 3 micron diamond paste and then finishing with 1 micron paste. The final touch on surface was given by colloidal silica (0.3 microns) polishing till a clear mirror surface was achieved. The specimen was cleaned thoroughly. The etching of surface was done electrolytically in an electrolyte solution of 60% HNO₃ + 40% demineralised water, by passing current density of 0.75 mA/mm². Over-etching may darken the image while light etching reveals only a shallow image of the microstructural features. The etching was done for atleast 15 seconds, till the grains were visible to the required level of clarity. Optical microscopic analysis was carried out using Carl Zeiss Axio observer and a personal computer interface was used to save the images in picture format.

b) Scanning Electron Microscope (SEM)

ABI tested specimen was examined under field emission gun scanning electron microscope (FEGSEM). The Carl Zeiss Supra 55 FEG-SEM equipped with electron backscattered detector (EBSD) was used for this purpose. No specimen preparation was required for just taking fractograph. The fractured surface of tested specimen was cleaned in ultrasonic bath and then loaded directly into SEM. In order to take SEM EBSD image of ABI tested specimen, the specimen was sectioned through the centre of indentation and was polished upto mirror finish using colloidal silica polishing as described in Section 2.4a. In order to obtain clearly visible Kikuchi pattern, besides colloidal gel polishing, electrolytic polishing was done on the surface using A2 solution. The same FEG-SEM was used to perform EBSD analysis, by subjecting the electron gun to an accelerating voltage of 20 kV. The distance

between the specimen surface and phosphor screen was 178 mm and an indexing algorithm based on eight detected bands was utilized. An aperture of 120 microns, a working distance of 16 mm, a tilt angle of 70°, sample–detector distance 178 mm and an indexing algorithm based on eight detected bands was utilized. A magnification of 500X and a scanning step size of 2 microns (square grids) required a scan time of ~10 hours. Automatic Aztec software was used for acquiring EBSD data and HKL-Channel 5 software was used for post processing of the data. Face centred cubic (FCC) iron phase was used as input for indexing the EBSD pattern.

c) Confocal Scanning Laser Microscopy

The 3D profile of indentation on ABI tested specimen was captured using Confocal Scanning Laser Microscopy (CLSM). CLSM rejects light not coming from the focal plane and therefore optical slicing is possible. The images captured from various focal planes are stacked over one another to build a 3D image.

d) Microhardness

Walter UHL-VMHT Vickers microhardness tester was used to obtain the hardness profile across the weld joint. The surface of weld joint specimen having all the regions was mirror polished upto 1 micron. A load of 200 gf was applied and held for 15 seconds. At the end of test, lengths of diagonals of permanent indentation on the surface were measured and the values of hardness were calculated.

e) Profilometer

The surface roughness of ABI test specimen was measured by using Talysurf CLI 1000 surface profilometer. Line profiling was done using non contact high resolution confocal point gauge. The gauge focused a beam on the surface through a lens with chromatic length aberration and due to the aberration, the focus points were at different Z-positions for

different wavelengths. A built-in spectrometer received the reflected light through a pin hole and provided an intensity curve depending on wavelength, from which the surface roughness could be obtained.

2.5 Finite Element Analysis (FEA)

2.5.1 FE simulation of ABI test

FEA was carried out using ABAQUS code^[120] to visualize the stress distribution inside the region of ABI specimen subjected to compression under the indenter, the resulting pileup phenomenon and the evolution of plastic zone with increasing depth of indentation. Taking advantage of geometrical and loading symmetry, an axisymmetric model of both indenter and the specimen was developed for this purpose (Fig. 2.9), in order to manage the computing time.

The indenter was modeled as a discrete rigid body assuming the deformation of indenter relative to that of specimen during contact is negligible. The spherical centre of the indenter was specified as the reference point. The specimen was modeled as a deformable part. Four noded bilinear axisymmetric quadrilateral (CAX4R) elements were used to create the FE model of the specimen. This element type is considered suitable for problems involving high stress or strain gradients and especially dealing with contact interaction^[120].

The elastic properties such as Young's modulus and Poisson's ratio were input as 200000 N/mm² and 0.3 respectively. The uniaxial true stress-true plastic strain data of 316L(N) SS upto the ultimate stress point was used to define the plastic behavior of the material. The contact interaction was created as finite sliding, surface-to-surface contact between the indenter (master surface) and the specimen (slave surface). The normal behavior was defined as hard contact.

The bottom nodes of the specimen were fixed in all directions. The indenter model was constrained from translation in x-direction and rotation. Seventeen steps were created to simulate one preloading stage, eight loading cycles and eight unloading cycles. The indenter was applied a velocity of 0.008 mm /s in each step. The time for each step was varied in order to cause required level of depth of indentation.

A mesh convergence analysis was performed initially to optimize the mesh size. This was done by running the analysis with various element sizes until no appreciable difference was found in the numerical values by reducing the element size further.

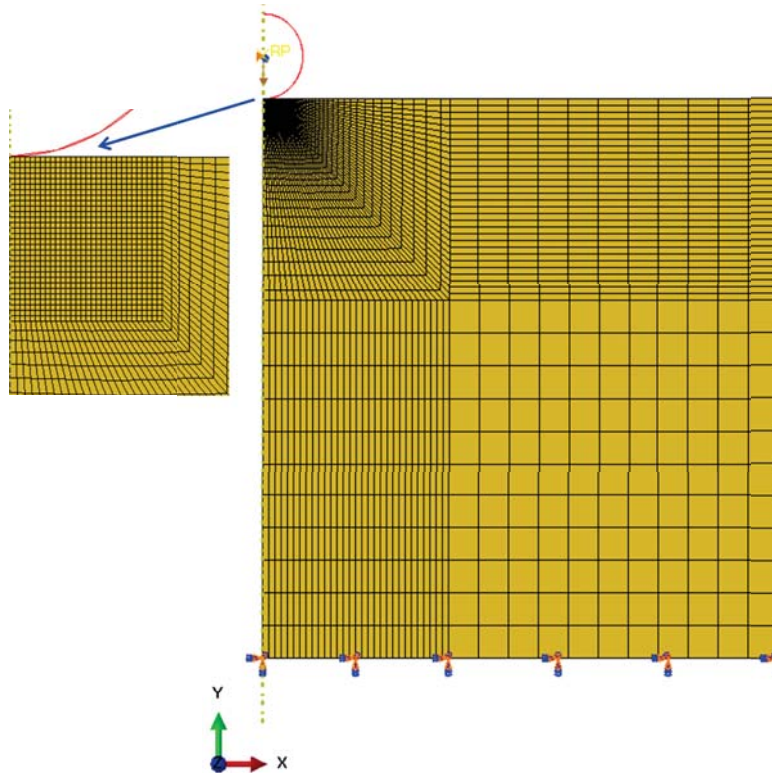


Fig. 2.9 Axisymmetric FE model of spherical indenter and specimen.

2.5.2 FE simulation of SPC test

FEA was performed using ABAQUS code to obtain the stress distribution in SPC specimen subjected to loading under a spherical indenter. An axisymmetric model of indenter, specimen, lower die and upper die was created by considering indenter, lower die and upper

die as discrete rigid bodies (Fig. 2.10). The centre of arc of axisymmetric model of indenter was taken as the reference point that was specified for defining load and boundary condition to the indenter. Though the shape of SPC specimen is square, it was modeled as an axisymmetric deformable body as it is understandable that the portion of specimen left out because of this assumption was held between upper and lower die and actually may not affect the results. The contact interaction was defined as finite sliding, surface-to-surface contact between the indenter and the specimen. The same interaction was defined between the specimen and the dies. Four noded bilinear axisymmetric quadrilateral (CAX4R) elements with reduced integration and hour glass control were used to create the FE model of the specimen. A finer mesh was applied (a) at the contact boundary between indenter and specimen (b) near the region of contact of specimen with the dies and (c) region in the specimen where necking is supposed to take place. Coarser mesh with large elements was used in the region of specimen clamped between the dies. The mesh convergence analysis was performed by reducing the element size till there was no significant change in the results.

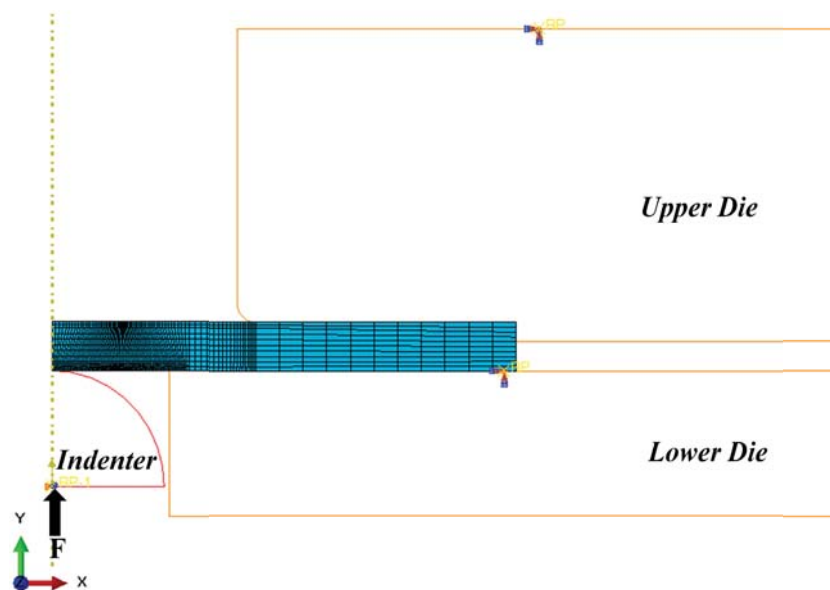


Fig. 2.10 Axisymmetric FE model of indenter and SPC specimen held between upper and lower dies.

The elastic and plastic behaviors of the material and contact interaction properties were defined as discussed in earlier section. The coefficient of friction between silicon nitride indenter and 316LN SS specimen was taken as 0.4^[121]. A user defined subroutine was written to define the creep behavior of the material. All degrees of freedom of both the upper die and lower die were fixed and the rotation of indenter was arrested. Analysis was carried out in two steps. In the first step, non-linear elastic-plastic model was incorporated and a load of 300 N was applied through the reference point of the indenter model. In the second step, the creep solution is started. The analysis was run upto the tertiary stage till the onset of necking occurs.

CHAPTER 3

Tensile Properties of 316L(N) SS using ABI Technique

In this chapter, the tensile behaviour of 316L(N) SS has been evaluated using ABI technique at several temperatures in the range 298-973 K. The procedures used for interpreting load-depth of indentation data measured from ABI tests, in order to determine the various tensile properties are described. The stress distribution in the region of specimen deformed under spherical indenter as determined through finite element analysis is discussed.

3.1 ABI analyses

The procedures used for analysing ABI load-depth of indentation data to calculate the various tensile properties are described in this section, using the results obtained at 298 K illustratively. Figure 3.1 shows the load-depth of indentation curve measured from ABI test at 298 K. The applied load increases linearly with increase in depth of indentation. The linearity is the consequence of two non-linear and opposing processes occurring simultaneously such

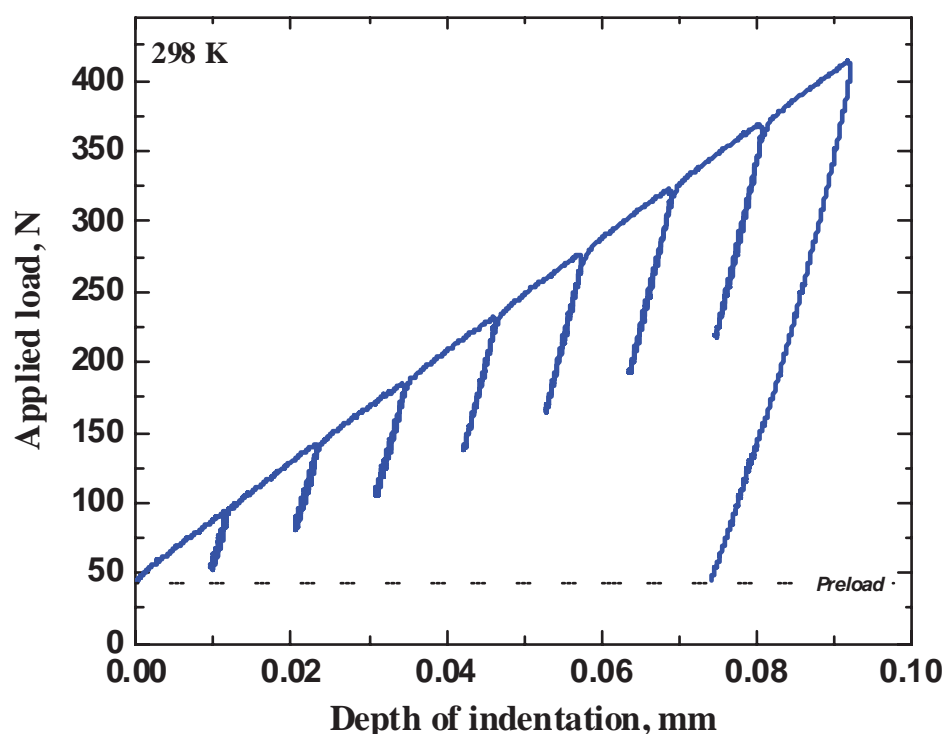


Fig. 3.1 ABI load-depth of indentation curve measured at 298 K.

as (i) the spherical geometry of the indenter resulting in non-linear increase in contact area with depth of indentation and (ii) the increase in load required for further indentation due to work hardening of the material. The unloading curves are linear in all the cycles because of the elastic recovery of the material. The slopes of the unloading curves at various cycles are not parallel and the slope increases with increase in depth of indentation. The slope increases because the volume of plastic deformation zone is increased while the specimen Young's modulus does not change with increase in indentation depth.

It may be noted from Fig. 3.1 that the zero depth of indentation corresponds to preload. The initial preload is applied to take care of the non-linearity in load-depth of indentation curve at small initial loads caused by surface tension effects, initial high friction between indenter and specimen, etc. The initial preload helps to overcome data scatter due to minor irregularities in the specimen surface when the indenter comes in contact with the test surface. It is necessary to determine the actual depth of indentation corresponding to applied preload. This was done through linear regression of first loading cycle and extrapolating to zero load as shown in Fig. 3.2. The x-intercept of the linear fit was then subsequently added to the raw data curve shown in Fig. 3.1 and the entire curve was shifted rightward to move the point of intercept to the origin. The resulting curve with corrected total depth of indentation is shown in Fig. 3.3.

In ABI test, both elastic and plastic deformations take place simultaneously during each cycle. The plastic depth (h_p) at the end of any cycle can be found out by deducting corresponding elastic depth (h_e) from total depth of indentation (h_t). The elastic depth is estimated by fitting linear regression to the unloading curve and extrapolating the same to zero load, thereby determining the plastic depth at that cycle, as shown in Fig. 3.3. The initial part of the unloading curve obtained from spherical indentation is closely related to specimen Young's modulus^[122]. In the present analyses, linear regression was done upto initial 30-50% of unloading curve, to take care of non-linearity at very low loads and yet

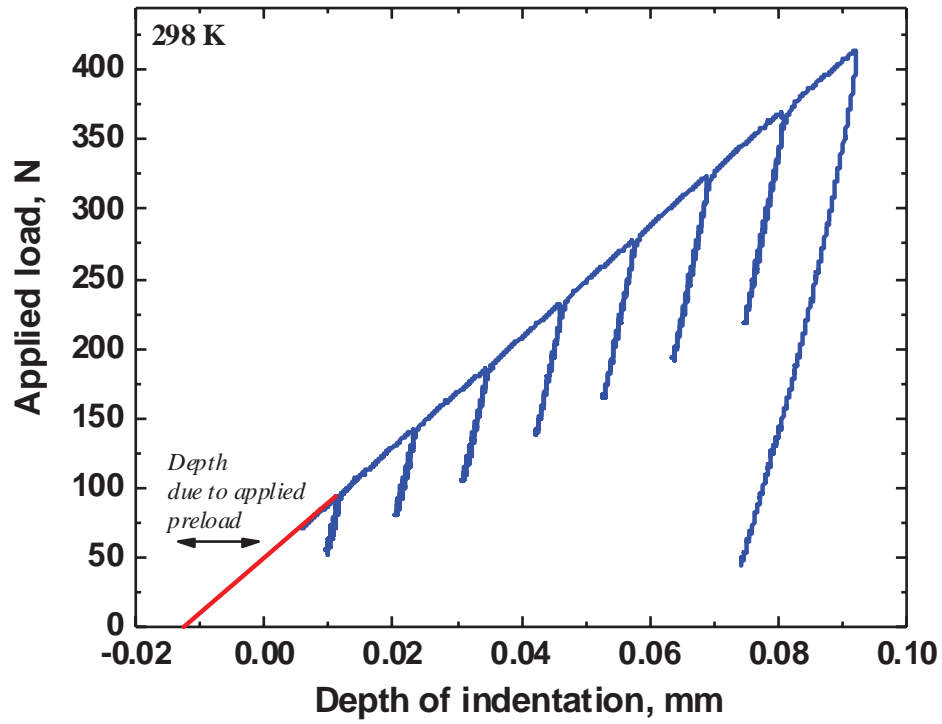


Fig. 3.2 Linear regression of first loading cycle, to estimate the depth of indentation corresponding to preload.

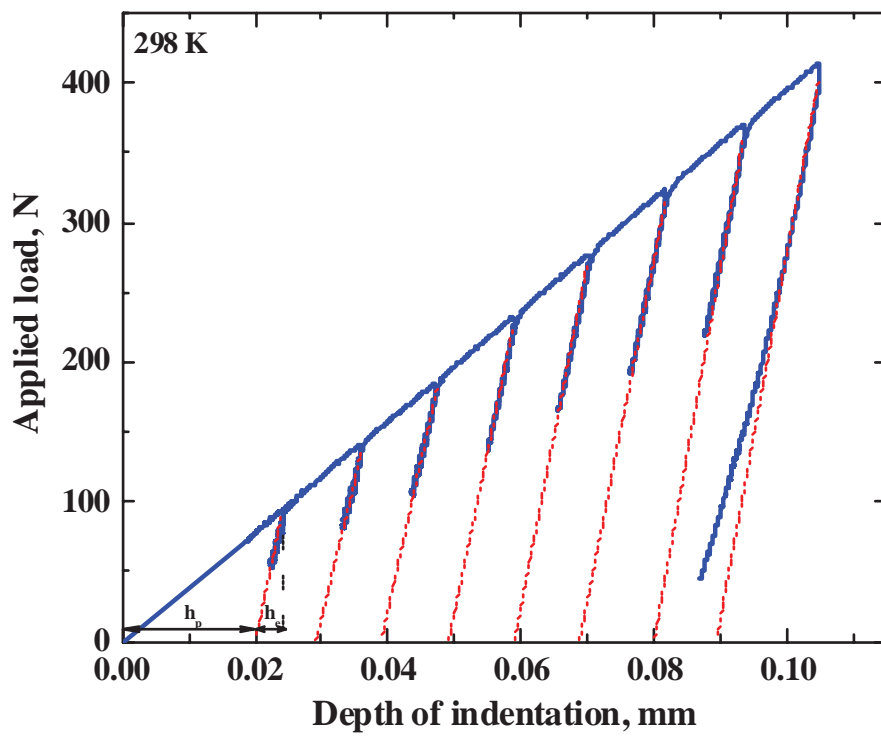


Fig. 3.3 Determination of plastic depth from total depth of indentation.

provide sufficient data for regression analysis. The derivation of plastic depth is based on the assumption that the entire unloading curve is linear. Alternatively the plastic depth is also evaluated by subtracting the product of elastic depth and indenter shape parameter ($=0.75$) from the maximum depth of indentation at that cycle ^[35]. Yamamoto et al. ^[123] also observed that the extrapolated plastic depth was actually slightly larger than the plastic depth obtained from 99% unloaded test and commented that linearity in unloading curve in ABI test may be due to the higher rigidity of the system used in it.

The indentation profile during an ABI test is shown schematically in Fig. 3.4 with a description of nomenclature used in this thesis.

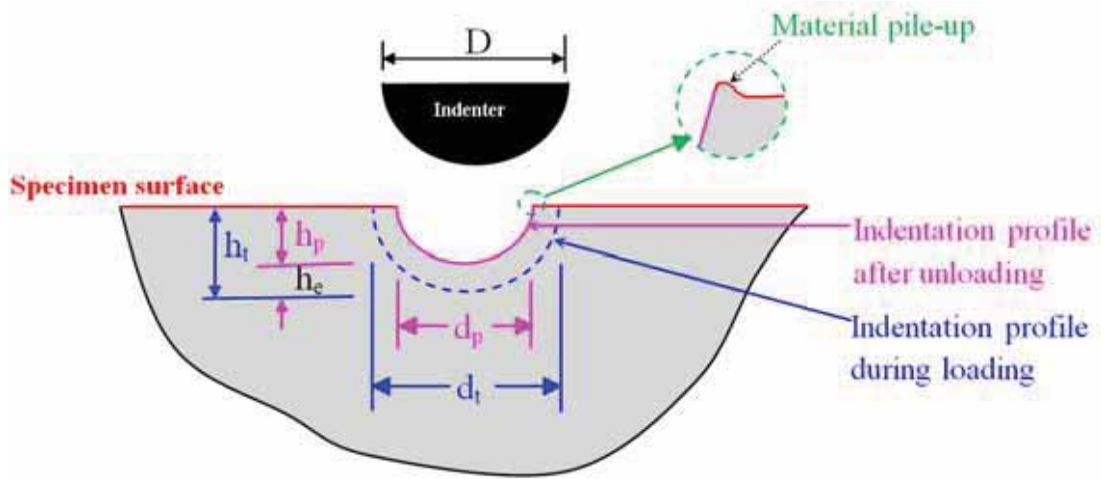


Fig. 3.4 Indentation profile during ABI test.

For each ABI loading cycle, the total depth of indentation (h_t) measured from the test was converted to total indentation diameter (d_t) using the geometrical relation,

$$d_t = 2 (Dh_t - h_t^2)^{1/2} \quad (3.1.1)$$

where, 'D' is the diameter of the indenter.

The plastic diameter (d_p) was calculated from plastic depth of indentation (h_p) using the following equation ^[14],

$$d_p = \sqrt[3]{(2.735 P D) \frac{\left[\frac{1}{E_{spec}} + \frac{1}{E_{ind}} \right] \left[4h_p^2 + d_p^2 \right]}{4h_p^2 + d_p^2 - 4h_p D}} \quad (3.1.2)$$

where, ‘P’ is the applied load, ‘E_{spec}’ and ‘E_{ind}’ are Young’s modulus of the specimen and indenter respectively. Since the term d_p is present on both sides of equation, it can be understood that Eqn. (3.1.2) is solved by iteration. For room temperature (298 K) tests, the Young’s modulus of tungsten carbide was taken as 630000 MPa in Eqn. (3.1.2). Assuming the variation of Young’s modulus of silicon nitride with temperature as not very significant, Young’s modulus of silicon nitride at all temperatures was taken as 320000 MPa in Eqn. (3.1.2). The Young’s modulus of 316L(N) SS at various temperatures were taken from RCC-MR code using the following equation^[124],

$$E = 201660 - 84.8 T, (20 \leq T \leq 700) \quad (3.1.3)$$

where, ‘T’ is temperature (in °C). The true plastic strain (ε_p) is then calculated as^[18],

$$\varepsilon_p = 0.2 (d_p/D) \quad (3.1.4)$$

It can be inferred from Eqn. (3.1.4) that the maximum true plastic strain that can be practically measured from ABI test is 0.2, when plastic diameter of indentation is equal to diameter of indenter used. The true stress (σ_t) is calculated from the mean pressure as^[18],

$$\sigma_t = \frac{4P}{\pi d_p^2 \delta_c} \quad (3.1.5)$$

where, ‘δ_c’ is the constraint factor for a given class of materials. The constraint factor is defined on the basis of three stages of development of plastic zone which in turn is specified by a parameter Φ given as^[19],

$$\Phi = \varepsilon_p E_{spec} / 0.43 \sigma_t \quad (3.1.6)$$

During initial yielding, at which the nucleation of plastic zone happens, the constraint factor is given as,

$$\delta_c = 1.12 \quad \Phi \leq 1 \quad (3.1.7a)$$

As the plastic zone grows in size at the cost of elastic zone, the constraint factor is given as a function of Φ as,

$$\delta_c = 1.12 + \ln \phi [(2.87 \alpha_m - 1.12) / \ln (27)] \quad 1 < \Phi \leq 27 \quad (3.1.7b)$$

where, α_m is a material dependent parameter, for a given class of materials, depending on its strain rate sensitivity and work hardening characteristics. The value of α_m typically varies from 0.90 to 1.25 for various structural steels ^[125]. In a fully developed plastic zone, the constraint factor is taken as,

$$\delta_c = 2.87 \alpha_m \quad \Phi > 27 \quad (3.1.7c)$$

It may be noted that the value of δ_c is based on Φ as inferred from Eqn. (3.1.7), whereas Φ is the function of σ_t (Eqn. 3.1.6) and σ_t in turn depends on δ_c (Eqn. 3.1.5) Therefore, Eqns. (3.1.5)-(3.1.7) are to be solved by iterations. The constraint factor is determined empirically by comparing flow curves obtained from both ABI and uniaxial tension tests. For an unknown material, α_m is initially taken as 1.1. In the present investigation, the parameter α_m was taken as 1.25 and 0.9 for analysing room temperature and higher temperature results respectively, on the basis of empirical correlation with uniaxial tensile test results. The value of α_m was similarly reported to be 1.14 for Type 308 SS weld ^[17] and 1.24 for P92 steel ^[39].

The yield stress marking the initiation of plastic deformation corresponds to $\phi=1$ in Eqn. 3.1.7a and the corresponding value of constraint factor is 1.12. However, using the value of $\phi=1$ in Eqn. 3.1.6, the true plastic strain is found as, $\epsilon_p = 0.43\sigma_t/E_{spec}$, which is too small value of strain to be measured during ABI test. The lowest strain practically measurable from this technique is 0.06. Hence the yield stress cannot be measured directly from the test as the minimum measurable strain for a nominal size indenter is generally about 20 times larger than the yield strain. Therefore, an indirect approach is used for the estimation of the yield stress by availing the following relationship,

$$\frac{P}{d_t^2} = A \left(\frac{d_t}{D} \right)^{m-2} \quad (3.1.8)$$

where, ‘m’ is the Meyer’s coefficient and ‘A’ is yield parameter. When the indenter penetrates deeper into the test material, both elastic and plastic deformations occur with the simultaneous occurrence of yielding and work hardening processes in each cycle^[15]. To take into account the occurrence of yielding in each cycle during the calculation of yield stress, the entire load-displacement curve has to be considered. Therefore the values of (P/d_t^2) obtained from all loading cycles are plotted against corresponding (d_t/D) . The yield parameter (A) is obtained by fitting power law as per Eqn. 3.1.8 to this curve and then extrapolating to maximum value of $d_t/D=1$, as shown in Fig. 3.5.

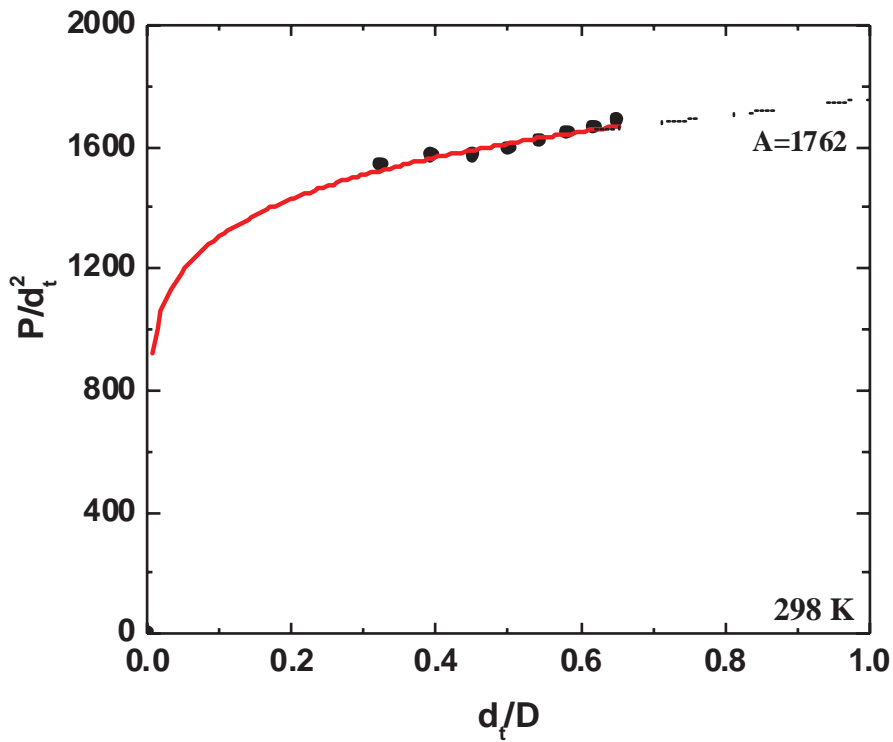


Fig. 3.5 Calculation of yield parameter (A) shown typically at 298 K.

The yield stress was calculated from the so obtained yield parameter using the following equation^[15],

$$\sigma_y = B + \beta A \quad (3.1.9)$$

where, ‘B’ is yield offset constant (in MPa) and ‘β’ is material yield slope which depend on the class of materials and the indenter diameter. The values of ‘B’ and ‘β’ were determined by comparing the yield parameter, calculated from ABI tests conducted on the various heats of 316LN SS at various temperatures, with corresponding yield stress (σ_y) obtained from uniaxial tensile tests^[112], as shown in Fig. 3.6. A linear fit was imposed on the plot between ABI yield parameter and uniaxial yield stress, thus obtaining the following relationship,

$$\sigma_y = -105 + 0.256 A \quad (3.1.10)$$

Taking B=-105 and β=0.256 in Eqn. 3.1.10, the yield stress was estimated by using yield parameter from ABI test. The values of β were similarly reported as 0.191 for 316L SS base metal and welds^[17] and 0.28 for P92 steel^[39].

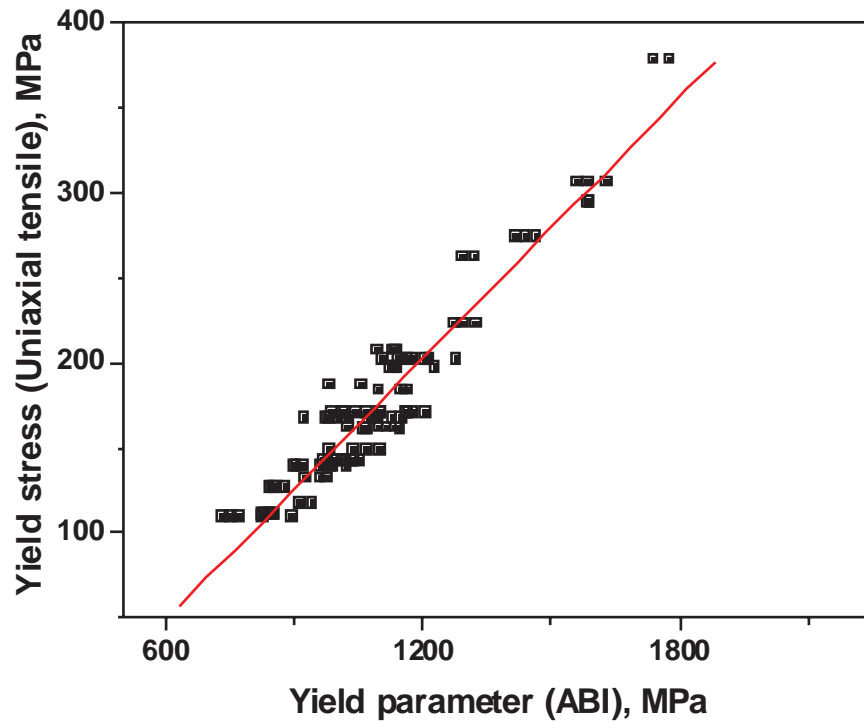


Fig. 3.6 Relationship between yield parameter and uniaxial yield stress.

Unlike uniaxial tensile test, the strain rate during the test cannot be kept constant in ABI test. This is due to continuous change in area of contact between indenter and the specimen though there may not be much variation in strain rate within a test cycle. Therefore, the strain

rate ($\dot{\epsilon}$) was calculated approximately for each cycle by relating rate of displacement of indenter (v_i) with the total indentation diameter (d_t) as ^[126],

$$\dot{\epsilon} \approx 0.4 (v_i/d_t) \quad (3.1.11)$$

The ball indentation strain rate was determined for each cycle from Eqn. 3.1.11 by substituting, $v_i = 0.008 \text{ mm s}^{-1}$ and ' d_t ' values determined for each cycle as per Eqn. 3.1.1. It is known that the total diameter keeps changing from cycle to cycle as the depth of indentation is increased. The effective ball indentation strain rate of the test as a whole was taken as the average of strain rate determined from all the cycles and it was found to be $8 \times 10^{-3} \text{ s}^{-1}$.

As a result of material pileup around the indentation, the actual contact radius is larger than the apparent contact radius without pileup. However, the effect of pile-up / sink-in phenomenon is ignored during the above calculation of plastic diameter, in order to simplify the analysis. The full unloading curve is assumed to be linear in the above analysis for the same reason. As more corrective functions are introduced into the analysis to improve the accuracy of calculation of plastic diameter, higher is the complexity in obtaining solutions for a wide range of materials. Even such corrective functions formulated for certain class of material may go wrong for another material; validation and modification of such complex functions may still add further complexity. Instead, corrections can be introduced in the analysis level, by adjusting the empirically correlated parameters such as yield slope and constraint factor, to provide quick and yet reliable results.

3.2 Influence of test parameters

ABI testing technique is largely utilized worldwide for various applications under diversified conditions. However, there is no universally accepted standard available for ABI testing currently. ABI test involves various parameters such as diameter and material of indenter,

surface finish of test specimen and indenter, maximum depth of indentation, number of cycles, etc. Though the underlying principles of ABI technique are common, the test parameters may actually vary across various laboratories. Initially, it is necessary to assess and understand the consequences of the values set for various parameters with respect to the material under investigation.

Generally, larger is the indenter diameter lower is the data scatter with good repeatability. The results biased due to localized heterogeneity across the test surface are averaged out with the use of indenter of larger diameter. The smaller indenters are very sensitive to specimen preparation. But it is known that ABI tests are generally sought for shortage of material available for testing. When a narrow or a thin specimen is taken out of a service component or weld joint for testing purpose, the smallest indenter possible has to be used. The indenter size is thus mainly decided by the amount of material actually available for testing.

Miraglia ^[127] studied the indenter size effect using indenters of various diameters such as 0.25, 0.51, 0.76 and 1.57 mm. It was revealed that the yield stress, ultimate tensile strength, strength coefficient increased with decrease in indenter diameter. The effective strain rate from ABI is inversely proportional to indenter diameter as inferred from Eqn. 3.1.11. As the indenter diameter decreases, the strain rate has to increase when the cross-head speed is the same and the change in strain rate may influence the results. The effect of indenter diameter is therefore dependent on the strain rate sensitivity of the material. However, the effect of indenter size is generally compensated by adjusting suitably the ABI analysis parameters (constraint factor, yield slope) used with the indenter size.

An indenter with a rough surface results in higher flow properties than a smooth indenter due to the requirement of additional initial load to overcome the friction before the starting of plastic flow ^[17]. Apart from the diameter and surface finish of indenter, the influence of other

parameters mentioned above is scarcely found in the literature. Therefore the effect of those parameters on ABI results has been assessed by conducting tests on 316LN SS at 298 K.

3.2.1 Material of indenter

Wheeler et al.^[128] reviewed the properties of several potential materials for making indenters including boron carbide, silicon carbide, boron nitride, diamond, etc. The present investigation employed tungsten carbide and silicon nitride indenters which are popularly used in ABI testing. The applied load-depth of indentation curves measured from ABI tests, by employing tungsten carbide and silicon nitride indenters, are shown in Fig. 3.7. For the same depth of indentation, the applied load decreased when silicon nitride indenter was used in place of tungsten carbide indenter. This is an indication of the extent of elastic deformation of silicon nitride indenter relative to tungsten carbide indenter. The material of indenter thus significantly affects the applied load through its contribution to the measured depth of indentation by means of its own deformation.

From the above load-depth of indentation data, the flow curves were determined using Eqns. 3.1.1-3.1.8. The value of constraint factor that was estimated from ABI tests using silicon nitride indenter was 2.72 whereas that obtained using tungsten carbide indenter was 3.1. Irrespective of the material of indenter, the flow curves that were determined by applying the above constraint factor values were found to be close to one another (Fig. 3.6). The constraint factor depends on the material properties of the tested specimen. The material with lower strain hardening exponent shows higher constraint factor and vice versa^[129]. In the present case, it may be noted that the empirical estimation of constraint factor is not only dependent on the material being investigated but also on the material of which the indenter is made of. The constraint effect was found to have decreased when silicon nitride indenter was used in place of tungsten carbide indenter.

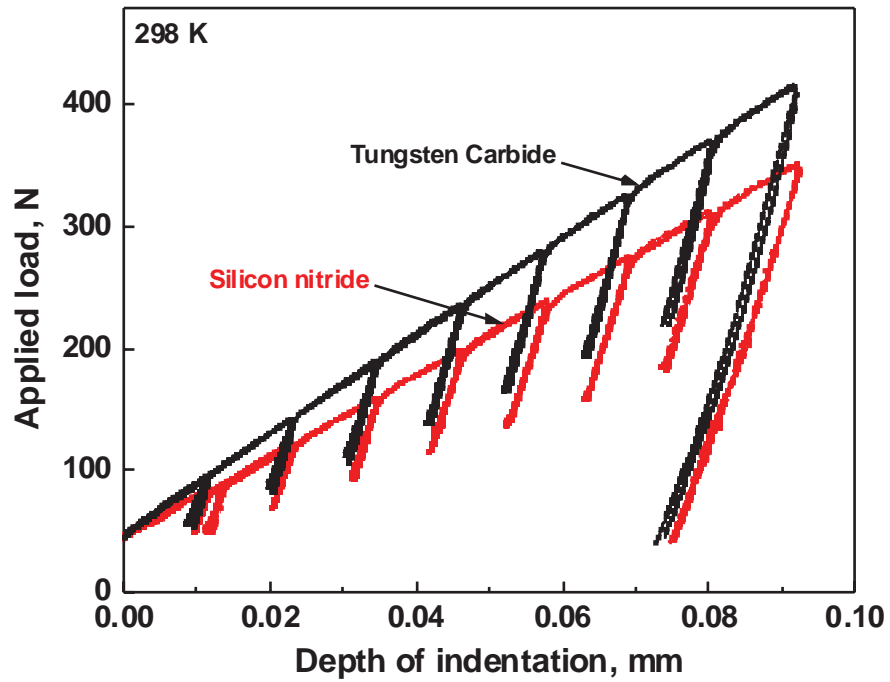


Fig. 3.7 Influence of indenter material on applied load for the same depth of indentation.

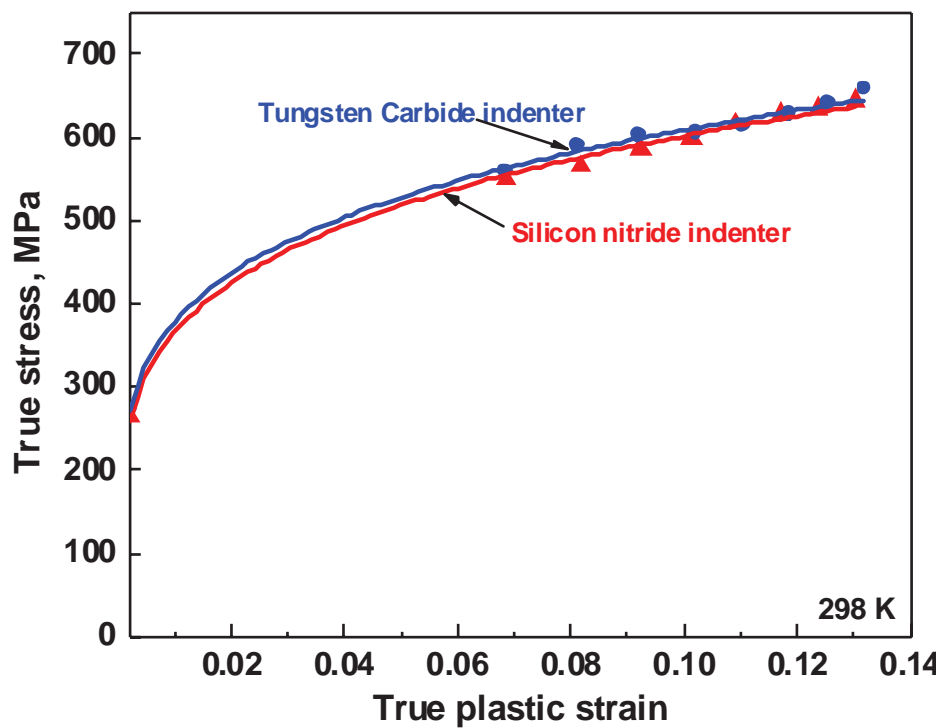


Fig. 3.8 Comparison of flow curves obtained using tungsten carbide and silicon nitride indenters.

As the material of indenter significantly affects ABI results, the indenter material must be selected judiciously. Because of its high Young's modulus 630 GPa and Vickers hardness being not less than 1500, tungsten carbide is the preferred material for indentation applications at room temperature. However, owing to chances of oxidation at higher temperature, use of tungsten carbide indenter is restricted up to 673 K whereas silicon nitride is relatively stable beyond that range. Gonzalez et al. ^[130] evaluated the elastic-plastic properties and contact damage evolution of silicon nitride upto 1273 K and concluded that the great stiffness and resistance to contact damage make silicon nitride as the right choice for indenters at high temperatures. He also obtained the Young's modulus of silicon nitride from Hertzian indentation tests and reported a slow linear decrease (18 MPa/°C) with increasing temperature upto ≈ 800 °C (1073 K). Hence relatively stable silicon nitride indenter can be used at high temperatures (> 673 K).

3.2.2 Surface finish

The influence of friction between the indenter and the specimen on ABI results has been investigated indirectly by varying the surface finish of the specimen. The test specimen was initially polished using P80 grit paper. Before conducting ABI test, the surface roughness of specimen was measured using surface profilometer. Subsequently, the specimen was further polished using P400, P800 and P1200 grit paper and the surface finish that was achieved after each level of polishing are tabulated in Table 3.1. ABI tests were conducted under each surface finish condition.

The load-depth of indentation curves that were obtained over the test specimen with various surface finish were found to overlap each other, as shown in Fig. 3.9. The same value of constraint factor was used to calculate stress-strain values. The stress-strain curves that were obtained from these tests are shown in Fig. 3.10. The various levels of surface finish of test

Table 3.1 Surface roughness achieved after each level of polishing.

Grade	Surface roughness, R_a (microns)
Initial	9.99
P80 grit	4.07
P400 grit	2.55
P800 grit	2.34
P1200 grit	2.02

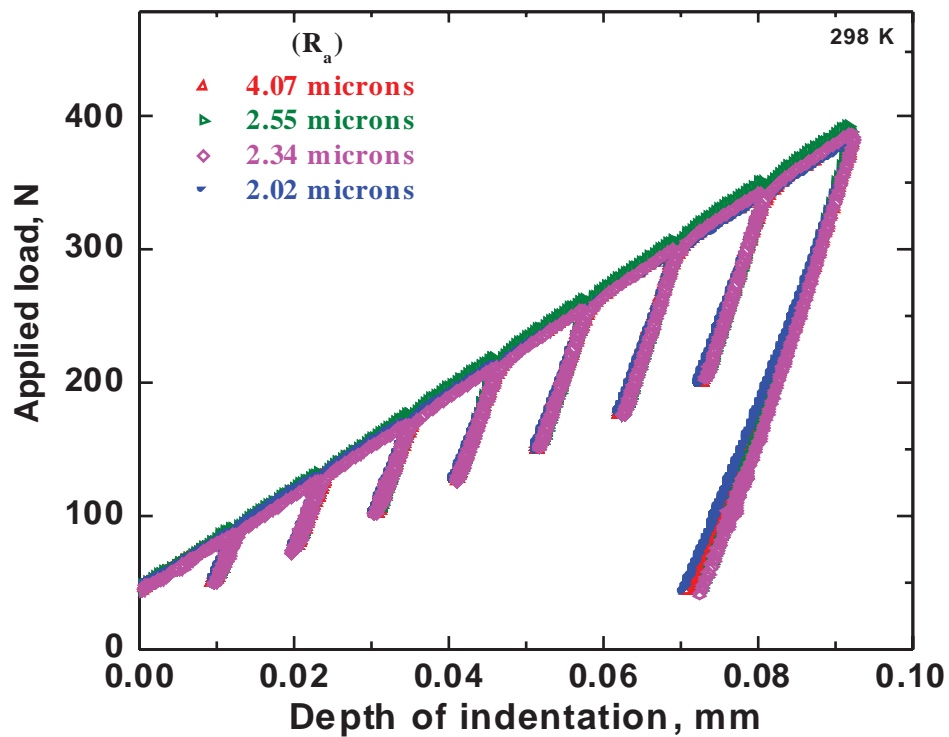


Fig. 3.9 Effect of surface finish of test specimen on measured data.

specimen in the R_a range 4.07-2.02 microns that were achieved through polishing in the range P80-P1200, did not appreciably affect the ABI test results. When the indenter comes in contact with the specimen, the asperities first flow plastically although the region under the specimen surface still behaves elastically. The surface roughness of the test specimen has little effect on the size of indentation produced, provided the indentation itself is large compared with the dimensions of those asperities ^[17]. Nevertheless, initial polishing (upto

1200 grit or mirror polishing) is necessary to eliminate small pits and projections on the testing surface to avoid large scatter in ABI results.

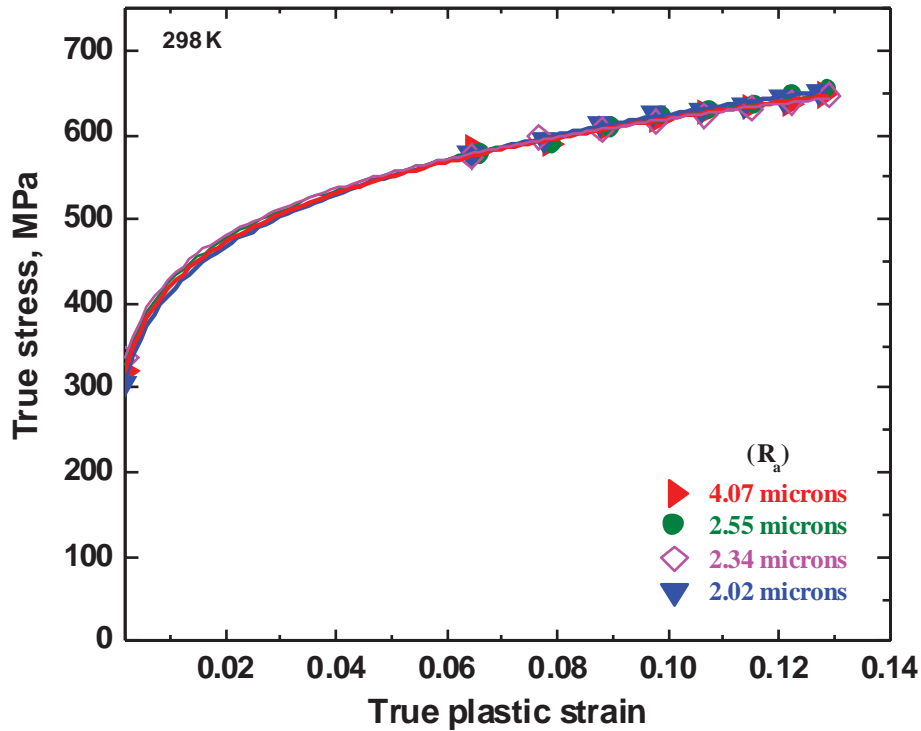


Fig. 3.10 Effect of surface finish of test specimen on flow curves of 316LN SS.

3.2.3 Maximum depth of indentation

The maximum strain value from ABI test is decided by the maximum depth of indentation. The setting for maximum depth of indentation is a function of percentage of indenter radius. ABI tests were conducted on 316LN SS by setting the maximum depth of indentation as 12, 24, 36, 42 and 50% of indenter radius. The optical micrographs of the indentations obtained by setting various maximum depth of indentation are shown in Figs. 3.11 (a)-(e). The increase in chordal diameter of indentation at the end of each test with increased maximum depth of indentation has been inferred from the same figures.

Figure 3.12 shows the load-depth of indentation curves measured by setting various maximum depth of indentation. The load-depth of indentation curve corresponding to 50% of indenter radius overlapped with the other curves corresponding to lower maximum depth of

indentation. The slope of load-depth of indentation curve did not change with change in maximum depth of indentation. The slope of unloading curve increased uniformly after each cycle, in all cases.

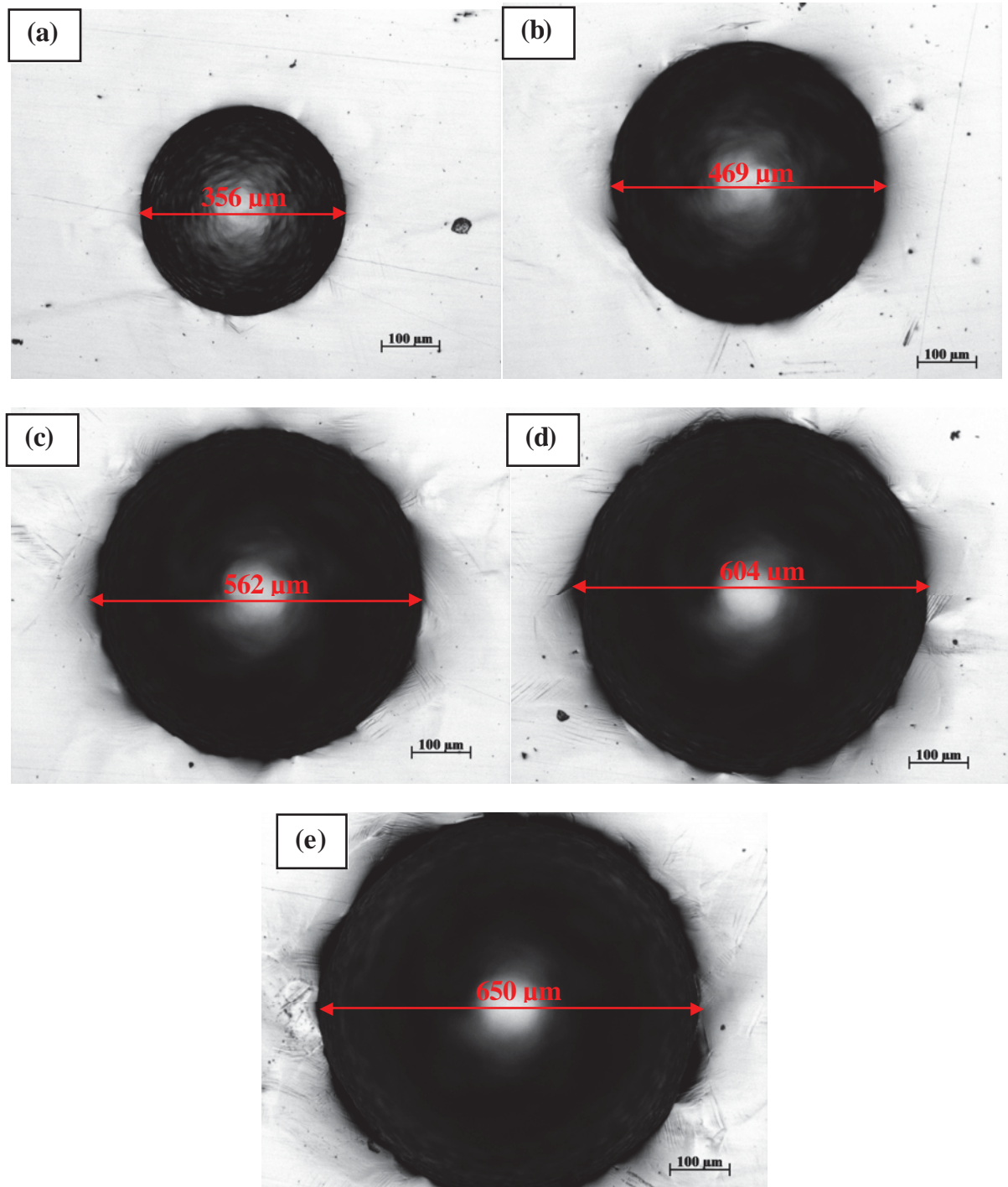


Fig. 3.11 Optical micrographs of indentations obtained by setting maximum depth of indentation as (a) 12% (b) 24% (c) 36% (d) 42% and (e) 50%.

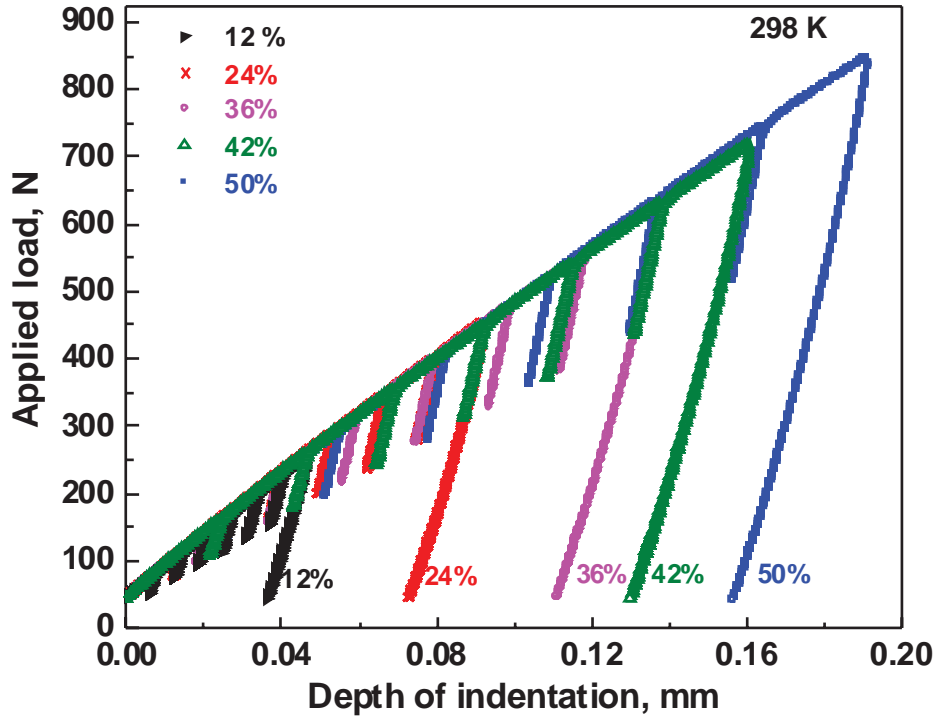


Fig. 3.12 Load-depth of indentation curves obtained by varying maximum depth of indentation.

The flow curves, shown in Fig. 3.13, exhibited no significant change with increase in maximum depth of indentation (in the range 12% to 50% of indenter radius). The same constraint factor was applied in all the cases which implied that the constraint imposed by specimen in response to load remained the same irrespective of maximum depth of indentation. When the maximum depth of indentation is chosen on the lower side of this range, it is difficult to precisely complete sufficient number of loading and unloading cycles, especially during high temperature test. Higher the maximum depth of indentation the more may be the chances of damage occurring in the indenter over a period of usage. From the observations based on above experiments, it is recommended to set the maximum depth of indentation as 24% of indenter radius.

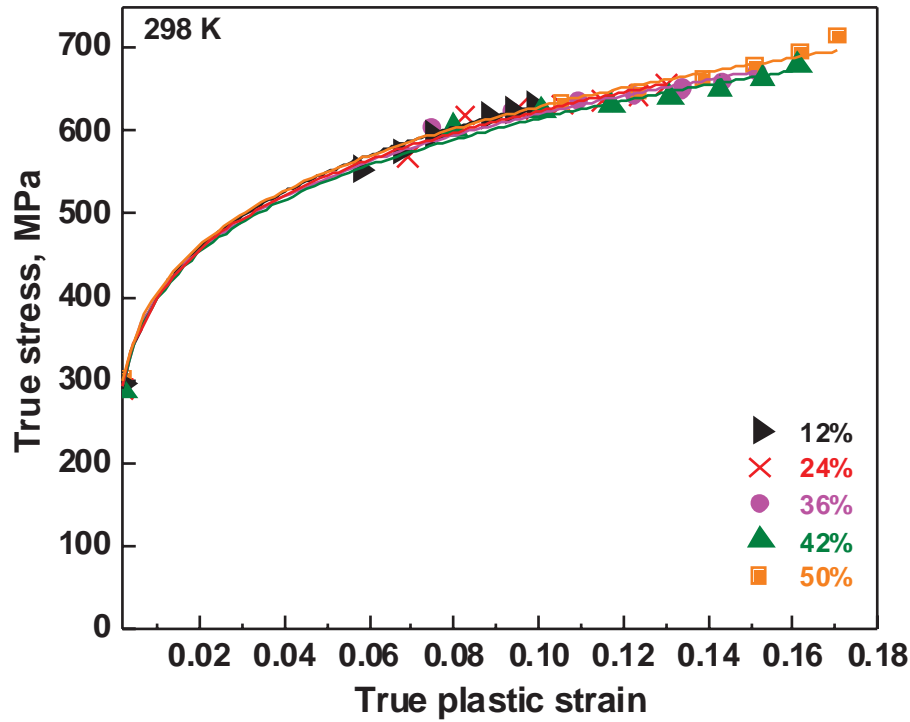


Fig. 3.13 Flow curves obtained by varying maximum depth of indentation.

3.2.4 Number of cycles

The number of cycles, each comprising loading and partial unloading, decides the number of data points available for plotting true stress-plastic strain curve. Keeping the other test parameters as the same, the number of cycles was varied. The maximum depth of indentation was set as 24% of indenter radius, i.e., 0.182 mm. The load-depth of indentation curves determined from ABI tests by setting various number of cycles of loading and unloading are shown in Fig. 3.14. The slope of load-depth of indentation curve seemed to be similar in all the cases. The scatter was observed only in the final unloading cycle. However, data upto initial 40% of unloading curve was usually taken for regression of unloading curve and within this range, there was not much scatter. The flow curves determined from these tests are shown in Fig. 3.15. It was observed that trend curves obtained by varying the number of cycles were closer to one another. The small extent of scatter visible in the plot may sometimes occur with tests even with the same test parameters.

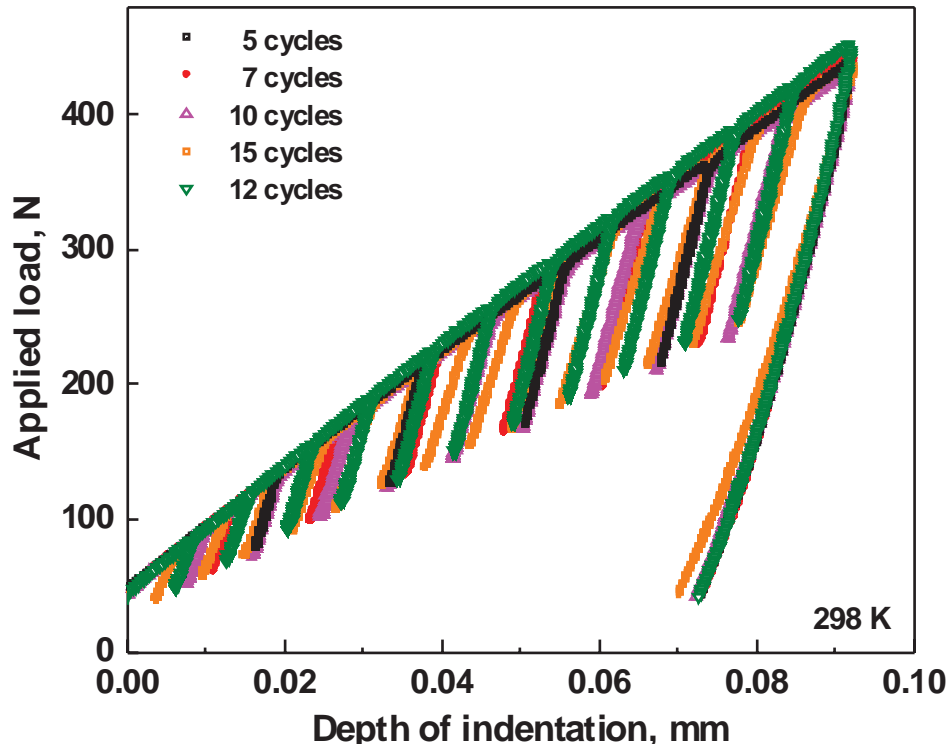


Fig. 3.14 Load-indentation depth curves measured by setting various number of test cycles.

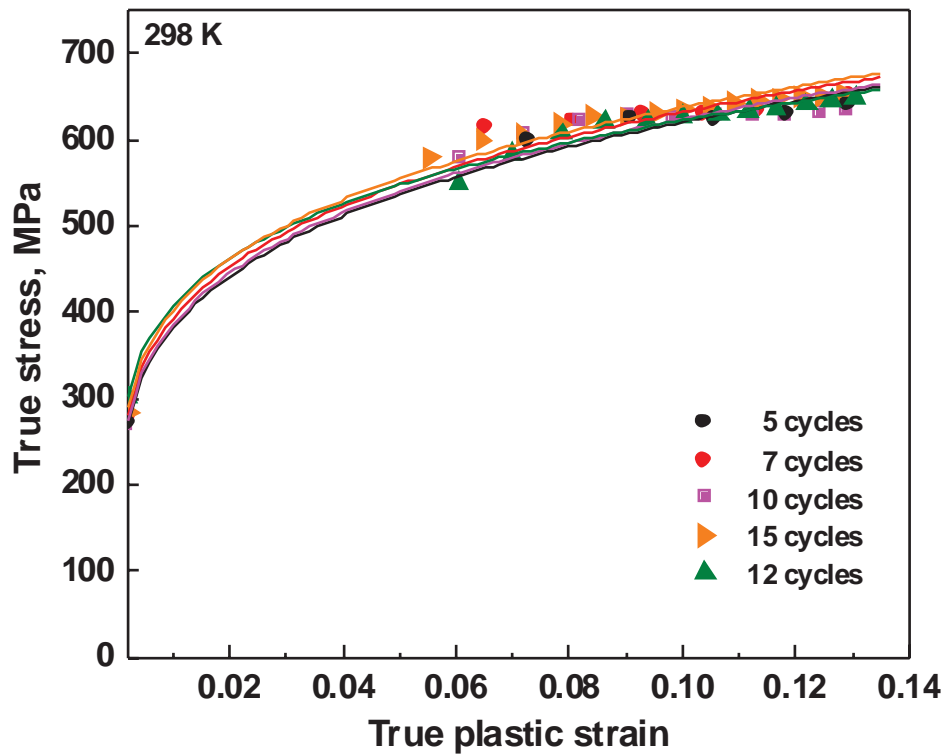


Fig. 3.15 Flow curves obtained for 316LN SS by setting various number of test cycles.

Increasing the number of cycles can increase the number of stress-strain data points, which can improve the fit for flow curve statistically. At the same time, the test time is increased. Also when the gap between successive cycles becomes shorter in load-indentation depth curve, errors arise in the automated control of loading and unloading and the same is reflected as scatter during analysis.

Therefore, by increasing the maximum depth of indentation (in the range 12% to 50% of indenter radius), number of cycles (in the range 5 to 12 cycles) and surface finish of test specimen (average roughness (R_a) in the range 2-4 microns) to higher values, at the cost of time and efforts, ABI results were not altered significantly. The parameters that were suitable for conducting ABI tests on the materials under investigation were also found. Then the high temperature tensile properties of 316L(N) SS were evaluated using ABI technique over the temperature range 298-973 K.

3.3 High temperature tensile properties of 316L(N) SS

Figure 3.16 shows the indentations on an ABI specimen subjected to test at 298 K. The optical micrograph of ABI specimen after indentation is shown in Fig. 3.17. The deformation around the indentation with pileup and lot of twins was clearly seen in the micrograph. The grain boundaries and triple point are relatively stronger regions in the microstructure. At higher magnification, the grain boundaries that are subjected to load just under the centre of indenter are shown clearly in Figs. 3.18. It was observed that though the total depth of



Fig. 3.16 ABI specimen tested at 298 K.

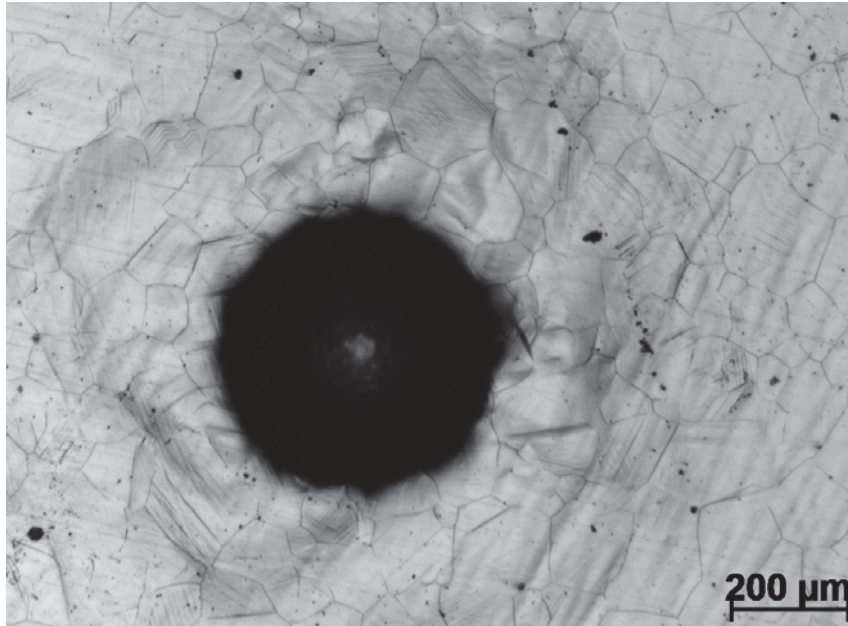


Fig. 3.17 Optical micrograph of ABI specimen tested at 298 K.

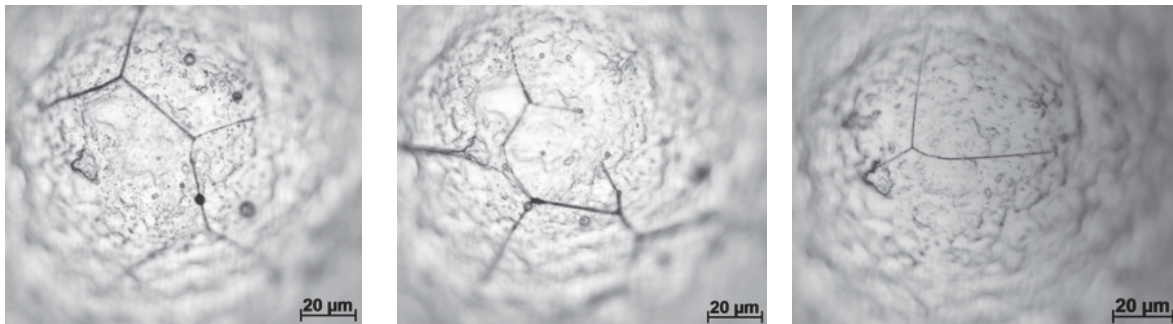


Fig. 3.18 Differences in microstructure subjected to indentation.

indentation and final diameter of indentation were the same during the tests, still the small level of scatter in results may be attributed to the difference in microstructures actually subjected to load.

The applied load-depth of indentation curves obtained for 316L(N) SS at various temperatures are shown in Fig. 3.19. For the same depth of indentation, the applied load decreased with increase in temperature. The load-depth of indentation data measured at various temperatures were analysed using Eqns. 3.1- 3.10 to determine various tensile properties such as yield stress, true stress-true plastic strain, strength coefficient, strain hardening exponent, ultimate tensile strength and uniform ductility.

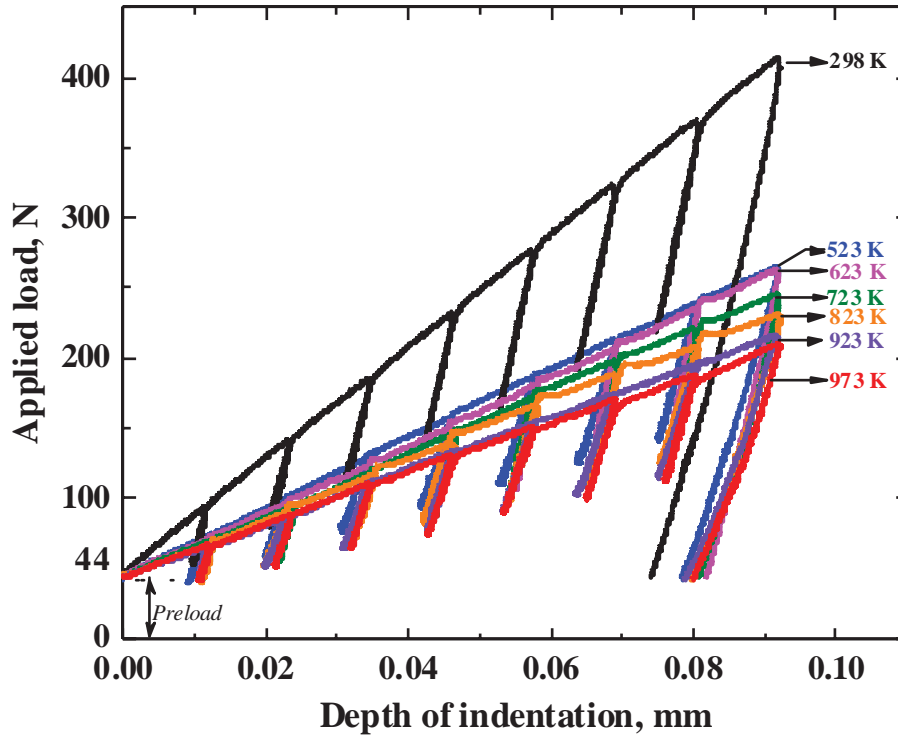


Fig. 3.19 Load-depth of indentation curves measured at various temperatures.

3.3.1 Yield stress

The yield stress was calculated from yield parameter using Eqn. 3.1.10, at several temperatures. The yield stress showed a decreasing trend with temperature as shown in Fig. 3.20. The yield stress curve determined from uniaxial tensile tests are superimposed as dotted line on the same figure, which implied that values obtained from ABI tests were closer to uniaxial tensile tests data.

3.3.2. Flow curves

In the present investigation, the parameter α_m was respectively taken as 1.25 and 0.9 for analysing room temperature and higher temperature tests. The different values of constraint factor taken at room temperature and at elevated temperatures were similarly reported for IN718 alloy ^[131]. For Ti-6Al-4V alloy, the constraint factor was reported as temperature

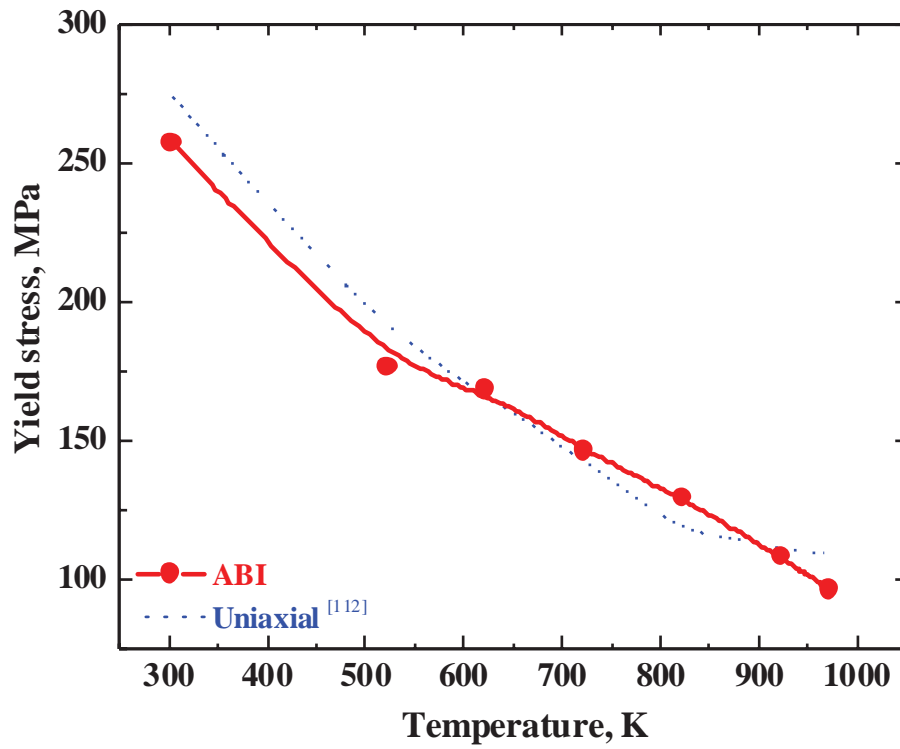


Fig. 3.20 Yield stress values plotted as a function of temperature.

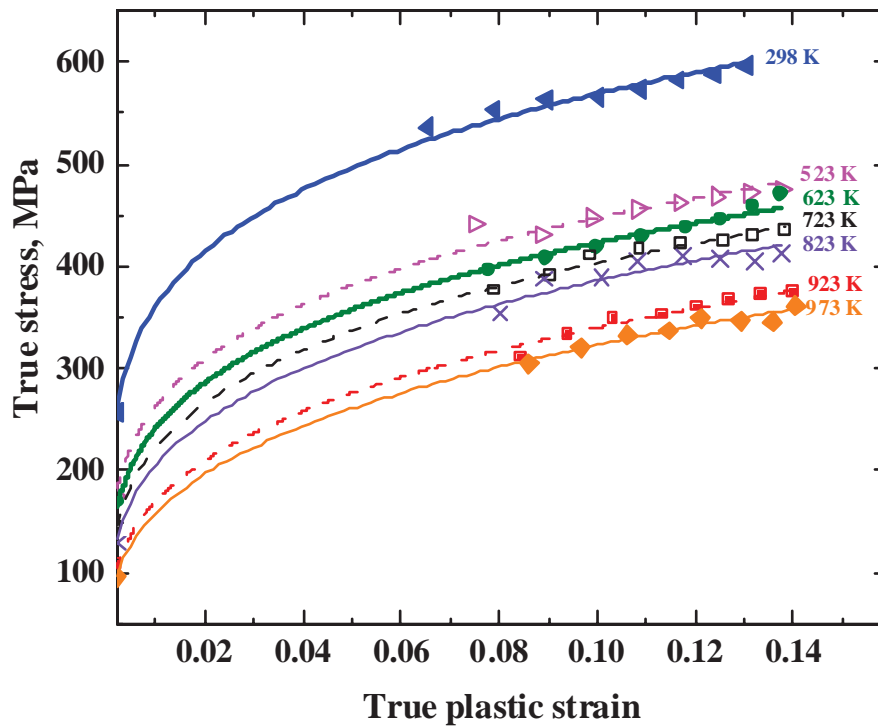


Fig. 3.21 Flow curves obtained for 316L(N) SS at various temperatures using ABI technique.

dependent only in elastic-plastic regime ^[132]. The flow curves for 316L(N) SS estimated at various temperatures using Eqns. 3.1.2 -3.1.7, are presented in Fig. 3.21. As expected, true stress decreased with increase in temperature for the same true plastic strain.

The true stress-true plastic strain values obtained from ABI tests are shown as scattered points over the corresponding uniaxial curves in Fig. 3.22. Generally, it may be observed that the ABI datapoints lie closer to uniaxial test values with less scatter in results, inspite of wide range of test temperatures under study. Similar kind of correlation between ABI and uniaxial test results was reported by K.L. Murty et al. ^[133].

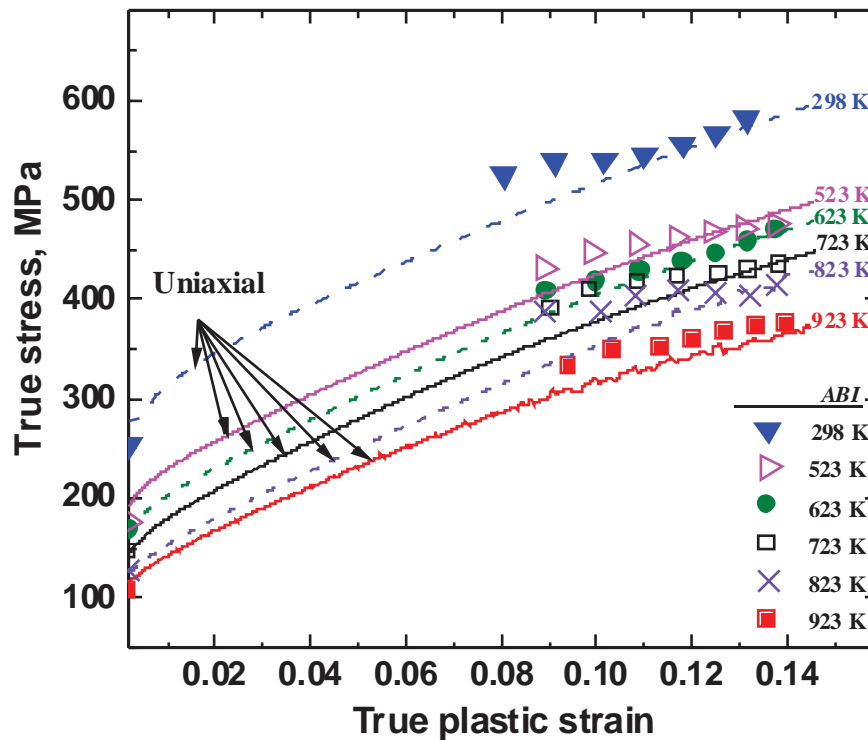


Fig. 3.22 Comparison of flow curves obtained from ABI and uniaxial tests.

3.3.3 Strength coefficient and strain hardening exponent

It has been known that the stress-strain behaviour of many metallic materials, especially 316LN SS, obey Holloman's equation,

$$\sigma_t = K \epsilon_p^n \quad (3.3.1)$$

where ‘K’ is the strength coefficient (in MPa) and ‘n’ is the strain hardening exponent. The strength coefficient and strain hardening exponent are estimated through the power law regression of flow curves as described in ASTM standard E646 ^[134]. The influence of temperature on strength coefficient and strain hardening exponent is shown in Fig. 3.23. The strength coefficient decreased and strain hardening exponent increased with increase in temperature. It is to be noted that ASTM standard E646 mentions that a single power law may not fit the entire curve and strain hardening exponent reported is the value averaged out of some specific strain interval on flow curve.

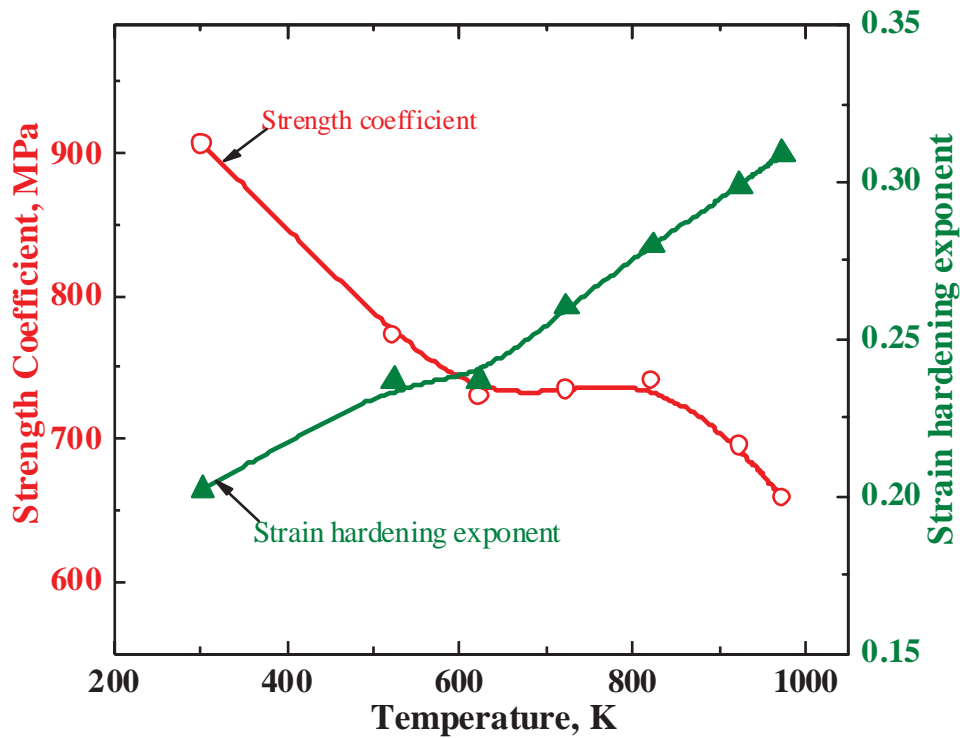


Fig. 3.23 Influence of temperature on strength coefficient and strain hardening exponent.

3.3.4 Ultimate tensile strength

In uniaxial tensile test, the stress at the point of necking is taken as ultimate tensile strength. As ABI specimen does not undergo necking or fracture under compressive loading, the ultimate tensile point is absent in the flow curve determined from ABI test. Hence, determination of ultimate tensile strength from ABI test is subjected to certain limitations.

The ultimate tensile strength (σ_{uts}) is obtained from ABI test through Considere criterion for plastic instability, which is applicable only to materials whose stress-strain behaviour obeys Holloman's equation. The Considere criterion states that the uniform strain at the onset of necking is equal to the strain hardening exponent. The engineering ultimate tensile strength (S_{uts}) can be obtained by taking uniform strain, $\epsilon_u=n$ in Hollomon's equation as,

$$S_{uts} = K \left(\frac{\epsilon_u}{e} \right)^n = K \left(\frac{n}{e} \right)^n, e \approx 2.71 \quad (3.3.2)$$

The strain hardening exponent values shown under section 3.3.3 were utilised in the calculation of ultimate tensile strength. The ultimate tensile strength values are plotted as a function of temperature in Fig. 3.24. As expected, the ultimate tensile strength decreased with increase in temperature.

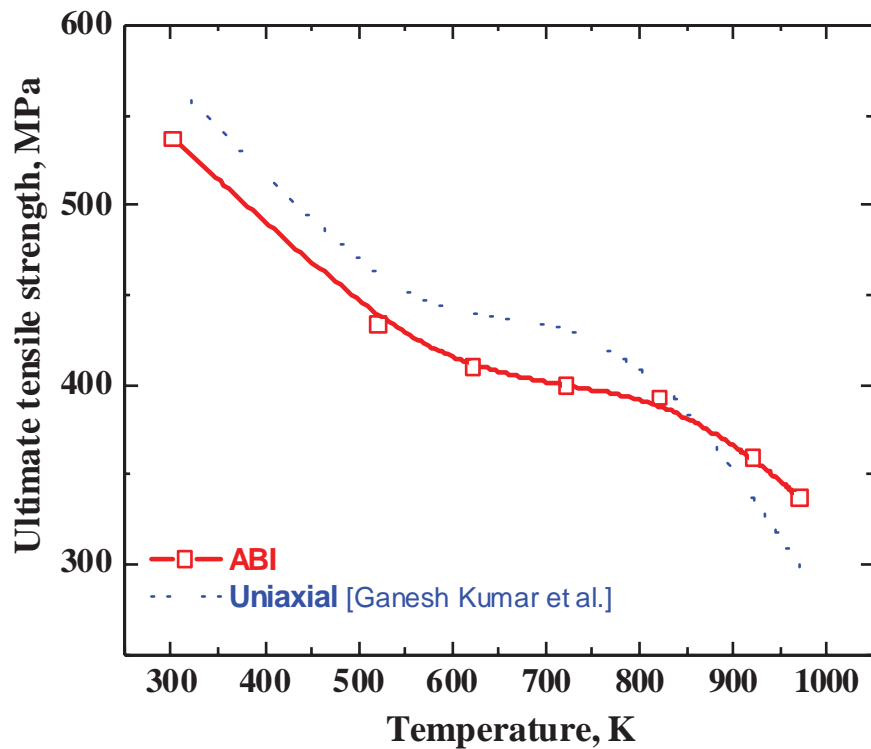


Fig. 3.24 Ultimate tensile strength plotted as function of temperature.

The trend curve surprisingly exhibited a plateau region in the temperature range 573-773 K. The trend curve for ultimate tensile strength determined from uniaxial tensile tests is also

shown in the same figure as dotted line. The plateau region was observed in the uniaxial tensile test curve almost in the same temperature range and this can be taken as an indication of occurrence of dynamic strain ageing (DSA) phenomenon in the material. Type A serrations were observed in the uniaxial tensile stress-strain curves for 316L(N) SS in the intermediate temperature range 773-973 K and has been attributed due to DSA ^[135]. However, no serrations were obtained physically in the load-depth of indentation curve. But serrated flow in stress-strain curve is not the only indication of DSA, as DSA may cause peak in variation of tensile strength with temperature, negative strain rate sensitivity on flow stress, minimum in ductility and change in fracture mode ^[136]. In the present case, values of ultimate tensile strength at various temperatures were normalized with respect to corresponding Young's modulus given by Eqn. 3.1.3. The variation of ultimate tensile strength/E with temperature, as shown in Fig. 3.25, exhibits three regimes. A decreasing trend was observed upto 623 K after which the trend reversed to reach the peak around 823 K. The region around peak temperature may be taken as DSA regime.

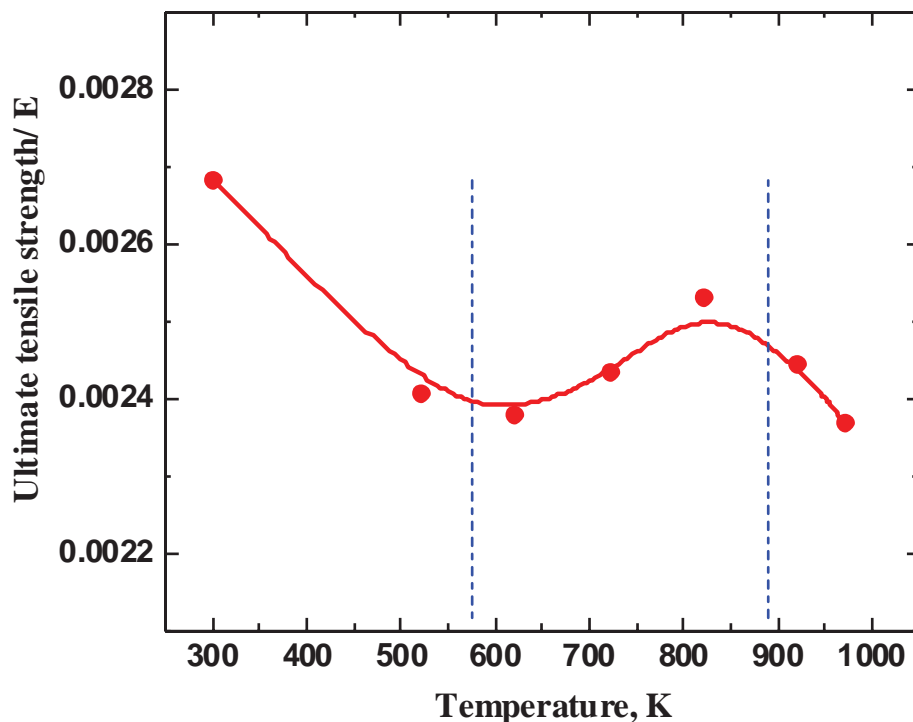


Fig. 3.25 Variation of ultimate tensile strength/E with temperature.

The yield ratio, which is defined as the ratio of yield stress to ultimate tensile strength, represents the extent of deformation a material can withstand during plastic stage. Yield ratio was considered as a useful indicator of material degradation by indentation technique ^[137]. Since yield ratio is related to ductility, a reactor material is expected to have sufficient yield ratio. The variation of yield ratio as a function of temperature is shown in Fig. 3.26. A higher yield ratio at room temperature implies that larger energy is required during plastic condition before causing failure at that temperature. As the temperature is increased, the work hardening capability of the material gets reduced.

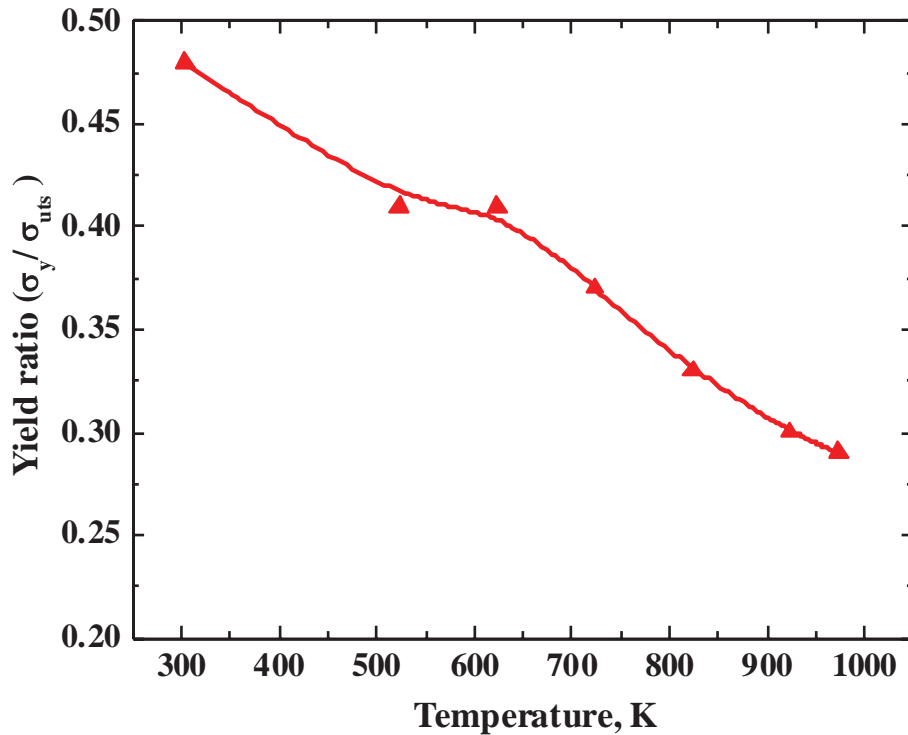


Fig. 3.26 Effect of temperature on yield ratio.

3.3.5 Uniform ductility

The strain measured upto the point of necking in uniaxial stress-strain curve is called uniform strain. As mentioned earlier, necking and rupture cannot be seen during ABI test. The uniform ductility is estimated indirectly from ABI test by drawing a tangent line to the true stress- engineering strain curve from the engineering strain value of -1.0, as shown in

Fig. 3.27. The x-value at the point of intersection of tangent line with true stress-engineering strain curve gives the uniform ductility. The uniform ductility as evaluated from ABI tests at several temperatures are plotted in Fig. 3.28 as the function of temperature. The uniform ductility gradually increased with increase in temperature.

3.3.6 ABI hardness

The calculation of hardness from ABI test is similar to Brinell hardness test since both use spherical indenter for penetrating into specimen and only the size of indenter is large for Brinell hardness testing ($\Phi 10$ mm). Brinell hardness number is usually specified with indenter diameter. ABI hardness was calculated using the following formulae,

$$BHN = \frac{2P_{\max}}{\pi D h_f} = \frac{2P_{\max}}{\pi D \left[D - \sqrt{D^2 - Dh_f} \right]} \quad (3.3.3)$$

where, P_{\max} is the maximum load at the end of last cycle, ' h_f ' is the depth of indentation at the end of loading in final cycle. The ABI hardness determined at several temperatures are shown in Fig. 3.29. ABI hardness decreased abruptly on raising the temperature from room temperature to 523 K and afterwards the hardness decreased gradually.

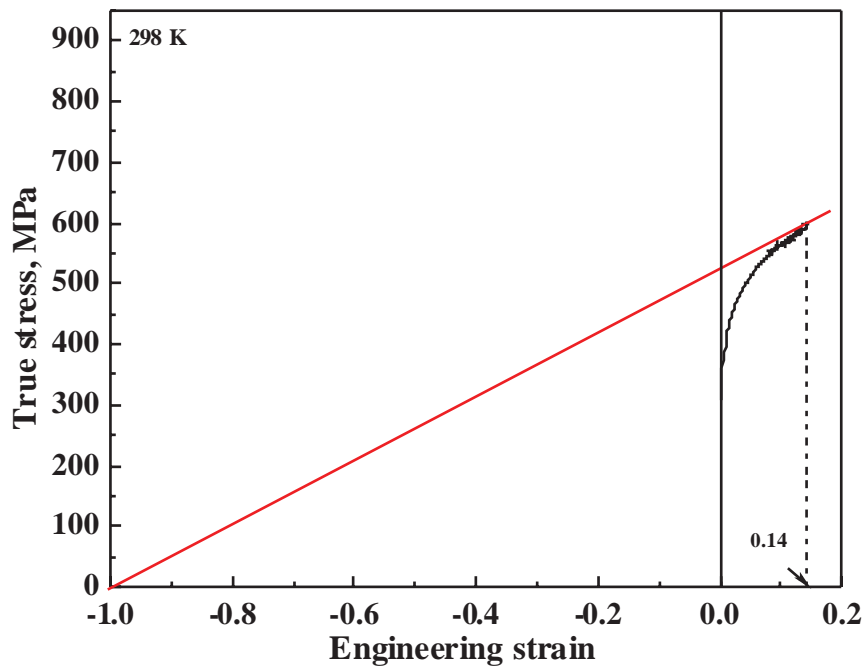


Fig. 3.27 Estimation of uniform ductility from ABI test conducted at 298 K.

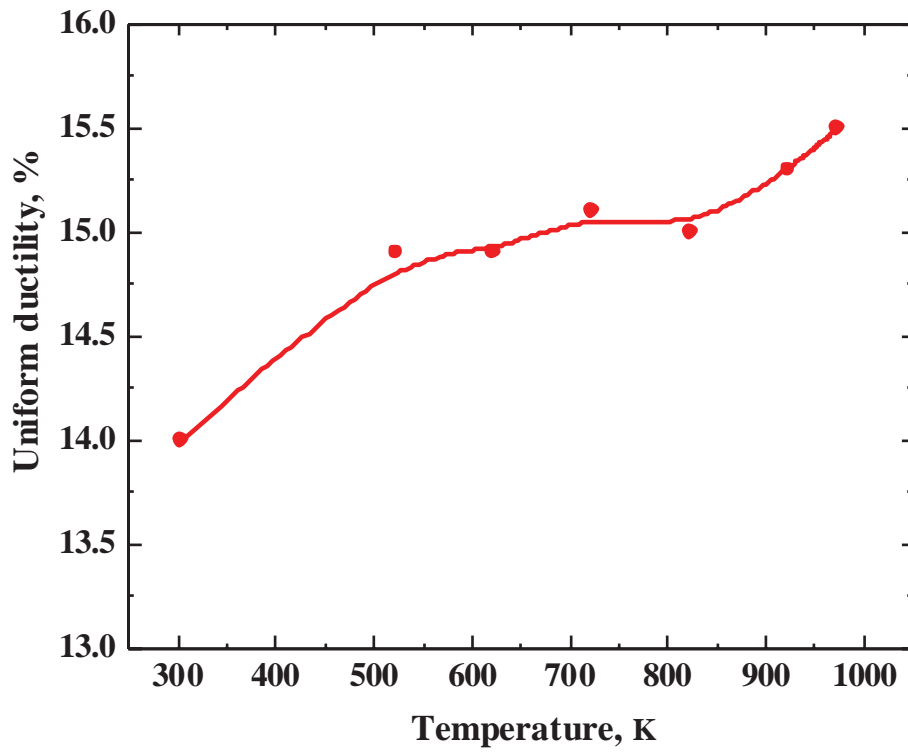


Fig. 3.28 Uniform ductility plotted as function of temperature.

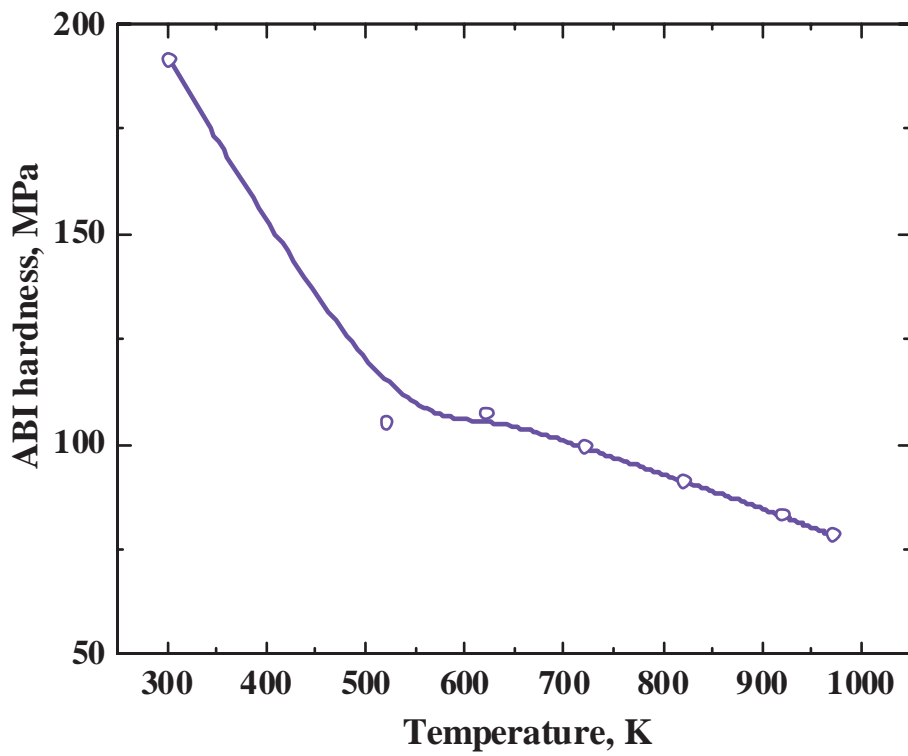


Fig. 3.29 ABI hardness obtained as function of temperature.

3.4 SEM EBSD analysis

SEM EBSD analysis revealed the crystallographic planes participating in the compressive deformation process beneath the indenter. Inverse pole figure (IPF) map for the deformed region around the contact surface is shown with legend triangle in Fig. 3.30. The different colours in the IPF maps indicated the crystallographic planes of the orientations as defined in legend. It was revealed that grains were largely compressed in the region of specimen near the contact surface and just below the indenter. The twin boundaries were fairly found all over the region of specimen beneath the indenter. The larger misorientation representing deformation was captured at each grain, which was used to map the strain values at various positions as shown in Fig. 3.31. The majority of the strain was observed to be accommodated in a specific region, which was visualized to be bounded by imaginary tangents to the spherical indenter at the contact boundary.

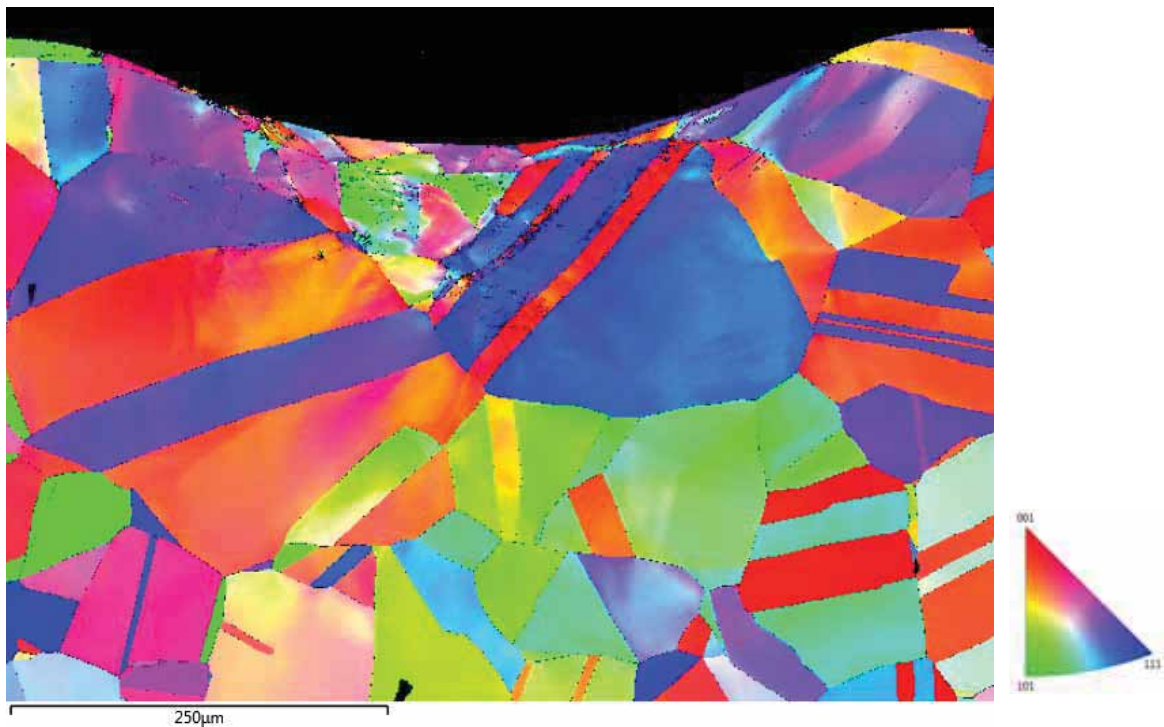


Fig. 3.30 SEM EBSD micrograph showing the orientation due to indentation load at 298 K.

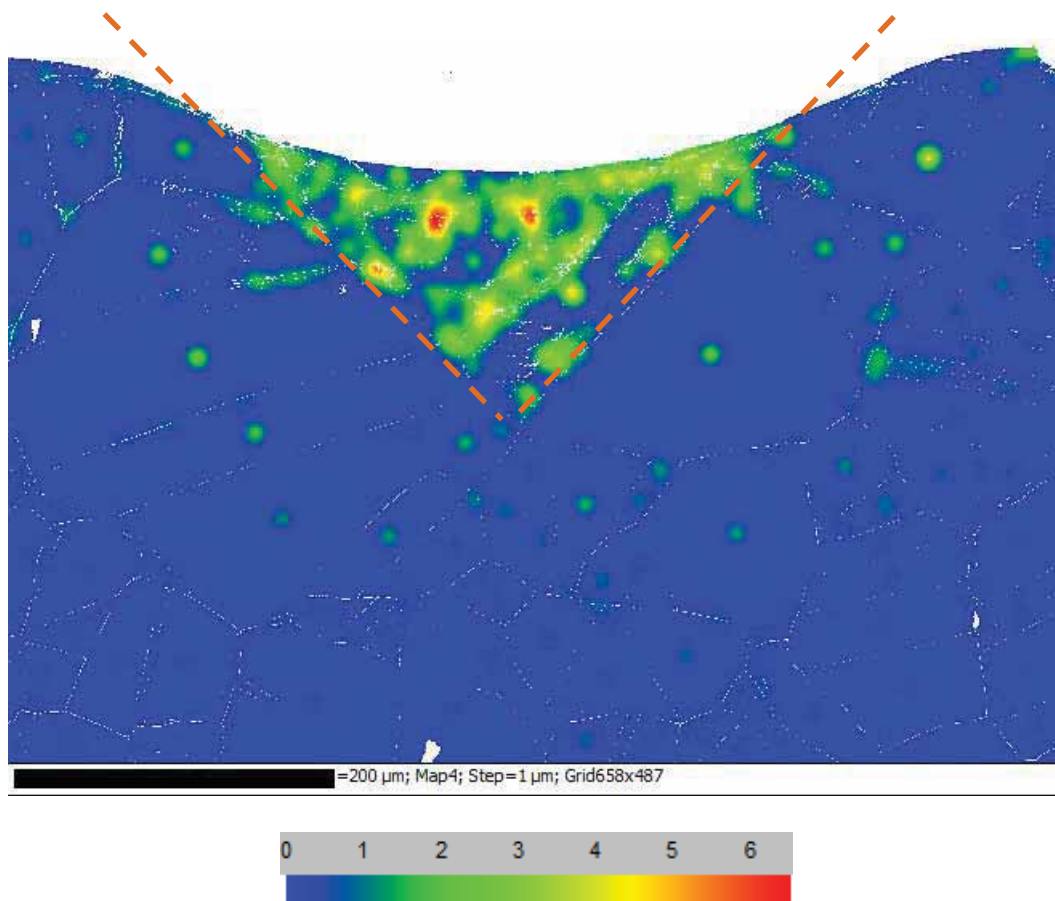


Fig. 3.31 Strain distribution in ABI specimen tested at 298 K.

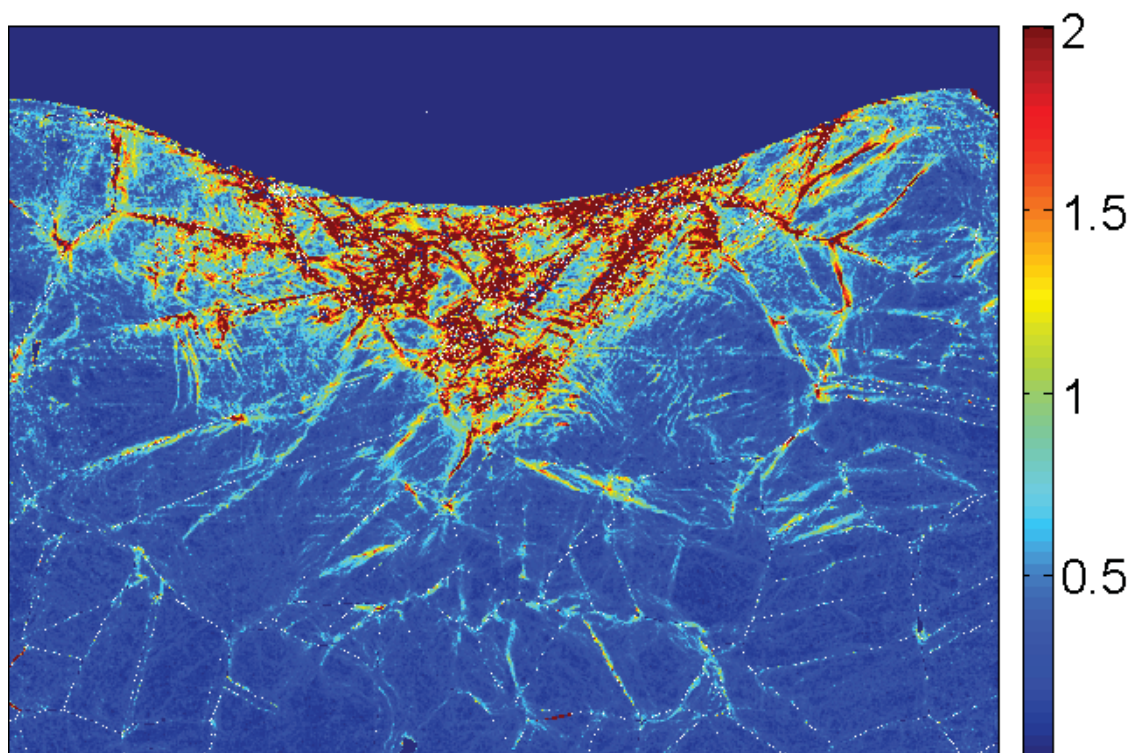


Fig. 3.32 Strain distribution obtained through KANM approach.

The strain mapping was also done over the misorientation data using Kernel Averaging Misorientation approach. A kernel is a set of points of prescribed size surrounding the scan point of interest. In Kernel Average Neighbour Misorientation (KANM), the misorientations between all neighbouring points within the kernel are averaged ^[138]. The strain map obtained using KANM approach is shown in Fig. 3.32. The strain patterns obtained from two different methods given in Figs. 3.31 and 3.32 are nearly the same. Additionally, it was observed from KANM map that the strain was found to have accumulated preferably along the grain boundaries.

3.5 FEA results

Finite element analysis (FEA) was performed to study the complicated triaxial stresses in the region of specimen below the indenter. The downward displacement of the indenter along the axis was taken as the depth of indentation. The applied load was determined indirectly as the sum of the reaction forces. The load-depth of indentation values obtained from both FEA results and test results are plotted together in Fig. 3.33. Both the curves almost overlapped each other, apart from the small deviation in the unloading curves. The mismatch between FEA and test curves sometimes happens due to machine compliance and consequently FEA shows higher load or stress for the same deformation. But in the present case, the test curve shown was already compliance corrected. Both the curves were found to coincide closely which may be taken as an indication of a good validation of FE model and the procedures adopted in the analysis.

The pressure acting on the surface of specimen due to contact with indenter is plotted for few number of cycles in Fig. 3.34. The contact pressure attained a peak value near the contact boundary and dropped afterwards to zero value. The overall contact pressure seemed to be larger than yield stress value even at preloading stage. Though the area of contact was

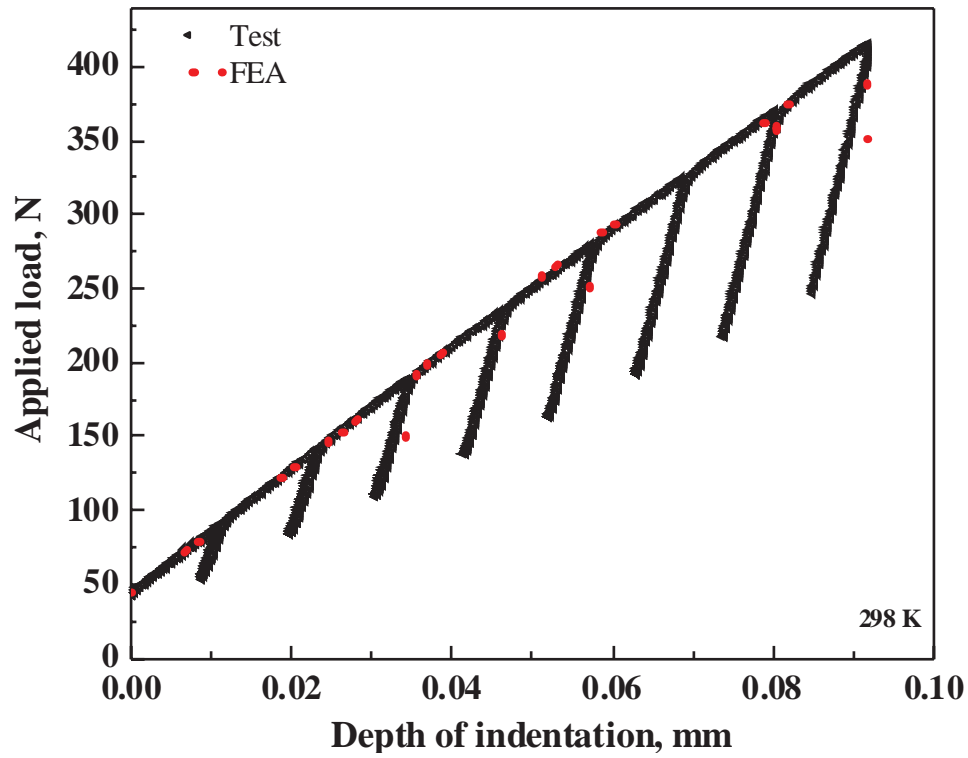


Fig. 3.33 Comparison of load-depth of indentation curves obtained from FEA and test.

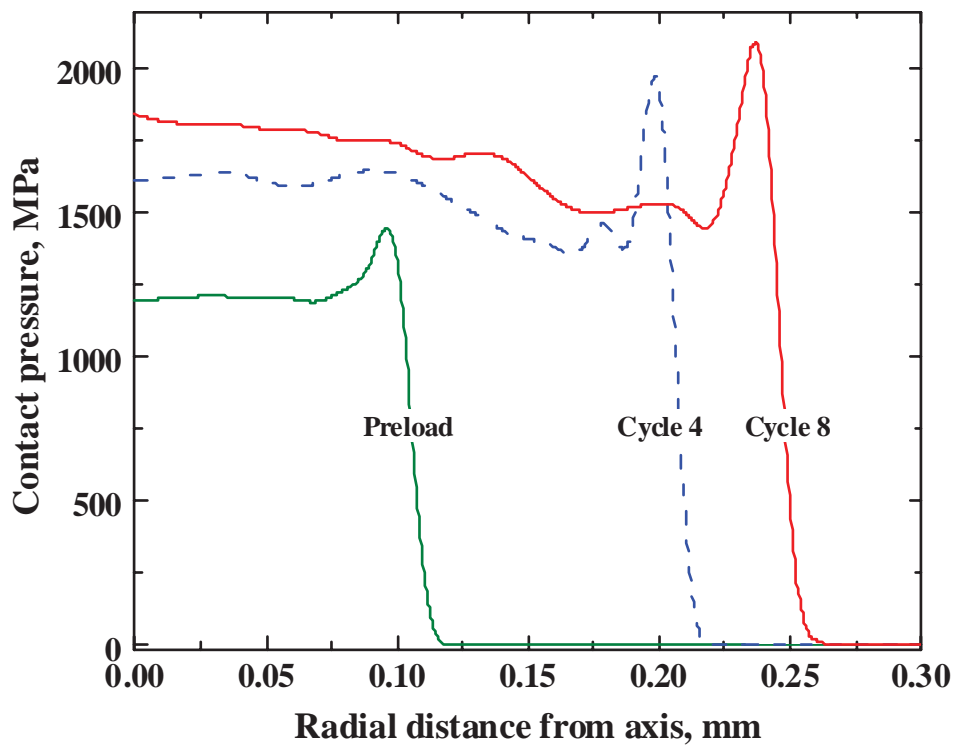


Fig. 3.34 Contact pressure at the surface of contact between specimen and indenter.

increasing in each cycle, still the contact pressure increased because of relatively larger increase in applied load with depth of indentation.

The development of different kinds of stresses with increasing depth of indentation was obtained at the end of each loading cycle. The stresses acting along the axis of symmetry and in the direction of loading are shown in Fig. 3.35a at various cycles. The axial stress acts beneath the indenter for the distance approximately upto twice the diameter of the indenter. The magnitude of the compressive stress increased with increase in test cycle. The radial stresses acting along the axis and in the direction perpendicular to axis showed a different pattern in Fig. 3.35b. The stress tuned from compressive to tensile in nature after certain distance beneath the indenter (approximately upto twice the diameter of the indenter), beyond which no radial stress was observed.

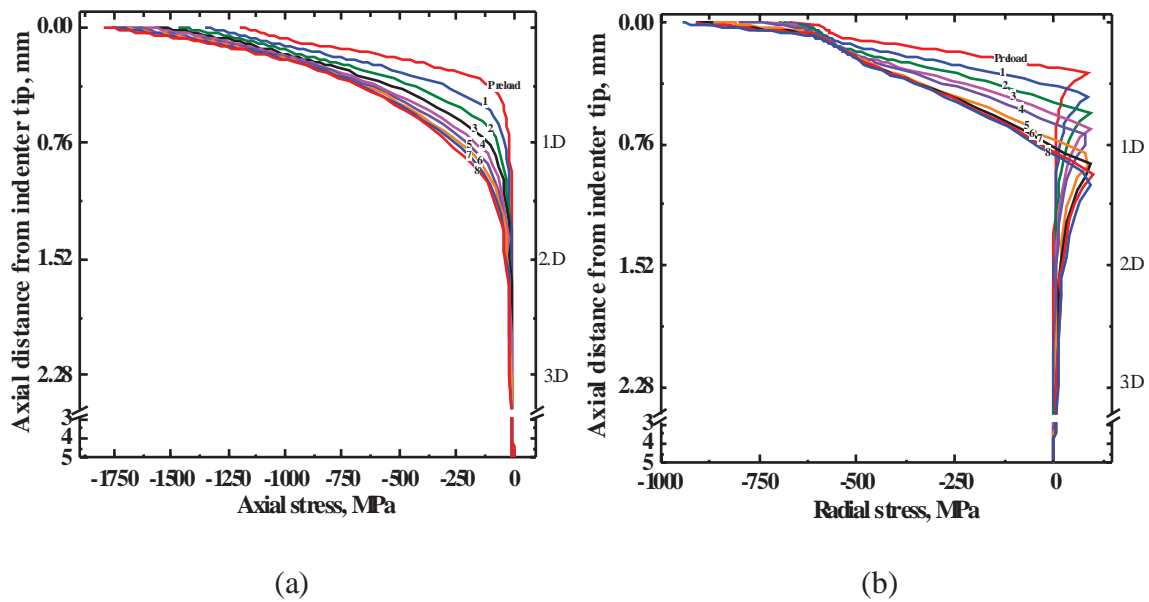


Fig. 3.35 (a) Axial stress and (b) radial stress developed below the indenter during each cycle.

One of the purposes of performing FEA analysis is to study the development of plasticity in ABI specimen. As von-Mises yield criterion is popularly used to identify plasticity, a better stress phenomenon that can be used to distinguish elastic and plastic zone is von-Mises

equivalent stress. The von-Mises equivalent stress (σ_{eq}) is defined as,

$$\sigma_{eq} = [1/2 \{ (\sigma_1 - \sigma_2)^2 + (\sigma_2 - \sigma_3)^2 + (\sigma_3 - \sigma_1)^2 \}]^{1/2} \quad \text{----- (3.5.1)}$$

where σ_1 , σ_2 and σ_3 are respectively maximum, mid and minimum principal stress. The contours of von-Mises stress corresponding to maximum load at the end of eighth cycle is shown in Fig. 3.36. The stress gradient occurs smoothly in layers with the maximum stress occurring near the contact boundary. The development of von-Mises stress along the axis of symmetry with increasing number of cycles is shown graphically in Fig. 3.37. The y-axis is marked in terms of once, twice and thrice the diameter of indenter (i.e., 0.76 mm). The vertical line drawn at yield stress clearly shows the region of transition from elastic to plastic zone. When the maximum depth of indentation was 24% of indenter radius, the region immediately below the indenter and upto the depth approximately upto 1.5 times the indenter diameter, showed higher level of plastic deformation.

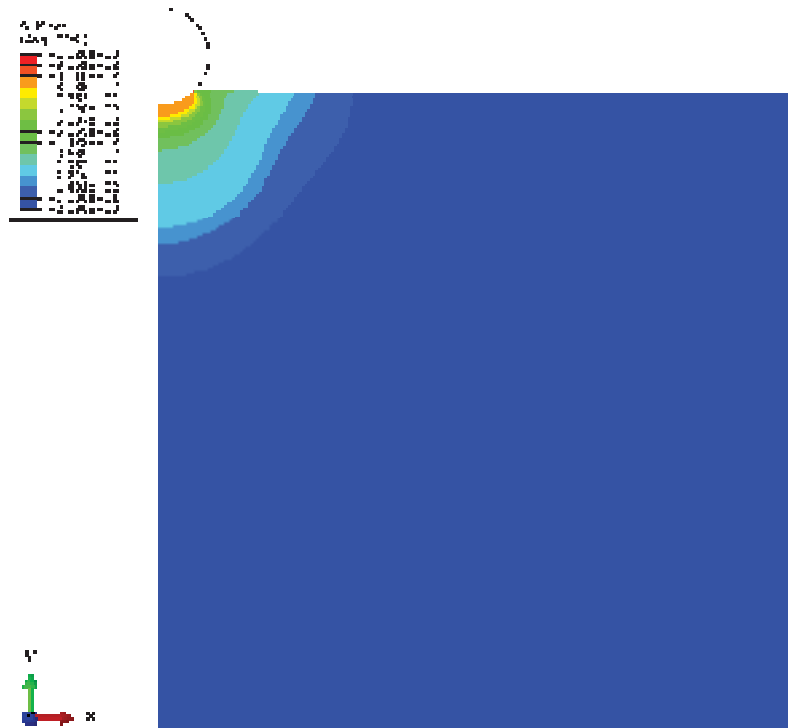


Fig. 3.36 Von-Mises stress developed under indenter during eighth cycle.

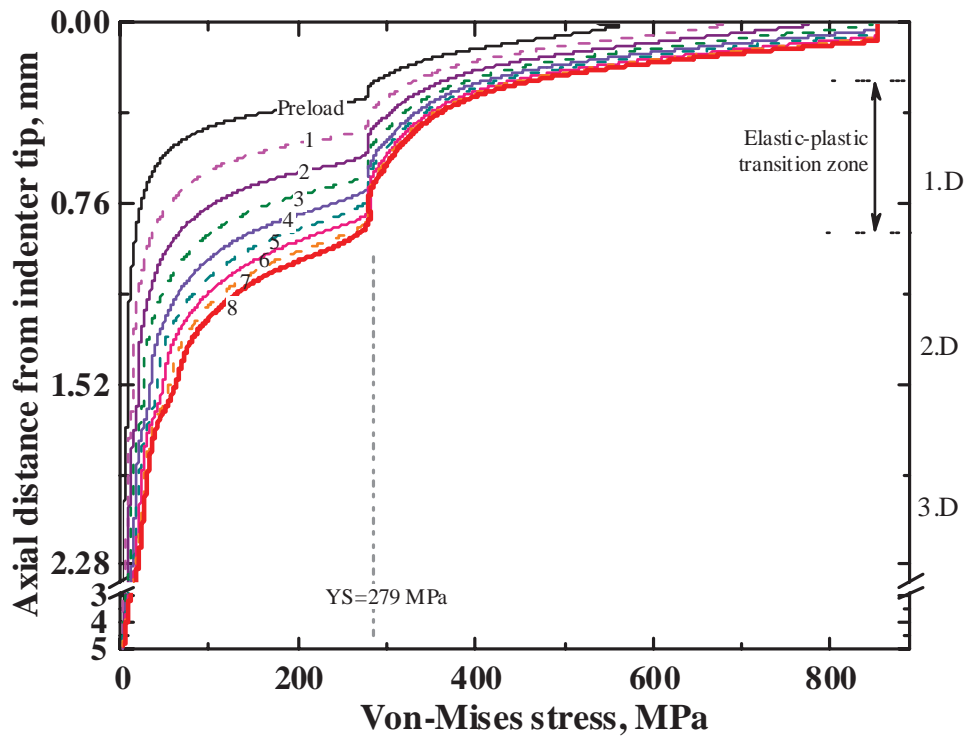


Fig. 3.37 Variations of von-Mises stress along the axis of symmetry.

The development of plastic zone with increasing depth of indentation in each cycle is pictorially visualised in terms of von Mises stress in Fig. 3.38.

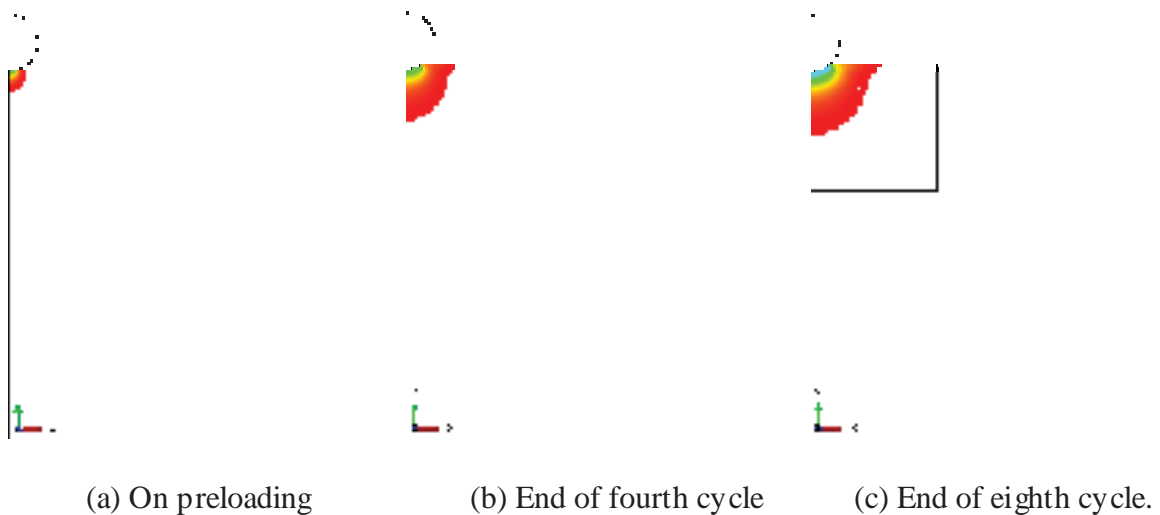


Fig. 3.38 Development of plastic zone relative to elastic zone.

Figure 3.39 shows the plastic strain accumulated in the specimen under the indenter, as estimated from FEA and strain mapping using KANM approach (Fig. 3.32). The region near the contact surface and around the centre of indenter tip experienced maximum plastic deformation, which was inferred similarly from both FEA and strain maps drawn using SEM EBSD misorientation data.

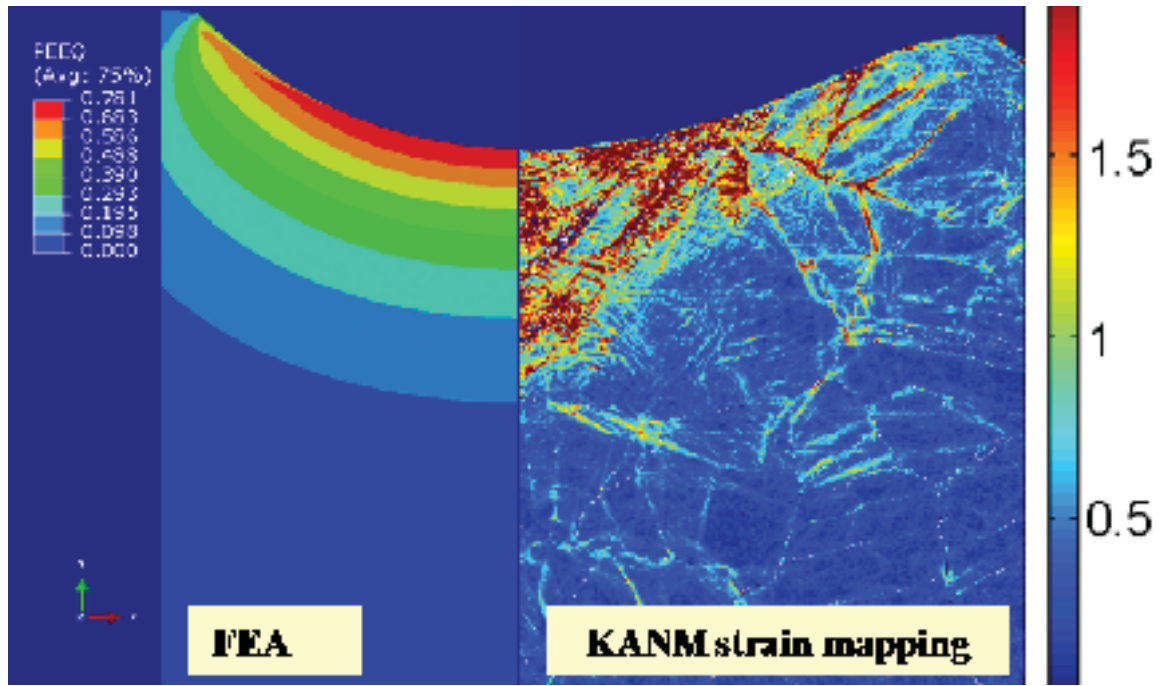


Fig. 3.39 Plastic strain accumulation along with strain mapping obtained through KANM approach.

The hydrostatic stress (σ_H) is defined as the average of the three principal stresses and is given by,

$$\sigma_H = (\sigma_1 + \sigma_2 + \sigma_3) / 3 \quad \text{----- (3.5.2)}$$

The hydrostatic stress plays a significant role in the growth and coalescence of voids leading to cracks ^[139]. The hydrostatic stress is shown as a user defined variable (UVARM1) in Fig. 3.40a. The hydrostatic stress was compressive in nature and increases near the contact

boundary on the surface of the specimen. Triaxiality factor (TF) is defined as the ratio of hydrostatic stress to von-Mises equivalent stress and is given as,

$$TF = (\sigma_1 + \sigma_2 + \sigma_3) / 3 \sigma_{eq} \quad \text{----- (3.5.3)}$$

Triaxiality factor is a relevant indicator of degree of constraint imposed on the plastic flow by means of developing triaxial stress state ^[140]. The triaxiality factor is 0.3 when the stress is acting only in one direction. In the case of ABI specimen, σ_2 and σ_3 components are generated additionally, though the indenter moves downward in single direction. The contours of triaxiality factor are shown as user defined variable (U VARM2) in Fig. 3.40b. As expected, the triaxiality appears to be maximum near the contact surface and just below the indenter.

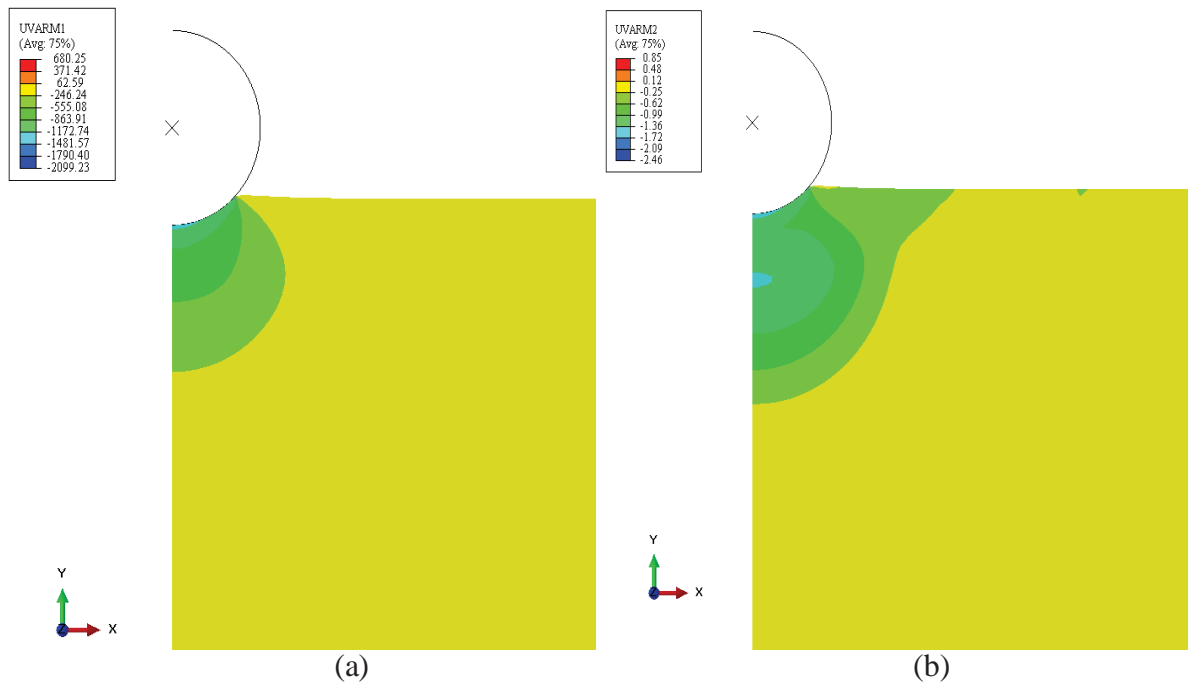


Fig. 3.40 Triaxial state of stress expressed by (a) hydrostatic stress and (b) Triaxiality factor.

The material pile-up phenomenon occurring over the specimen surface during indentation was studied. The extent of pile-up can be expressed in terms of strain hardening exponent (n) as ^[35],

$$C^2 = \frac{5(2-n)}{2(4+n)} \quad (3.5.4)$$

where, C is a dimensionless constant and is usually mentioned as the ratio of actual contact radius to the apparent contact radius without pileup. The value of $C^2 > 1$ implies pile-up whereas $C^2 < 1$ implies sink-in phenomenon. The value of $C^2 = 1$ marks the boundary between pile-up and sink-in and the corresponding value of strain hardening exponent is 0.28. The pileup was reported as more pronounced when the strain hardening exponent decreases with increase in yield ratio ^[141]. In the present case, substituting $n=0.205$ in Eqn, 3.5.4 gives $C^2=1.07 (>1)$ and hence pileup is expected.

The plastic flow of material is closely related with von-Mises equivalent stress, as discussed earlier. However, the flow of material occurring in a particular direction to cause pile-up over ABI tested surface can be better understood from the direction and magnitude of principal stresses. The maximum principal stresses, shown in Fig. 3.41, seemed to act in the direction tangential to the indenter at the contact surface and the same direction was continued well below the indenter also. The minimum principal stress developed in ABI specimen is shown in Fig. 3.42, which implied that the minimum principal stress act almost normal to the indenter surface. It may be noted that the maximum principal stress discussed here is algebraically maximum. The minimum principal stress which is compressive in nature is actually the largest in magnitude among the principal stresses. Both the principal stresses increased with radial distance from the axis of specimen model attaining peak value at the contact boundary and then gradually dropped to zero value away from the contact boundary.

The tendency of the minimum principal stress seemed to compress the plastically deformed material towards the elastic zone whereas the maximum principal stress tends to displace the material towards the surface. Due to the combined effect of these stresses, the direction of movement of material towards the free surface was resulted.

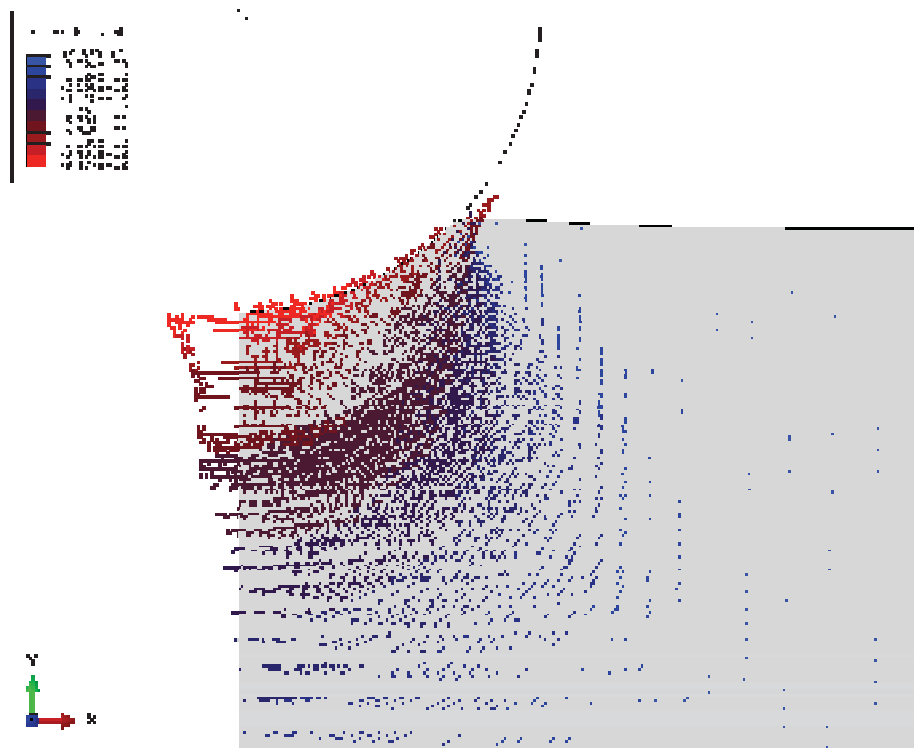


Fig. 3.41 Direction and magnitude of maximum principal stress during eighth cycle.

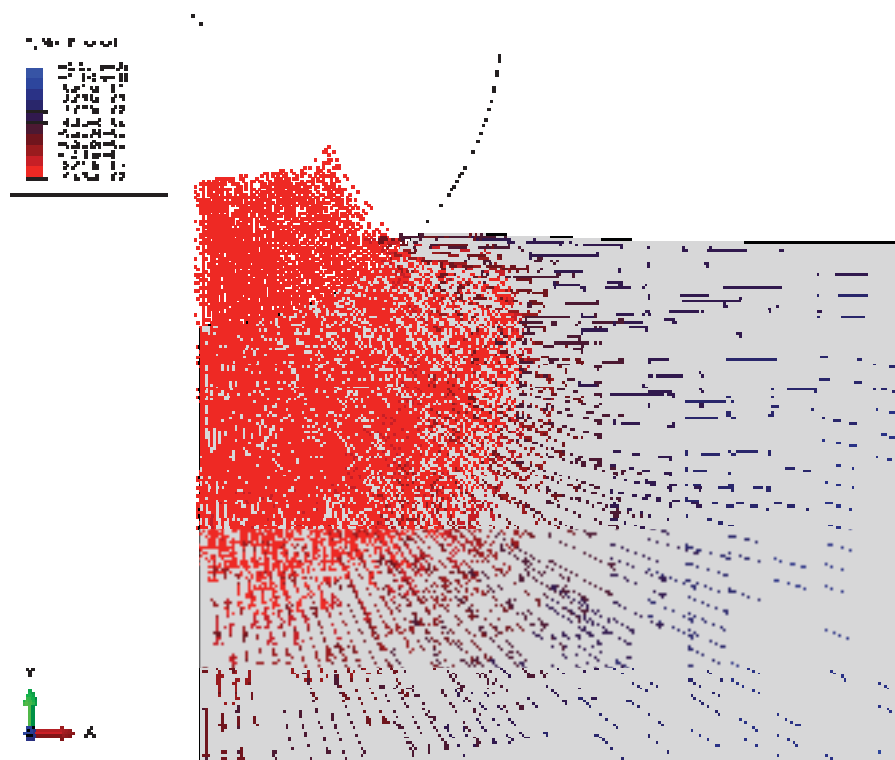


Fig. 3.42 Direction and magnitude of minimum principal stress during eighth cycle.

The pile-up phenomenon was visualised using the direction of resultant displacement represented by vector symbol plot in Fig. 3.43. The material under the tip of the indenter always showed the downward displacement towards compressing the elastic zone. At the end of loading in first cycle, the material near the contact boundary initially tried to accommodate within the elastic zone to some extent. As the depth of indentation was further increased the material started to flow outwards towards the surface. The 3D profile image of pileup of material actually observed in ABI tested specimen was captured using confocal selective laser microscope and is shown in Fig. 3.44.

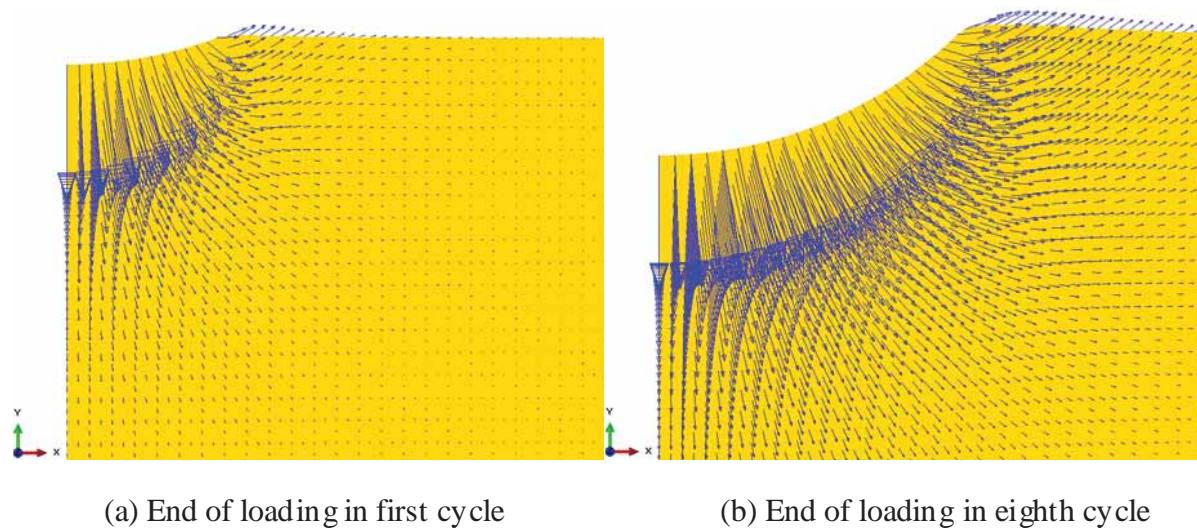
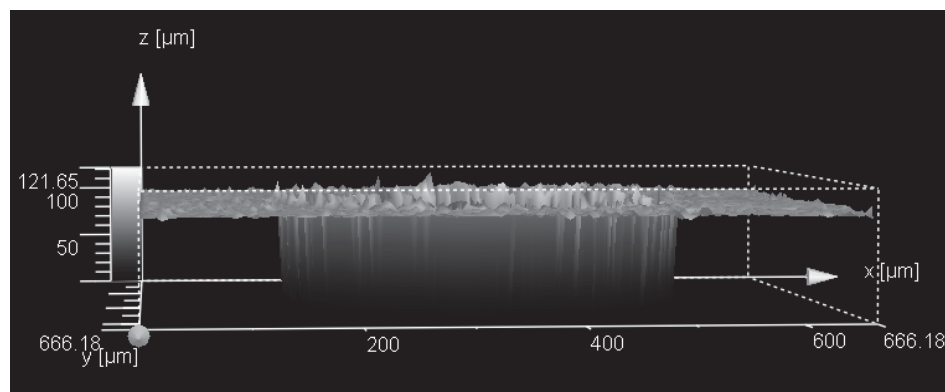
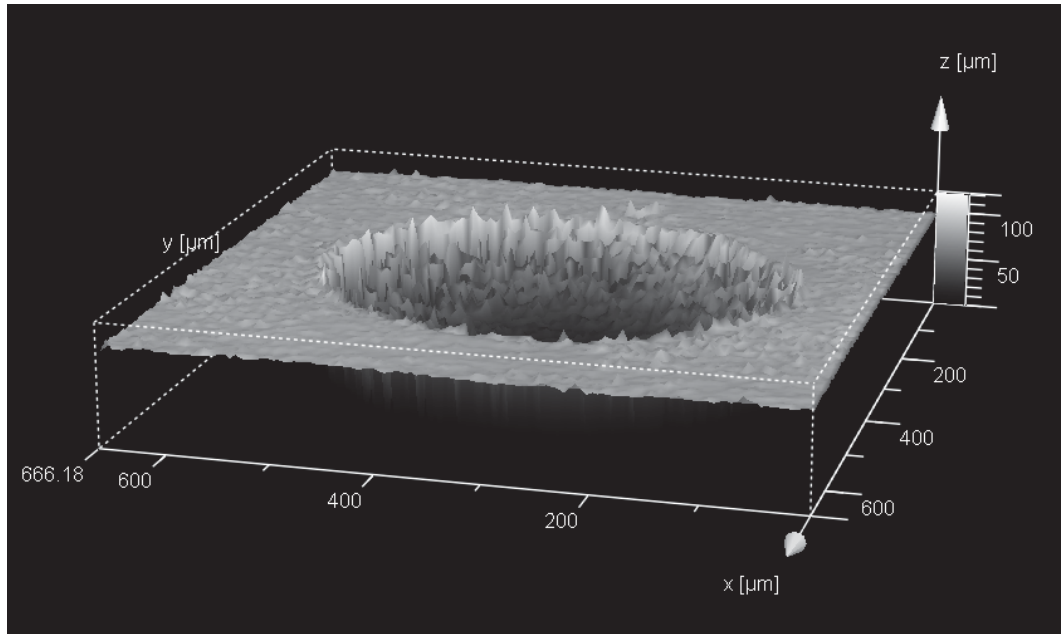


Fig. 3.43 Pictorial representation of pileup on increasing depth of indentation, using vector symbol plot of resultant displacement.



(a)



(b)

Fig. 3.44 CSLM 3D profile images of indentation in ABI specimen tested at 298 K: (a) lateral view and (b) isometric view.

As far as uniaxial tensile test is concerned, the stress calculated as the ratio of load to area of cross-section of tensile specimen is uniform for the whole length of test specimen, upto necking. Whereas, the stress varies inside the ABI specimen as the depth of indentation and area of contact between specimen and indenter keeps changing. It is generally known that the stress developed in ABI specimen is converted to equivalent uniaxial stress using semi-empirical relationships. It is interesting to visualise the region of specimen in finite element model which actually experienced such calculated value of equivalent uniaxial stress. The region of occurrence of stress calculated at the end of eighth cycle (discussed in Section 3.3) was highlighted in von-Mises stress contour diagram in Fig. 3.45. Similarly, the regions of occurrence of stresses at the end of other cycles were located. It was found that the calculated equivalent uniaxial stress occurred in the part of specimen that was away from the centre of

the indenter at the distance approximately equal to depth of indentation at that cycle. As the indenter was penetrating deep into the specimen, the region representing equivalent uniaxial stress moved far away from the contact boundary to the same level.

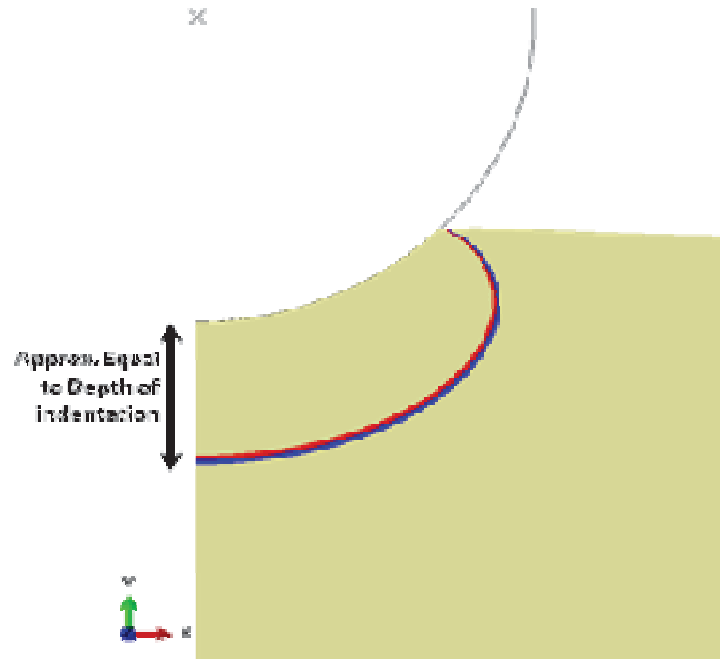


Fig. 3.45 Region of occurrence of calculated stress in eighth cycle.

Thus, the tensile behaviour of 316L(N) SS has been evaluated at high temperatures using ABI tests and supported by SEM EBSD and finite element analyses. The above results can serve as part of baseline database for future structural integrity assessment of service components at high temperature.

CHAPTER 4

Small Punch Creep Behaviour of 316L(N) SS

In this chapter, the Small Punch Creep (SPC) behaviour of 316L(N) SS (containing 0.07 wt.% nitrogen) evaluated at various test conditions and correlated with uniaxial creep results, is discussed. The details of analyses on transient, secondary and tertiary stages of SPC deformation are discussed. The stresses developed in SPC specimen as calculated through finite element analysis are presented.

4.1 SPC results

4.1.1 Rupture life and deflection rate

In order to estimate the scatter in test results on account of use of small specimens, initially SPC tests were repeated three times at a load of 400 N at 923 K. The deflections measured from these three tests are shown in Fig. 4.1. The rupture life and secondary creep rate obtained from each test are tabulated within the same figure. The maximum scatters of rupture life and deflection rate among these tests were 2.2% and 4% respectively about their mean value. These values convey that SPC tests express good repeatability in their results.

The deflections measured from SPC tests carried out on 316L(N) SS at 923 K and at various loads in the range 300-1000 N are shown in Fig. 4.2. The instantaneous deflection due to loading increased with an increase in the applied load. On instantaneous loading, the deflection curves clearly exhibited distinct primary, secondary and tertiary stages of creep deformation. The deflection at rupture in SPC tests showed almost no significant variation with applied load and similar observations were reported by Kim et al.^[89] and Komazaki et al.^[142].

The SPC deflection was obtained by subtracting the instantaneous deflection due to loading from the total (measured) deflection. The creep time (t) normalised with rupture life (t_r) is

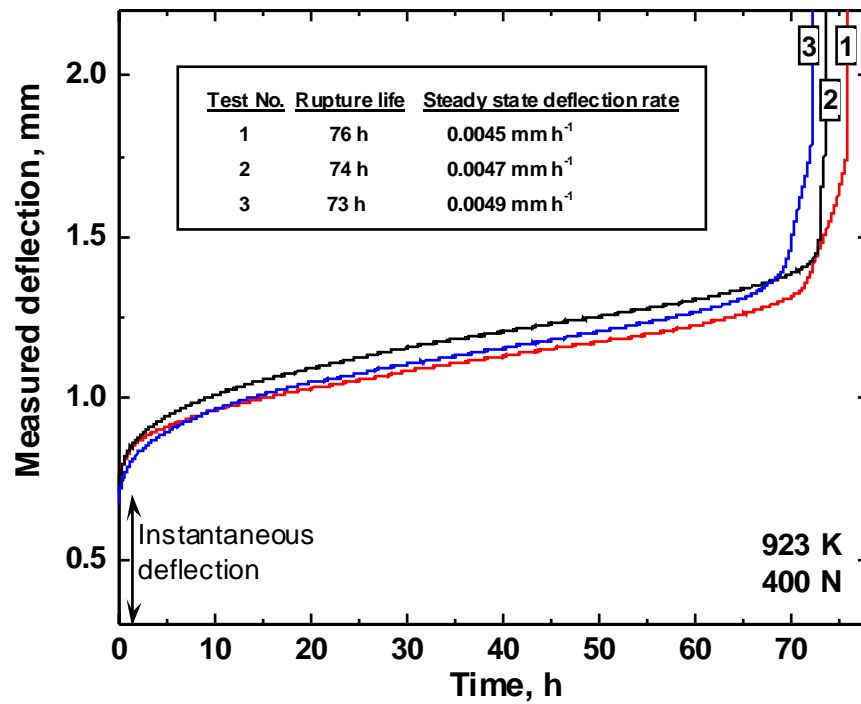


Fig. 4.1 Examination of repeatability of SPC test results.

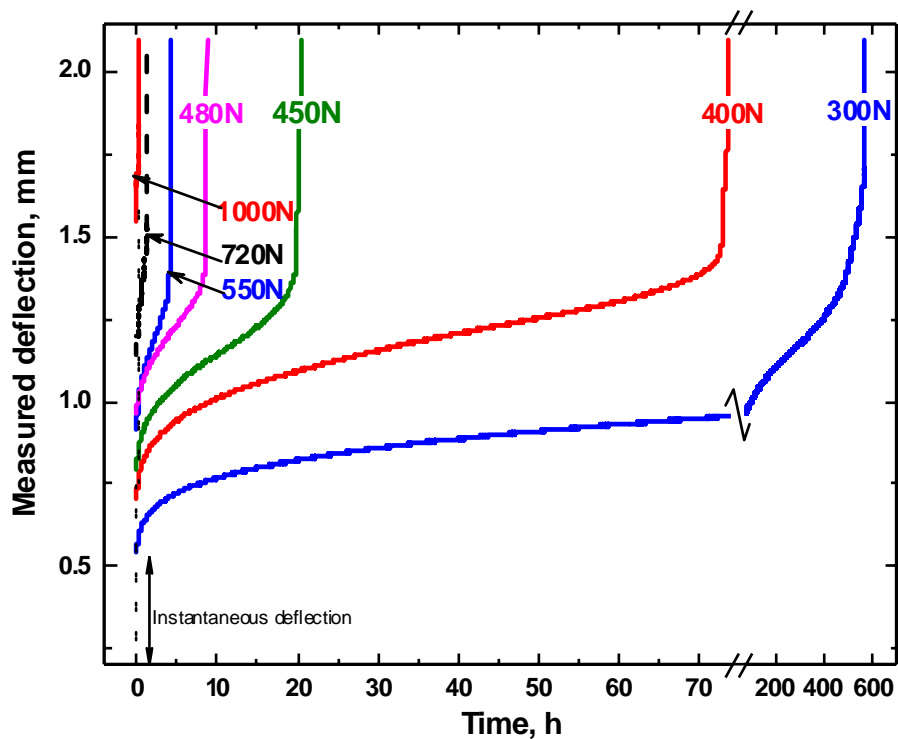


Fig. 4.2 Total deflection measured from SPC tests on 316L(N) SS at 923 K.

generally mentioned as creep life fraction (t/t_r). In order to assess the relative contribution of each stage of creep to the total rupture life and also its dependence on load, the SPC deflection curves are plotted against creep life fraction in Fig. 4.3. It was observed that the different stages of creep contributed almost to the same extent, irrespective of the load. The creep deflection, which was obtained as the difference between total and instantaneous deflection, increased with decrease in load. This is because the total deflection at rupture was almost the same irrespective of applied load and the instantaneous deflection was decreased with decrease in load.

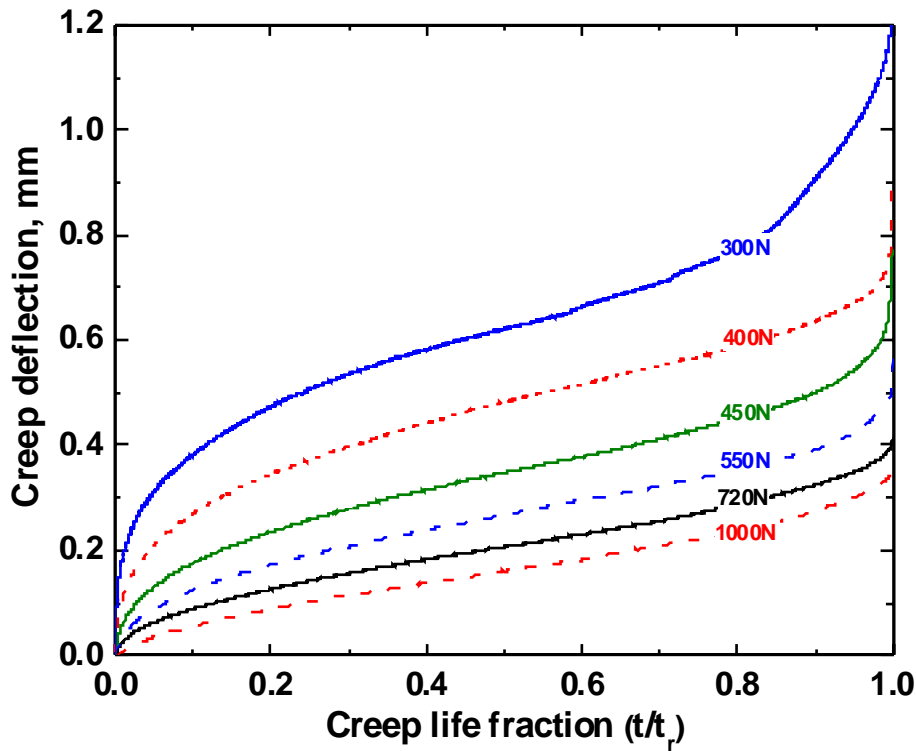


Fig. 4.3 Creep deflection curves for 316L(N) SS at 923 K.

Figure 4.4 shows the rate of deflection values that were determined by differentiating SPC curves at various loads. The curves corresponding to various loads show a minimum value in the deflection rate. More than four orders of magnitude change in the minimum deflection rate was observed as the applied load was varied in the range of 300 to 1000 N. A cross plot of Fig. 4.4 was obtained by plotting deflection rate values against creep life fraction for

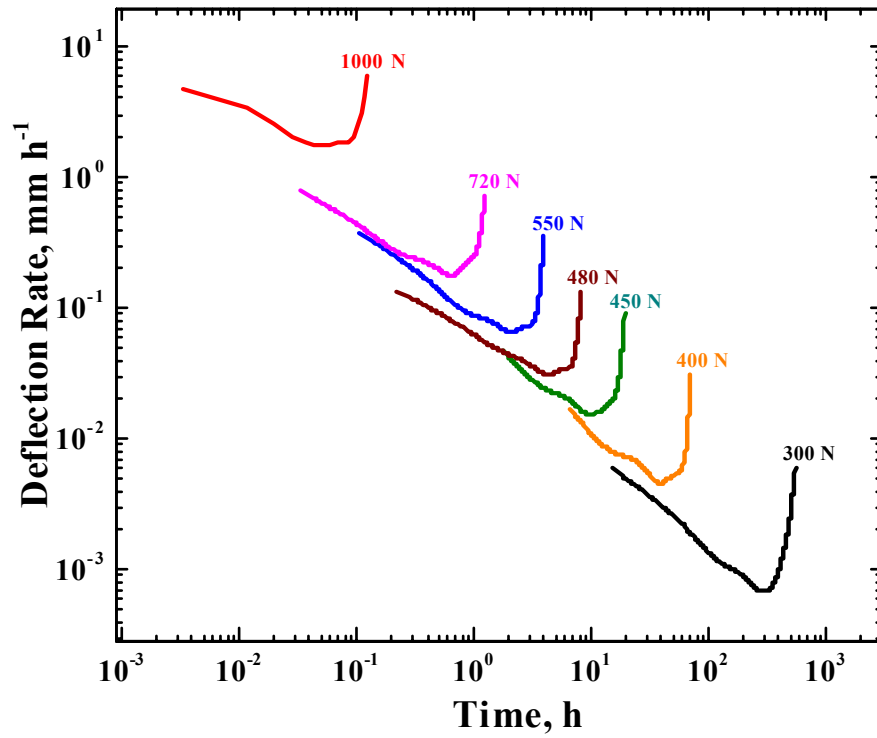


Fig. 4.4 Rate of deflection curves for 316L(N) SS at 923 K.

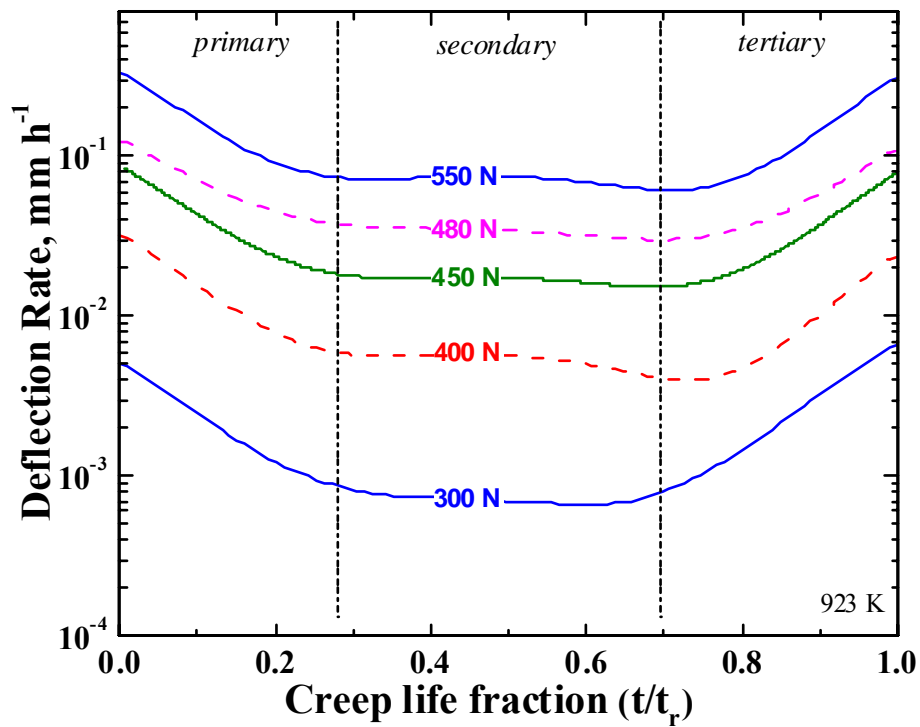


Fig. 4.5 Rate of deflection curves for 316L(N) SS plotted against normalised time at 923 K.

various loads in Fig. 4.5. In all cases, the rate of deflection decreased during the primary stage remained almost at the same rate during the secondary stage and finally increased in the tertiary stage, leading to rupture. It may be noted that the time spent in each stage, expressed as a fraction of rupture life, is almost the same for all the loads. However, the rate of deflection at any stage generally increased with increase in applied load.

Though both bending and membrane stretching modes of deformation occur at all stages of SPC, bending is the dominant mode of deformation in primary creep stage. The membrane stretching, controlled by reduction in thickness, is the dominant mode of deformation in secondary and tertiary creep stages^[80,143]. The rapid increase in deflection rate in the tertiary region is on account of localization of deformation, nucleation and growth of cracks.

The rupture life followed a power law relationship with applied load as shown in Fig. 4.6, on log-log scale. The rupture life increased with decrease in applied load.

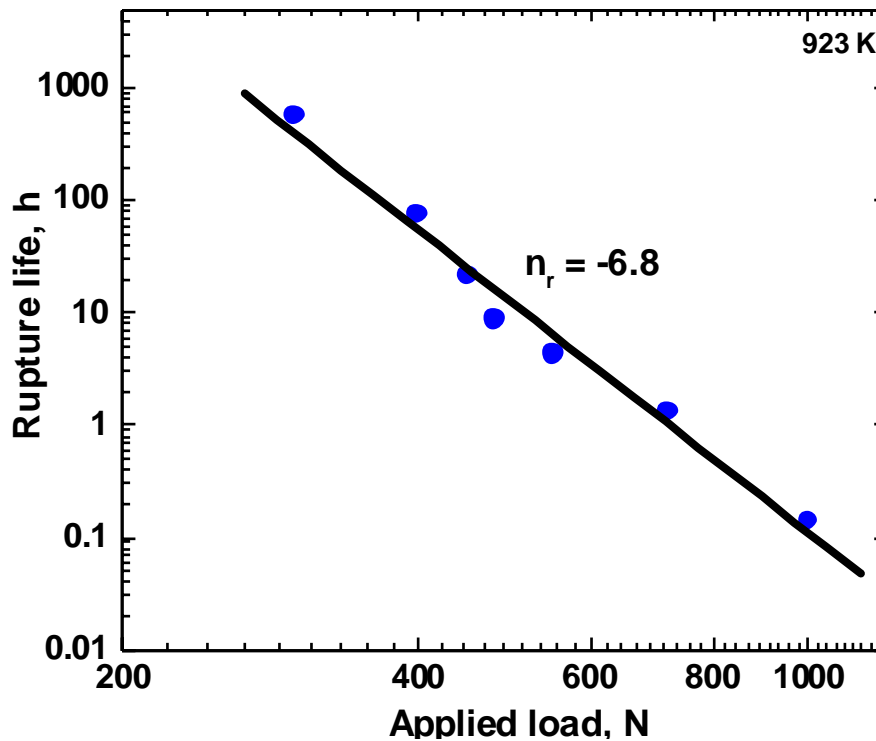


Fig. 4.6 Isothermal rupture curve obtained for 316L(N) SS at 923 K.

4.1.2 Optical and SEM micrographs

Figure 4.7a shows the SPC specimen tested at 923 K at 300 N, along with the indenter penetrating through the specimen to cause rupture. The lateral view of ruptured SPC specimen tested at 923 K at 480 N is shown in Fig. 4.7b. The radius of the receiving hole in the upper die is marked in the same figure. Figure 4.8a shows the typical scanning electron micrograph of fractured SPC specimen tested at 923 K at 720 N.

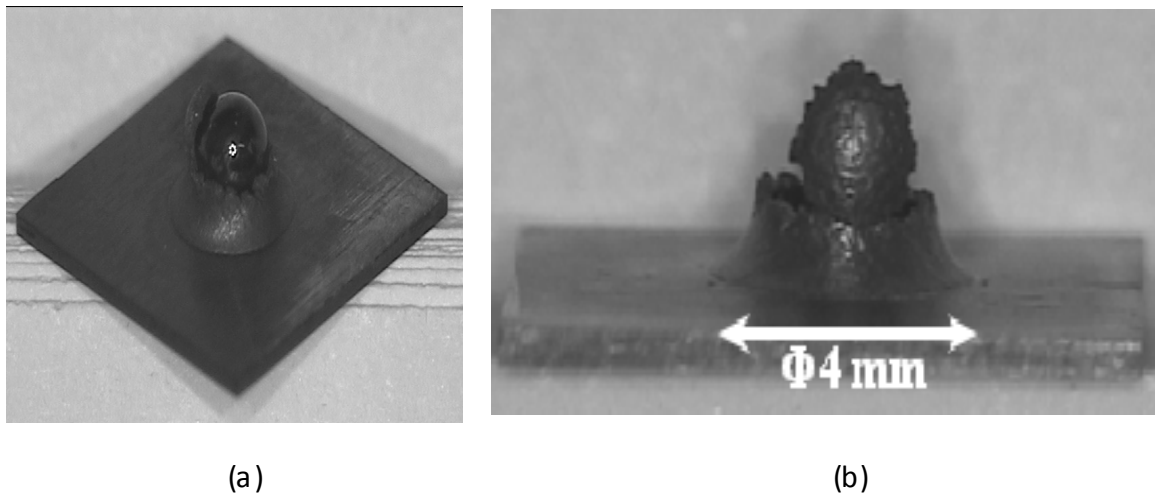
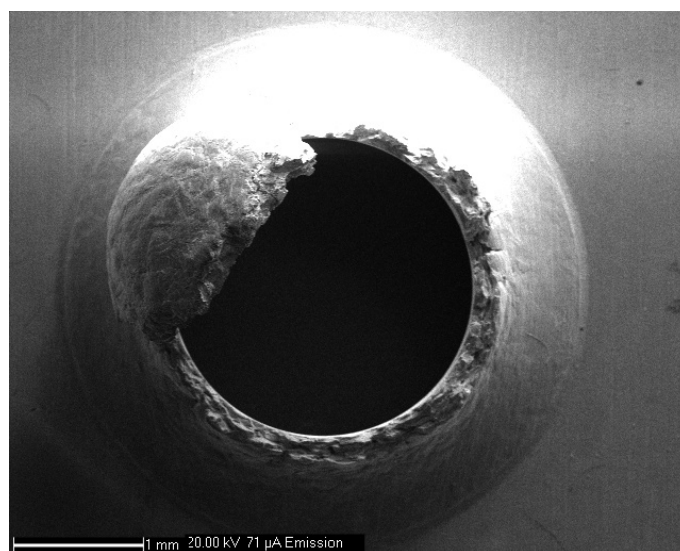
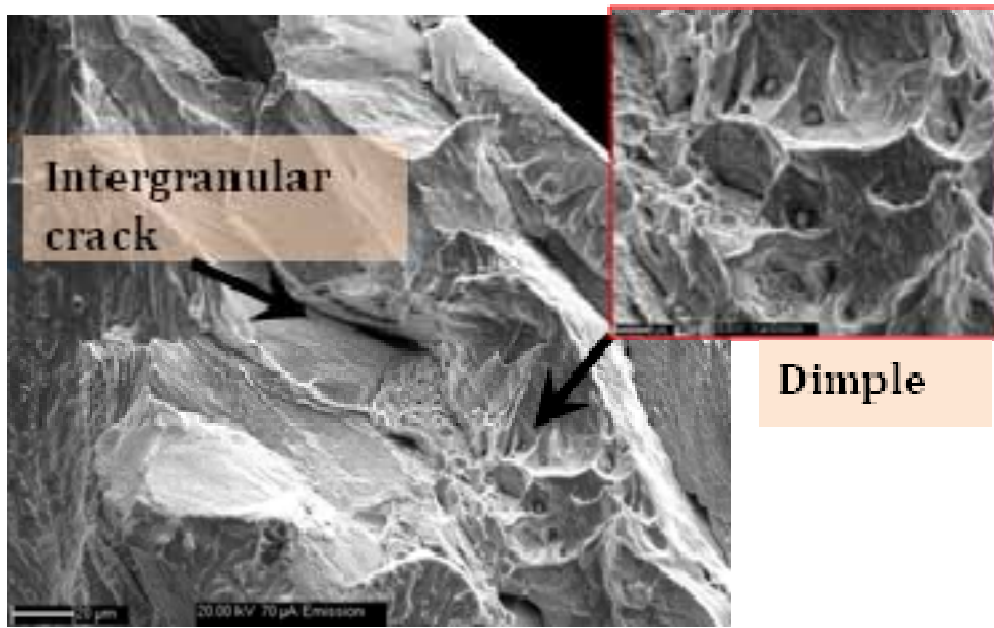


Fig. 4.7 Ruptured SPC specimen tested at 923 K at (a) 300 N along with indenter and (b) 480 N (lateral view).



(a)



(b)

Fig. 4.8 (a) SEM fractograph of SPC specimen tested at 923 K at 720 N (b) Higher magnification image of same surface.

On increasing the magnification, predominantly intergranular cracks and ductile features such as dimples were observed on the fractured surface, as shown in Fig. 4.8b. Overall, the ductile features were relatively less owing to biaxial state of stress prevailing during SPC deformation.

4.1.3 Derivation of strain from central deflection

A membrane stretch model, which was proposed by Chakrabarty^[144] for the stretch forming of a circular blank over a hemispherical punch head, has been used for calculating strain from the central deflection measured in a SPC test^[145]. The central deflection is geometrically related to the central strain^[58,94] and such a relationship was reported as approximately independent of load, temperature and creep behaviour^[145]. The membrane stretch model assumes that material is isotropic and plastic and also neglects the effect of friction between indenter and specimen. Since the specimen thickness is very small relatively to the indenter,

the deformation is assumed to take place under the membrane stresses alone. Chakrabarty^[144] proved that the radial and circumferential strains are equal and the compressive thickness strain can be taken as the equivalent strain. Figure 4.9 shows the geometry of deformation of SPC test specimen with a description of nomenclature used in this paper and is listed as: h - thickness of the specimen; r -radius of spherical indenter; R_h - radius of the receiving hole; x - radial distance; θ -angle made by the surface normal with the vertical axis; θ_1 - value of θ at $x=R_h$; θ_0 -value of θ at the contact boundary.

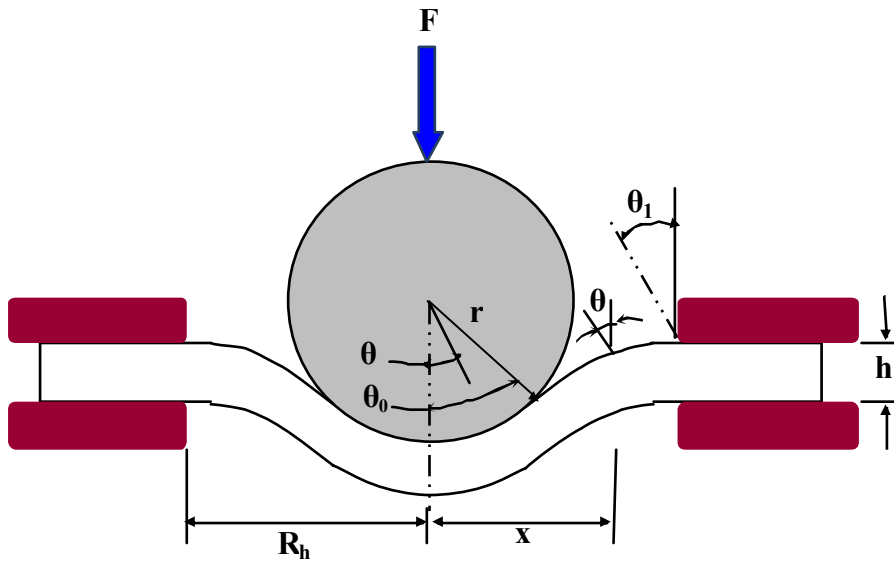


Fig. 4.9 Geometry of deformation of SPC test specimen.

The compressive thickness strain is given generally as ^[144],

$$\varepsilon = 2 \ln \frac{(1 + \cos \theta)(1 + \cos \theta_1)}{(1 + \cos \theta_0)^2} \quad (4.1.1)$$

Taking $\theta=0$ in Eqn. (4.1.1), the maximum strain at the centre of the disc (ε_{\max}) is obtained as,

$$\varepsilon_{\max} = 2 \ln \frac{2(1 + \cos \theta_1)}{(1 + \cos \theta_0)^2} \quad (4.1.2)$$

where, the angles θ_1 and θ_0 are related as ^[144],

$$\sin \theta_1 = \frac{r}{R_h} \sin^2 \theta_0 \quad (4.1.3)$$

The strain at the contact boundary (ϵ_{cont}) is obtained by taking $\theta = \theta_0$ in Eqn. (4.1.1) as,

$$\epsilon_{\text{cont}} = 2 \ln \frac{(1 + \cos \theta_1)}{(1 + \cos \theta_0)} \quad (4.1.4)$$

The central deflection of specimen is given as a function of R_h , r , θ_1 and θ_0 by ^[144],

$$\delta = R_h \sin \theta_1 \ln \frac{\tan \frac{\theta_0}{2}}{\tan \frac{\theta_1}{2}} + r(1 - \cos \theta_0) \quad (4.1.5)$$

Taking the values of $r=1.19$ mm, $R_h=2$ mm from the experimental setup (discussed in Chapter 2) and by setting the values of θ_0 from 0 to 90°, the corresponding values of θ_1 were computed using Eqn. (4.1.3). By substituting these values in Eqns. (4.1.2) and (4.1.5), the values of ϵ_{max} and δ were determined individually. A polynomial expression was fitted to the curve plotted between maximum strain (ϵ_{max}) and deflection (δ), as shown in Fig. 4.10. The maximum strain at the centre can thus be derived from the central deflection using the relation,

$$\epsilon_{\text{max}} = -0.0167 + 0.408 \delta + 0.249 \delta^2 \quad (4.1.6)$$

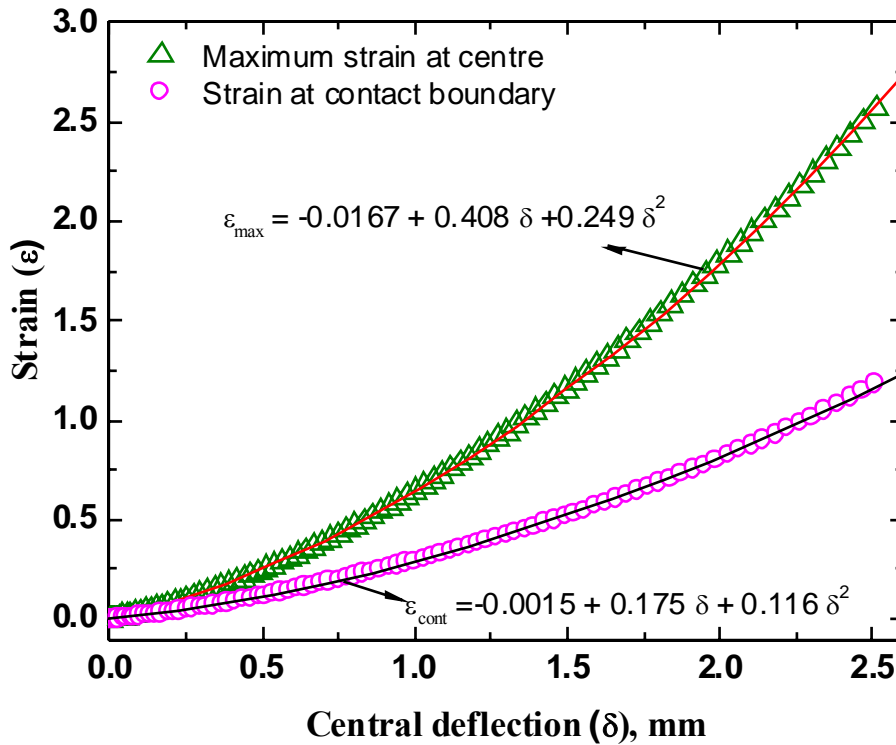


Fig. 4.10 Relationship derived between measured SPC deflection and strain.

Similarly, the strain values at the contact boundary (ϵ_{cont}) that were computed using Eqn. (4.1.4) were plotted against central deflection in the same figure. A polynomial regression model was fitted to this curve to relate ϵ_{cont} and δ as,

$$\epsilon_{\text{cont}} = -0.0015 + 0.175 \delta + 0.116 \delta^2 \quad (4.1.7)$$

The ϵ_{max} curves derived from SPC deflection measured at several loads, using Eqn. (4.1.6), are shown in Fig. 4.11 on semi-log scale. It may be noted that the relationships represented in Eqns. (4.1.6) and (4.1.7) are applicable for specific geometry and is not valid when the indenter radius or the radius of the receiving hole is changed.

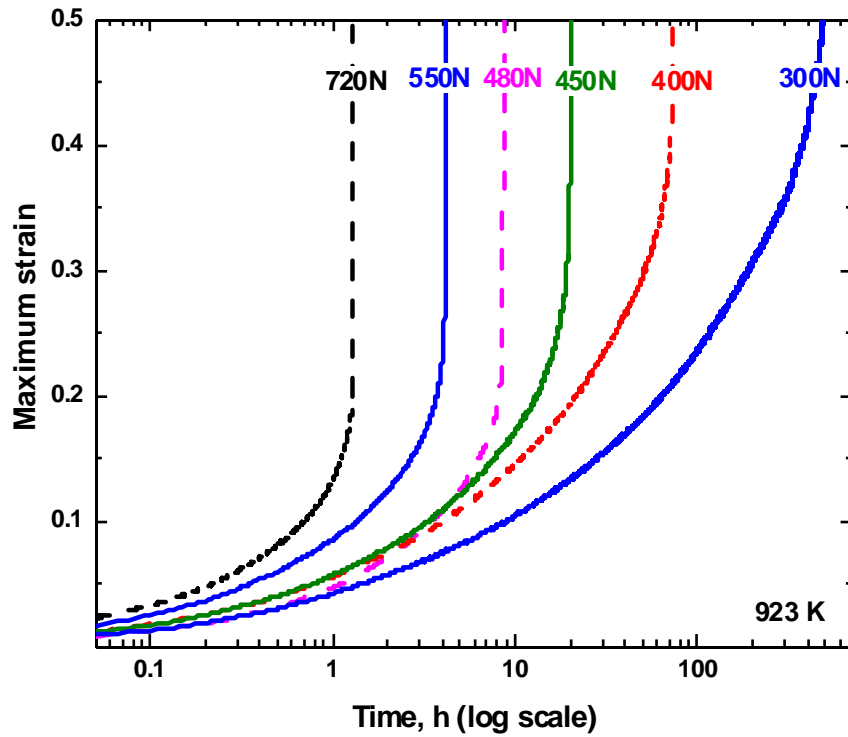


Fig. 4.11 Maximum strain curves derived from SPC deflection for 316L(N) SS.

It is generally observed that rupture life and steady state deflection rate have been largely dealt in the literature, with less emphasis on the whole SPC deformation curve. In this research work, attention has been given on deformation that occurs during various stages of SPC in detail.

4.2. Analysis of SPC deformation

Though a uniaxial creep curve is classified into three stages, the phenomenon of strain hardening and recovery occur simultaneously throughout the creep deformation and only the dominance of one over another varies from stage to stage. The strain hardening is found to be dominant in primary or transient stage whereas recovery along with cavity growth is dominant in tertiary stage. The steady value of creep rate in the secondary stage is considered as a balance between stain hardening and recovery. Webster et al. ^[146] proposed the first order reaction kinetics theory for transient creep deformation, under uniaxial creep condition, by stating that the rate of change of creep rate is proportional to the change of creep rate and describing creep rate ($\dot{\epsilon}$) according to the equation,

$$\frac{d(\dot{\epsilon} - \dot{\epsilon}_s)}{dt} = -\frac{(\dot{\epsilon} - \dot{\epsilon}_s)}{\tau} \quad (4.2.1)$$

where, $\dot{\epsilon}_s$ is the steady state creep rate, τ is the relaxation time for rearrangement of dislocations during dislocation climb controlled transient creep. The activation energy for creep was observed to be the same in the transient and secondary stages and is independent of the creep strain or stress, when dislocation climb is the operative mechanism ^[147]. It has been suggested that the rearrangement of dislocations during transient creep controlled by dislocation climb process follows first order kinetics which depends on stress and temperature similar to steady state creep. The strain (ϵ) at time (t) during transient and secondary stages of creep deformation, as represented by Garofalo's equation ^[147], can be derived by integrating Eqn. (4.2.1) twice as,

$$\epsilon = \epsilon_0 + \epsilon_T(1 - e^{-r't}) + \dot{\epsilon}_s t \quad (4.2.2)$$

where, ϵ_0 is instantaneous strain on loading, ϵ_T is limiting transient creep strain and r' is the rate of exhaustion of transient creep, which is the same as relaxation frequency ($1/\tau$), in Eqn. (4.2.1). The tertiary creep also follows first order reaction rate theory with the rate of

acceleration of tertiary creep depending on stress and temperature similar to steady state creep rate ^[148]. The strain over the entire uniaxial creep curve, including all stages of creep deformation, was given by Dobes and Cadek ^[149] as,

$$\varepsilon = \varepsilon_0 + \varepsilon_T (1 - e^{-r't}) + \dot{\varepsilon}_s t + \varepsilon_3 e^{[p(t-t_{r-uc})]} \quad (4.2.3)$$

where, p is the rate of acceleration of tertiary creep, t_{r-uc} is uniaxial creep rupture life and ε_3 is tertiary creep strain.

Even though microstructural changes due to long term creep exposure may not occur in short term SPC tests, several researchers have successfully attempted to apply uniaxial creep equations to SPC data ^[67-70, 72]. When the creep equation does not include terms for addressing long term effects (such as nucleation and growth of precipitates, sub-grains, etc.), it can be used for short term SPC data, provided the deformation mechanism remains the same. As discussed later in section 4.3, dislocation creep mechanism governs the SPC deformation of 316L(N) SS under investigated conditions. Therefore, in this investigation, an expression analogous to Eqn. (4.2.3) is proposed for defining SPC deflection (δ) as,

$$\delta = \delta_0 + \delta_T (1 - e^{-\kappa t}) + \dot{\delta}_s t + \delta_3 e^{[\phi(t-t_r)]} \quad (4.2.4)$$

where, δ_0 is instantaneous deflection on loading at time $t=0$, δ_T is limiting transient creep deflection, κ is the rate of exhaustion of transient creep, $\dot{\delta}_s$ is steady state deflection rate, ϕ is rate of acceleration of tertiary creep, δ_3 represents tertiary creep deflection and t_r is SPC rupture life.

Figure 4.12 shows the schematic illustration of SPC curve analysis with the description of nomenclature used in this paper. A straight line was drawn over the portion of SPC curve representing secondary creep stage. The slope of this straight line was taken as the steady state deflection rate and the intercept of the line was taken as the limiting transient creep deflection (δ_T). Since it may be difficult to accurately locate the onset of tertiary creep, the

deflection δ_3 , which was used to represent tertiary creep deflection, was arrived by deducting $\dot{\delta}_s t_r$ from the rupture deflection (δ_r).

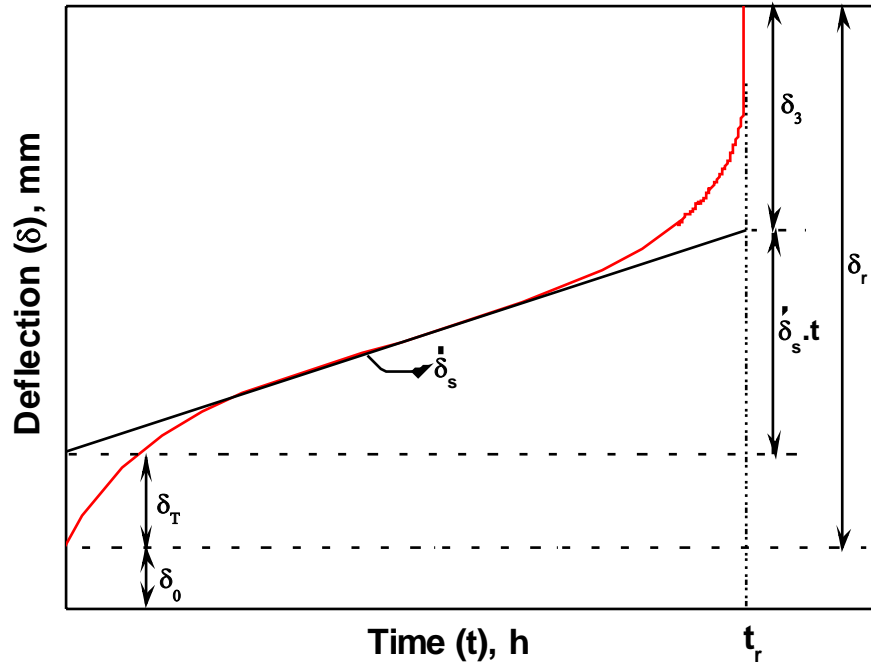


Fig. 4.12 Schematic illustration of analyses of transient and tertiary creep deflection.

4.2.1 Steady state creep

The steady state deflection rates are plotted against applied load in Fig. 4.13 on log-log scale. It was observed that dependence of steady state deflection rate ($\dot{\delta}_s$) on applied load (F) obeyed Norton's power law and was expressed as,

$$\dot{\delta}_s = 1.8 \times 10^{-19} F^{6.4} \quad (4.2.5)$$

Monkman-Grant Relationship describes the relation between steady state creep rate ($\dot{\epsilon}$) and uniaxial creep rupture life (t_{r-w}) as,

$$t_{r-w} \cdot \dot{\epsilon}^m = C, \quad (4.2.6)$$

where m , C are constants. If these constants are determined for a given material, the rupture life can be estimated, once the steady state creep is attained, without any need to continue the test till specimen ruptures, especially in the case of low loads.

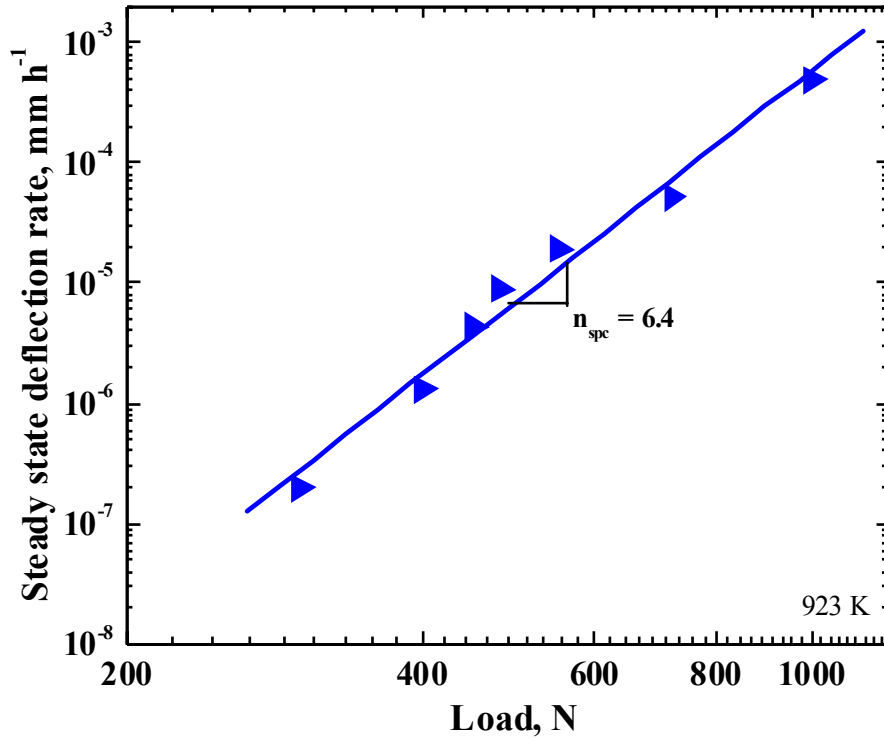


Fig. 4.13 Norton power law relationship shown for 316L(N) SS.

The Monkman-Grant relationship can be expressed for SPC deflection as ^[69, 85, 150],

$$t_r \dot{\delta}_s^p = C_{\text{spc}} \quad (4.2.7)$$

where p , C_{spc} are constants. The steady state deflection rate values are plotted against rupture lives (t_r) on log-log scale in Fig.4.14 and the Monkman-Grant type relationship was determined using SPC results as,

$$t_r \dot{\delta}_s^{1.06} = 0.24 \quad (4.2.8)$$

The exponent of steady state deflection rate in the above relation was closer to unity. The exponent of steady state creep rate in Monkman-Grant relation being equal to unity is result of first order kinetics and the concept of Monkman-Grant relation extends to totality of deformation and fracture ^[151]. The applicability of uniaxial creep equations analogously to SPC data are confirmed through the above relationships involving steady state deflection rate.

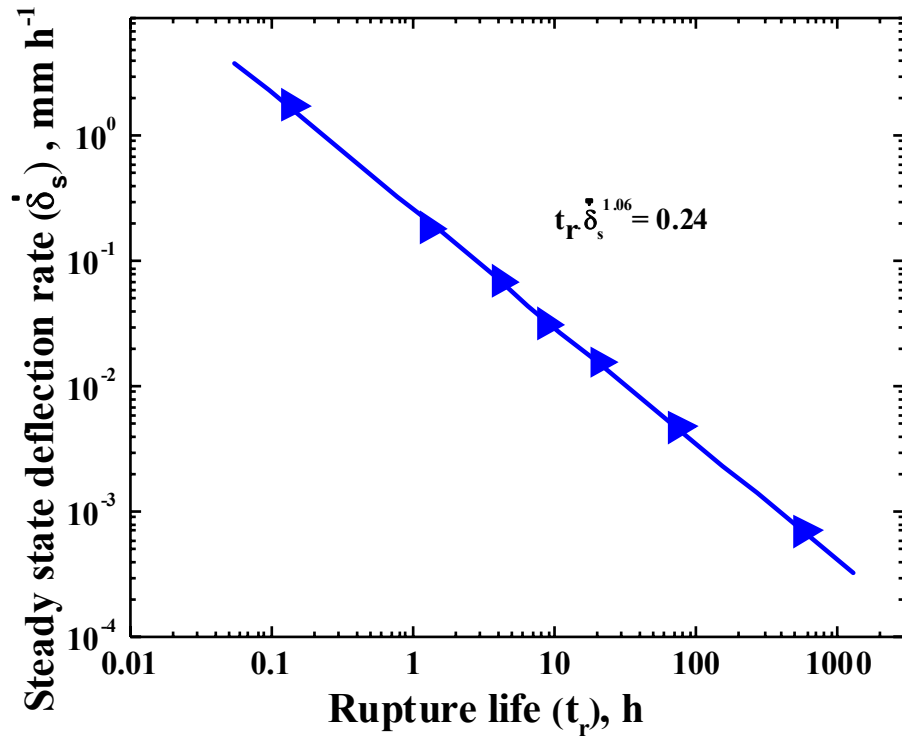


Fig. 4.14 Monkman-Grant relationship established for 316L(N) SS at 923 K.

4.2.2 Transient creep analysis

The data pertaining to deformation occurring in transient and secondary creep stages play a significant role in the design and damage assessment of fast reactor components. The SPC deflection during transient stage can be expressed by excluding the term for tertiary creep in Eqn. (4.2.4) as,

$$\delta = \delta_0 + \delta_T (1 - e^{-\kappa t}) + \dot{\delta}_s t \quad (4.2.9)$$

The rate of exhaustion of transient creep can be calculated by rearranging the above equation and taking natural logarithm as,

$$\kappa = -\frac{1}{t} \ln \left(1 - \frac{(\delta - \delta_0 - \dot{\delta}_s t)}{\delta_T} \right) = -\frac{1}{t} \ln \left(1 - \frac{\Delta_1}{\delta_T} \right) \quad (4.2.10)$$

where, $\Delta_1 = \delta - \delta_0 - \dot{\delta}_s t$, is the transient creep deflection component which becomes zero at $t=0$ and closer to δ_T at time to attain steady state deflection rate. The rate of exhaustion of

transient creep (κ) was calculated graphically as the slope of $\ln(1-\Delta_1/\delta_T)$ versus 't' plot, for each load. When creep deformation obeys first order kinetic reaction rate theory, proportionality between initial creep rate, steady state creep rate and relaxation frequency (inverse of rate of exhaustion of transient creep) are expected ^[146]. The rate of exhaustion of transient creep values are plotted against corresponding steady state deflection rate in Fig. 4.15. It was observed that rate of exhaustion of transient creep and steady state deflection rate were closely related to each other as,

$$\kappa \dot{\delta}_s^{-1.07} = 52 \quad (4.2.11)$$

The steady state deflection rate was linearly dependent on the rate of exhaustion of transient creep. The similar proportionality between rate of exhaustion of transient creep and steady state creep rate was also observed from the uniaxial creep tests conducted on nickel, zinc, iron ^[151] and austenitic stainless steel of type 304 ^[152].

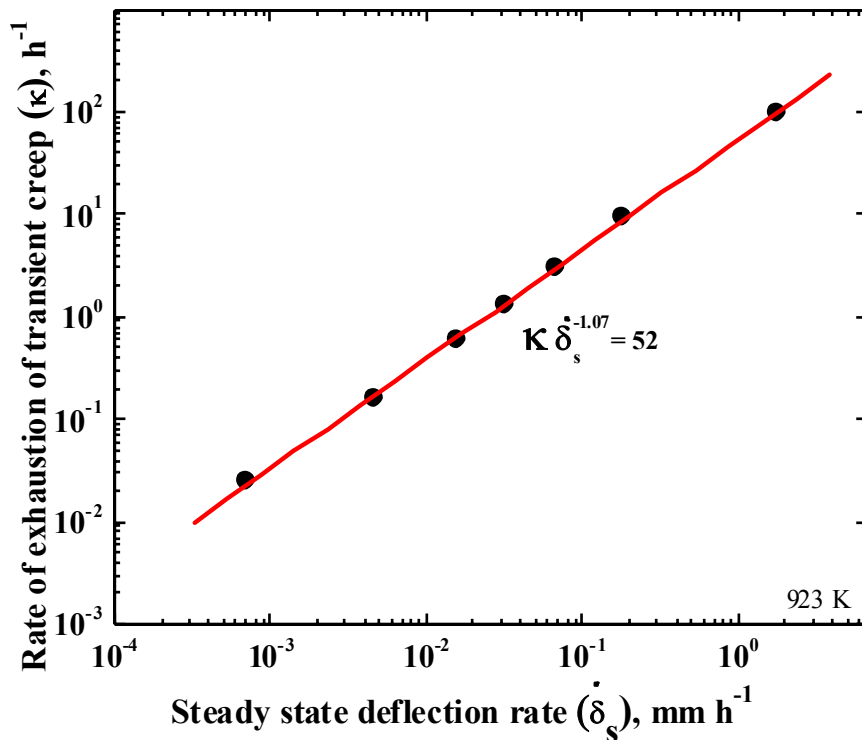


Fig. 4.15 Relationship between rate of exhaustion of transient creep and steady state deflection rate.

The rate of exhaustion of transient creep is related to the recovery phenomenon operating in the material. From the studies on superalloy Nimonic 80A, Sidey and Wilshire^[153] showed that the rate of recovery occurs slowly during the transient stage in comparison with the corresponding work hardening rate and Eqn. (4.2.2) is applied when creep rate is proportional to rate of recovery. By slugging the recovery, the creep rate of the material can be retarded. The role of 'κ' ends when the steady state deflection rate is attained. The relationship between rate of exhaustion of transient creep and time to attain steady state deflection rate (t_s) was obtained as shown in Fig. 4.16 as,

$$\kappa t_s^{0.9} = 4 \quad (4.2.12)$$

The rate of exhaustion of transient creep was almost inversely proportional to the time to attain steady state deflection rate.

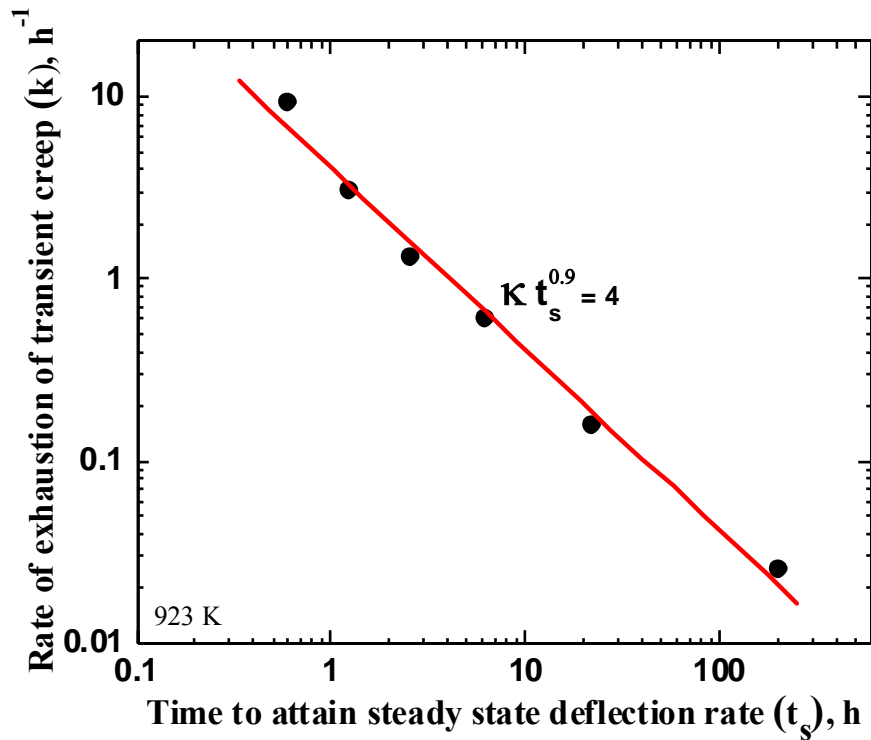


Fig. 4.16 Relationship between rate of exhaustion of transient creep and time to attain steady state deflection rate.

The initial creep deflection rate ($\dot{\delta}_i$) was derived by differentiating Eqn. (4.2.9) with respect to time and then taking time $t=0$, to obtain $\dot{\delta}_i = \kappa \delta_T + \dot{\delta}_s$. The initial creep deflection rate was related to steady state deflection rate as shown in Fig. 4.17 as,

$$\dot{\delta}_i \cdot \dot{\delta}_s^{-0.8} = 3.5 \quad (4.2.13)$$

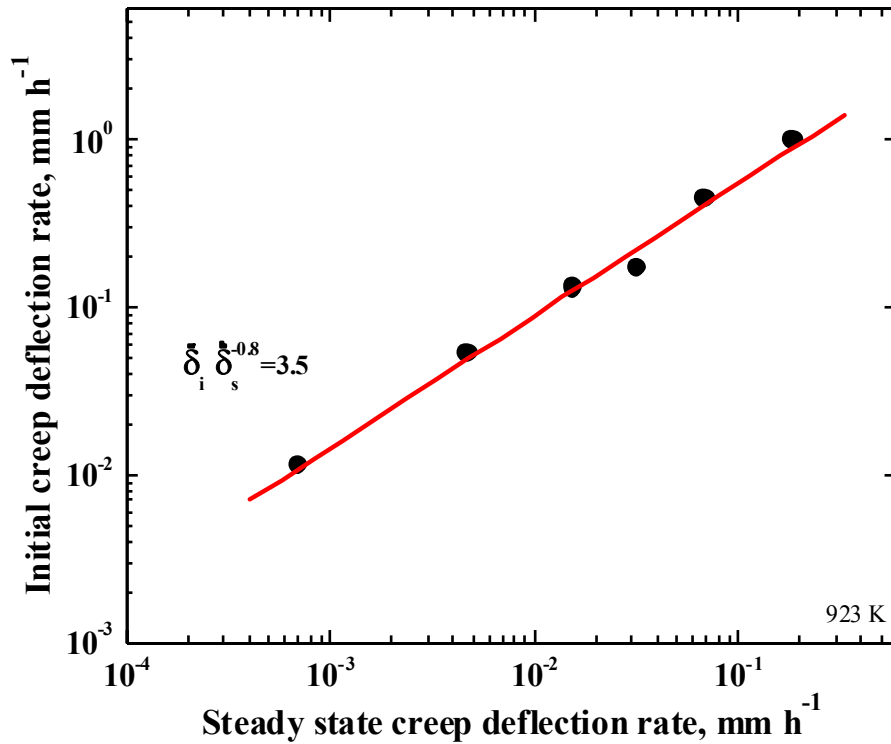


Fig. 4.17 Relationship between initial creep deflection rate and steady state creep deflection rate.

In uniaxial creep test, the proportionality constant between initial creep rate and steady state creep rate was reported as 3.3 for 304 SS^[152], 3.26 for 316 SS^[154], 9.97 for Ni-61%Fe alloy^[155], 4.1 for quenched and tempered 9Cr-1Mo steel in high stress regime^[156], 3.94 for NiAl hardened austenitic steel^[157] and 1.9 for RA FM steel^[158]. Good correlations of transient creep parameters such as initial creep rate and rate of exhaustion of transient creep, with the steady state creep parameter indicate that the basic mechanism of deformation is the same for both the stages of creep^[157]. The relationships between 'κ' and steady state

deflection rate, ' κ ' and time to attain minimum deflection rate, initial creep deflection rate and steady state deflection rate as given by Eqns.(4.2.11-4.2.13) respectively, implied that SPC deformation of 316LN SS was governed by first order kinetic reaction rate theory throughout the transient creep regime.

Amin et al.^[159] observed that for a given metal or alloy, there exists a universal high temperature transient and steady state creep curve of the form $(\varepsilon - \varepsilon_0) = f(\dot{\varepsilon}_s t)$ and also plotted those curves for Al, Cu, Ag, Pt, pure iron, low C-Ni and stainless steel. On analysing the uniaxial creep results for type 304 SS, it was reported that for a given set of stress exponent, limiting stain and constant of proportionality between rate of exhaustion of transient creep and steady state deflection rate, the transient and steady state creep obeying same kinetics law could be described by a unique master curve by plotting $(\varepsilon - \varepsilon_0)$ against $\dot{\varepsilon}_s t$ ^[152]. It was therefore attempted to analogously construct a master curve for transient creep deflection of 316LN SS by plotting $(\delta - \delta_0)/\delta_T$ against $\dot{\delta}_s t/\delta_T$ obtained from SPC tests, as shown in Fig 4.18.

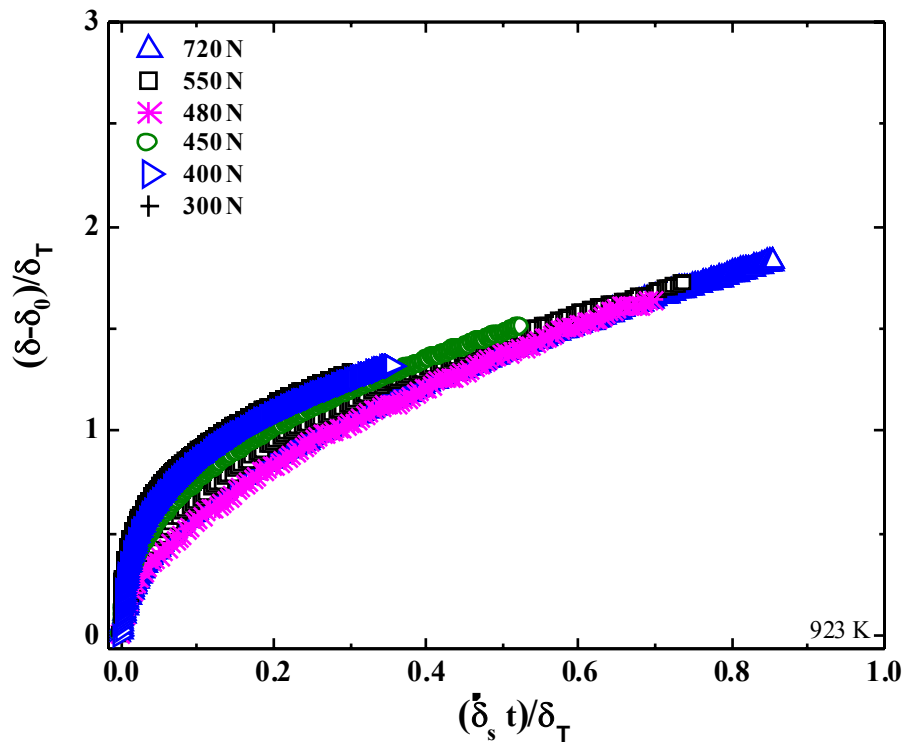


Fig. 4.18 Master curve obtained for transient SPC deflection.

Though some scattering was observed initially as consequence of wide range of loads and rupture lives, a fairly representative master curve was obtained for transient creep deflection. The master curve may be useful to assess the creep deformation and especially aid in assessment of degradation in creep strength of service exposed material during residual life assessment.

4.2.3 Tertiary creep analysis

Similar to transient creep stage, the first order reaction rate theory was found applicable to tertiary creep stage by taking the change of creep rate during tertiary stage as proportional to the difference between the tertiary and steady state creep rate values ^[160,161]. From SPC test, the rate of acceleration of tertiary creep (ϕ) may be calculated by rearranging Eqn. (4.2.4) and taking natural logarithm as,

$$\phi = -\frac{1}{(t-t_r)} \ln\left(\frac{\delta - \delta_0 - \delta_T - \dot{\delta}_s t}{\delta_3}\right) = -\frac{1}{(t-t_r)} \ln\left(\frac{\Delta_3}{\delta_3}\right) \quad (4.2.14)$$

where, $\Delta_3 = \delta - \delta_0 - \delta_T - \dot{\delta}_s t$, is the tertiary creep deflection component which becomes $\Delta_3=0$ at time to reach steady state deflection rate and approaches to δ_3 at time to rupture. The values of ϕ were calculated graphically as the slope of curve of $\ln\left(\frac{\Delta_3}{\delta_3}\right)$ plotted against $(t-t_r)$, for each load. The rate of acceleration of tertiary creep values are plotted as a function of steady state deflection rate in Fig. 4.19. Like in the case of rate of exhaustion of transient creep, the rate of acceleration of tertiary creep and steady state deflection rate were interrelated to each other. The relationship between ' ϕ ' and steady state deflection rate was determined as,

$$\phi \dot{\delta}_s^{-1.2} = 218 \quad (4.2.15)$$

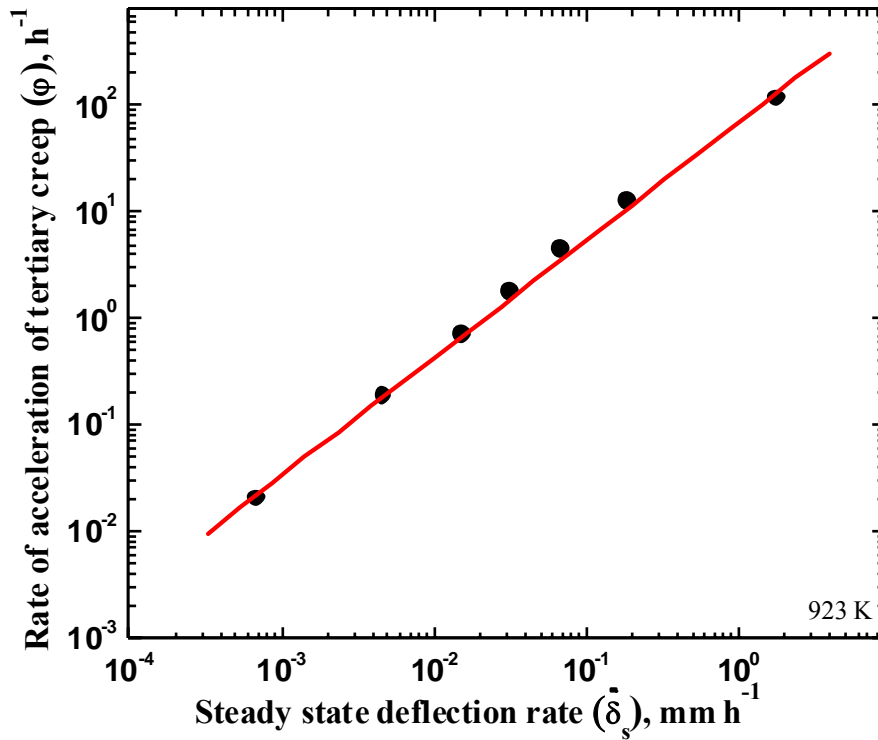


Fig. 4.19 Relationship between ϕ and steady state deflection rate.

The constant of proportionality between rate of acceleration of tertiary creep and steady state creep rate was reported in the literature as 32-118 for type 304 SS ^[160], 230 for 9Cr-1Mo steel ^[161] and 127 for RAFM steel ^[162].

The tertiary life or time spent in tertiary stage represents the ability of the material to delay the rupture, even though cavities start nucleating at this stage. Any measures such as, self-healing of nucleated cavity will extend the tertiary stage to increase rupture life. The time spent in tertiary stage was approximately calculated by deducting time for onset of tertiary creep from rupture life ($t_r - t_{ot}$). The time spent in tertiary stage was decided by rate of acceleration of tertiary creep as shown in Fig. 4.20. When the rate of acceleration of tertiary creep is decreased, the tertiary creep deformation accumulation rate is decreased thereby time spent in tertiary stage was found to be prolonged.

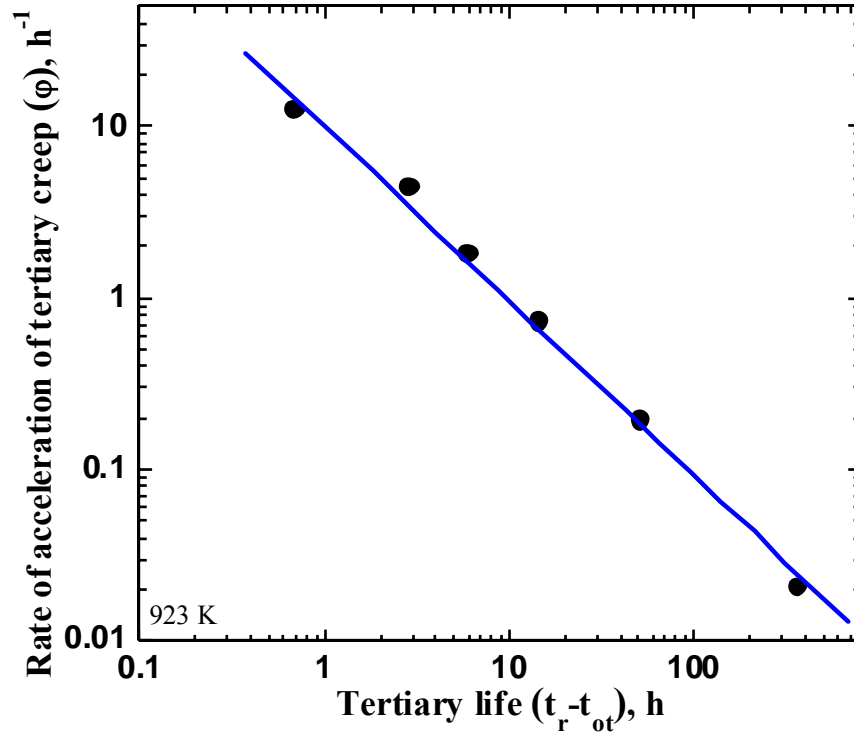


Fig. 4.20 Dependence of time spent in tertiary stage on rate of acceleration of tertiary creep.

The relationship between ϕ and tertiary life was obtained as,

$$\phi (t_r - t_{ot}) = 10 \quad (4.2.16)$$

The values reported for the proportionality constant in Eqn. 4.2.16 from uniaxial creep tests are in the range 4.5-7 for various materials such as 304 SS ^[160], RAFM steel ^[162] and Cu, α -brass, iron, zinc ^[163].

On differentiating Eqn. (4.2.4) with respect to time, rate of deflection at time 't' was obtained as,

$$\dot{\delta} = \kappa \delta_T e^{-\kappa t} + \dot{\delta}_s + \phi \delta_3 e^{[\phi(t-t_r)]} \quad (4.2.17)$$

During tertiary creep stage, the influence of transient creep deflection term in the above equation was negligible. By ignoring the transient creep term in Eqn. (4.2.17) and substituting $t=t_r$, the final creep deflection rate ($\dot{\delta}_f$) was obtained as $\dot{\delta}_f = \phi \delta_3 + \dot{\delta}_s$. The values of final creep deflection rate are plotted against steady state deflection rate in Fig. 4.21.

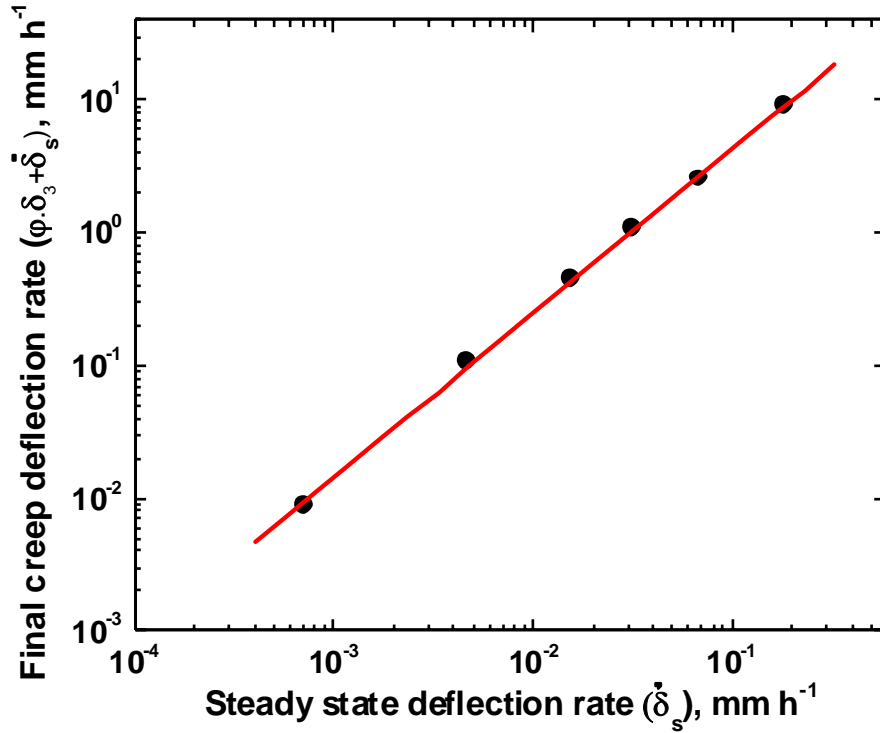


Fig. 4.21 Relationship between final creep deflection rate and steady state deflection rate.

The final creep deflection rate and steady state deflection rate were related as,

$$\dot{\delta}_f \dot{\delta}_s^{-1.2} = 75 \quad (4.2.18)$$

The constant of proportionality between final creep rate and steady state creep rate was reported in the literature as 5-8.4 for 304 SS ^[160] and 105 for 9Cr-1Mo steel ^[161]. The near linear relationships between (i) 'φ' and steady state deflection rate (ii) 'φ' and time spent in tertiary stage (iii) final creep deflection rate and steady state deflection rate, revealed that tertiary SPC deformation obeyed first order kinetic reaction rate theory.

When tertiary creep behaviour follows first order reaction rate theory, it may be possible to construct unique tertiary master curve under uniaxial creep condition ^[160-162]. In this investigation, it was attempted to construct master curve for tertiary SPC deformation by plotting $(\delta - \delta_0 - \delta_T)$ against $\dot{\delta}_s t$, as shown in Fig. 4.22. During the latter part of tertiary stage and just before rupture, say about last 5-15% of rupture life, the role of growth of cavities growth

is more dictated by applied load rather than creep resistance and hence the master curve may not be truly applicable in this range. Those data were eliminated while drawing the master curves for tertiary creep deflection.

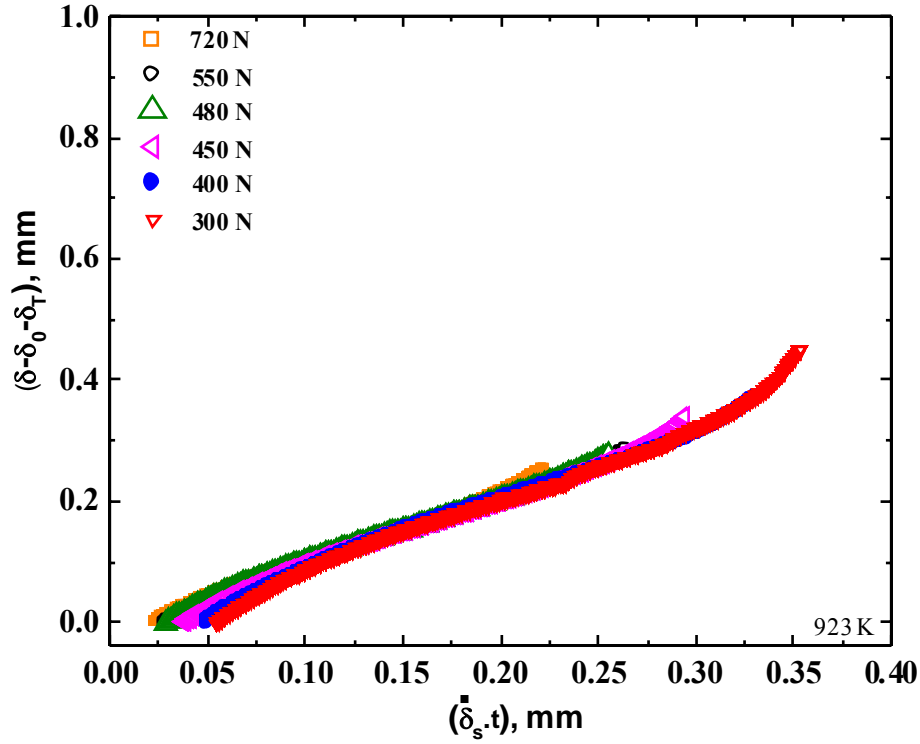


Fig. 4.22 Master curve obtained for tertiary SPC deflection.

The curves derived from tertiary SPC data at various loads were found to result in a fairly representative master curve. The master curve obtained for tertiary SPC deformation can be utilized during future investigations on assessment of degradation in creep strength of the same material on service exposure.

4.2.4 Role of κ and ϕ on rupture life

The values of κ , $\dot{\delta}_s$ and ϕ showed significant impact on SPC rupture life, as shown in Fig. 4.23. The steady state deflection rate, the rate of exhaustion of transient creep and rate of

acceleration of tertiary creep were found to follow similar decreasing trend with rupture life. The increase in rupture life on increasing the tungsten content in RAFM steel was reported as a consequence of decrease in both rate of exhaustion of transient creep and rate of acceleration of tertiary creep ^[158,162].

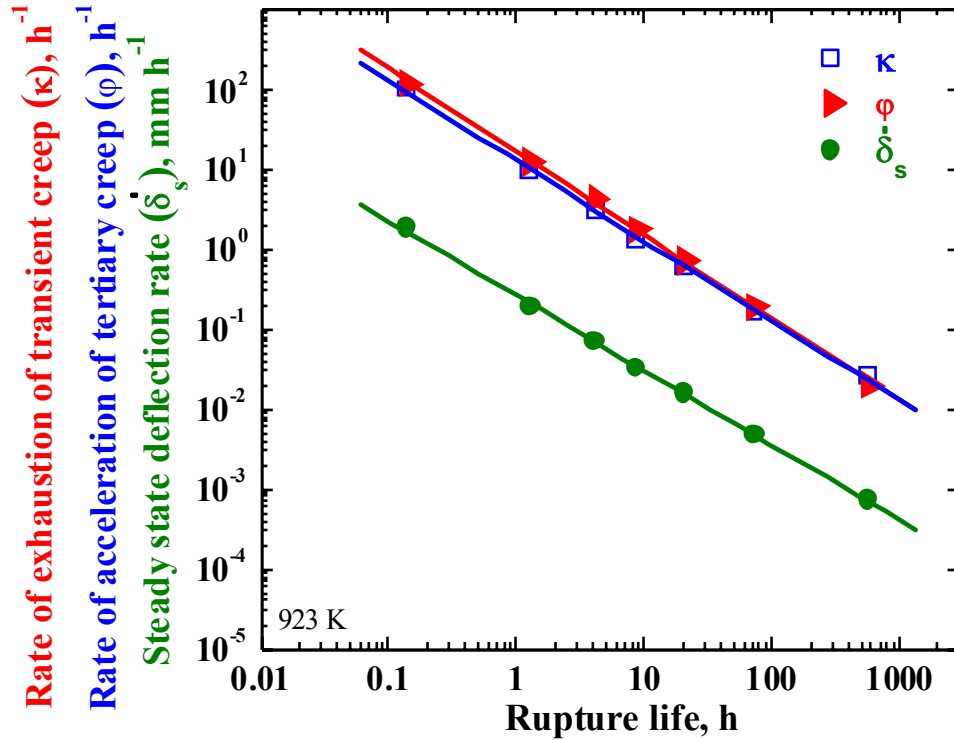


Fig. 4.23 Trends of variation of rate of exhaustion of transient creep, steady state deflection rate and rate of acceleration of tertiary creep with rupture life.

Both steady state deflection rate and rupture life are related to rate of exhaustion of transient creep and rate of acceleration of tertiary creep, which in turn are dependent on the applied load. Figure 4.24 shows the dependence of transient and tertiary creep parameters on the applied load. Both κ and ϕ decreased with decrease in load, resulting in longer transient and tertiary creep stages, which might have caused the proportional increase in rupture life. The variation of steady state deflection rate with applied load is also shown with a power law relationship in the same figure. Both rate of exhaustion of transient creep and rate of

acceleration of tertiary creep interestingly exhibited a similar kind of dependence on load as that of steady state deflection rate.

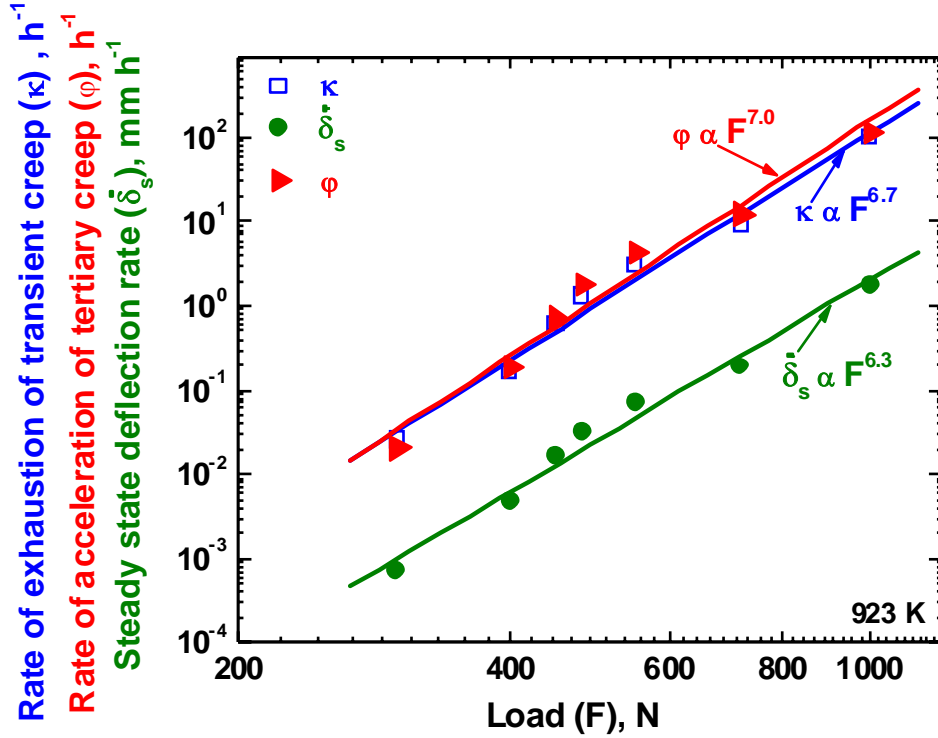


Fig. 4.24 Dependence of transient, secondary and tertiary creep parameters on applied load.

It may be noted from the relationships, $\dot{\delta}_s \propto F^{6.3}$, $\kappa \propto F^{6.7}$ and $\phi \propto F^{7.0}$, that the values of load exponent seemed to be closer to each other, implying that the dependence of deflection rate on applied load was similar at all stages of creep. The above results implied that all stages of SPC were closely interrelated to each other.

4.2.5 Interrupted tests results

In order to study the deformation occurring in SPC specimen at various creep stages leading to rupture, three SPC tests were conducted at 923 K with the same applied load of 400 N and were interrupted at secondary stage, tertiary stage and just before rupture.

The optical micrographs of the half-sectioned region of SPC specimen whose tests were interrupted at different stages are shown in Fig. 4.25. In SPC test, the formation of cracks occurs before the onset of tertiary stage. During secondary stage, permanent plastic deflection was observed with start of few cavities (Fig. 4.25a). The initiation and growth of cavities leading to cracks was observed closer to the end of secondary stage (Fig. 4.25b). The formation of cracks was reported to have occurred even at the primary SPC stage for super duralumin ^[164]. The presence of cavities and twins were found in the latter part of tertiary stage (Fig. 4.25c). It was observed similar to uniaxial creep that cavities nucleate at grain boundaries and then grow to form cracks.

4.3 SPC mechanism

The mechanism governing the creep deformation is usually identified by analyzing the steady state creep rate. In conventional creep tests, the stress (σ) and temperature (T) dependence of the steady state creep rate ($\dot{\epsilon}_s$) could be described by Arrhenius type equation,

$$\dot{\epsilon}_s = A_1 \sigma^{n_{uc}} \exp\left(-\frac{Q}{RT}\right) \quad (4.3.1)$$

where, A_1 is a constant, n_{uc} is stress exponent, Q is apparent activation energy for creep and $R=8.314$ J/K/mol is universal gas constant. SPC is a thermally activated process following Arrhenius type expression with characteristic activation energy for the rate controlling mechanism. Analogous to uniaxial creep tests, an Arrhenius form of equation can be used to express the load (F) and temperature dependence of steady state deflection rate as,

$$\dot{\delta}_s = C_s F^{n_{spc}} \exp\left(-\frac{Q}{RT}\right) \quad (4.3.2)$$

where, C_s is constant, ' n_{spc} ' is load exponent of steady state deflection rate. The activation energy of two different structures of Fe28Al3Cr0.02Ce alloy were calculated based on the steady state deflection rate obtained from SPC tests in the temperature range 773-873 K ^[165].

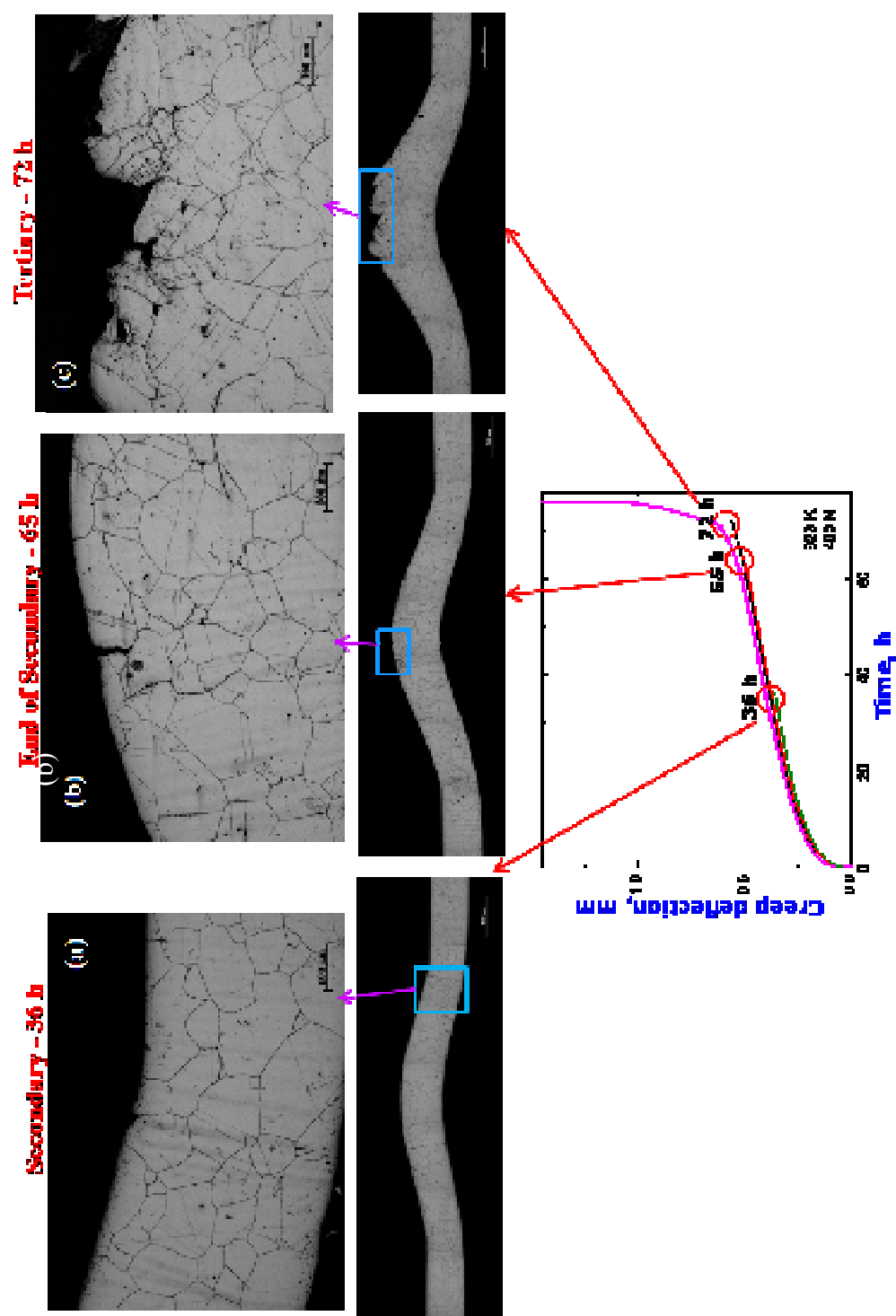


Fig. 4.25 Optical micrograph of sectioned SPC specimen tested at 923 K at 400 N and interrupted at (a) secondary stage – 35h

(b) tertiary stage 65 h and (c) just before rupture 74 h (rupture life at same load is around 75 h).

In order to estimate the activation energy for the investigated material, SPC results obtained over the temperature range of 898-973 K at 400 N were used. The influence of temperature on SPC deformation is shown in Fig. 4.26. The rupture life increased and steady state deflection rate decreased with decrease in test temperature.

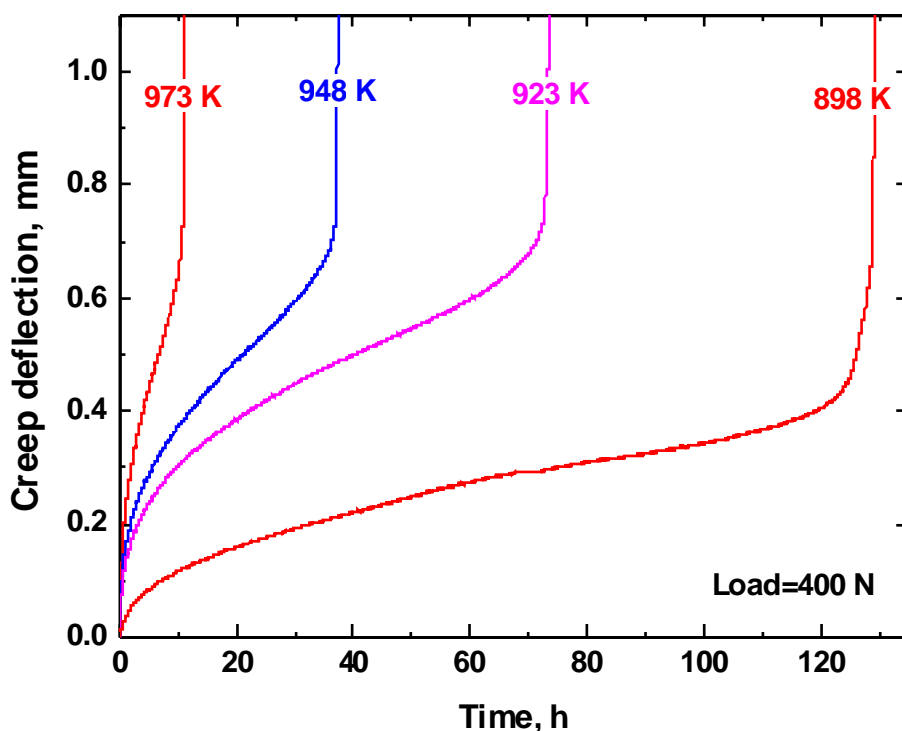


Fig. 4.26 Influence of temperature on SPC deformation at 400 N.

The steady state deflection rate values are plotted against inverse of temperature (in absolute scale) on a semi-logarithmic plot in Fig. 4.27. The load exponent of steady state deflection rate as inferred from the slope of the plot is $n_{\text{spc}}=6.4$. From the value of slope ($= Q/R$), the apparent activation energy for creep was determined as 352 kJ/mol which was higher than the activation energy for self-diffusion of iron in γ -iron or austenite matrix (284 -295 kJ/mol^[166]). The load exponent value obtained above can be taken as equivalent to stress exponent while referring the mechanisms associated with dislocation and diffusion creep processes. It is because the equivalent stress and load are related by simple ratio, called effective area parameter, which may not alter the slope of the plot between steady state deflection rate and

equivalent stress. From the values of load exponent ($n_{\text{spc}} = 6.35$) and apparent activation energy for creep deformation ($Q = 352 \text{ kJ/mol}$), it may be concluded that the mechanism that governs SPC deformation in the investigated range of temperature and load is dislocation creep.

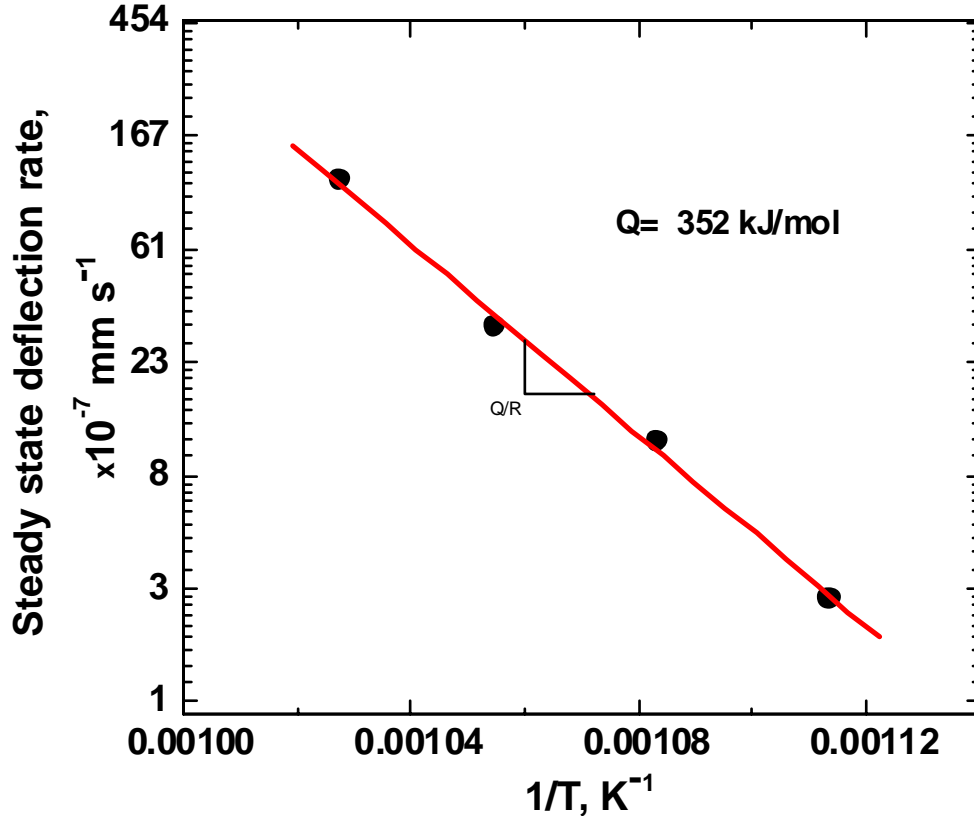


Fig 4.27 Determination of SPC activation energy; Temperature range: 898-973 K.

The SPC mechanism is also assessed on measuring the activation energy for fracture using rupture life data. The load and temperature dependence of SPC rupture life (t_r) can be described using a modified form of Dorn equation as^[67,167,168],

$$t_r = C_r F^{-n_r} \exp\left(\frac{Q_f}{RT}\right) \quad (4.3.3)$$

where, C_r is a constant, n_r is load exponent of rupture life and Q_f is activation energy for fracture. In the present investigation, the activation energy for fracture was also calculated

using the rupture life data. From the slope of the plot between applied F and t_r (Fig 4.3), the load exponent of rupture life was obtained as, $n_r=6.8$, which seemed to be closer to the value of n_{spc} ($= 6.4$). The SPC rupture lives obtained at various temperatures are plotted against inverse of temperature (in absolute scale) on a semi-logarithmic plot in Fig 4.28. From the slope of the curve ($= Q_f/R$), the activation energy for fracture was obtained as, $Q_f = 233$ kJ/mol. The value of Q_f was comparable with activation energy for self-diffusion of iron in γ -iron but was appreciably far away from Q value.

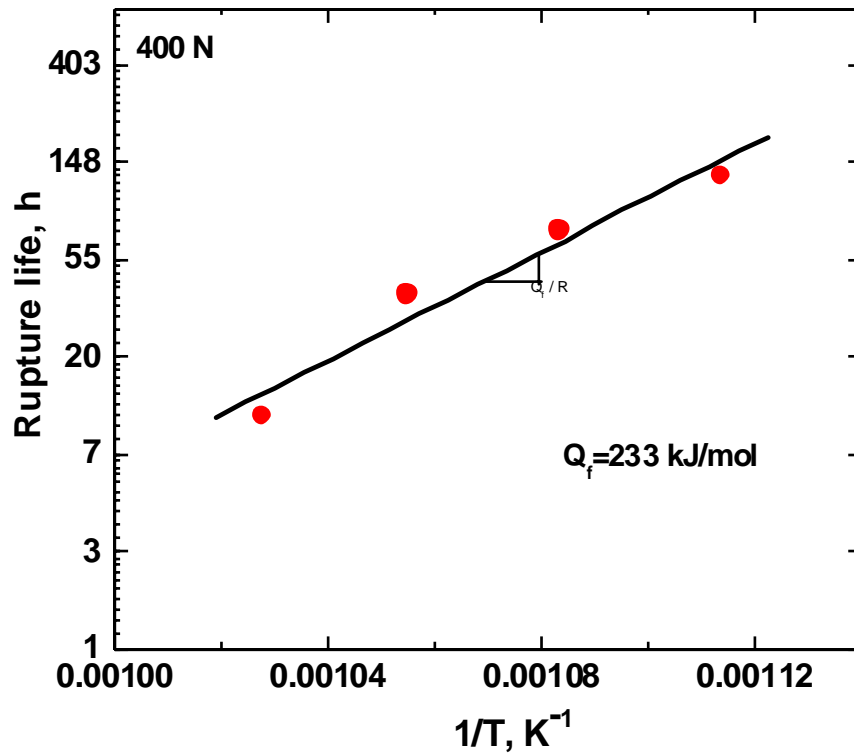


Fig. 4.28 Dependence of SPC rupture life on temperature. Temperature range: 898-973 K.

From the plot of t_r Vs $\dot{\delta}_s$ data (Fig 4.29), obtained in the temperature range 898-973 K, the Monkman-Grant relationship was expressed as,

$$t_r \dot{\delta}_s^{0.66} = 1.5 \quad (4.3.4)$$

The reduction in thickness accompanied by nucleation of cavities in the tertiary stage dictates the fracture. Both bending and membrane stretching modes of deformation occur at all stages

of creep, the dominance of one over another differing from stage to stage. The mixed modes of deformation at different stages may have dictated different mechanism for creep deformation and fracture.

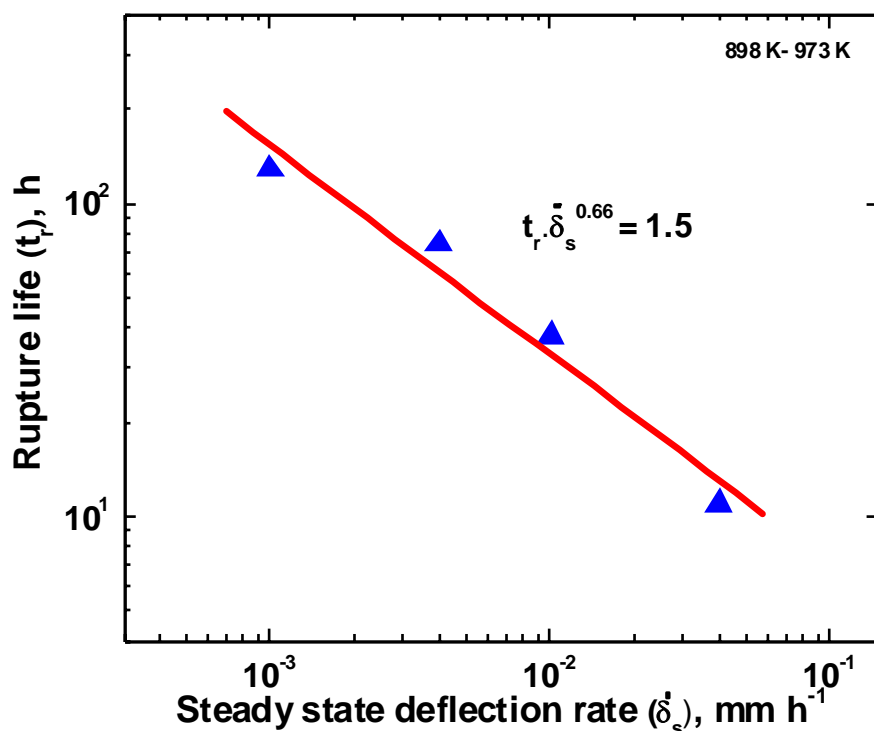


Fig. 4.29 Monkman-Grant relationship established over SPC data in the temperature range 898-973 K.

4. 4 Correlation with uniaxial creep results

It is necessary to validate correlation between SPC and conventional creep tests, in order to utilize SPC data for residual life assessment. The uniaxial creep test results that were available for the same material under investigation at 923 K^[111] are utilized for this correlation. Of the various creep parameters, rupture life is generally used as common axis to compare SPC and uniaxial creep results, due to similarity in physical meaning as well as unit of measurement. Taking rupture life as common in abscissa, the SPC loads and conventional creep stresses are plotted together as ordinates in Fig. 4.30. The trend of isothermal rupture curve in SPC test was similar to that of uniaxial creep test. In a set of rupture lives

overlapping between both the test results, a conventional creep stress was found approximately equivalent to each SPC load resulting in the same rupture life. A similar linear relationship was found to be obeyed by both SPC and uniaxial data (on log-log scale).

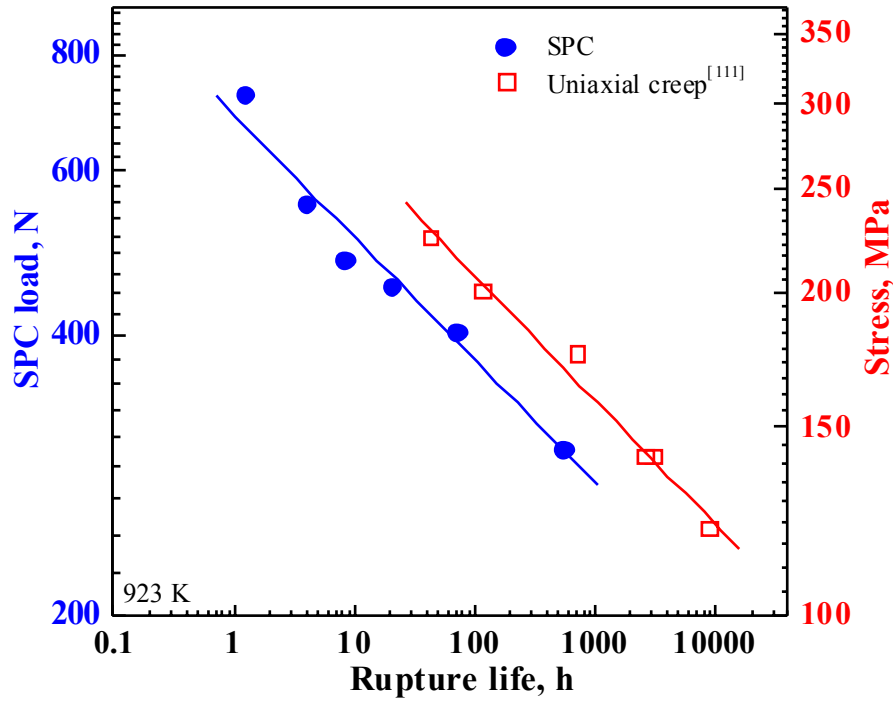


Fig. 4.30 Comparison of SPC loads with conventional creep stress, taking rupture life as common in abscissa.

The equivalent uniaxial stress for SPC load was determined as per CEN CoP equation ^[74],

$$F/\sigma = 3.33 K_{SP} R_h^{-0.2} r^{1.2} h \quad (4.5.1)$$

On substituting the values of $R_h=2$ mm, $r=1.19$ mm, $h=0.5$ mm and taking $K_{SP}=1$ in above equation, $F/\sigma (= \alpha) \approx 1.8$ (mm²). Similarly, several values were used for correlating SPC load and uniaxial stress for various materials such as 1.76 for 2¼-1Mo V modified steel ^[86], 2.8 for P91 steel ^[58], 2.7 for 1¼Cr½Mo pearlitic steel ^[72], 2.0 for AZ31 magnesium alloy ^[73], 0.43 for F82H steel ^[92], 0.794 for Al-1%C-0.8%O alloy ^[169], 2.1 for 2124 aluminium reinforced with SiC particulates ^[170] and 1.25 for P92 steel ^[171]. In the present case, the SPC equivalent uniaxial stresses are calculated by dividing load F by 1.8. The rupture lives

obtained from uniaxial creep tests^[111] are plotted in log-log scale in Fig 4.31. The corresponding SPC equivalent stresses are plotted as scatter over the fit on uniaxial creep data. It was generally found that equivalent SPC stresses generally fall within 10% scatter bands of fit on uniaxial creep results.

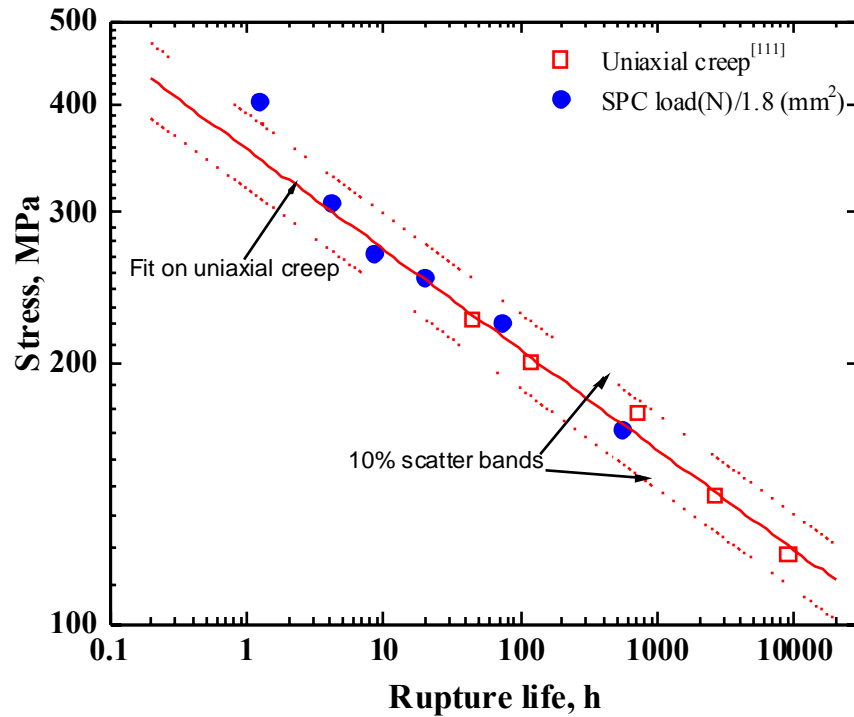


Fig 4.31 Correlation of SPC equivalent stress with uniaxial creep stress.

The SPC steady state deflection values were compared with steady state creep rate values determined from uniaxial creep tests in Fig 4.32, taking rupture life as common axis. It was observed that the steady state deflection rate exhibited a trend similar to that of uniaxial creep test with rupture life. The steady state creep rate values that were calculated from the maximum strain curves (as presented in section 4.1.3), are plotted as scatter over the fit on corresponding steady state creep values obtained from conventional creep tests in Fig 4.33. It was generally observed that the steady state creep values calculated from SPC strain-time curves were very closer to those obtained from conventional uniaxial creep tests.

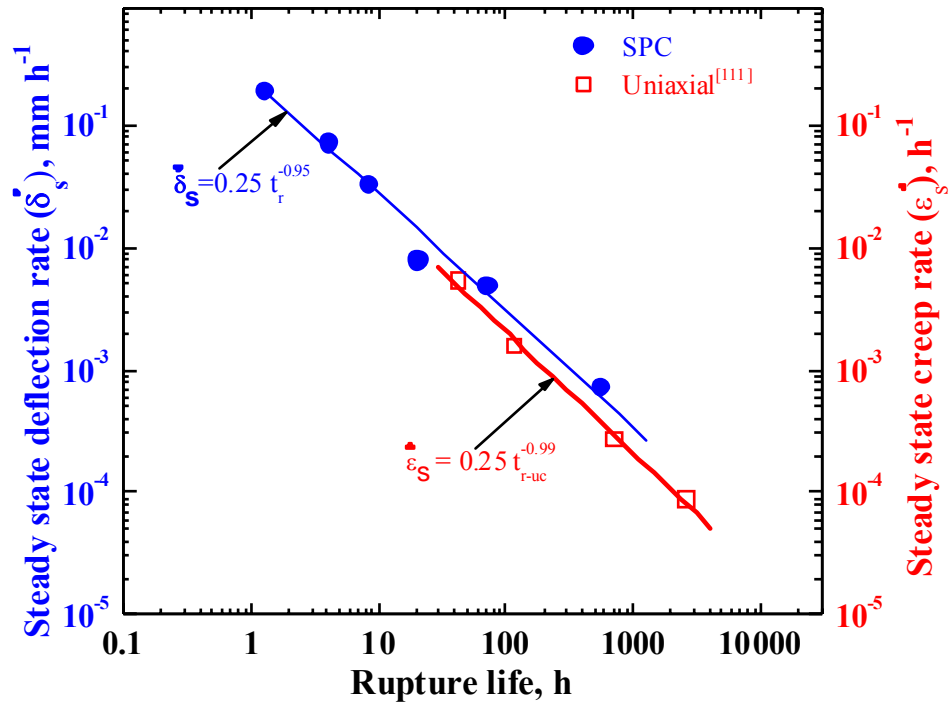


Fig. 4.32 Comparison of variations of SPC steady state deflection rate and conventional creep steady state creep rate with rupture life.

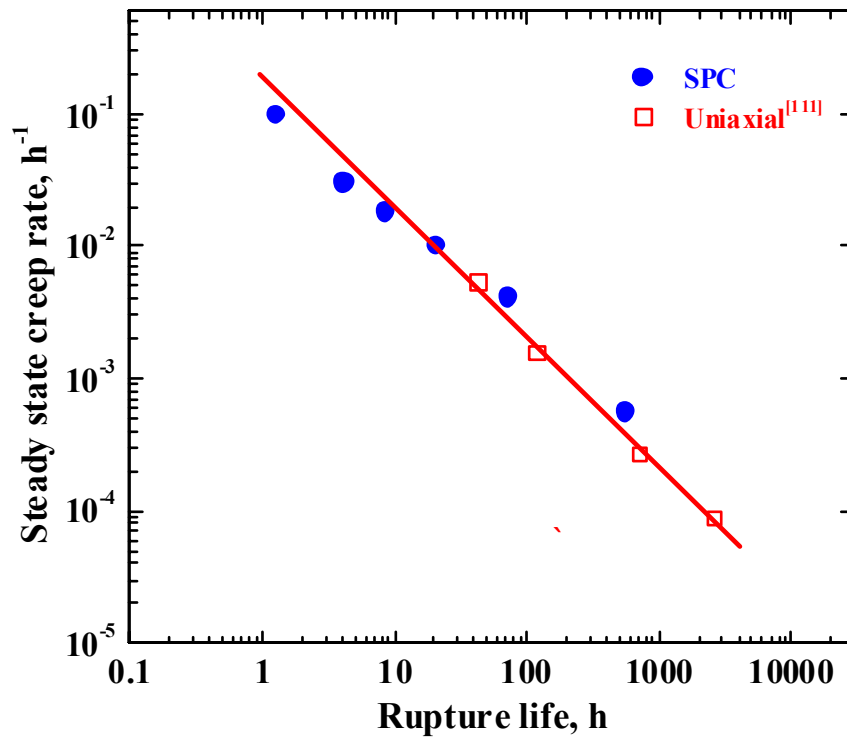


Fig. 4.33 Comparison of steady state creep rate values determined using derived strain curves with conventional test results.

The comparison of SPC and uniaxial creep results have largely been dealt with rupture life and steady state deflection rate. It has been attempted to correlate the deformation behaviour of SPC and uniaxial creep tests. Komazaki et al. [85] revealed that creep curves obtained from SPC tests were qualitatively similar to those obtained from uniaxial creep tests and reflected closely the degradation of creep rupture strength of the materials. Since the transient creep deformation do have significant role during design as well as life assessment of components in service, it is necessary to study and compare the transient creep region of both SPC and uniaxial creep curves.

The uniaxial creep test results^[11] were analysed to compute the values of rate of exhaustion of transient creep. These values were compared with rate of exhaustion of transient creep obtained from SPC tests. The rate of exhaustion of transient creep (r'), under uniaxial creep condition, can be determined by rearranging Eqn. (4.2.9) for creep strain (ε) as,

$$r' = -\frac{1}{t} \ln \left(1 - \frac{(\varepsilon - \varepsilon_0 - \dot{\varepsilon}_s t)}{\varepsilon_T} \right) = -\frac{1}{t} \ln \left(1 - \frac{\Delta}{\varepsilon_T} \right) \quad (4.5.2)$$

where, $\Delta (= \varepsilon - \varepsilon_0 - \dot{\varepsilon}_s t)$, is the transient creep strain component whose value ranges from $\Delta=0$ at time $t=0$ and becomes closer to ε_T at time to attain steady state creep rate. The rate of exhaustion of transient creep (r') was calculated graphically as the slope of $\ln(1-\Delta/\varepsilon_T)$ versus 't' plot obtained for each stress. The rate of exhaustion of transient creep values are plotted against corresponding steady state creep rate and time to attain steady state creep rate (t_{s-w}), as shown in Figs. 4.34 and 4.35 respectively. The rate of exhaustion of transient creep increased with increase in steady state creep rate and decreased with increase in time to reach steady state creep rate.

The following relationships obtained for uniaxial transient creep parameter (r') were found to be analogous to SPC Eqns. (4.2.11) and (4.2.12) as,

$$r' \dot{\varepsilon}_s^{-0.93} = 1.2 \quad (4.5.3)$$

$$r' \cdot t_{s-w}^{-1.05} = 7.7 \quad (4.5.4)$$

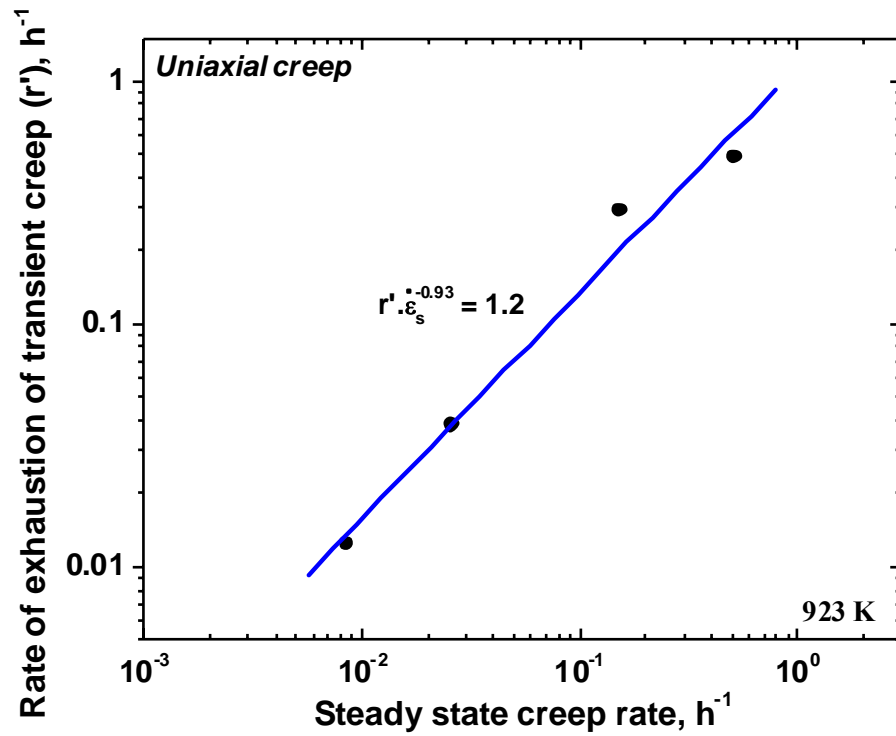


Fig 4.34 Relationship between rate of exhaustion of transient creep and steady state creep rate calculated from uniaxial creep tests.

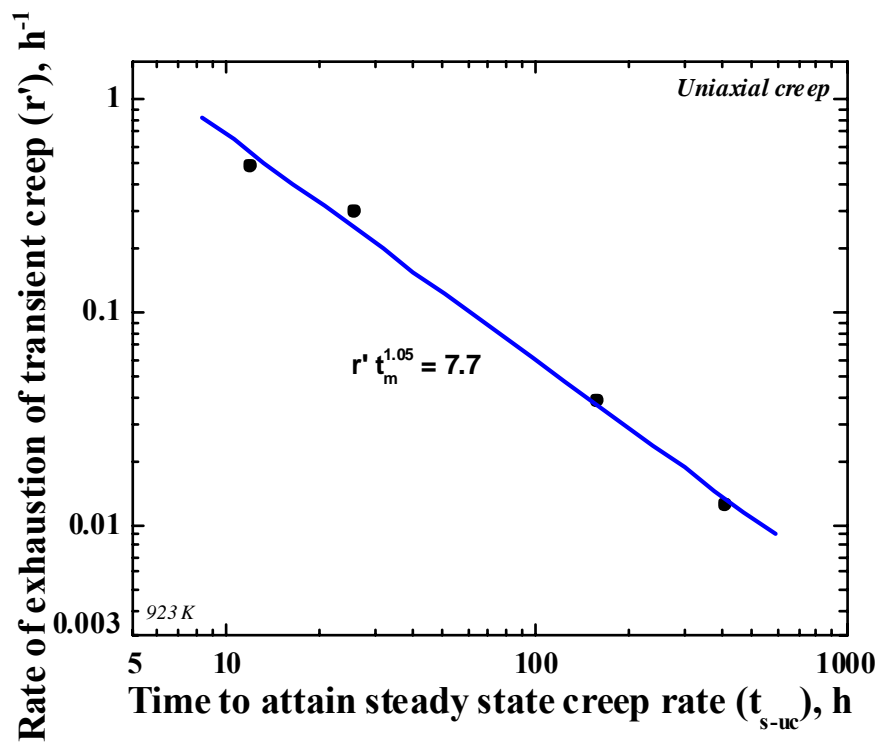


Fig 4.35 Variation of rate of exhaustion of transient creep with time to attain steady state creep rate.

The rate of exhaustion of transient creep obtained from SPC and uniaxial creep tests were compared with each other, as a function of rupture life, as shown in Fig 4.36. The trends of variation of rate of exhaustion of transient creep with rupture life seemed to be closer to each other for both SPC and uniaxial creep tests.

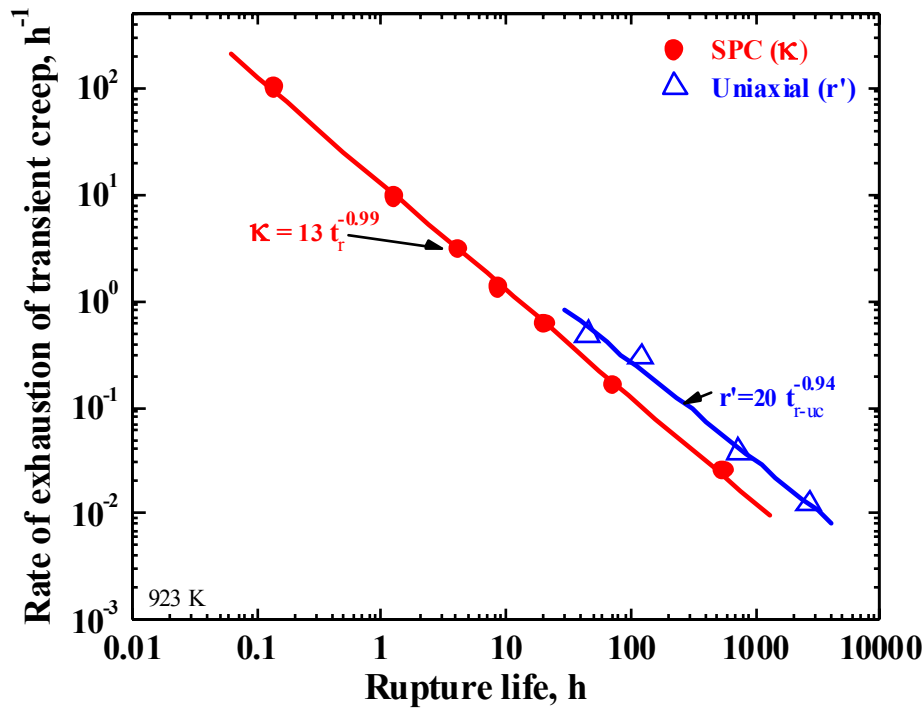


Fig. 4.36 Variation of rate of exhaustion of transient creep with rupture life, as obtained from uniaxial creep and SPC tests.

The rate of exhaustion of transient creep and rupture life are inversely proportional to one another under both SPC and uniaxial creep conditions. In case of 316L(N) SS, SPC load was divided by an empirical factor, $\alpha=1.8$, to obtain the equivalent uniaxial stress. The rate of exhaustion of transient creep (κ) values obtained from SPC tests were multiplied by the same empirical value of 1.8. The so obtained values are plotted as scatter over the fit on r' (from uniaxial creep) in Fig 4.37. It was observed that rate of exhaustion of transient creep values of SPC and uniaxial creep exactly overlapped each other, implying good correlation between SPC and uniaxial creep test.

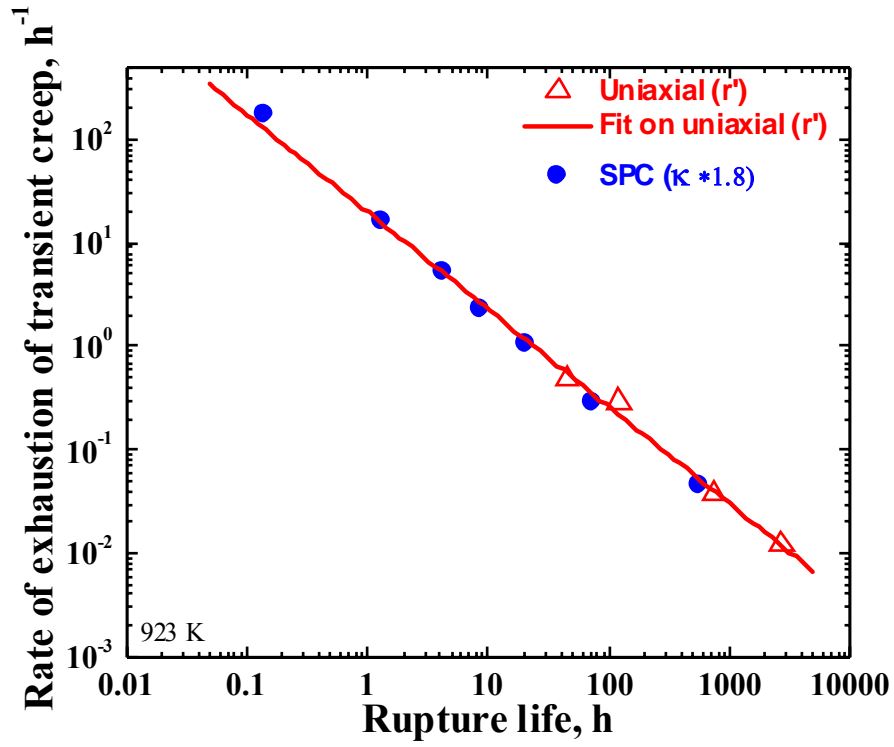


Fig. 4.37 Variation of rate of exhaustion of transient creep with rupture life, as obtained from uniaxial creep and SPC tests on multiplying ' κ ' value by empirical factor 1.8.

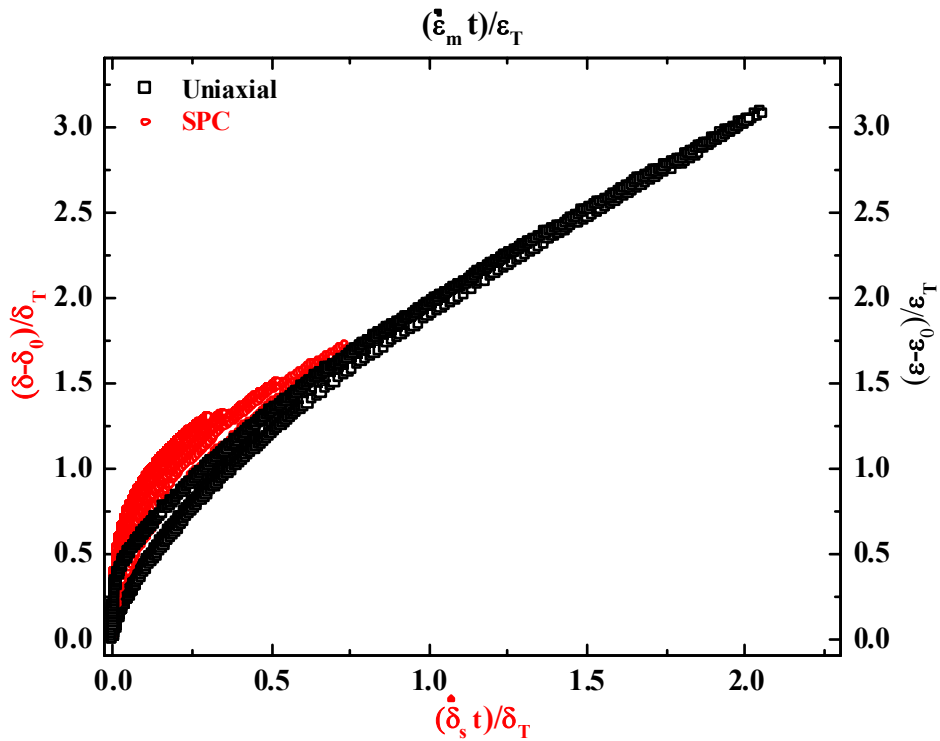


Fig. 4.38 Master curves for transient creep deformation as estimated from SPC and uniaxial creep tests.

The master curve for uniaxial transient creep deformation was obtained by plotting $(\varepsilon - \varepsilon_0)/\varepsilon_T$ against $\dot{\varepsilon}_s t / \varepsilon_T$. The master curves for transient creep as determined from uniaxial creep and SPC tests are plotted together in Fig. 4.38. The master curves for transient creep obtained from both the tests were found to be in good agreement to one another. From the close correlation between SPC and uniaxial creep tests, as implied from above discussions, it may be concluded that same deformation mechanism may be followed in the transient creep stage in both SPC and uniaxial creep tests.

It may also be noted that the above comparisons were made with results of SPC tests with a maximum duration not exceeding 569 hours, which might seem to be shorter relative to conventional creep tests. One of the limitations in interpreting short term SPC test results is that the microstructural changes due to long term creep may not be observed.

4.5 Finite Element Analysis (FEA)

Though a constant load is applied during SPC test, the stresses developed in the specimen actually changes as a function of both time and position. Finite element method can be helpful to calculate the stresses in SPC specimen. The analysis can be simplified by defining creep behaviour using Norton's creep law involving steady state creep rate ($\dot{\varepsilon}$) as,

$$\dot{\varepsilon} = A\sigma^n \quad (4.6.1)$$

where, n is the stress exponent of steady state creep rate determined from uniaxial creep results. FEA employing Norton's creep model has been used to obtain the creep coefficient values closer to uniaxial creep test values ^[172]. Continuum damage mechanics (CDM) has also been used to reliably predict the creep deformation and rupture life considering the various stages of creep. The creep damage generally occurs due to formation, growth and coalescence of cavities. The CDM model proposed by Kachanov ^[173] uses a scalar damage variable (ω) to define the creep damage accumulation. The advantage of this CDM model is

its compatibility with FEA and hence this approach has been popularly used for creep solutions. The sets of results obtained from FEA using both Kachanov and Norton models were found to be in good agreement with one another ^[174].

The study of creep behaviour can be complete in all aspects when all three stages of creep are considered. In this investigation, the tertiary creep behaviour is included in the material model by coupling FEA with Kachanov model.

As per Kachanov model, the creep strain rate and damage rate are expressed as a function of damage parameter as,

$$\dot{\varepsilon} = A_d \left(\frac{\sigma}{1 - \omega} \right)^{n_{uc}} \quad (4.6.2)$$

and

$$\dot{\omega} = \frac{B \sigma^\chi}{(1 - \omega)^\phi} \quad (4.6.3)$$

where A_d , n_{uc} , B , χ and ϕ are material parameters. The values of these parameters were derived using the uniaxial creep curves available for 316L(N) SS ^[111]. The values of A_d and n are calculated using Eqn 4.6.1 relating steady state creep rate with stress. The parameters B , ϕ and χ are derived from the relationship between rupture life and stress expressed as,

$$t_{r-uc} = \frac{1}{B(1 + \phi)\sigma^\chi} \quad (4.6.4)$$

The slope of the plot between rupture life and stress on log-log scale gives the value of χ and the intercept gives value of $B(1 + \phi)$. The values of B and ϕ are obtained by trial and error method so that the derived curves are closer to the original creep curves. The value of B , based on uniaxial creep curves, is further fine-tuned for use with SPC model. The parameters finally used in defining creep model are given in Table 4.1. The equations 4.6.2 and 4.6.3 were incorporated in CREEP subroutine to provide user-defined material creep property for the analysis. The analysis was run up to the onset of necking.

Table 4.1 Parameters used for defining creep model

Parameter	A_d	n_{uc}	χ	B	ϕ
Value	1.13×10^{-22}	8.3	7.72	1.86×10^{-21}	7.02

During SPC test, the displacement of the indenter is measured as deflection. The same logic is applied for FEA by taking the displacement of indenter along the axis of symmetry as the deflection. The deflection-time curves predicted by FEA are compared with corresponding SPC test curves at various loads in Fig. 4.39.

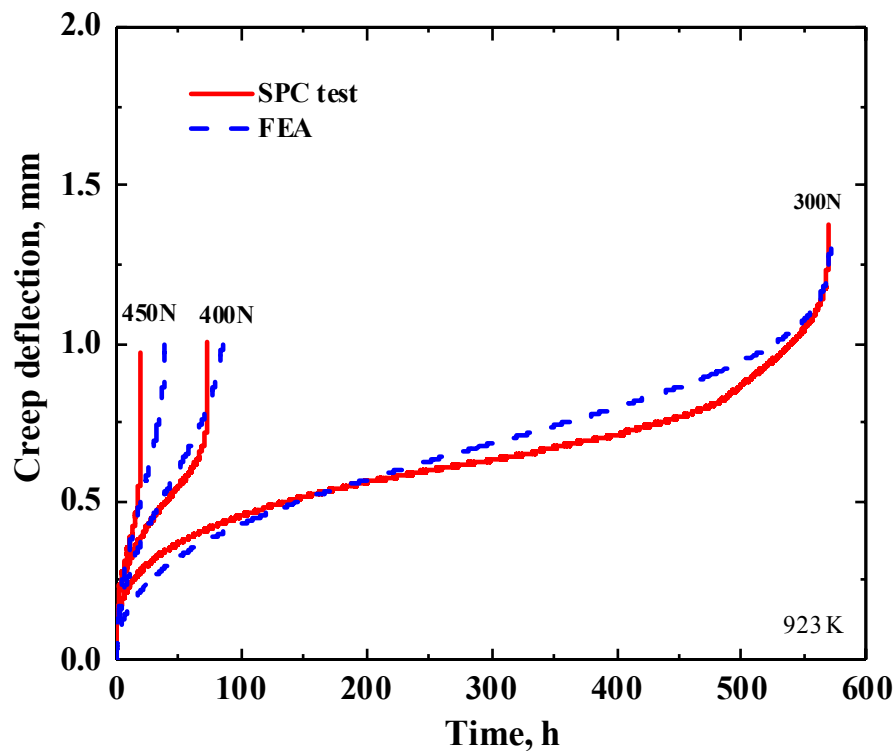


Fig. 4.39 Comparison of FEA predicted curves with test results.

Although Kachanov model defines only secondary and tertiary creep, the primary creep stage was observed in the FEA predicted curves. The primary creep region was also observed by Hyde et al.^[174] while carrying out FEA over SPC test specimen using Kachanov model, although no clear explanation was presented. The redistribution of stresses, which were developed during initial contact between indenter and specimen, would have resulted in

occurrence of primary creep stage. Notwithstanding this, the FEA curve is very closer to SPC test at 300 N. At higher loads, small deviations are observed as FEA predicted more rupture life than test values. Similar discrepancies between FEA and SPC test results were reported at high forces, and were attributed to high instantaneous strain after loading not being adequately described by creep equations ^[175]. Hence the preliminary results obtained at 300 N with closer prediction were only considered further in this section.

The creep cavities nucleate around stress concentration sites produced as a result of non-uniform plastic deformation. The von-Mises stress causing plastic flow of material can be held responsible for creep cavitation ^[176]. The von-Mises stress developed in SPC specimen at the onset of necking is shown in Fig. 4.40. The stresses were found to be higher near the contact boundary.

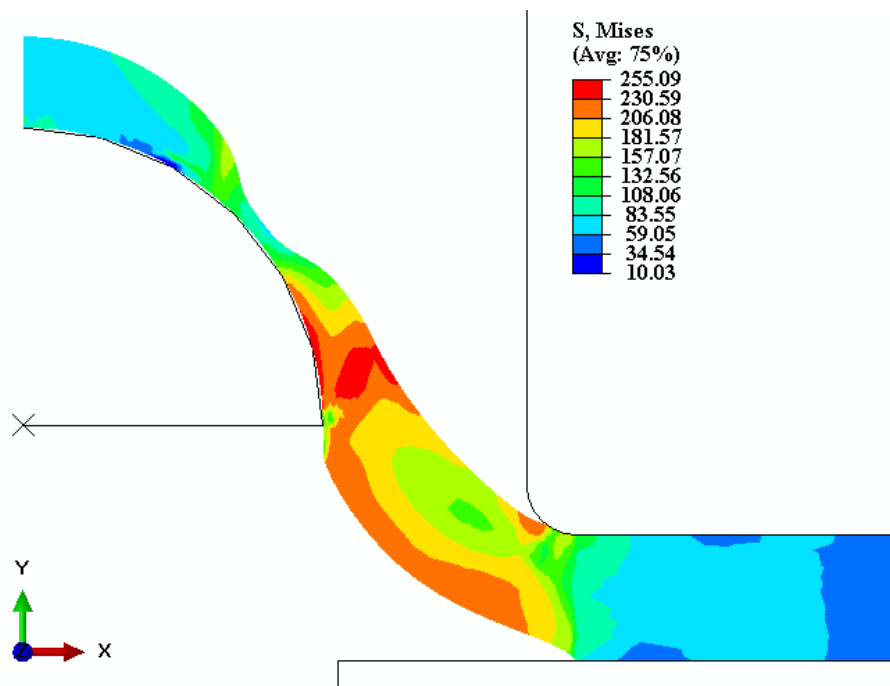


Fig. 4.40 Von-Mises stress in SPC specimen.

The strain rate was calculated based on the damage variable (ω). The damage variable was defined as a state dependent variable (SDV) in the analysis, is shown in Fig. 4.41 during the onset of necking.

The diffusive growth of intergranular cracks is linked with maximum principal stress acting on those grain boundaries that are perpendicular to the cracks. The direction and magnitude of maximum principal stress are shown in Fig. 4.42. The results discussed above are preliminary and further detailed studies have been carried out by fine-tuning the material parameters to represent the SPC deformation.

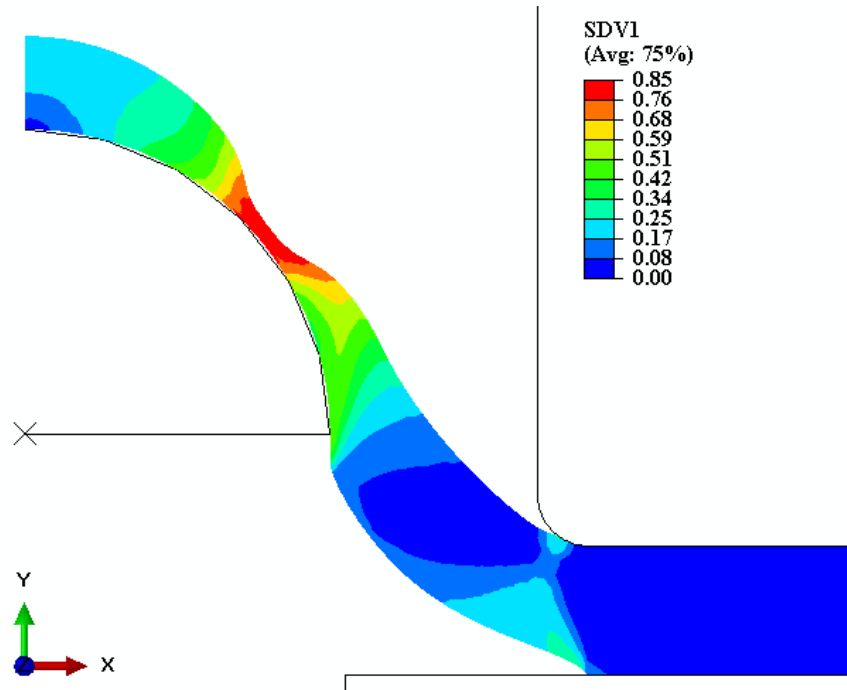


Fig. 4.41 Damage accumulation in the deformed specimen.

The values of parameters in Table 1 were derived from uniaxial creep curves of very long duration. There are possibilities that such parameters may not accurately provide a material model for short term SPC tests. The parameters are further required to be fine-tuned to check this discrepancy. However, the so obtained results can be used to qualitatively understand the state of stress. The accuracy of the magnitude of stress can be improved further by modifying the creep model parameters.

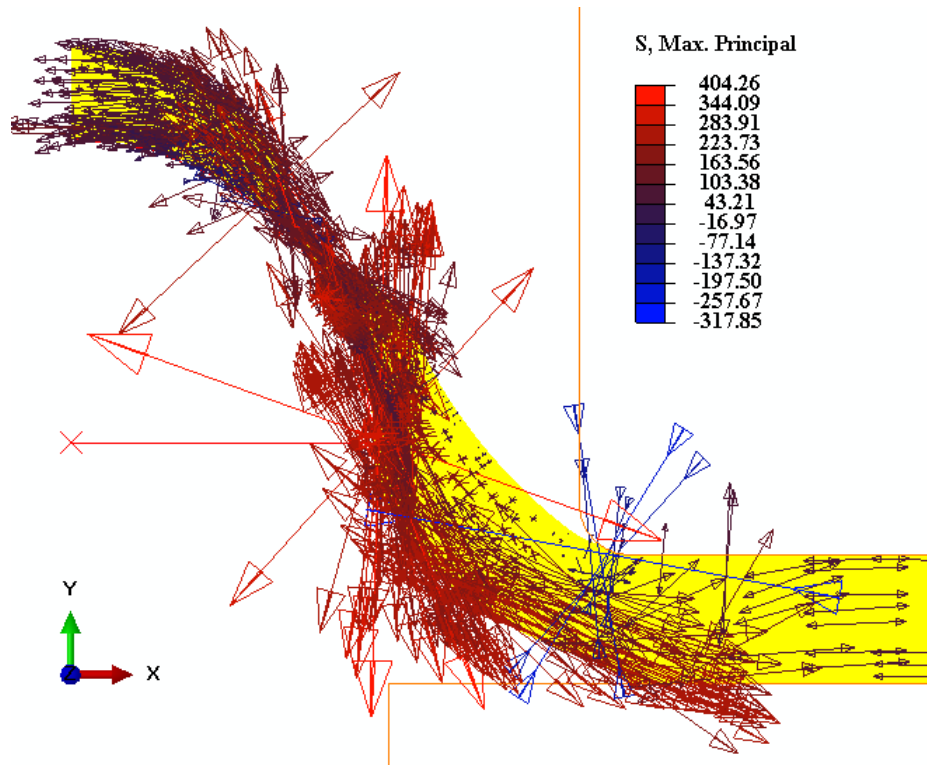


Fig 4.42 Symbol plot of Maximum principal stress.

Thus, besides obtaining the rupture data from SPC tests and correlation of SPC results with uniaxial creep results, the SPC deformation behaviour and mechanism of 316L(N) SS was investigated. The experience gained from above studies using ABI and SPC testing provides confidence to apply those techniques to further investigations such as optimisation of nitrogen content in 316LN SS and localised characterisation across 316LN SS weld joint, as discussed in the subsequent chapters.

CHAPTER 5

APPLICATION-I

Effect of Nitrogen on Tensile and Creep Behaviour of 316LN ss

**EFFECT OF NITROGEN CONTENT ON TENSILE AND CREEP BEHAVIOUR
OF 316LN SS**

The application of ABI and SPC techniques to evaluate the tensile and creep behaviour of heat resistant alloys under development is beneficial because (a) the limited volume of testing material required from each heat under development leads to considerable savings in cost, time and efforts during the production stage; (b) Multiple iterations can be readily carried out and (c) SPC test duration is generally short thus enabling quick screening of materials.

In this chapter, it has been attempted to demonstrate the feasibility of application of ABI and SPC techniques to fix the chemical composition of an alloy under development. The influence of nitrogen content on the tensile and creep properties of 316LN SS as implied from ABI and SPC tests are discussed.

5.1 Effect of nitrogen on tensile properties of 316LN SS using ABI technique

ABI technique has been used to estimate the effect of nitrogen on the tensile properties of 316LN SS. ABI tests were conducted on 316LN SS containing 0.07, 0.11, 0.14 and 0.22 wt.% nitrogen at several temperatures in the range 298 K- 973 K. These four heats are respectively designated as 7N, 11N, 14N and 22N for discussion purpose.

The load-depth of indentation curves obtained for the four heats at 723 K are typically compared in Fig. 5.1. The maximum depth of indentation was kept as the same in all the tests. The load required to cause the same depth of indentation increased with increase in nitrogen content. The load-depth of indentation data obtained for 7N, 11N, 14N and 22N steels were analysed using the procedures explained in Chapter 3.

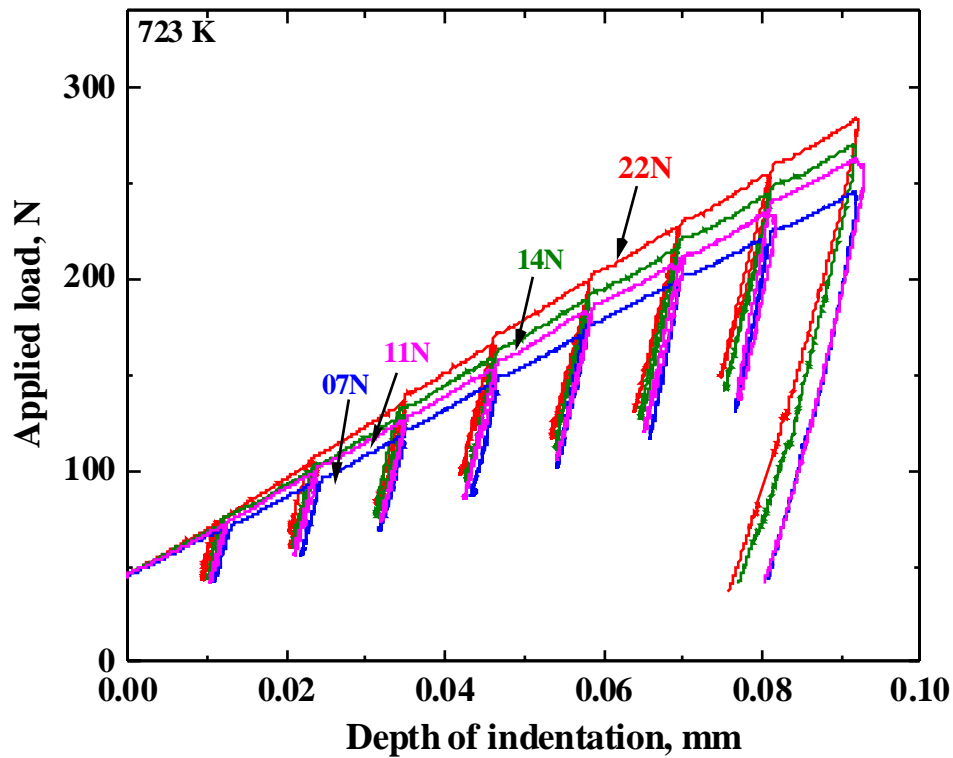
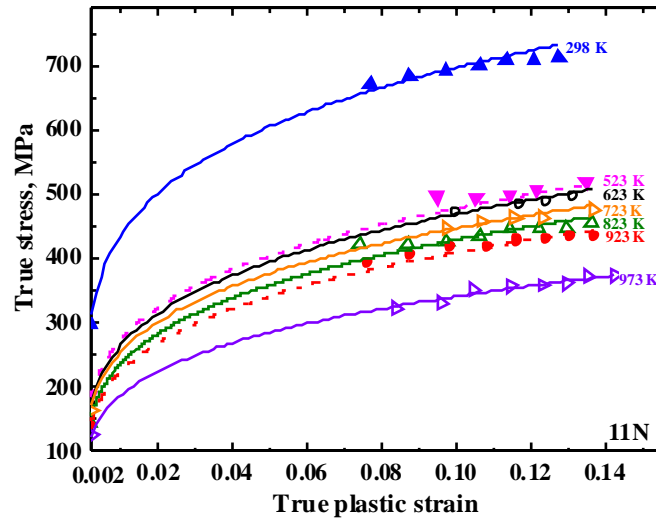
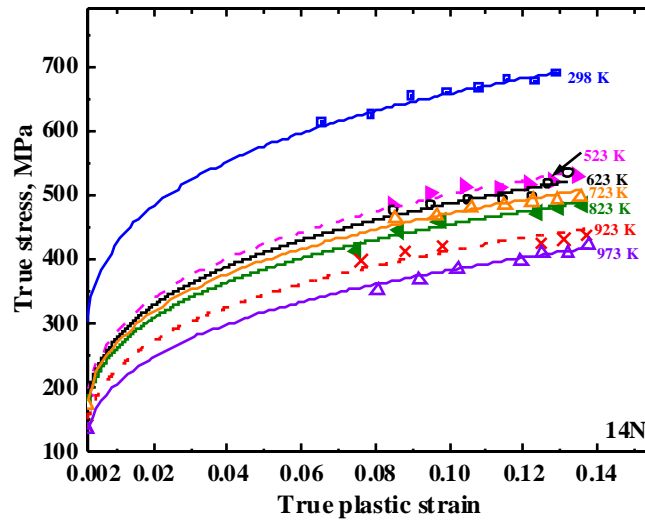


Fig. 5.1 Effect of nitrogen on load-depth of indentation curves for 316LN SS at 723 K.

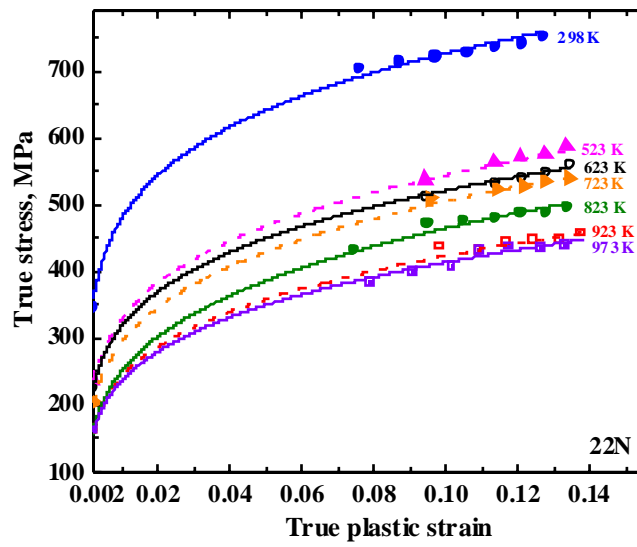
The value of the parameter α_m was respectively taken as 1.25 and 0.9 for analysing room temperature and higher temperature tests, as discussed in Section 3.1. Similarly, the same values of material yield slope ($\beta=0.256$) and yield offset constant $B=-105$ MPa were used in the analyses of ABI data obtained for all the four heats and at all the temperatures. The effect of test temperature on true stress-true plastic strain curves for 11N, 14N and 22N steels are shown respectively in Figs. 5.2(a), (b) and (c). The flow curves obtained for 7N steel are already shown in Chapter 3. In all cases, the true stress corresponding to any true plastic strain decreased with increase in temperature. The flow curves obtained for the various heats are compared typically at 973 K in Fig. 5.3. For the same true plastic strain, the true stress of 316LN SS increased with increase in nitrogen content. As the flow curves follow Holloman's equation (Eqn. 3.3.1), the strength coefficient and strain hardening exponent can be determined from the power-law fit on flow curves.



(a)



(b)



(c)

Fig. 5.2 Flow curves obtained for (a) 11N (b) 14N and (c) 22N steels.

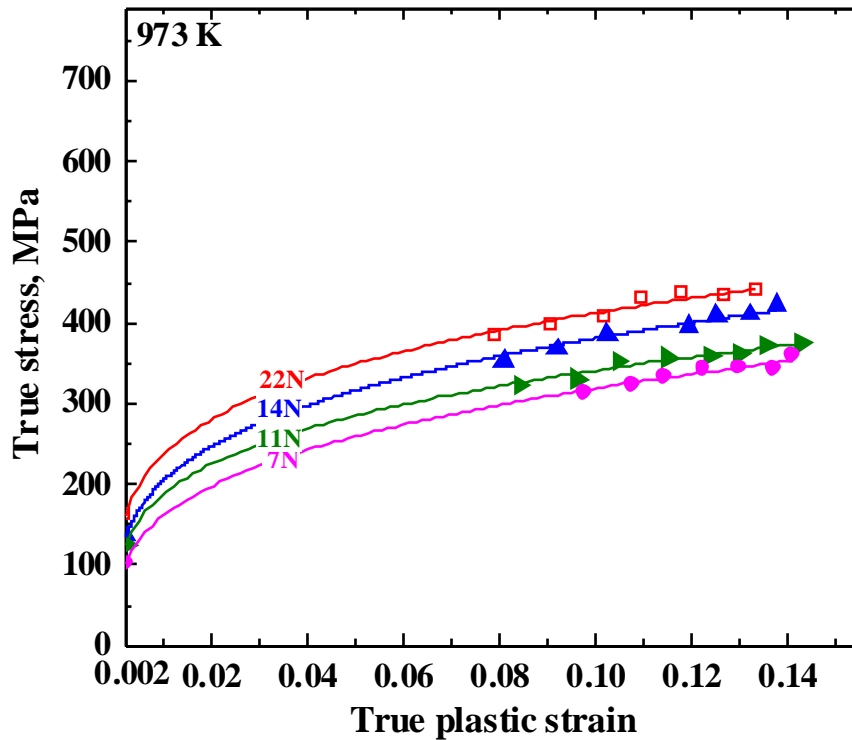


Fig. 5.3 Typical comparison of flow curves obtained for various heats at 973 K.

The variations of strain hardening exponent at various temperatures are shown as the function of nitrogen content in Fig. 5.4. In general, the strain hardening exponent increased with increase in temperature and nitrogen content has significant influence on it. At room temperature, there is not much influence on nitrogen content on strain hardening exponent. But as the temperature increases, the strain hardening exponent was found to decrease significantly with increase in nitrogen content.

The strength coefficient increased with increase in nitrogen content at all temperatures (Fig. 5.5), the effect of which was more predominant at lower temperature. The addition of nitrogen generally decreases the ductility of 316LN SS. Nitrogen introduces strong elastic distortions in the crystal lattice and also increases the internal friction that makes the movement of dislocations through the lattice more difficult ^[114]. The increase in strength coefficient and decrease in strain hardening exponent implied the corresponding decrease in rate of work hardening of 316LN SS, with increase in nitrogen content.

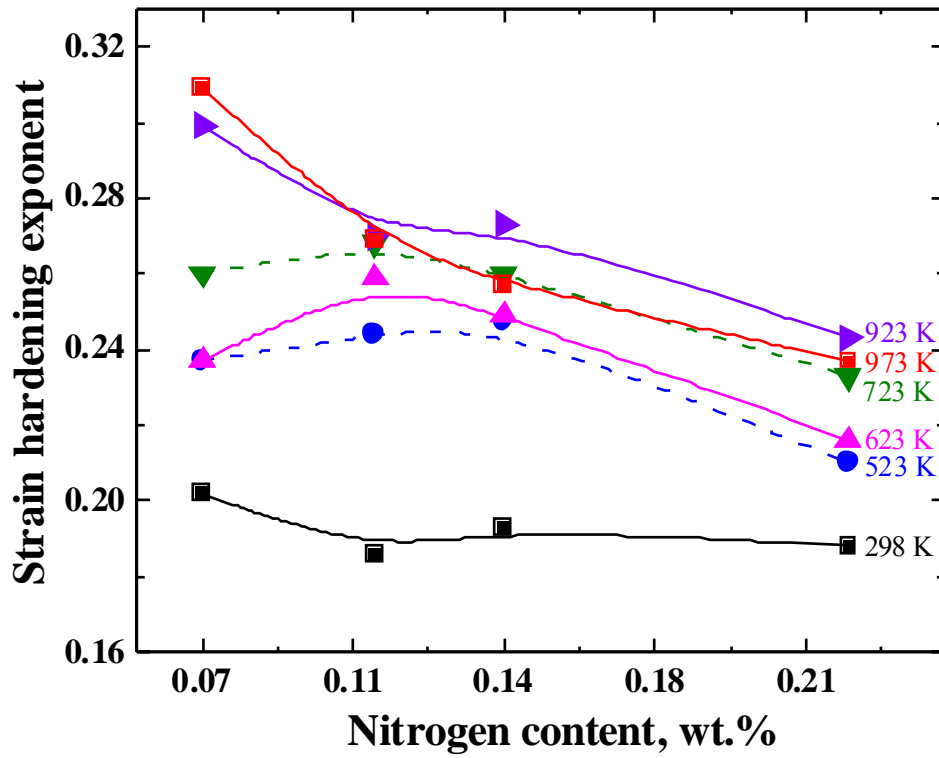


Fig. 5.4 Strain hardening exponent at various temperatures as function of nitrogen content.

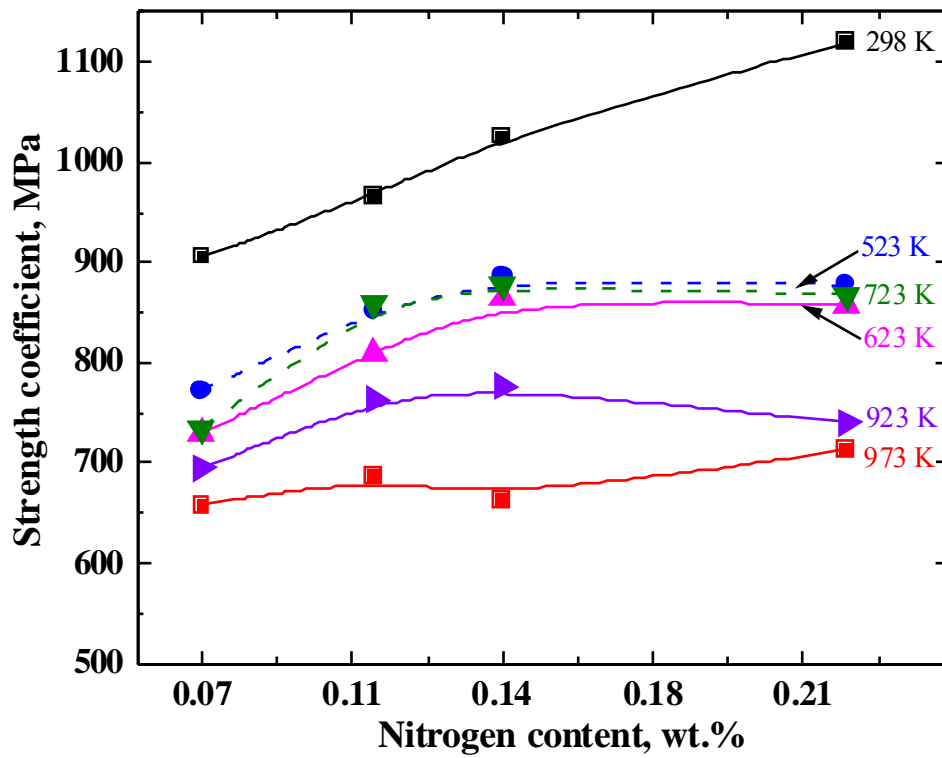


Fig. 5.5 Strength coefficient at various temperatures as function of nitrogen content.

The yield stress (YS) and ultimate tensile strength (UTS) values were determined at all temperatures for 316LN SS with various nitrogen content, based on the procedures discussed in Section 3.1 and 3.3. The YS values obtained for the four heats at all investigated temperatures are shown in Fig. 5.6. In general, the trend curves for yield stress with temperature were higher with increase in nitrogen content, although scatter in the trend was observed at some temperatures.

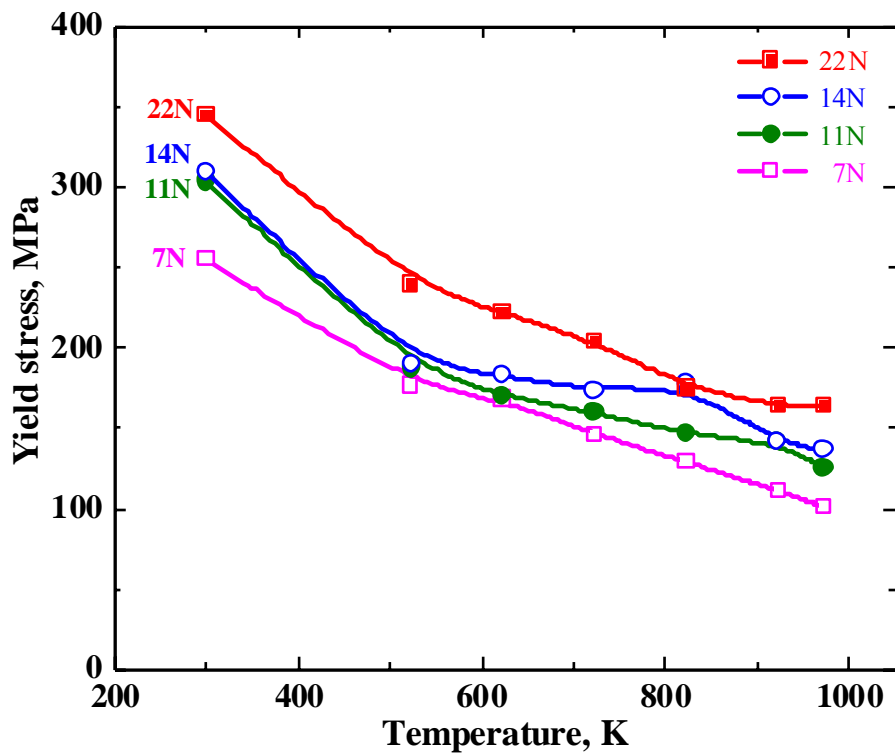


Fig. 5.6 Influence of nitrogen content on yield stress at different temperatures.

Similarly, the ultimate tensile strength (UTS) obtained for 316LN SS increased with increase in nitrogen content at all the temperatures under investigation, as shown in Fig. 5.7. Several reasons have been proposed for increase in strength due to addition of nitrogen. Nitrogen is an interstitial solid solution strengthener occupying octahedral sites in FCC lattice. The crystal structure of steels containing nitrogen shows an increase in concentration of free electrons leading to promotion of metallic interatomic bonding. The concentration of free

electrons in nitrogen containing austenitic SS is about one order of magnitude higher than the austenitic steels containing same amount of carbon ^[177]. Stacking fault energy (SFE) is an important parameter influencing deformation behaviour and is determined by the fraction of free electrons in the alloy. Higher the free electrons, lower is the SFE ^[178]. Nitrogen makes electron exchange between atoms less directional and distribution of electrons in the crystal structure more homogenous. Consequently, dislocation glide takes place without weakening of inter-atomic bonds.

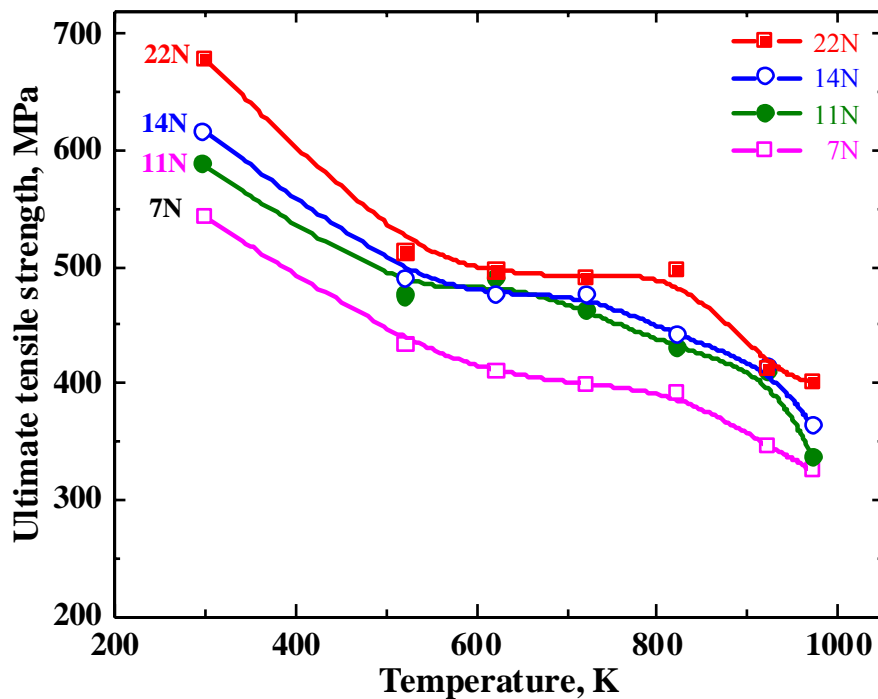
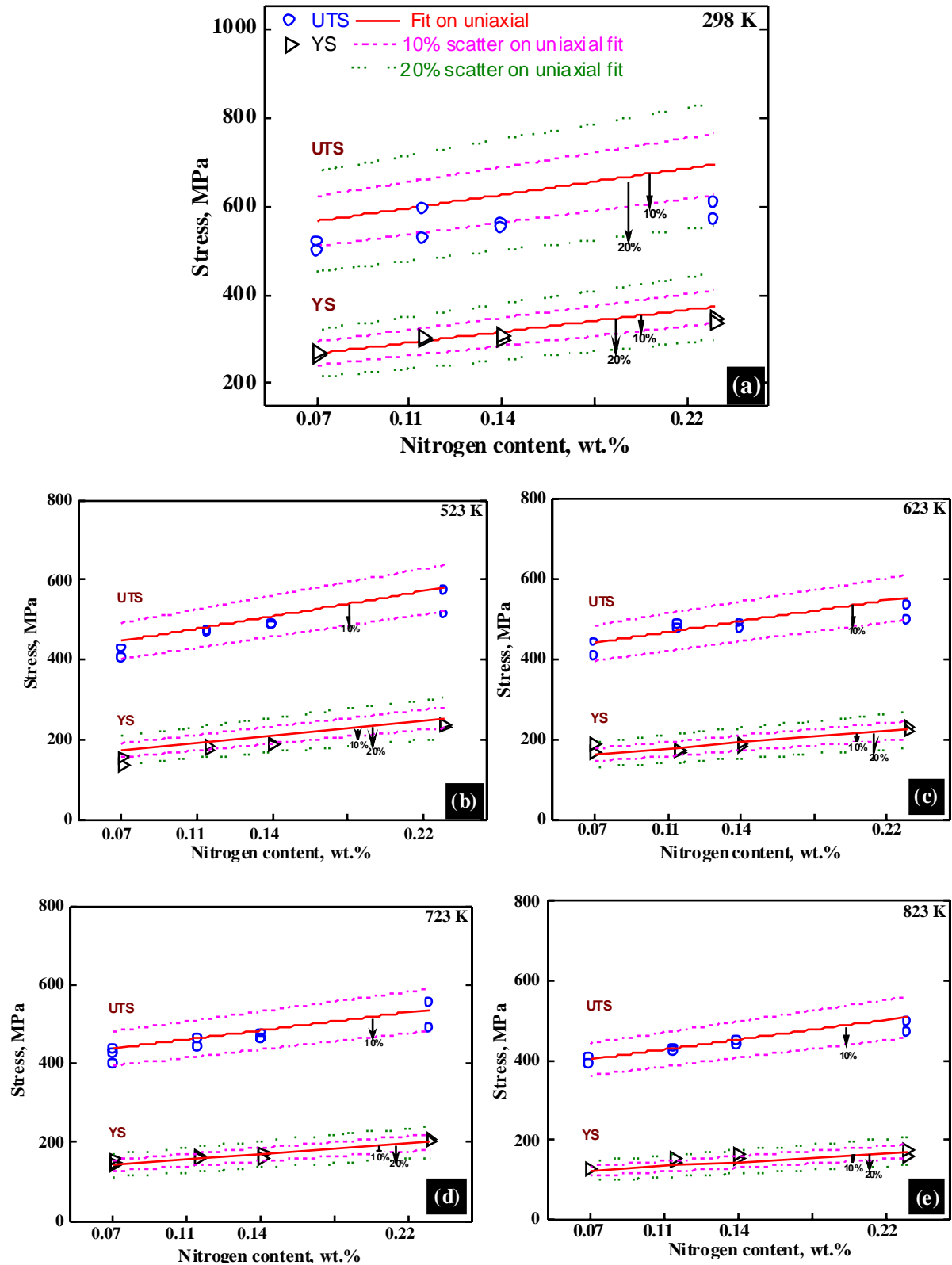


Fig. 5.7 Influence of nitrogen content on UTS at different temperatures.

The YS and UTS obtained from ABI tests were compared with corresponding uniaxial tensile test values at various temperatures in Figs. 5.8 (a)-(g). The increasing linear trend curves for both YS and UTS with nitrogen content as implied from uniaxial tensile tests^[112] are shown as solid lines. The ABI test values are scattered as symbols around the linear fit on uniaxial data at all temperatures. In general, it can be observed that the ABI test results were closer to tensile test results at all temperatures. In order to quantify the extent of scatter, upper and

lower scatter bands representing 10% and 20 % scatter are added to conventional test trend curves in the same figure. All ABI values were found to fall almost within 10% scatter limits on tensile test values.



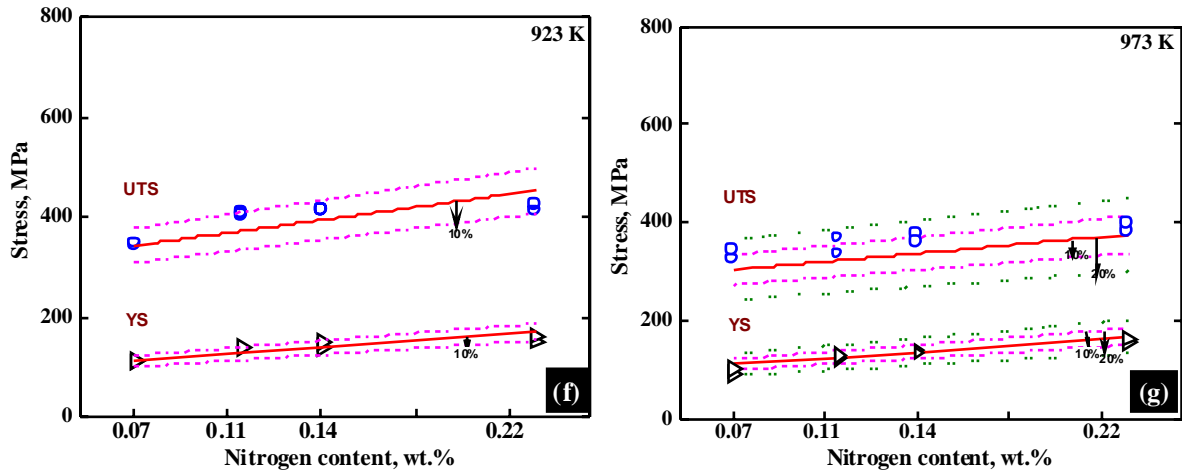


Fig. 5.8 YS and UTS plotted as a function of nitrogen content at (a) 298 K (b) 523 K (c) 623 K (d) 723 K (e) 823 K (f) 923 K and (g) 973 K.

ABI results implied increasing trends of YS and UTS with increase in nitrogen content, similar to that observed from uniaxial tensile tests. Thus ABI technique can be applied to study the influence of alloying element on the tensile properties of heat resistant steel alloys.

5.2 Effect of nitrogen on creep properties of 316LN SS using SPC technique

Small Punch Creep (SPC) technique has been used to estimate the influence of nitrogen content on the creep deformation and rupture behaviour of 316LN SS.

5.2.1 Rupture life and deflection rate

The SPC curves obtained for the heats 11N, 14N and 22N are shown in Figs. 5.9, 5.10 and 5.11 respectively. The SPC curves for 7N steel are shown in Fig 4.1. In all cases, three distinct stages of creep were observed in SPC curves. The rupture life increased and steady state deflection rate decreased with decrease in applied load.

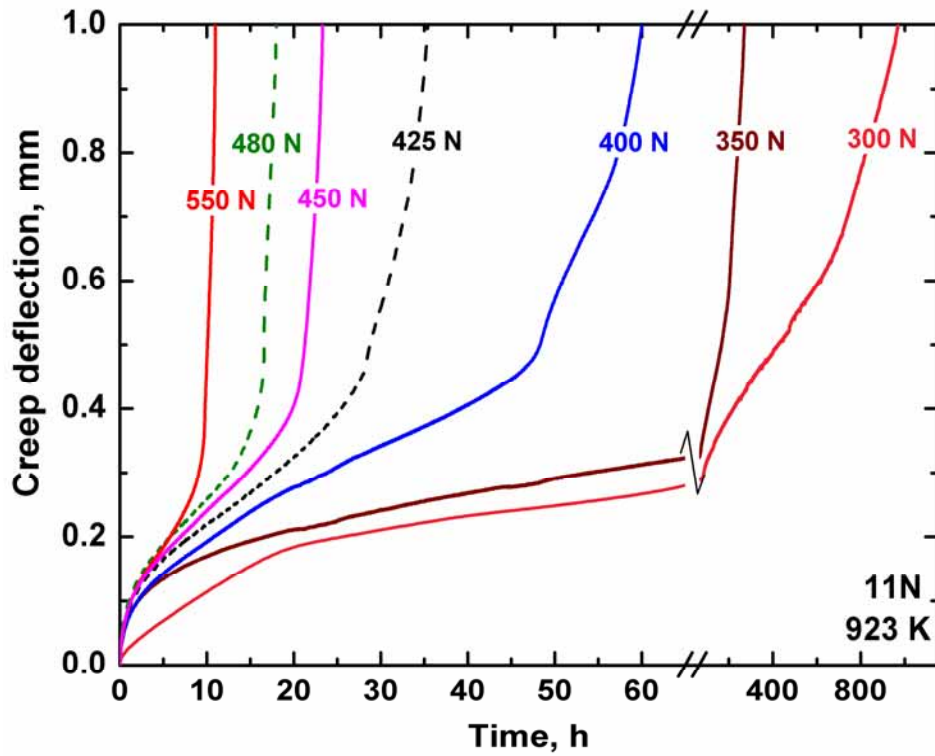


Fig. 5.9 SPC curves obtained for 11N steel at 923 K.

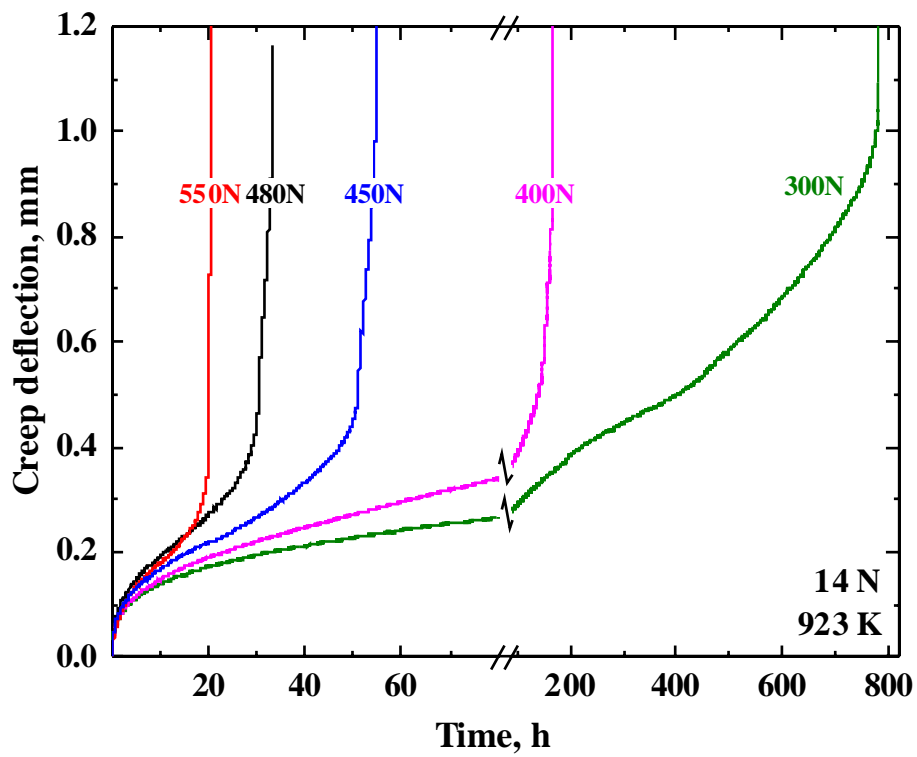


Fig. 5.10 SPC curves obtained for 14N steel at 923 K.

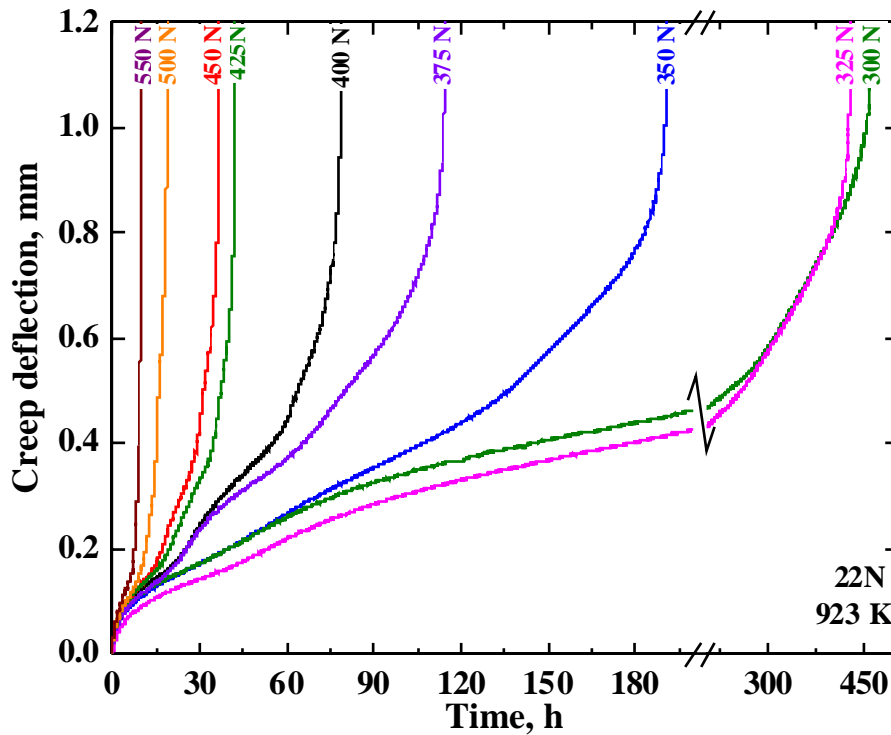


Fig. 5.11 SPC curves obtained for 22N steel at 923 K.

The influences of nitrogen content on SPC curves at various common loads are shown in Figs. 5.12 (a)-(d). In general, the deflection at the same duration was observed to be reduced considerably due to addition of nitrogen content. However, it was very difficult to quickly arrive at any conclusion by referring these curves; since the influence of increase in nitrogen content was not found to be consistent at all loads. This may be attributed to scatter inevitably experienced in any small specimen testing technique because of localised material testing. However, such a scatter can be averaged out by studying the trend curve as a whole rather than focussing on individual data points. The isothermal rupture life curves at 923 K, plotted in Fig. 5.13, for various nitrogen content clearly implied an increase in rupture life with increase in nitrogen content clearly upto 14N steel. The rupture curve for 22N steel crossed over the curves for 7N and 11N and was always below the 14N curve. Thus 14N steel was found to have better creep strength than the other investigated steels.

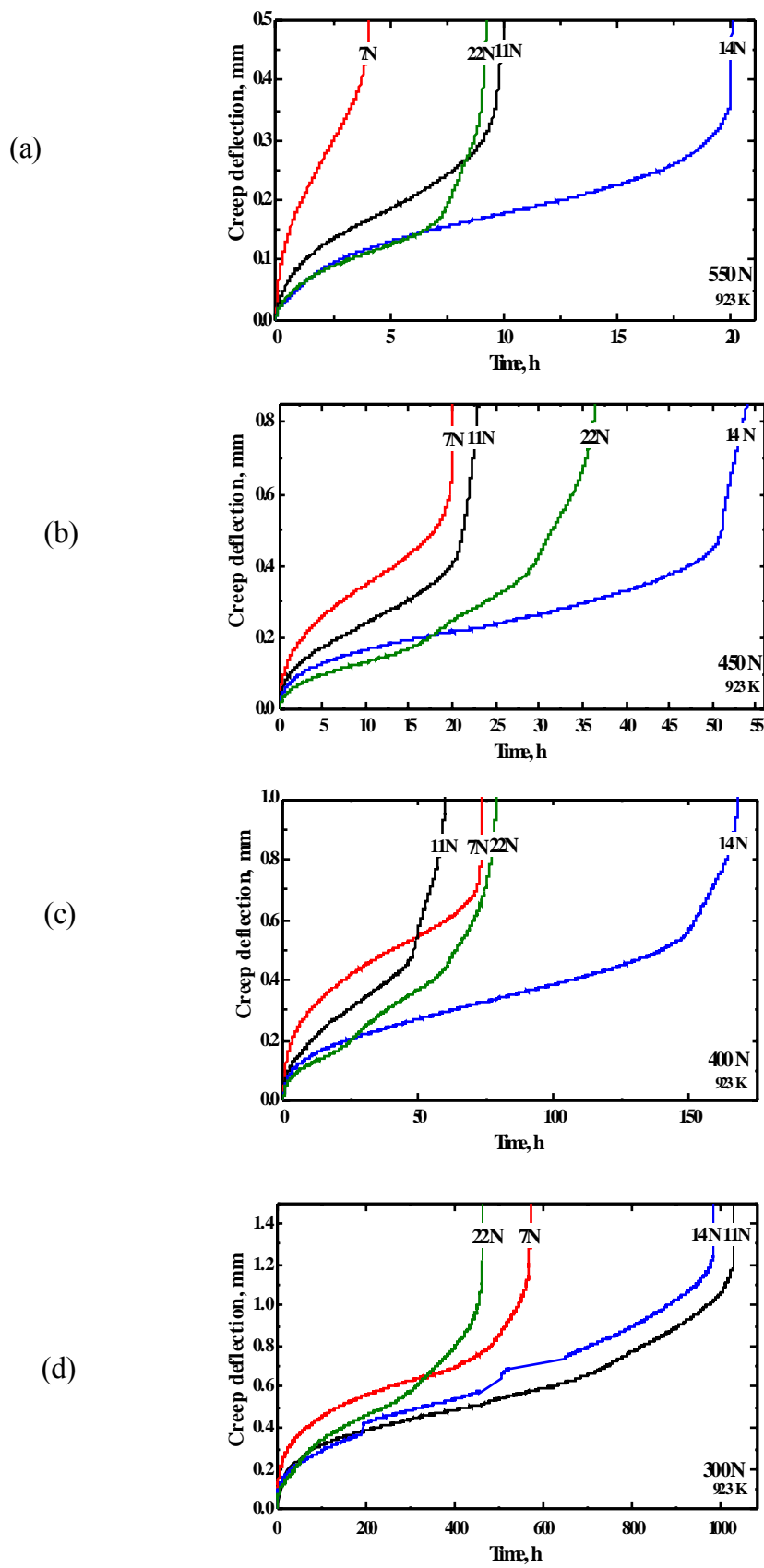


Fig 5.12 Influence of nitrogen content on SPC curves for 316LN SS at (a) 550 N (b) 450 N (c) 400 N and (d) 300 N.

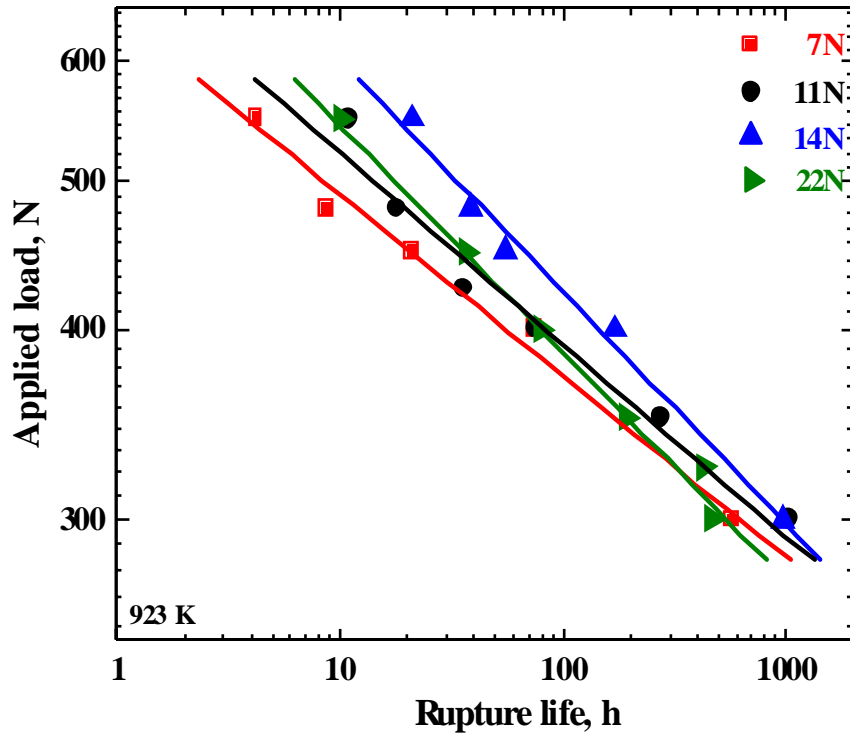


Fig. 5.13 Isothermal rupture life curves determined for various nitrogen content.

The above observation was also reflected in the variations of steady state deflection rate curves with applied load, shown in Fig. 5.14. The steady state deflection rate increased with increase in applied load for all the heats. For the same load, the steady state deflection rate generally decreased by increasing nitrogen content upto 0.14 wt.%. In all cases, 14N steel seemed to be the lowest among the investigated steels. At lower loads, 22N steel showed higher value in comparison to 7N and 11N steel and a crossover was seen at higher loads. It may be noted that influence of nitrogen content on both rupture life and steady state deflection rate was more pronounced at higher loads. The values are closer enough at lower loads with relatively longer test duration.

In order to get better insight, the rupture lives and steady state deflection rate are re-plotted as a function of nitrogen content in Figs. 5.15 and 5.16. Both the plots revealed an increasing trend with nitrogen content upto 0.14 wt.%, after which the trend was reversed.

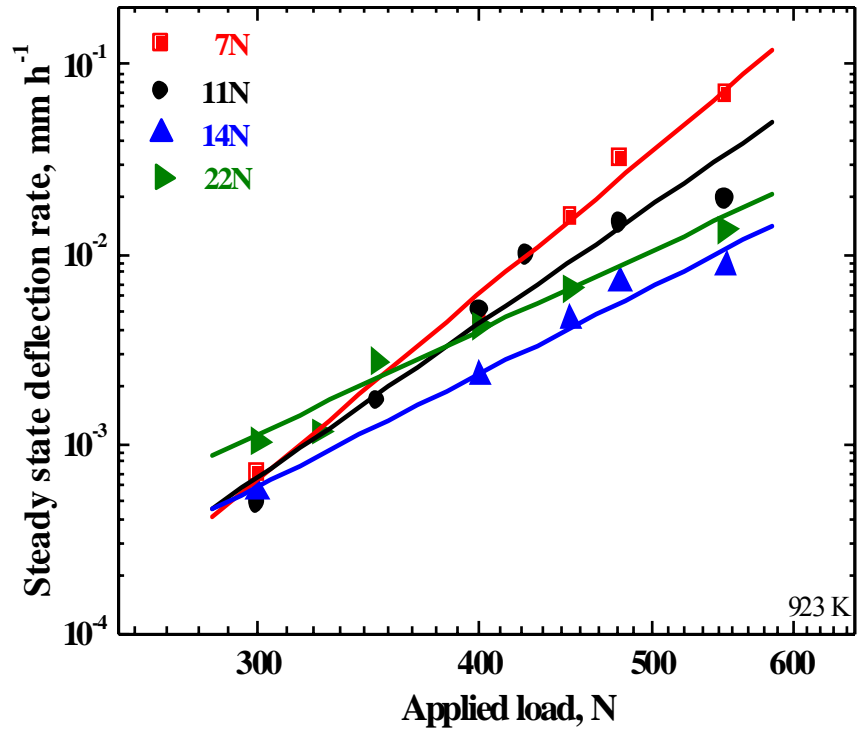


Fig 5.14 Dependence of steady state deflection rate on applied load shown for various nitrogen content.

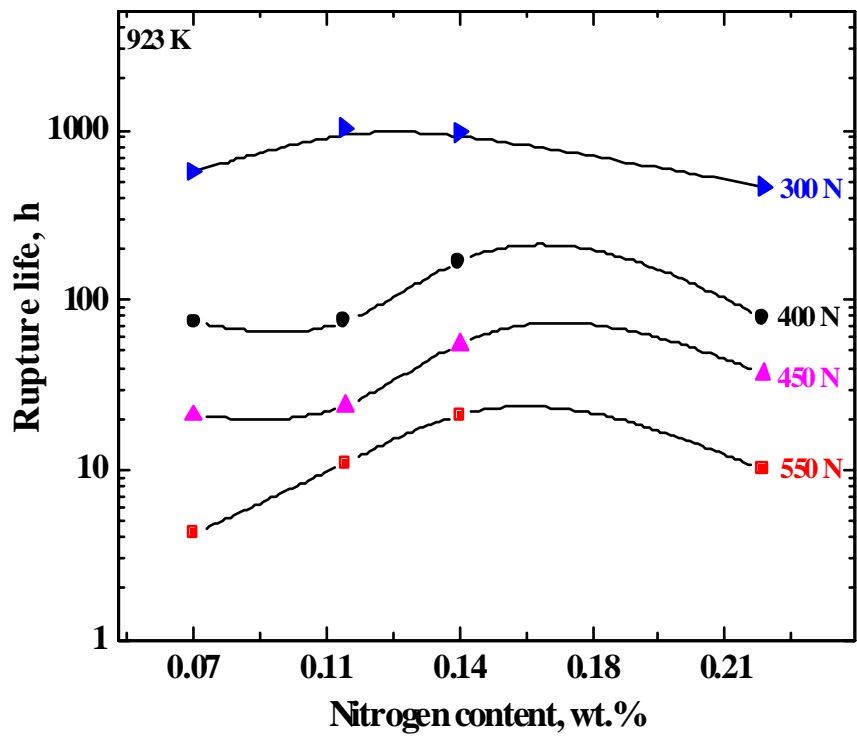


Fig 5.15 Rupture lives plotted as function of nitrogen content.

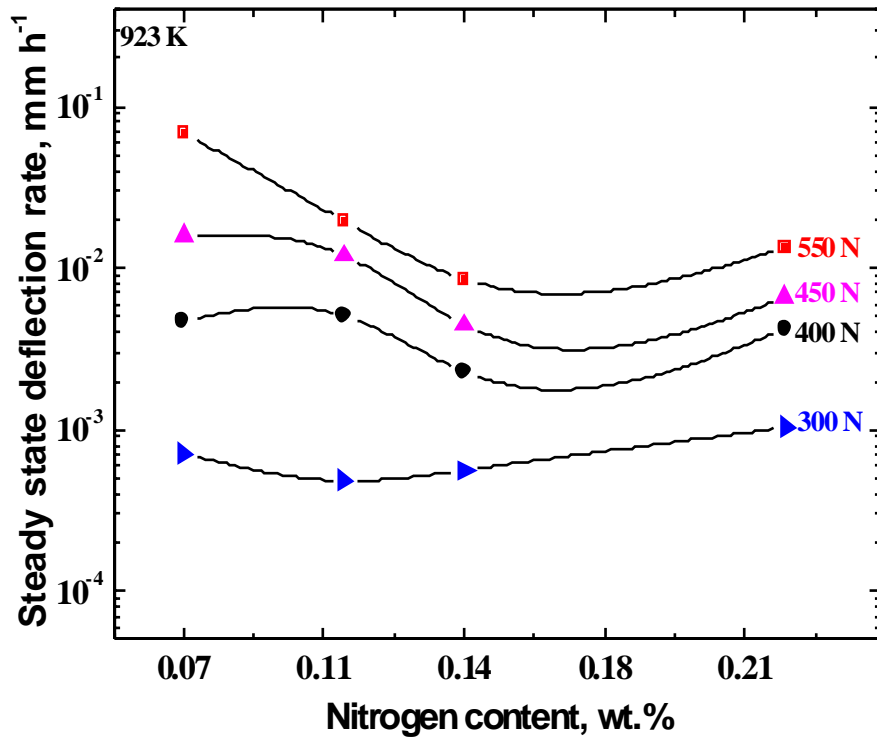
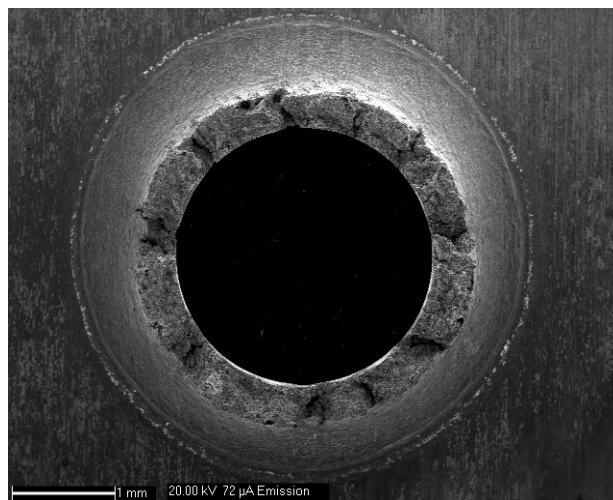
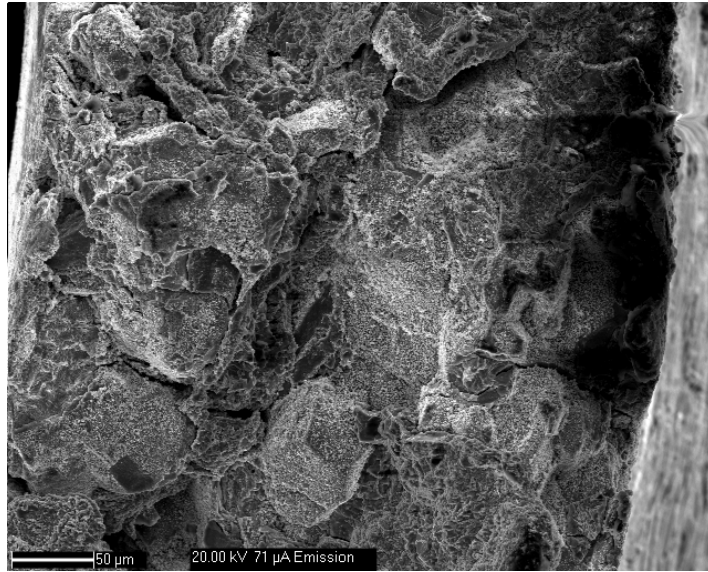


Fig 5.16 Steady state deflection rate plotted as function of nitrogen content.

The SEM fractographs of the specimens made of 11N and 14N steel are shown in Figs. 5.17 and 5.18. The ruptured surface exhibited lot of intergranular cracks though ductile features were scarcely observed owing to the biaxial state of stress prevailing during SPC deformation.



(a)



(b)

Fig 5.17 SEM fractograph of SPC specimen of 11N steel tested at 923 K taken at (a) lower and (b) higher magnification.

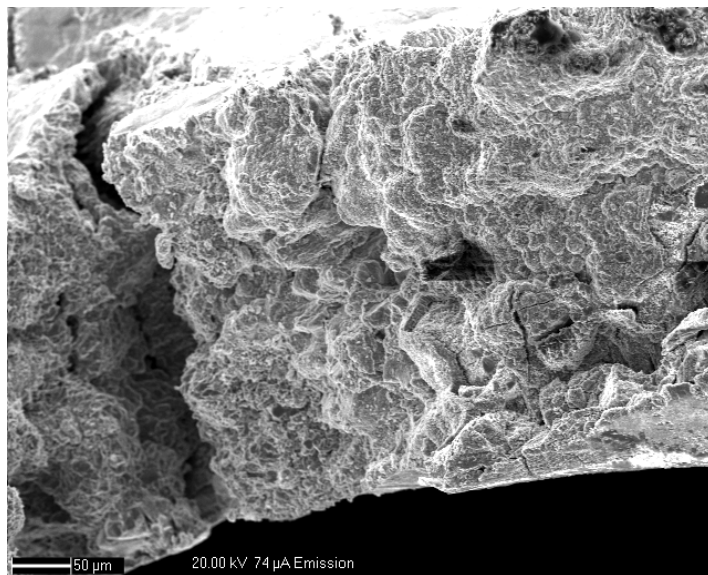


Fig 5.18 Fractured surface of 14N steel specimen tested at 923 K.

Decrease in stacking fault with increase in nitrogen content is reported for 316LN SS ^[112]. The increase in creep strength is generally attributed to solid solution strengthening decrease in stacking fault energy, precipitation strengthening etc. with the addition of nitrogen in

316LN SS. The addition of nitrogen delays the onset of precipitation of any phase that has lower solubility for it, till all the nitrogen is removed as precipitate. Nitrogen retards carbide nucleation and shifts the precipitation of $M_{23}C_6$ carbides to longer ageing times. Nitrogen is known to delay the rate of coalescence of $M_{23}C_6$ carbides in austenitic steels ^[179]. Nitrogen in $M_{23}C_6$ decreases the mismatch between precipitate and austenite matrix thereby reducing the interfacial energy and inhibits precipitate coarsening.

However, it was revealed that 22N steel with highest creep strength among the investigated steels during uniaxial creep test, was behaving differently under biaxial state of stress. The effect of state of stress can be further explained by considering the case of multi-axial creep studies on the same material. It was observed from the creep tests on V-notched specimens made of the same four grades of 316LN SS that the rupture life showed a peak value at 0.14 wt.% nitrogen content ^[180]. The ratio of rupture life of plain to notched specimen decreased with increase in the nitrogen content implying that the notch strengthening effect decreased significantly at high nitrogen levels.

Thus the creep studies on both notched specimens (representing triaxial state of stress) and SPC specimen (representing biaxial state of stress) revealed that the creep rupture strength of 22N steel was lower than that of 14N steel. It can be mentioned here that ranking a material based on uniaxial creep strength alone is not sufficient. Thus ABI and SPC studies performed under multiaxial state of stress are necessary to understand the complete creep behaviour of the material.

5.2.2 Effect of nitrogen on transient SPC deformation

The SPC deformation behaviour of 316LN SS with different nitrogen content have been analysed in the framework of first order kinetics approach according to Eqn. 4.2.4, proposed for SPC deflection, $\delta = \delta_0 + \delta_T (1 - e^{-kt}) + \dot{\delta}_s t + \delta_3 e^{[\varphi(t-t_r)]}$. The rate of exhaustion of transient

creep defined by Eqn. 4.2.10, was calculated graphically at each load for 7N, 11N, 14N and 22N steels.

The rate of exhaustion of transient creep was plotted against steady state deflection rate for all the four heats in Fig. 5.19. All the data points were found to be within a narrow scatter band implying that the relationship between rate of exhaustion of transient creep and steady state deflection rate follows a common trend irrespective of nitrogen content as,

$$\kappa. \dot{\delta}_s^{-1.1} = 117 \quad (5.2.1)$$

The rate of exhaustion of transient creep was closely related to steady state deflection rate and hence it is even possible to obtain a rough estimate of the time to rupture based on rate of exhaustion of transient creep.

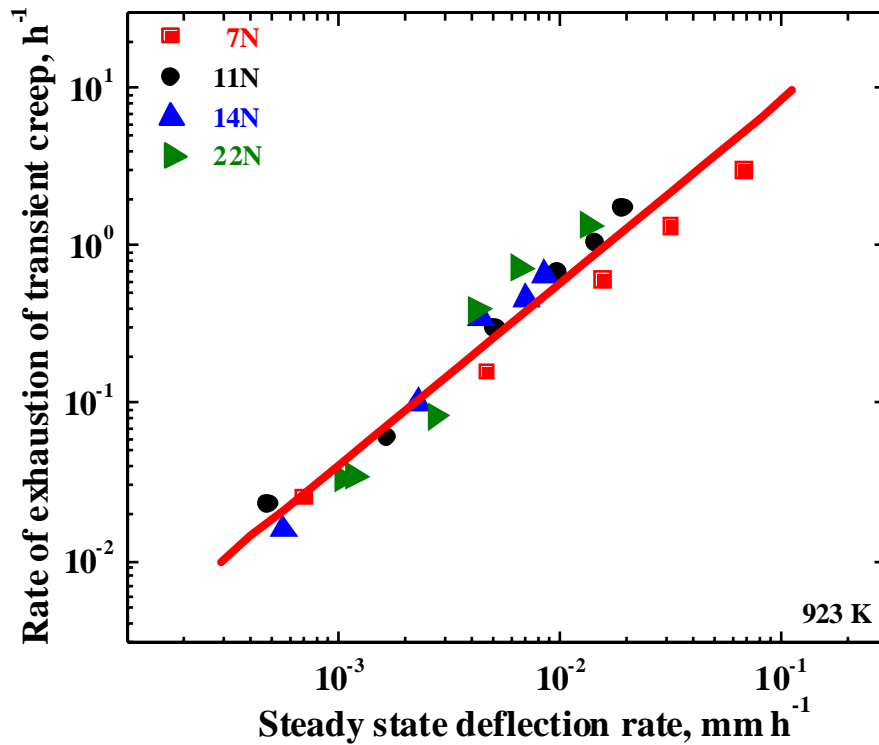


Fig. 5.19 Relationship between rate of exhaustion of transient creep and steady state deflection rate for the four heats.

The relationship between κ and t_s was obtained for 316LN SS without having much effect of nitrogen content as (Fig. 5.20),

$$\kappa.t_s^{0.93} = 4.14 \quad (5.2.2)$$

The time to attain steady state deflection rate increased with decrease in rate of exhaustion of transient creep for all the heats.

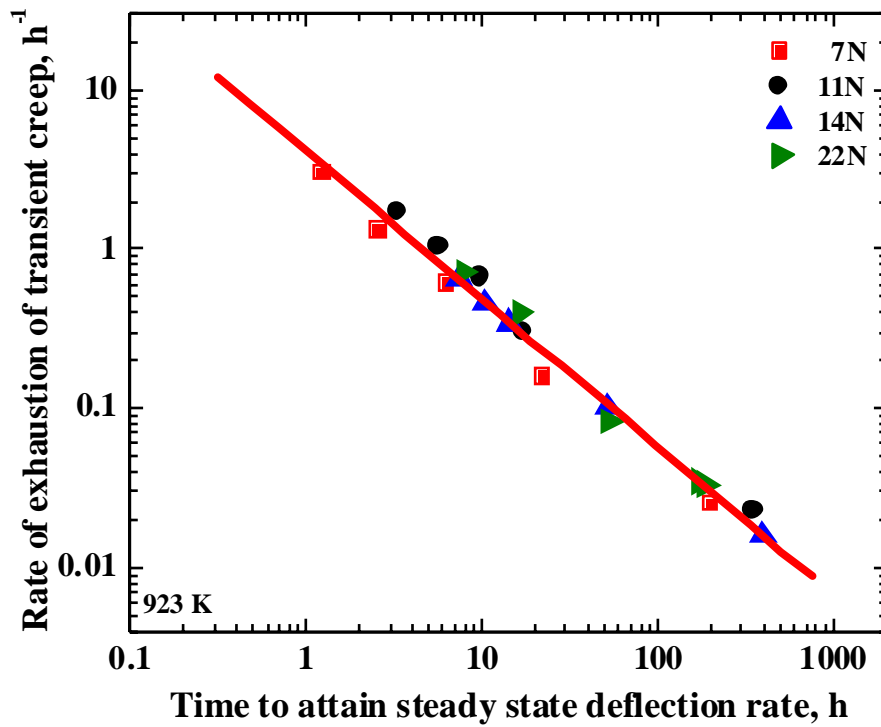


Fig. 5.20 Relationship between rate of exhaustion of transient creep and time to attain steady state deflection rate, for the four heats.

The initial creep deflection rate ($\dot{\delta}_i = \kappa. \delta_T + \dot{\delta}_s$) was related to steady state deflection rate, as shown in Fig. 5.21 as,

$$\dot{\delta}_i \dot{\delta}_s^{-0.89} = 4.94 \quad (5.2.3)$$

The initial creep deflection rate and steady state deflection rate also appeared to be independent of nitrogen content.

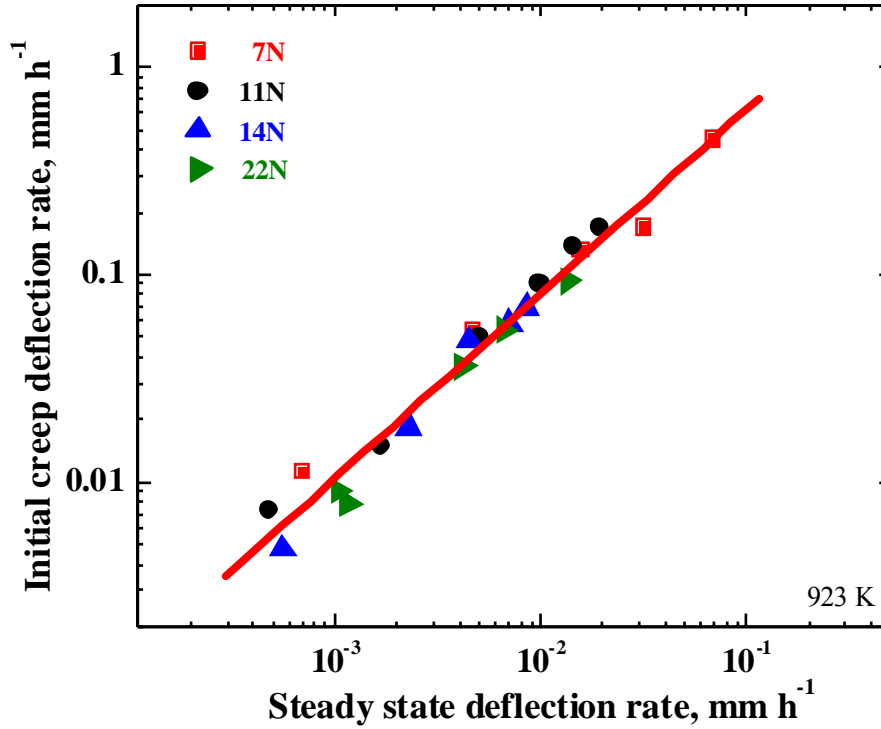


Fig. 5.21 Relationship between initial creep deflection rate and steady state deflection rate, for the four heats.

From the relationships inferred from Eqns. 5.2.1-5.2.3, among κ , t_s , $\dot{\delta}_s$ and $\dot{\delta}_i$, it can be concluded that first order reaction rate theory was prevalent in SPC deformation of 316LN SS with different nitrogen content, throughout the transient creep stage. Therefore it is possible to construct a master curve for transient creep deflection for all the four heats of 316LN SS (as discussed in Section 4.2.2). The master curve for transient creep deflection was obtained for all the four heats by plotting $(\delta - \delta_0)/\delta_T$ against $(\dot{\delta}_s t)/\delta_T$, as shown in Fig 5.22. It can be seen that the master curves for the various heats were found to overlap with one another.

The rate of exhaustion of transient creep was found to have significant impact on the rupture life, as shown in Fig 5.23. The rupture life increases with decrease in rate of exhaustion of transient creep, for all the investigated steels.

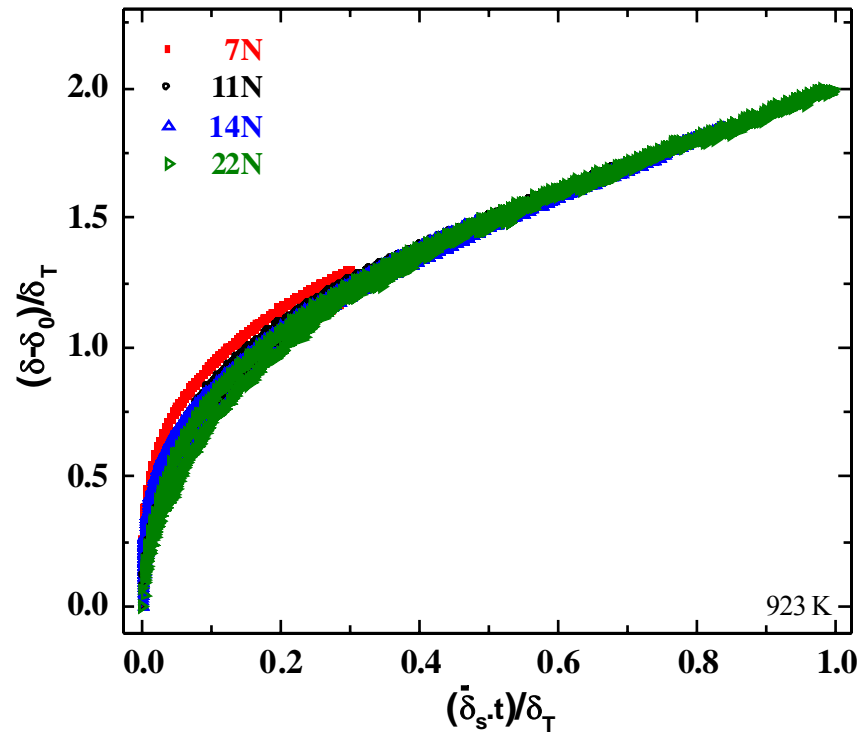


Fig 5.22 Master curves for transient creep deflection determined for four heats.

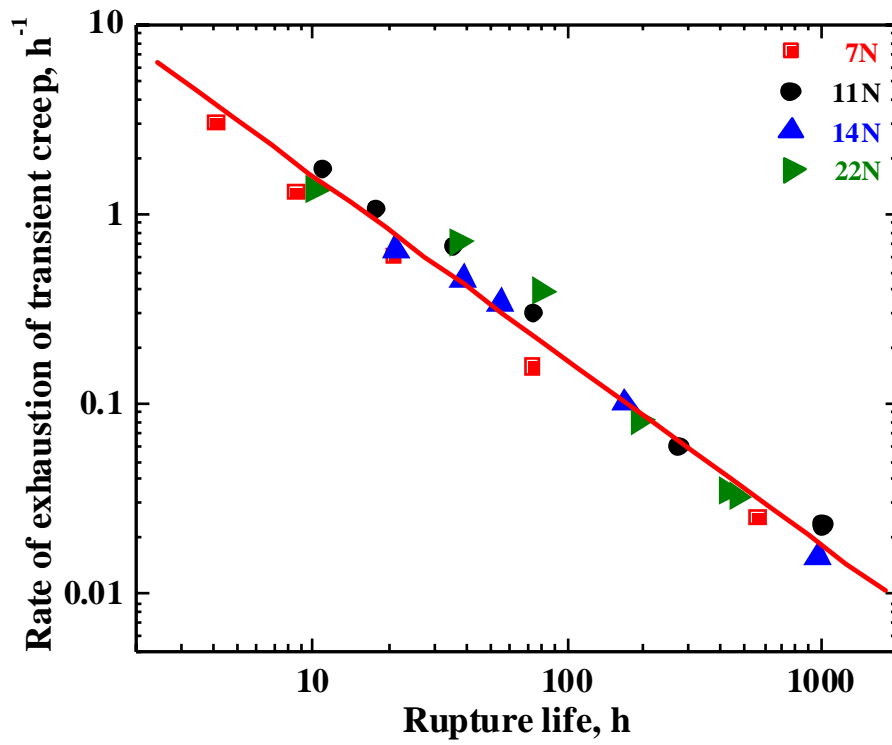


Fig 5.23 Estimation of rupture life based on rate of exhaustion of transient creep.

The relationships among the various parameters, as obtained above, seem to be independent of nitrogen content. The effect of nitrogen content is actually evident when the rate of exhaustion of transient creep is plotted against the applied load, as shown in Fig. 5.24. The rate of exhaustion of transient creep increased with increase in applied load for all the investigated steels. For the same load, 14N exhibited lowest rate of exhaustion of transient creep among the investigated steels.

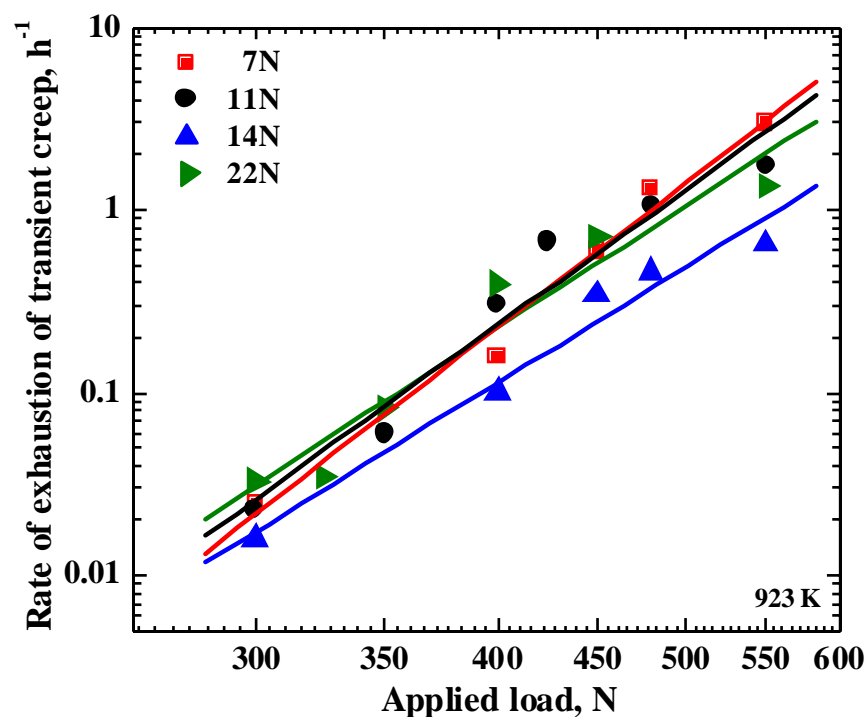


Fig. 5.24 Dependence of rate of exhaustion of transient creep on applied load.

Figure 5.25 is the cross-plot of the same figure where κ values are plotted as a function of nitrogen content for various loads on semi-log scale on vertical axis. The rate of exhaustion of transient creep showed a decreasing trend with clear dip at 0.14 wt.% nitrogen content after which the trend reversed.

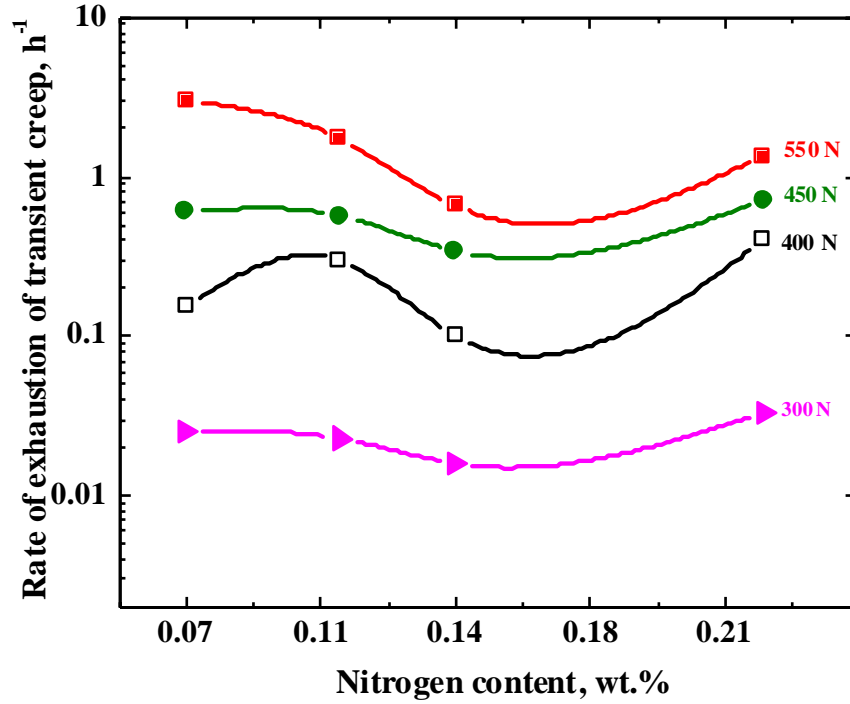


Fig 5.25 Rate of exhaustion of transient creep plotted as function of nitrogen content.

5.2.3 Effect of nitrogen on tertiary SPC behaviour

The rate of acceleration of tertiary creep (ϕ) was calculated at each load for 316LN SS with various nitrogen content, using Eqn. 4.2.14. The rate of acceleration of tertiary creep showed increasing trend with steady state deflection rate for all the four heats, as shown in Fig 5.26. The relationship between ϕ and steady state deflection rate seemed to be independent of nitrogen effect and is given as,

$$\phi \cdot \dot{\delta}_s^{-1.2} = 150 \quad (5.2.4)$$

The rate of acceleration of tertiary creep decreased with increase in tertiary life for all nitrogen content, as shown in Fig 5.27. The rate of acceleration of tertiary creep was related to tertiary life as,

$$\phi (t_r - t_{ot})^{1.08} = 12 \quad (5.2.5)$$

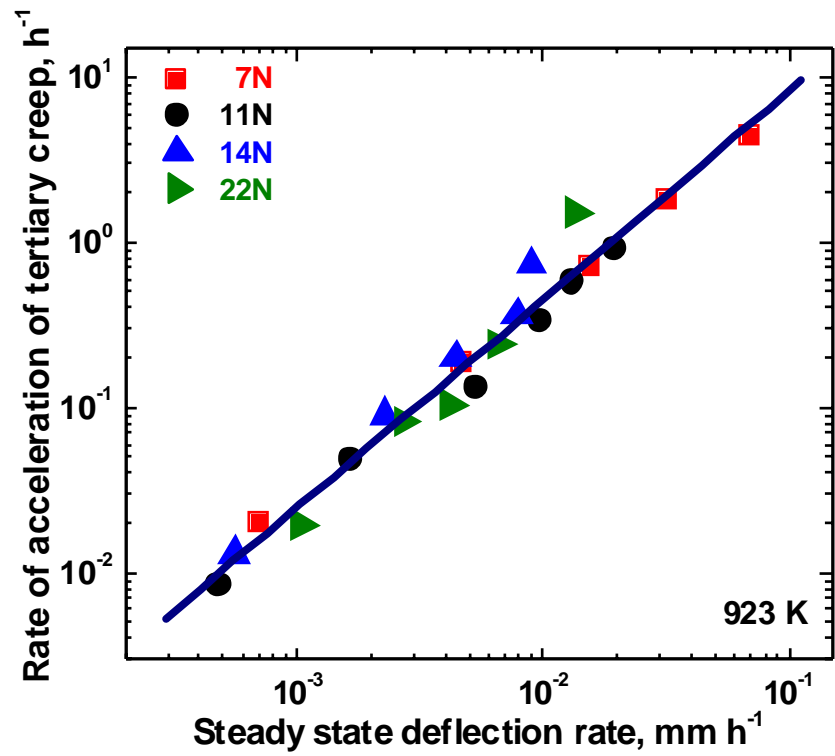


Fig. 5.26 Relationship between rate of acceleration of tertiary creep and steady state deflection rate.

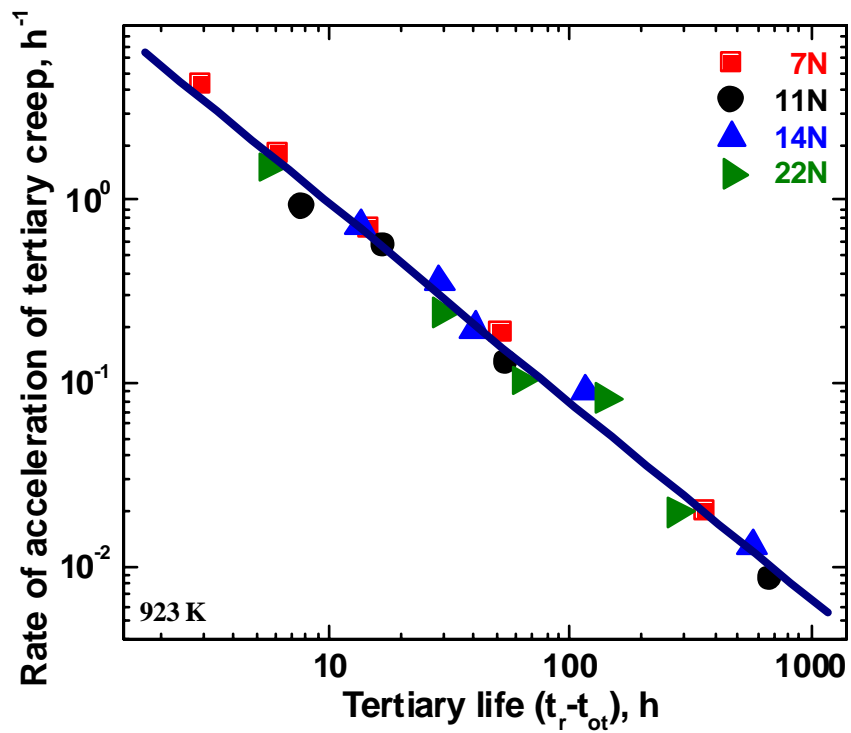


Fig. 5.27 Relationship between rate of acceleration of tertiary creep and tertiary life.

The final creep deflection rate was calculated for the various heats as discussed in section 3.3.2. The relationship between final creep deflection rate and steady state deflection (shown in Fig. 5.28) was commonly expressed for all nitrogen content as,

$$\dot{\delta}_f \dot{\delta}_s^{-1.18} = 89 \quad (5.2.6)$$

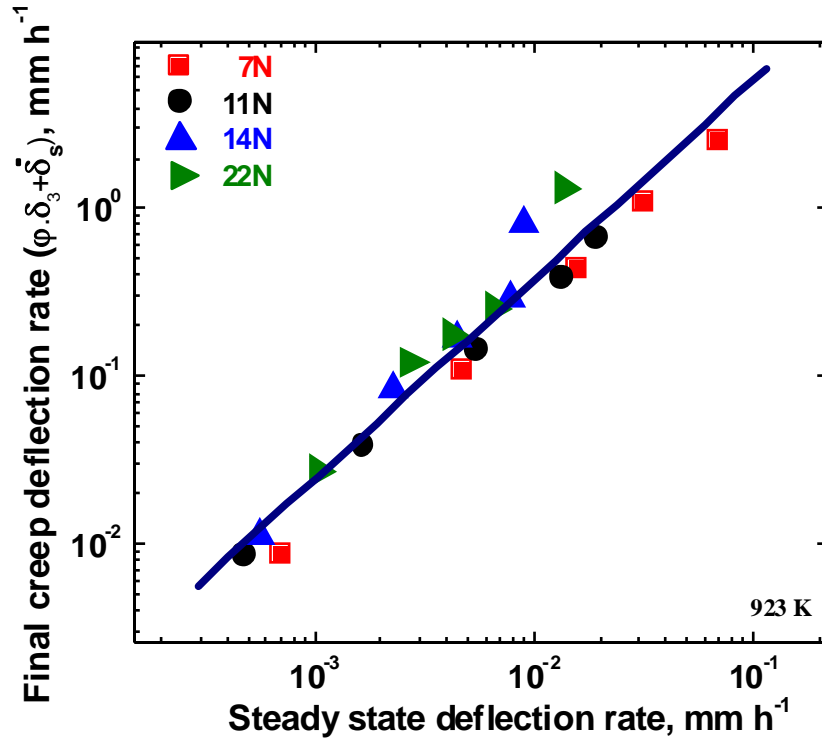


Fig. 5.28 Relationship between final creep deflection rate and steady state deflection rate.

It may be stated from the relationships determined from Eqns. 5.2.4-5.2.6 that the tertiary creep deformation also follows first order reaction rate theory in all the investigated steels. It was attempted to construct master curves for tertiary SPC deformation, as discussed in section 4.2.3. The master curves were derived for all the investigated steel by plotting $(\delta - \delta_0 - \delta_T)$ against $\dot{\delta}_s t$, as shown in Fig. 5.29. The master curves for tertiary creep deflection so determined for various nitrogen content seemed to overlap each other, as observed in case of transient creep deflection.

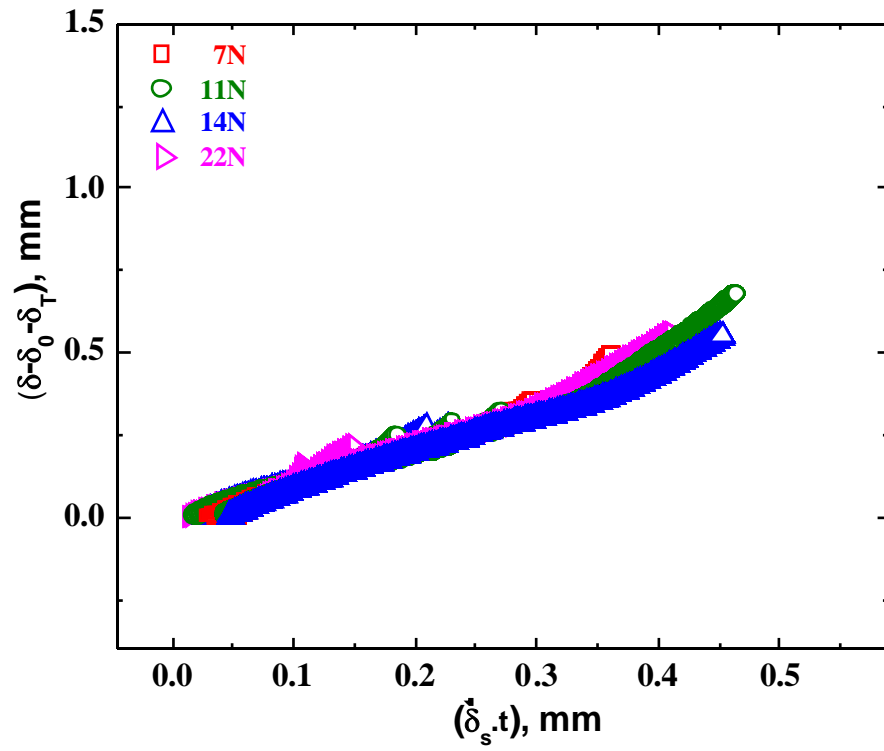


Fig. 5.29 Master curves for tertiary creep deflection.

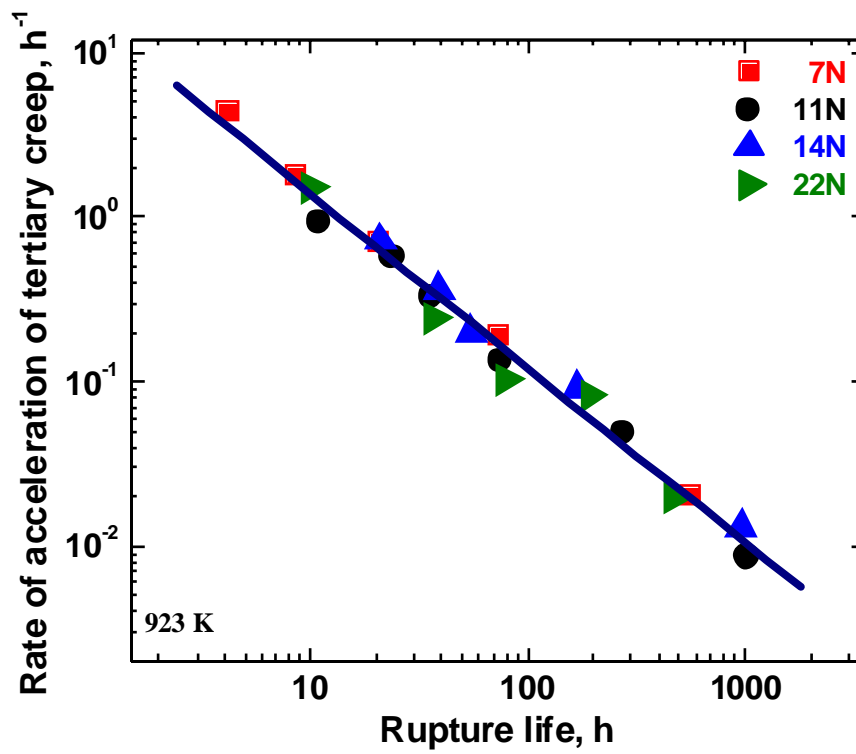


Fig. 5.30 Variation of rate of acceleration of tertiary creep with rupture life.

Figure 5.30 shows the variation of ϕ value with rupture life for all nitrogen content. The rupture life increased with decrease in ϕ value for all the heats. The dependence of rate of acceleration of tertiary creep on the applied load is shown for the four heats in Fig. 5.31. The ϕ value exhibited increasing trend with applied load for all the heats. For the same load, the ϕ value was observed to be lowered with increase in nitrogen content from 0.07 to 0.14 wt.%. The trend curve for 22N showed a cross-over from 7N to 11N but it is always higher than 14N steel for all loads. Therefore, by increasing the nitrogen content in 316LN SS upto 0.14 wt.%, the ϕ value may be decreased for the same range of loads, resulting in higher rupture life.

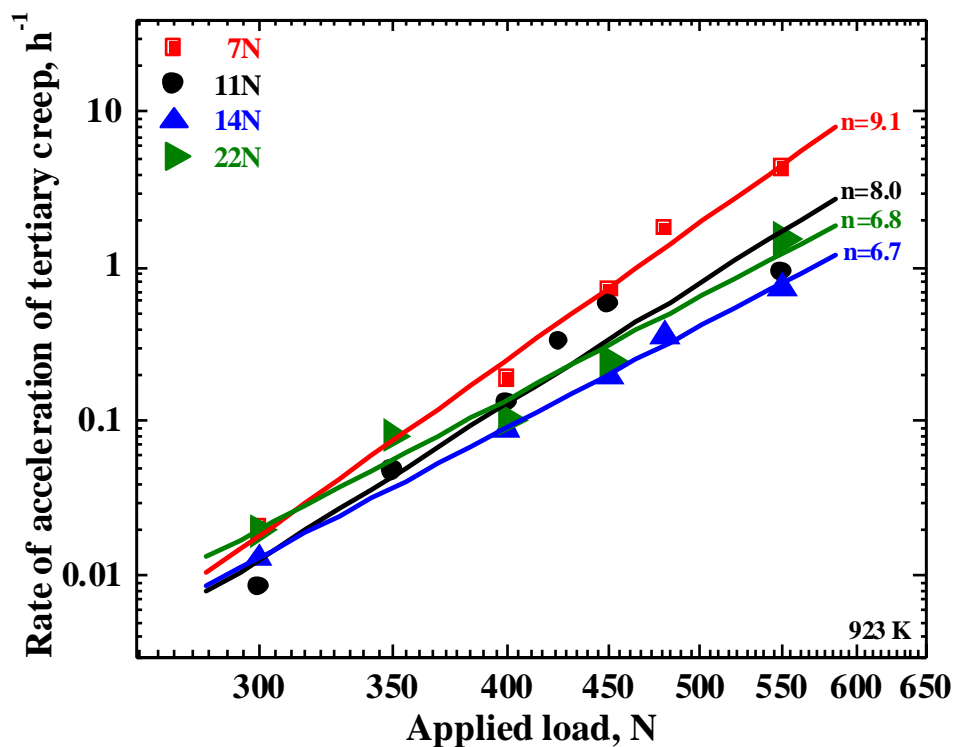


Fig. 5.31 Dependence of rate of acceleration of tertiary creep on applied load.

By increasing the nitrogen content in 316LN SS from 0.07 to 0.14 wt.%, the parameters such as rate of exhaustion of transient creep, steady state deflection rate and rate of acceleration of

tertiary creep were decreased for the same applied load, thereby prolonging each stage of SPC, thus resulting in higher rupture life of the steel. It may be concluded based on SPC results that the creep strength is improved by increasing the nitrogen content from 0.07 to 0.14 wt.% in 316LN SS.

Thus ABI and SPC techniques can be effectively utilised for evaluating heat to heat variations in tensile and creep strength, using small quantity of testing material from each heat, saving lot of time and efforts. The necessity of multi-axial creep studies for complete understanding of creep behaviour of material is emphasised.

CHAPTER 6

APPLICATION-II

Localised Characterisation of 316LN SS Weld Joint

LOCALISED CHARACTERISATION OF 316LN SS WELD JOINT

The strength of weld joint is very critical for the performance of high temperature applications due to geometrical discontinuity and heterogeneous microstructure existing in it. ABI and SPC techniques have been applied to assess 316LN SS weld joint comprising various zones such as base metal, heat affected zone (HAZ) and weld metal. In this chapter, the variations in tensile and creep behaviour across 316LN SS weld joint as estimated using ABI and SPC techniques are discussed.

6.1 Tensile strength variation across weld joint using ABI technique

The variation of tensile strength across 316LN SS weld joint was estimated using ABI technique. Initially, the weld joint specimen was manually polished to achieve surface finish of around 1 μm . The polished surface was then etched with 60% nitric acid in distilled water (60 ml HNO_3 + 40 ml H_2O) to view the different constituents of the weld joint. Figure 6.1 shows the microstructural heterogeneity seen across 316LN SS weld joint. The base metal consisted of fully austenite phase with nearly equiaxed grains distributed uniformly in the austenitic matrix. Relatively coarse grains were observed in heat affected zone. The weld metal consisted of duplex structure containing delta-ferrite distributed uniformly in parent austenite matrix. ABI tests were conducted across the base metal, HAZ and weld metal regions of 316LN SS weld joint at 300 K, 523 K and 923 K.

Typical load-depth of indentation data obtained from ABI tests on the weld metal, HAZ and base metal at 923 K are shown in Fig. 6.2. For the same depth of indentation, the applied load was higher for HAZ when compared to other regions of the weld joint. The load-depth of indentation data obtained across the weld joint at various temperatures were analysed as

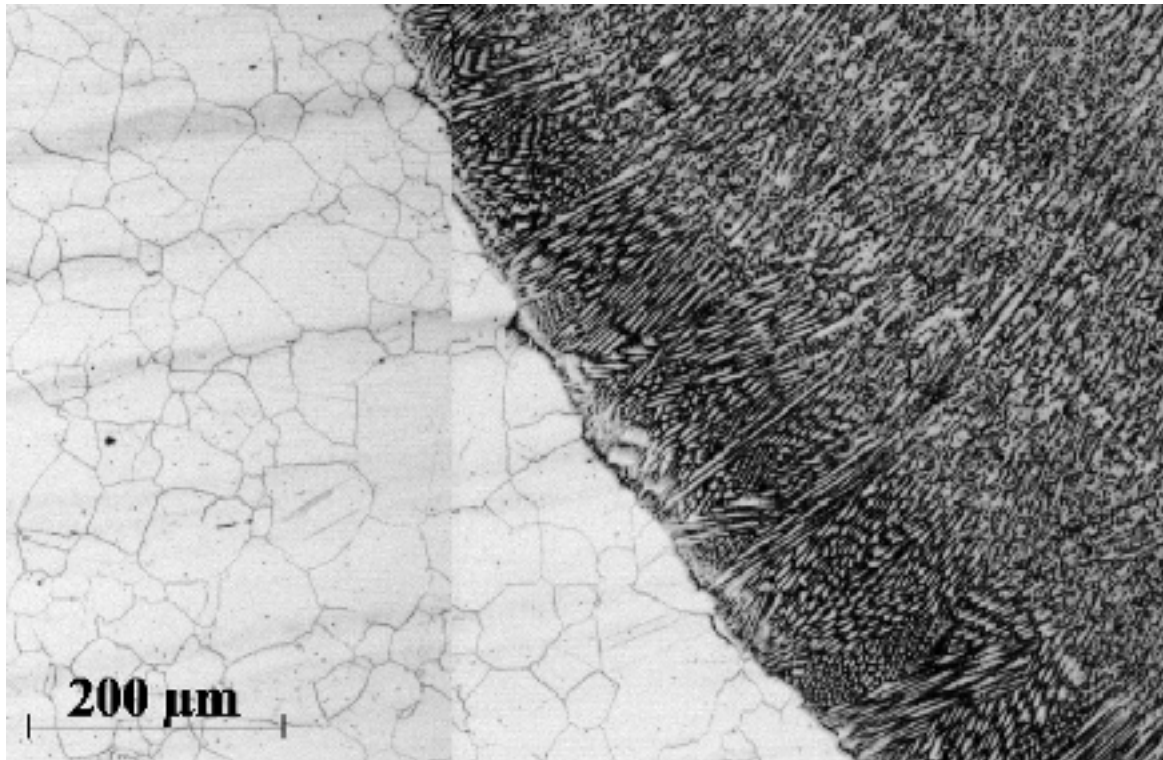


Fig. 6.1 Microstructural heterogeneity across 316LN SS weld joint.

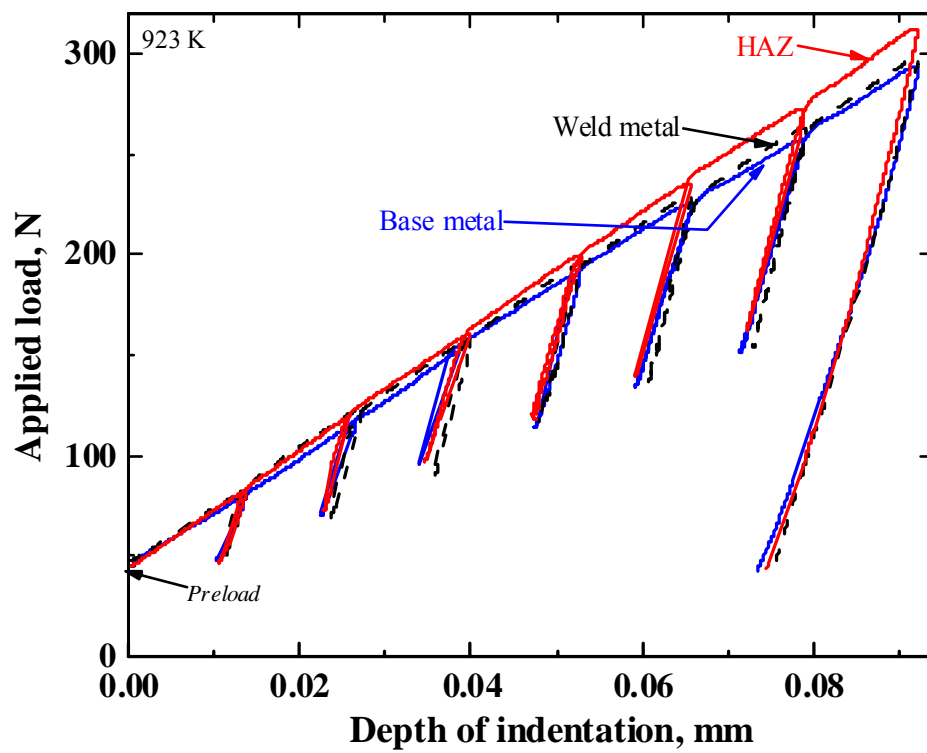


Fig. 6.2 Load-depth of indentation curves obtained across 316LN SS weld joint at 923 K.

discussed in chapter 3. The value of α_m was taken as 1.5 in the analysis of weld metal data. In order to study the narrow regions in weld joint, the smallest indenter (Φ 0.25 mm) was used in this case. The constraint factor of base metal was adjusted to consider the indenter size effect and the value of α_m is taken in the range 1.28-1.42 in the analysis of base metal data depending on the temperature. The same constraint factor was used in the analyses of both base metal and HAZ.

The true stress versus true plastic strain curves obtained for the base metal and weld metal from uniaxial tensile tests at 298 K are shown in Fig. 6.3. The values obtained from ABI tests under similar conditions are shown as symbols scattered over the corresponding uniaxial tensile curves. The ABI test results were found to be consistent with those obtained from uniaxial tensile tests. The small extent of HAZ prevents to carry out conventional tensile test and therefore the flow curve obtained for HAZ from ABI test alone is shown in the same figure.

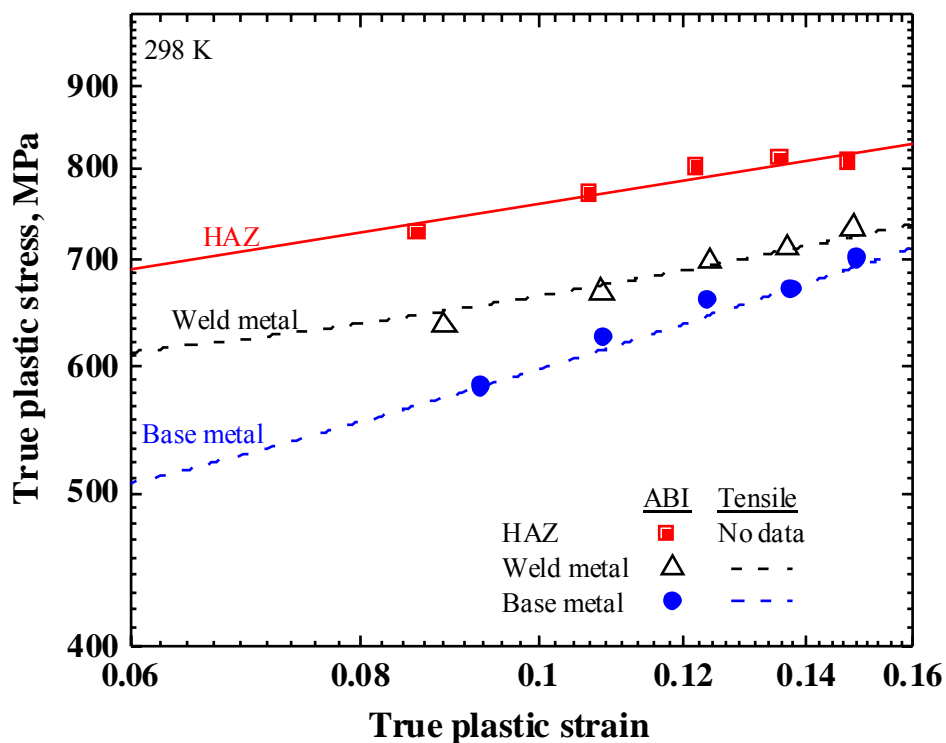


Fig. 6.3 Correlation of results from ABI and uniaxial tensile tests on weld joint.

The true stress versus true plastic strain curves obtained for various zones of the weld joint at 298 K and 923 K are shown in Fig. 6.4. The flow curve for base metal was lower than those for weld metal and HAZ at 298 K; whereas the base metal curve crossed over the weld metal curve at 923 K. Though the flow curve for HAZ was lower than that for weld metal initially, the increase in stress with strain was more in HAZ relative to the weld metal at both the temperatures, implying that higher work hardening was observed in the heat affected zone. During the welding process, heavy deformation takes place in HAZ due to repeated weld thermal cycles, resulting in higher dislocation density, which in turn can be responsible for its work hardening behaviour ^[181,182].

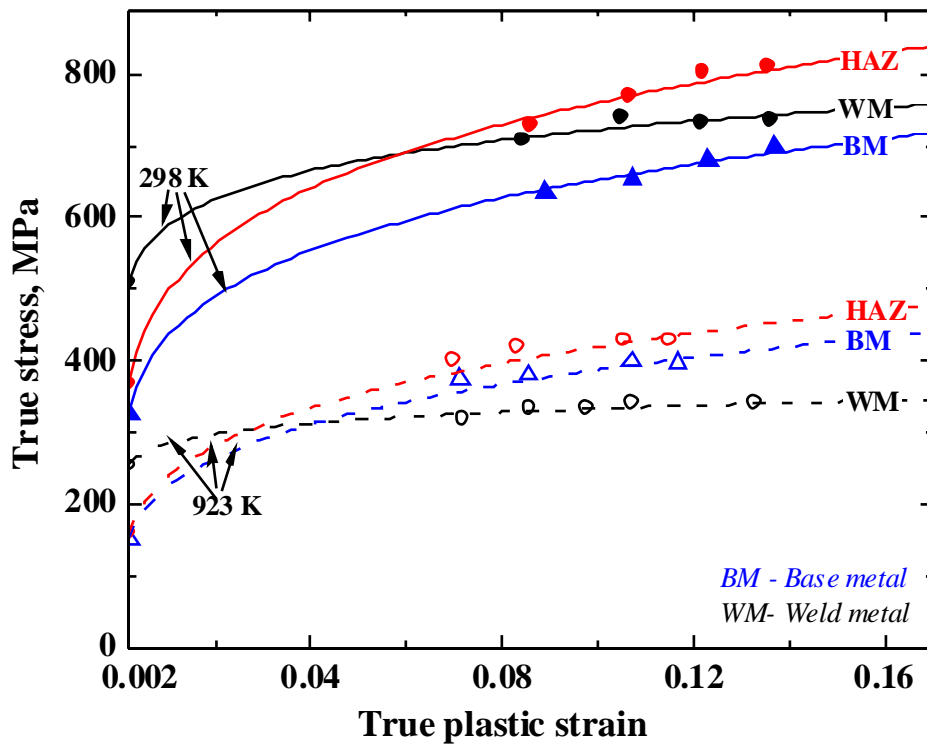


Fig. 6.4 Flow curves for various zones of 316LN SS weld joint.

A significant application of ABI technique is the characterization of narrow HAZ which may not be possible with conventional tensile tests. The flow curves determined for HAZ at various temperatures are presented in Fig. 6.5. The effect of temperature on the flow curves

for HAZ was clearly obtained from ABI tests.

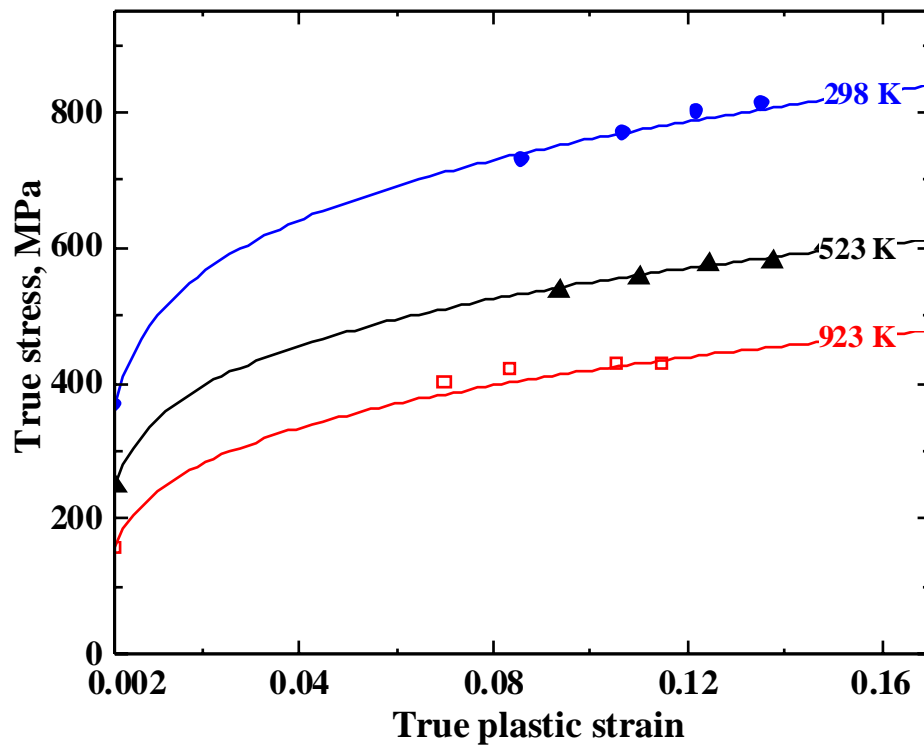


Fig. 6.5 Flow curves obtained on HAZ of weld joint at various temperatures.

The optical micrograph of ABI specimen tested at 298 K with indentations across the various zones of the steel weld joint is shown in Fig. 6.6. Though the size and material of indenter used was the same, the pattern of deformation around indentation varied across the various zones of weld joint. The optical micrographs of indentations on HAZ, base metal and weld metal under the same condition are shown at higher magnification in Figs. 6.7 (a), (b) and (c) respectively. In case of base metal and HAZ, the deformation was found to be distributed all around the indentation with generation of lot of twins. This may be due to nearly equiaxial grain structure in the base metal. Whereas the deformation in the weld metal was found to be accumulated in the specific directions that may be due to the highly heterogeneous and columnar structure existing in the weld metal. However, a further detailed investigation has to be done to understand the phenomenon lying behind this pattern of deformation.

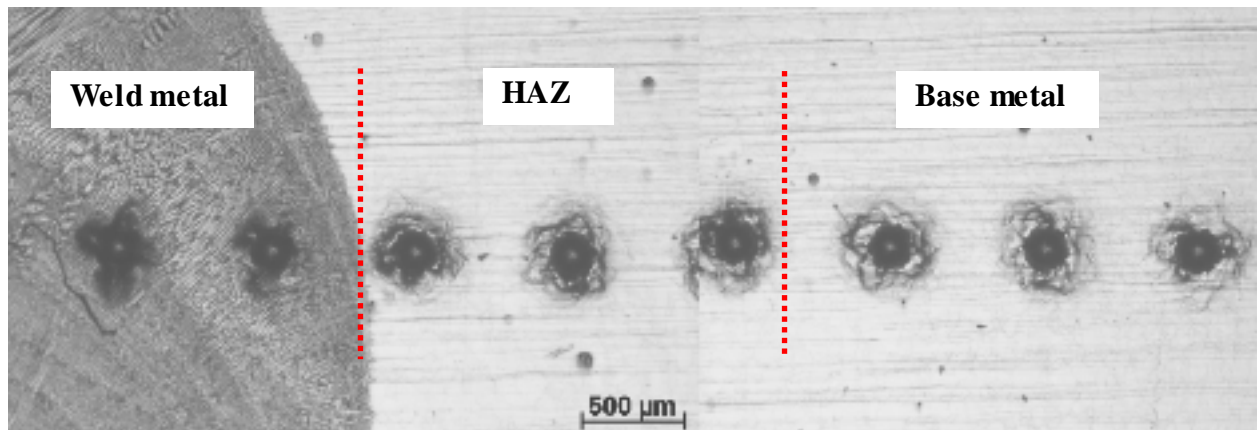
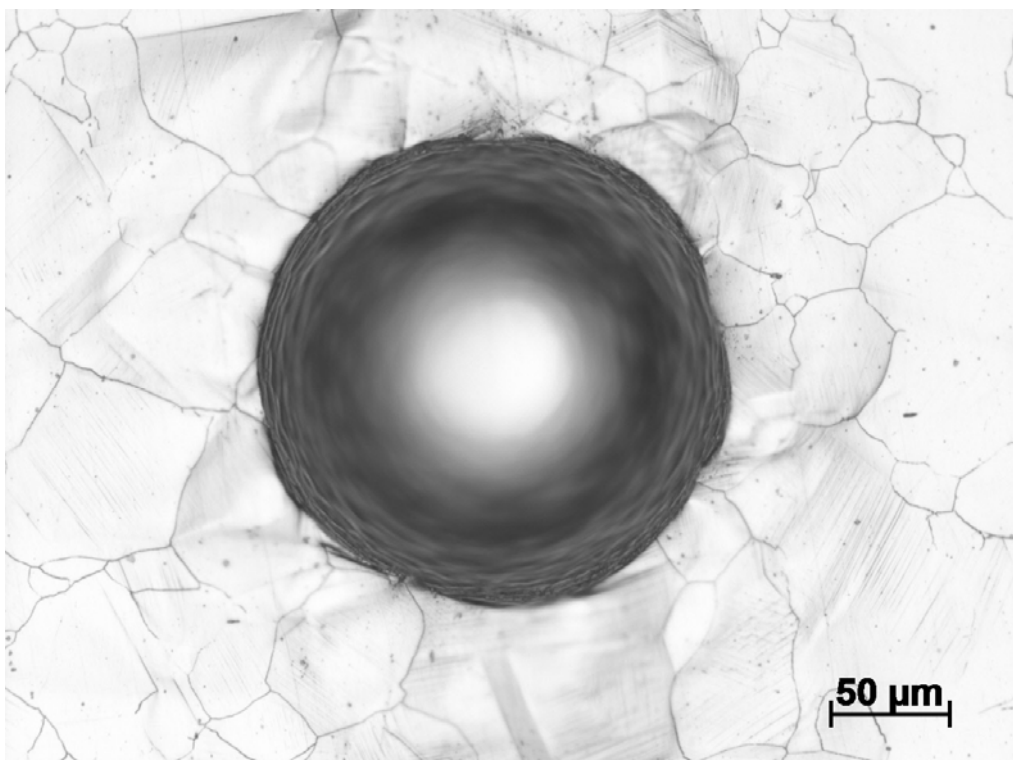
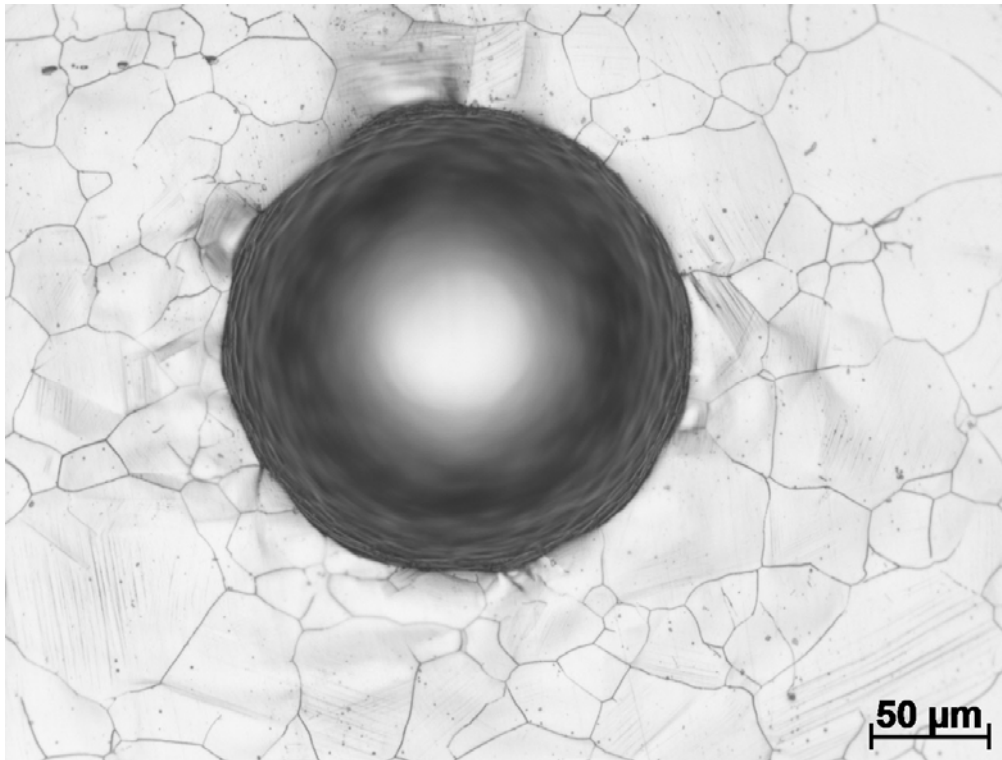


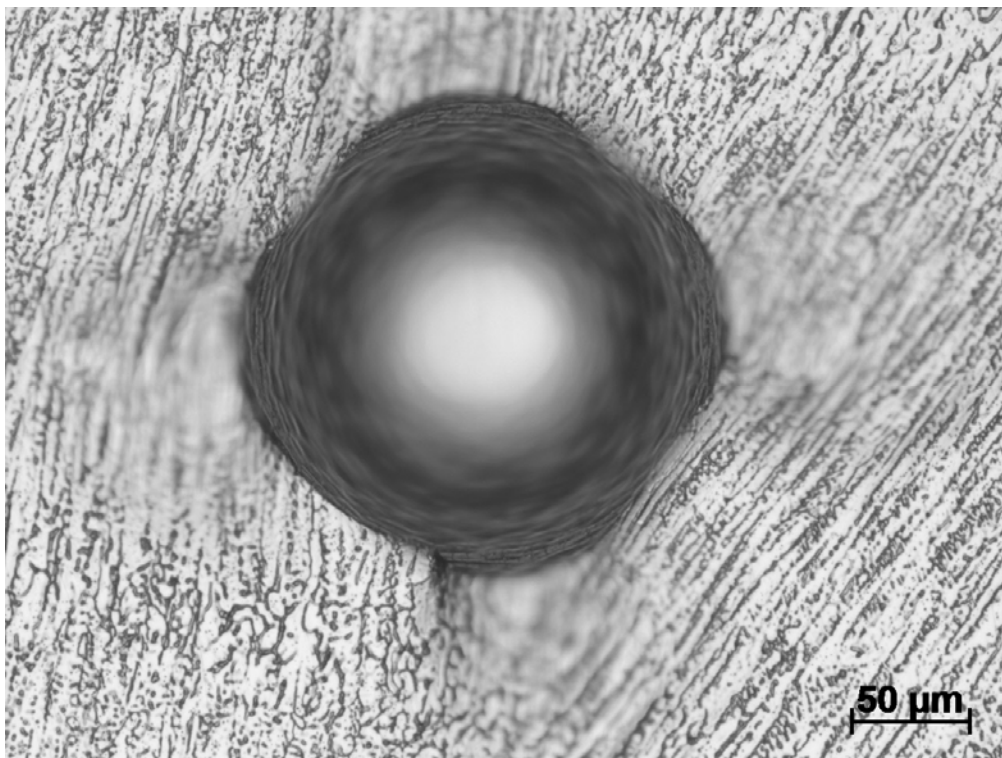
Fig. 6.6 Optical micrograph of indentations across 316LN SS weld joint at 298 K.



(a)



(b)



(c)

Fig. 6.7 Optical micrograph of indentation at 298 K on (a) HAZ (b) base metal (c) weld metal.

The variation of yield stress (YS) across the weld joint is shown in Fig. 6.8. The highest YS value was observed in the weld metal region at all temperatures and the YS values obtained for HAZ were slightly higher than those obtained for the base metal. The UTS values determined across the weld joint at various temperatures were plotted in Fig. 6.9. The UTS values obtained in HAZ were higher than those obtained in the other regions of the weld joint at all temperatures. At 298 K and 523 K, the UTS for the weld metal were closer to the values obtained for HAZ. At 923 K, the UTS value for the base metal was closer to that obtained for HAZ and higher than that for the weld metal. A better interpretation of UTS and YS trend curves may be achieved by UTS/YS ratio that represents the work hardening of a material, as shown in Fig. 6.10. The UTS/YS ratio was observed to be nearly the same in the weld metal region irrespective of temperature. However, UTS/YS ratio in the base metal and HAZ increased with increase in temperature.

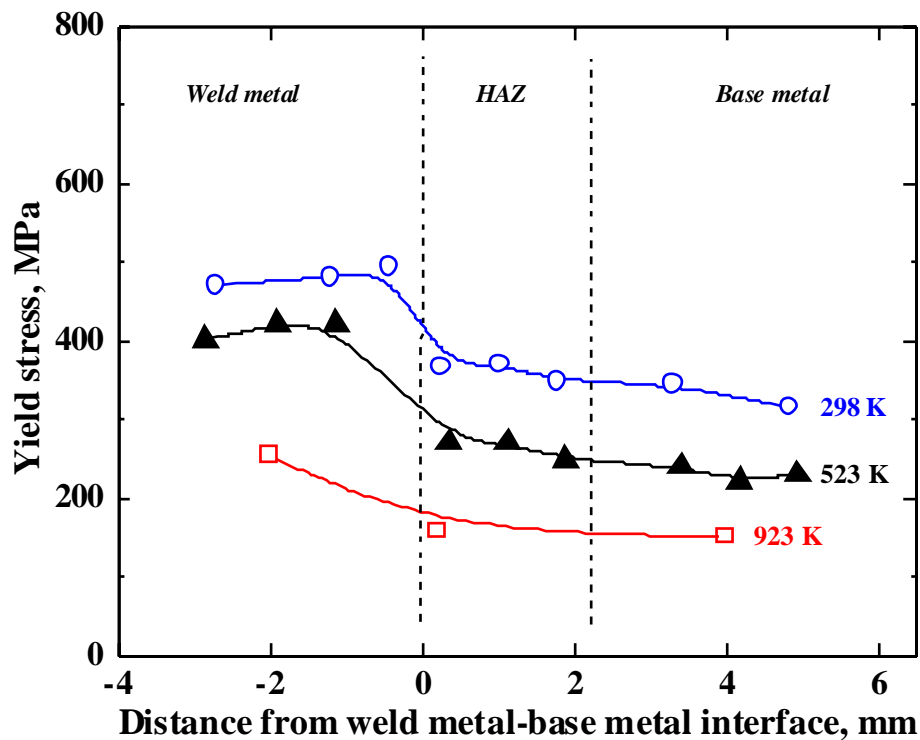


Fig. 6.8 Evaluation of yield stress across 316LN SS weld joint.

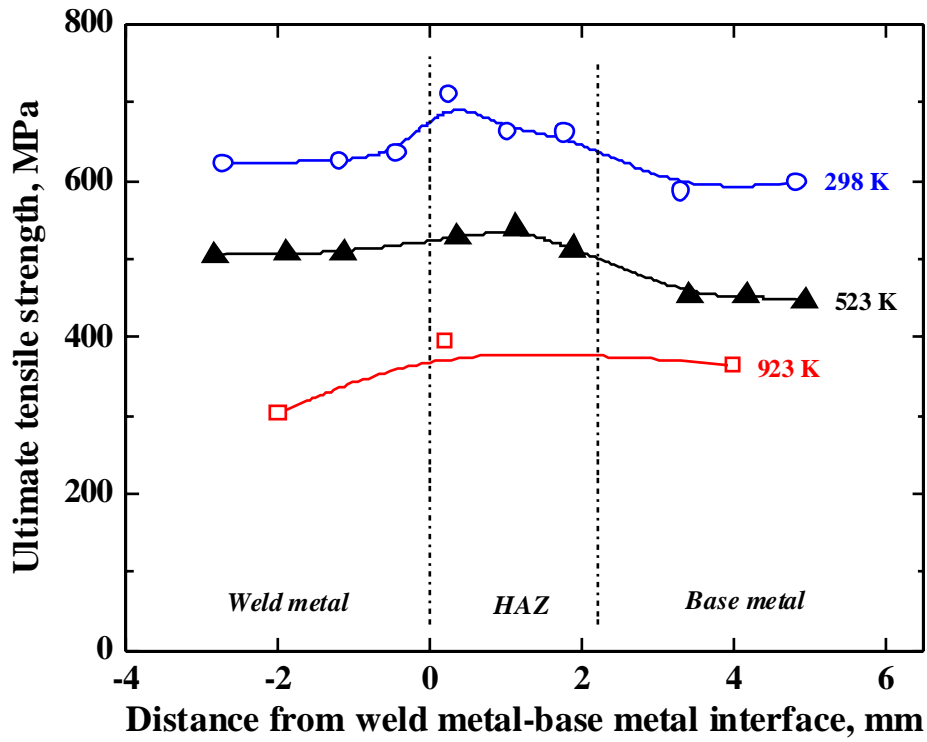


Fig. 6.9 Evaluation of ultimate tensile strength across 316LN SS weld joint.

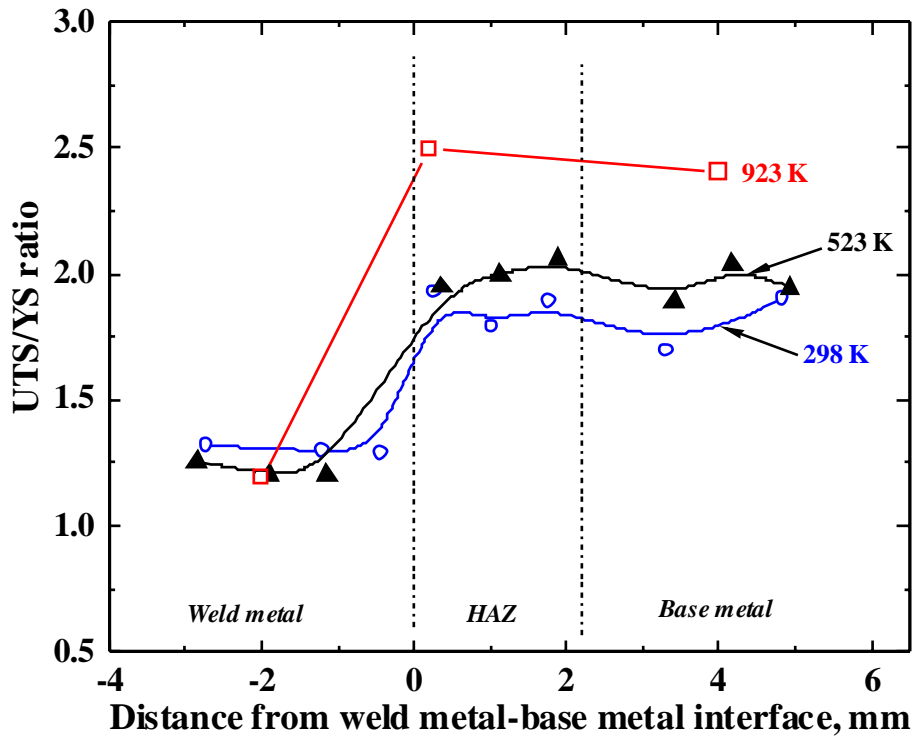


Fig. 6.10 Estimation of UTS/YS ratio across 316LN SS weld joint.

As multi-pass welding was carried out in the investigated weld joint, the variation of tensile strength at several passes within the weld metal region was examined. The UTS and YS were measured at various passes in the weld metal region from the root to the crown of the weld joint. These values are plotted with respect to distance from the root of the weld joint in Fig 6.11.

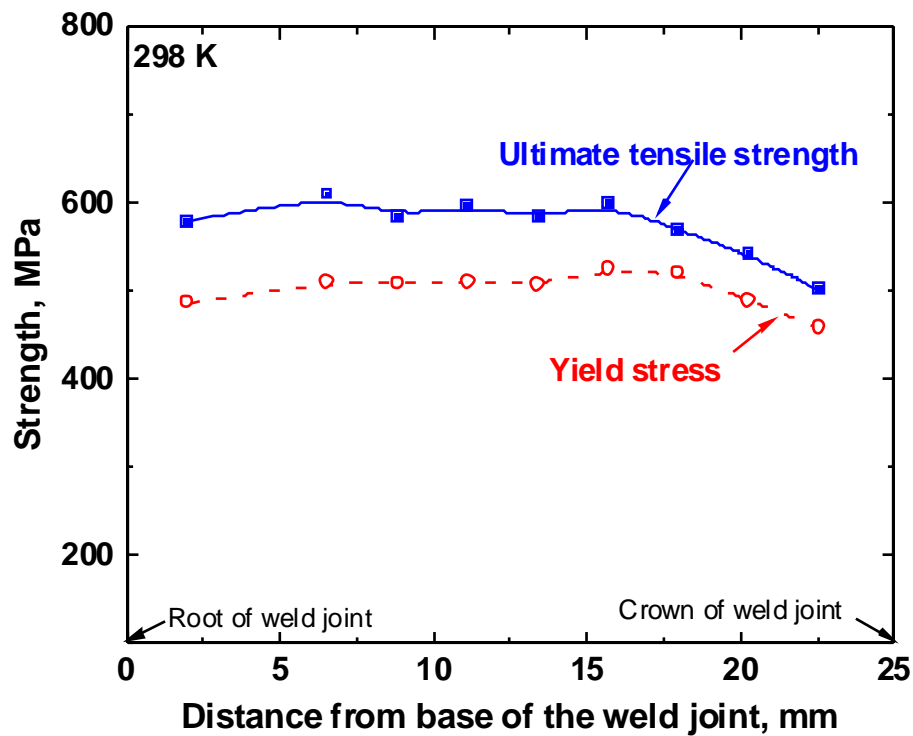


Fig. 6.11 Variation of strength at several passes of 316LN SS weld joint at 298 K.

Both UTS and YS remained almost the same at various passes except at the passes near the crown region of the weld joint. As this investigation was carried out across the weld joint in locations away from the crown region, the results obtained can therefore be considered independent from the effect of pass.

6.2 Creep strength variation across 316LN SS weld joint using SPC technique

The SPC curves obtained over the weld metal and HAZ regions of 316LN SS weld joint are seen with clear distinct stages as shown in Figs. 6.12 and 6.13 respectively.

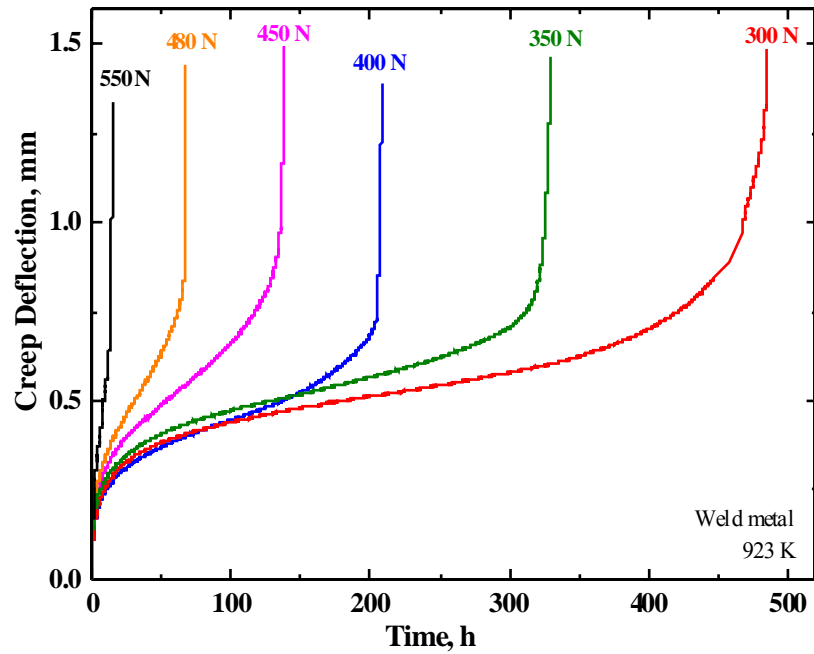


Fig. 6.12 SPC curves obtained for weld metal at 923 K.

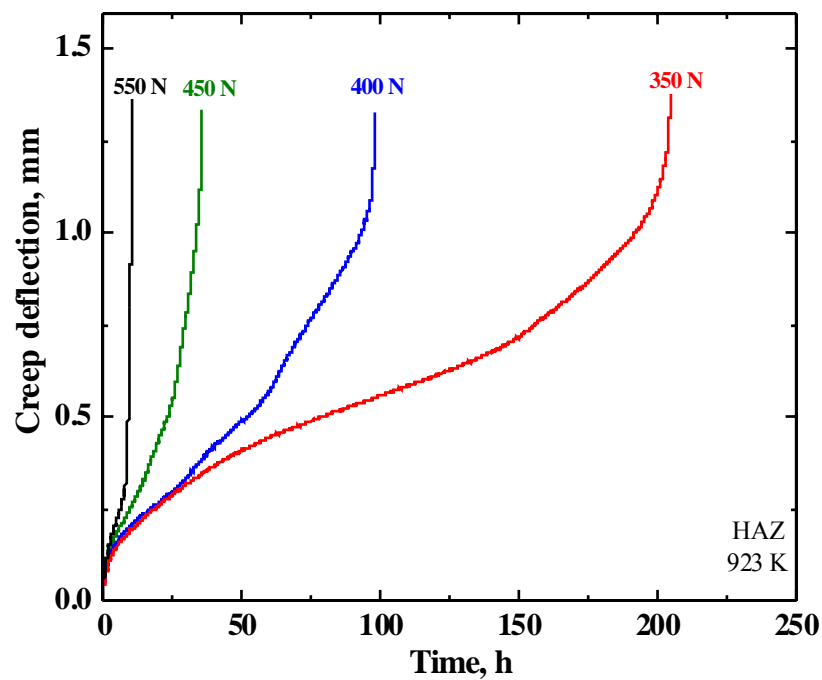


Fig. 6.13 SPC curves obtained for HAZ at 923 K.

The SPC rupture lives obtained from various zones of 316LN SS weld joint are compared in Fig. 6.14. The weld metal exhibited highest rupture life among the three zones. The HAZ curve lied slightly above the base metal. The values of steady state deflection rate obtained over various zones are shown in Fig. 6.15. The trend curves for HAZ and base metal were closer to each other and both showed considerably higher value than weld metal.

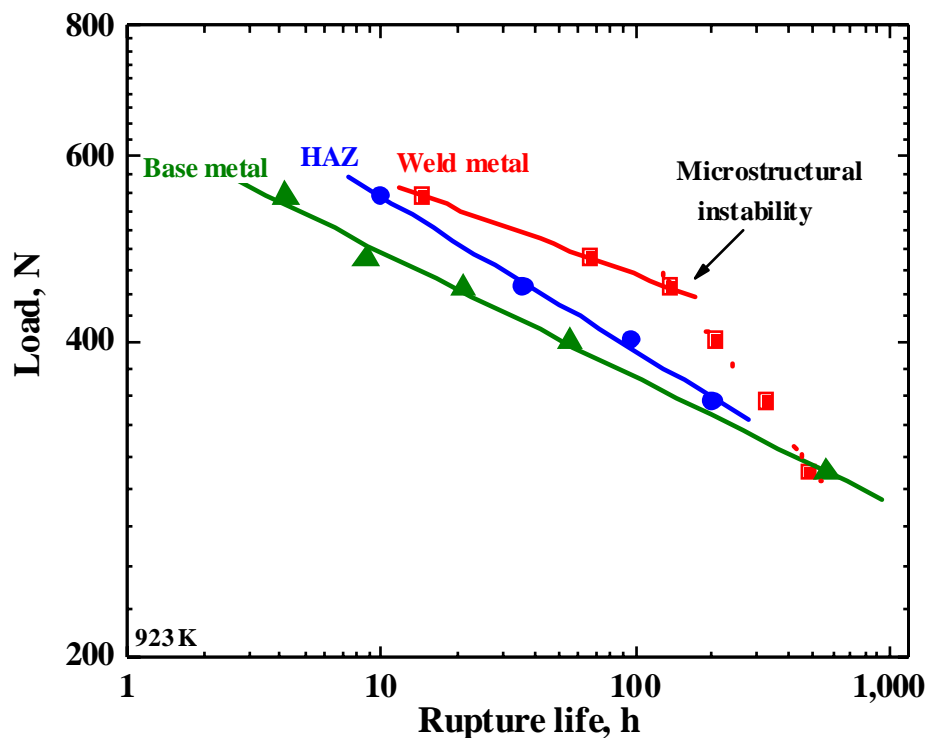


Fig. 6.14 Rupture curves obtained from various regions of 316LN SS weld joint.

However, it may be noted that the results discussed above are based on short term SPC tests. The influence of δ -ferrite (present in the weld metal) on the creep deformation behaviour is related with the duration of test. During short term creep test, the network of δ -ferrite is relatively stable. During long term creep test, the δ -ferrite network breaks down into various phases including precipitation of intermetallic phases such as σ , χ and η in weld metal that significantly lowers its creep strength ^[114]. In the same figures, when the load decreases, the difference between the rupture lives and deflection rate values of weld metal and base metal

narrows down, thus giving a hint that the strength of weld metal may be lower than base metal during long term tests. The possibility of reversal of the above observed trend during long term creep exposure can be taken up for further investigation.

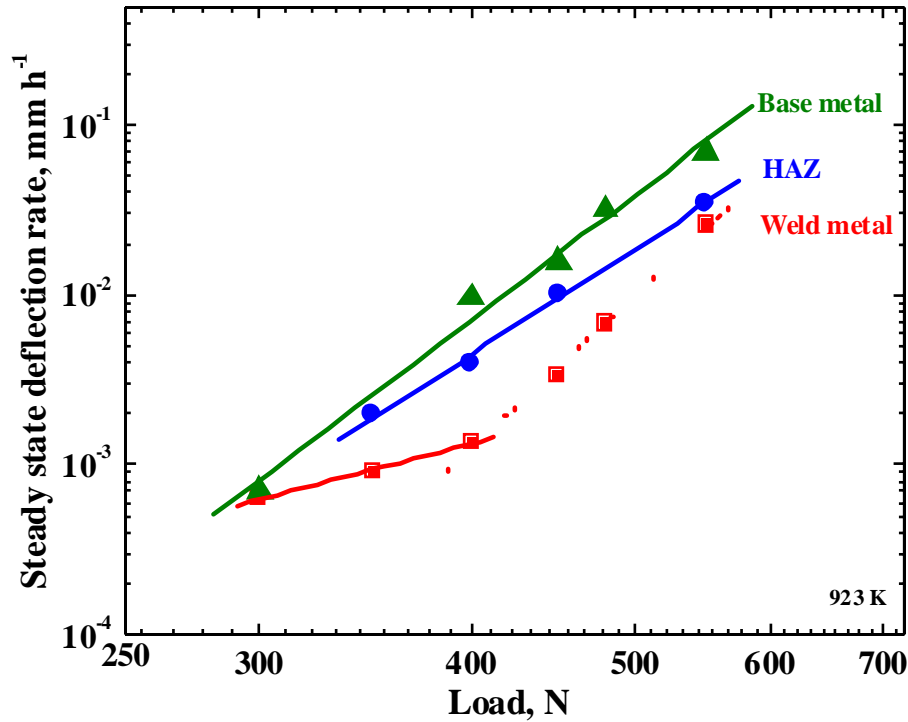


Fig. 6.15 Steady state deflection rate obtained from various regions of 316LN SS weld joint.

The SEM fractographs of the HAZ and weld metal of the weld joint tested at 923 K are shown in Figs. 6.16 and 6.17. Both the regions showed intergranular cracks on the fractured surface.

In order to estimate the variation of creep strength across 316LN SS weld joint, SPC tests were conducted on specimens sliced out from various regions across the weld joint at 923 K at 400 N. The load 400 N corresponds to high stress regime for 316LN SS. The total cumulative duration required for completing this set of tests was considered to apply this load. The variation in rupture life across various regions of 316LN SS weld joint is shown in Fig. 6.18.

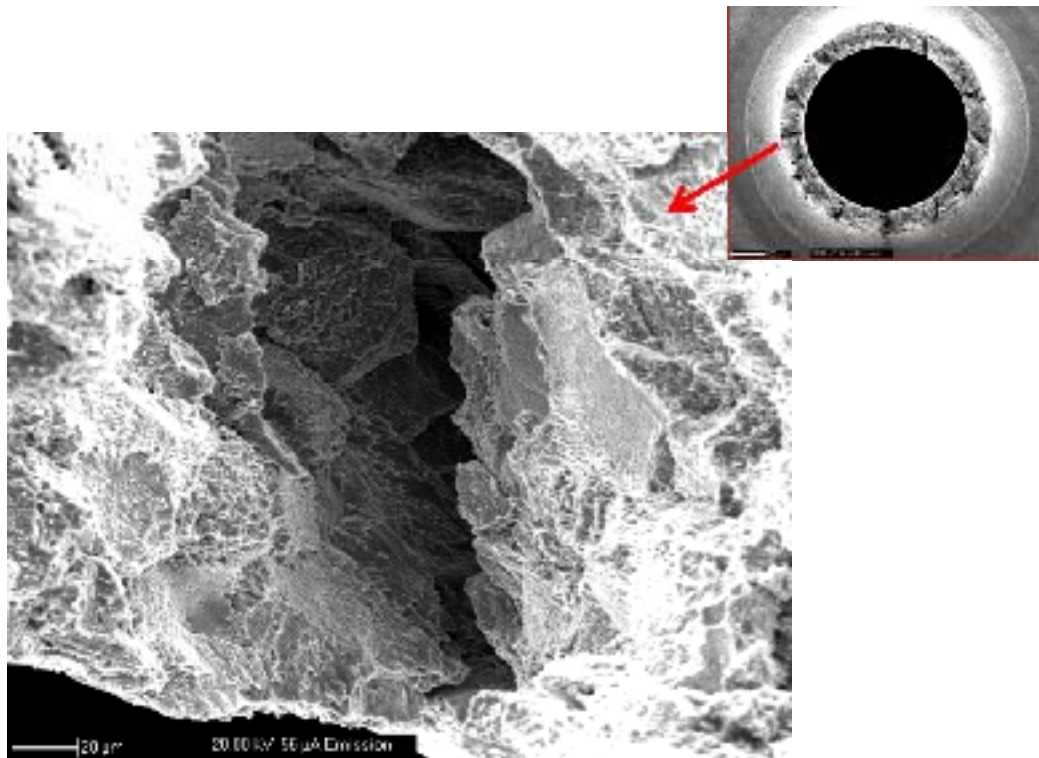


Fig 6.16 SEM fractograph of SPC specimen sliced out of HAZ region and tested at 923 K.

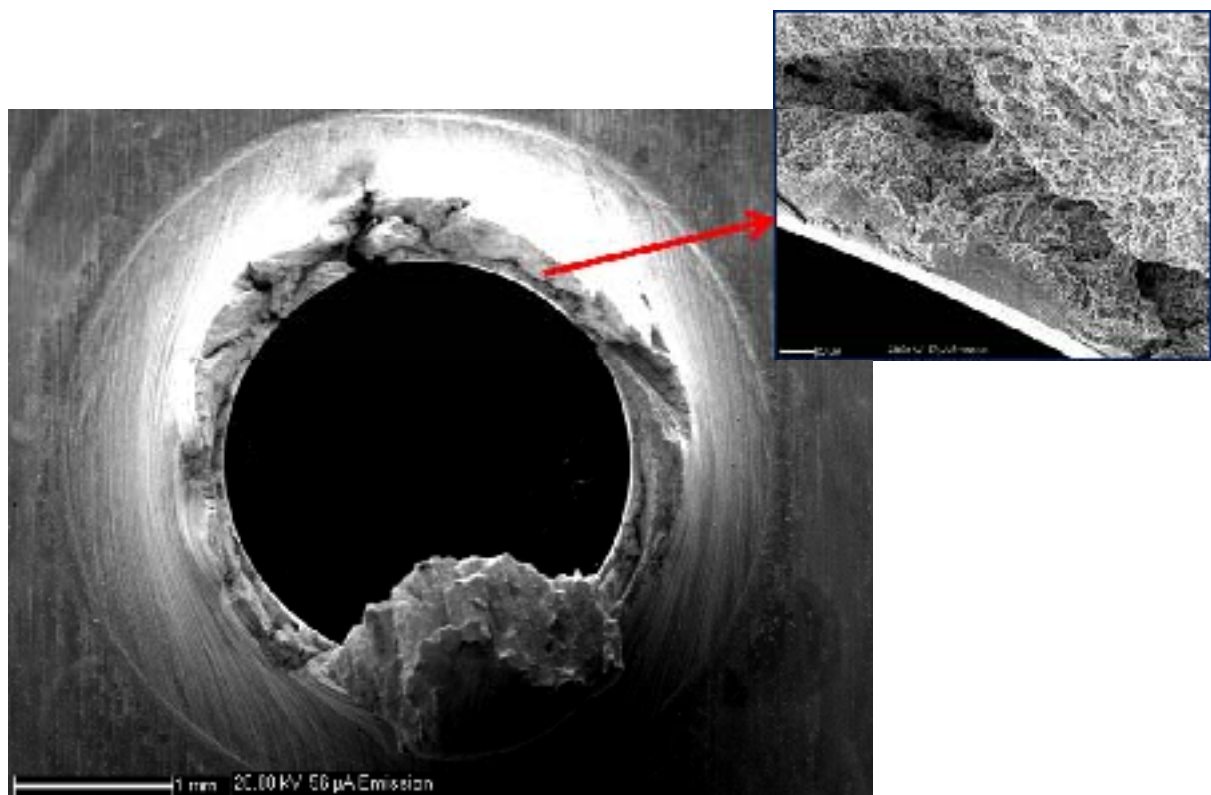


Fig 6.17 SEM fractograph of weld metal specimen tested at 923 K.

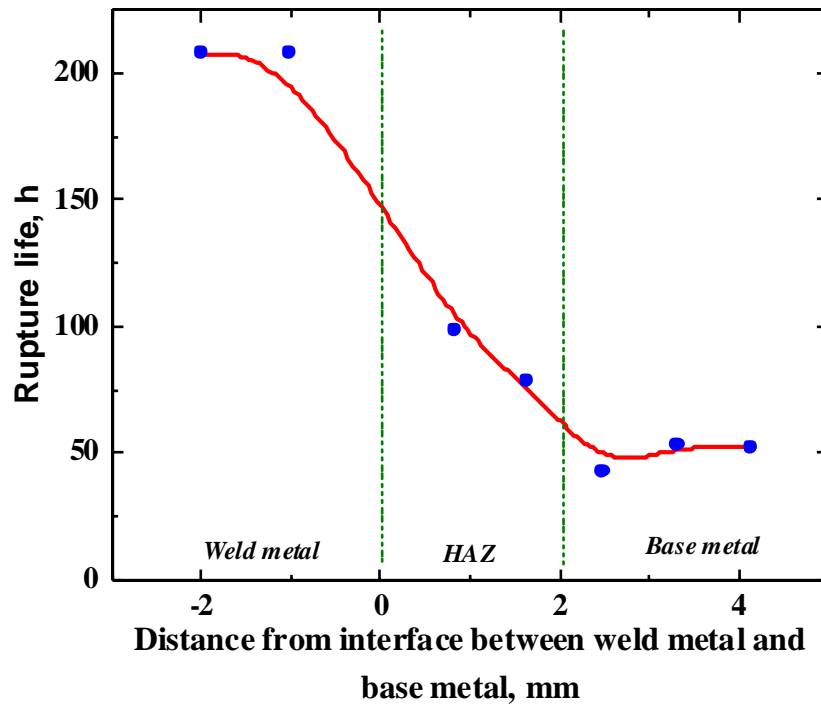


Fig. 6.18 Variation of creep strength across various zones of 316LN SS weld joint.

It was observed that the weld metal showed highest rupture strength among the three regions of 316LN SS weld joint. In case of SPC tests over P92 steel also, the weld metal showed about 1.5 times longer rupture life than the base metal and was attributed to addition of nickel content in weld metal^[183]. Though the rupture curve at HAZ was lower than weld metal, the increase in rupture strength of HAZ was significant when compared to the base metal. Even within the HAZ region, the portion near to weld metal revealed higher creep strength when compared to base metal side. This resulted in a smooth gradient from higher to lower creep life across the weld joint from weld metal to base metal.

The SPC curves obtained for the base metal, HAZ and weld metal of 316LN SS weld joint were analyzed according to Eqn. 4.2.4. The rate of exhaustion of transient creep, steady state deflection rate and rate of acceleration of tertiary creep were calculated for various regions and are plotted in Fig. 6.19.

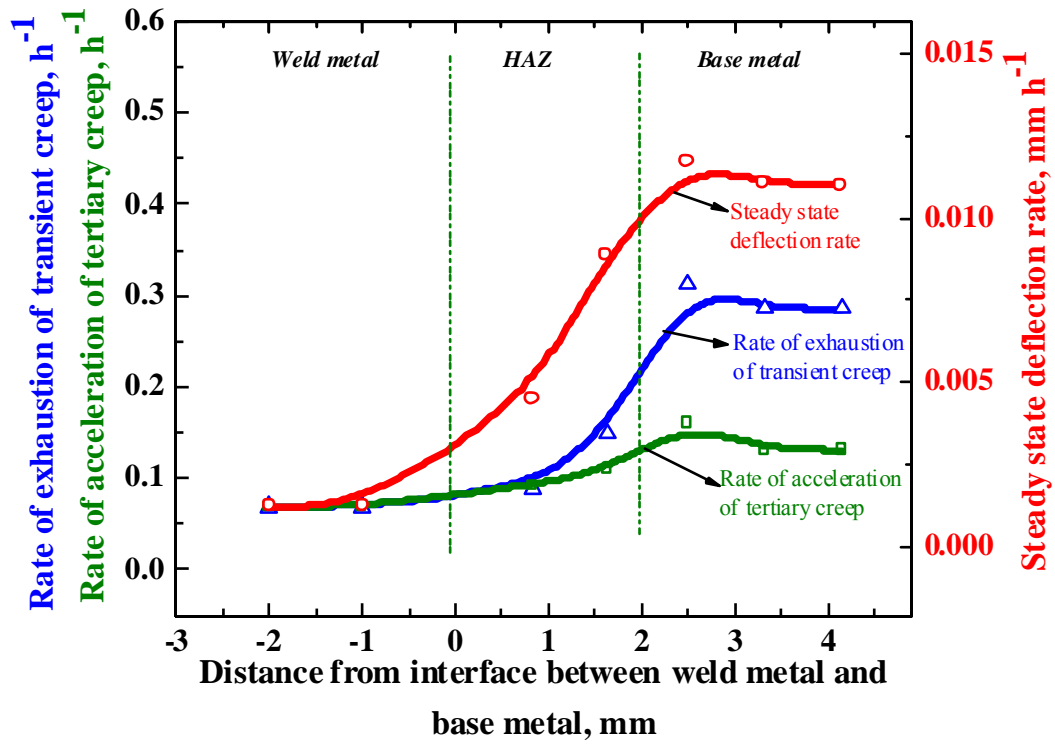


Fig. 6.19 Variations of κ , $\dot{\delta}_s$ and ϕ across the weld joint.

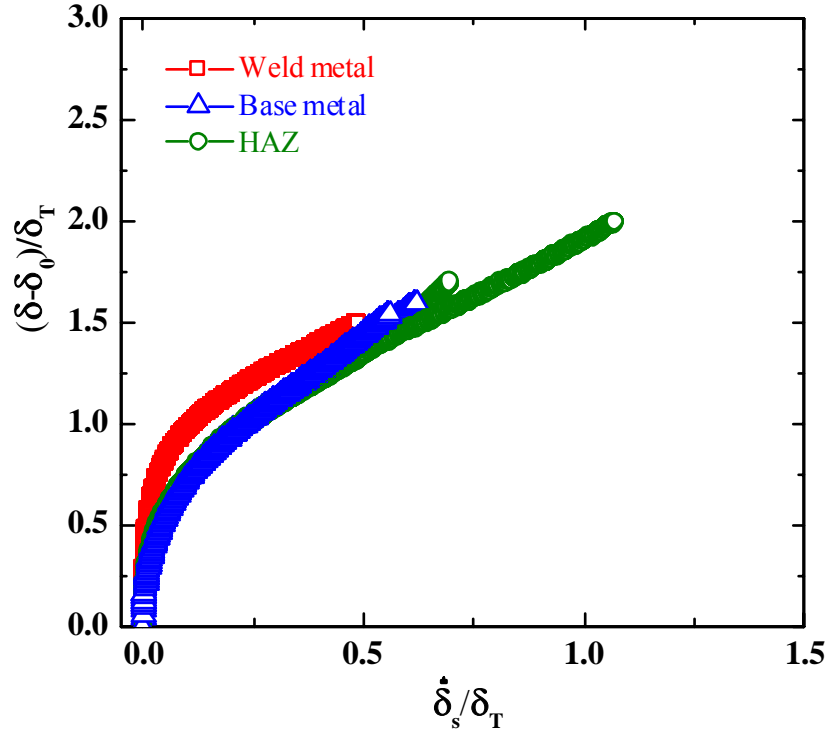


Fig. 6.20 Master curves for transient creep deflection for various zones across 316LN SS weld joint.

The values of κ , $\dot{\delta}_s$ and ϕ calculated for the same conditions exhibited increasing trend across the weld joint from weld metal to base metal. These trends were consistent with the trend of rupture life across the weld joint (Fig. 6.18). However, the extent of increase in value of those creep parameters from weld metal to base metal was observed differently at various stages of SPC deformation. The same data were utilised for deriving the master curves for transient creep deflection. The master curves that were drawn by plotting $(\delta - \delta_0)/\delta_T$ against $(\dot{\delta}_s t)/\delta_T$ values obtained from various regions of weld joint, were found to follow closely with one another, as shown in Fig. 6.20.

Thus the above studies emphasized that ABI and SPC techniques can be effectively utilised in the study of weld joints used in high temperature applications. These results can be further applied to ABI and SPC studies over the estimation of degradation in strength in weld joints in high temperature service.

CHAPTER 7

Conclusions and Future Work

7.1 Conclusions

Automated Ball Indentation (ABI) technique has been used to assess the high temperature tensile properties of 316L(N) SS. Initially, the influence of some test parameters on ABI results has been investigated. It was found that by increasing the maximum depth of indentation (in the range 12% to 50% of indenter radius), number of cycles (in the range 5 to 12 cycles) and surface finish of test specimen (average roughness (R_a) in the range 2-4 microns) to higher values, ABI results are not altered significantly. But the material of indenter significantly affects the ABI test results and has to be chosen judiciously. ABI tests were conducted on 316L(N) SS at several temperatures in the range 298-973 K. The decreasing trend of yield stress, strength coefficient, yield ratio, hardness and the increasing trend of strain hardening exponent with temperature were obtained from ABI tests. The ABI test results were correlated with corresponding uniaxial tensile test results. The development of plastic zone in the ABI specimen under spherical indenter was studied through finite element analysis.

Small Punch Creep (SPC) technique has been used to evaluate the creep behaviour of 316L(N) SS. With decrease in applied load, the rupture life increases whereas the steady state deflection rate decreases. The transient and tertiary creep deformation behavior have been analysed according to the equation proposed for SPC deflection, $\delta = \delta_0 + \delta_T (1 - e^{-\kappa t}) + \dot{\delta}_s t + \delta_3 e^{[\varphi(t-t_r)]}$. The rate of exhaustion of transient creep (κ), steady state deflection rate ($\dot{\delta}_s$) and rate of acceleration of tertiary creep (φ) followed similar decreasing trends with rupture life and increasing trends with applied load. The transient, secondary and tertiary stages of SPC deformation are found to be interrelated. It was revealed

that first-order reaction rate theory governed SPC deformation throughout the transient and tertiary stages. An attempt has been made to construct the master curves for transient and tertiary SPC deflection. From the estimated values of load exponent of steady state deflection rate ($n_{\text{spc}} = 6.35$) and apparent activation energy for creep deformation ($Q_{\text{spc}} = 352 \text{ kJ/mol}$), the mechanism of SPC deformation was determined to be dislocation creep under the investigated conditions. The SPC load was correlated with the corresponding uniaxial creep stress. The rate of exhaustion of transient creep (r') values that were determined from uniaxial creep tests were correlated with those obtained from SPC tests. Master curves representing transient creep deformation have been derived from both SPC and uniaxial creep tests and their near coincidence brings unique equivalence between both kinds of test. Finite element analysis was performed to understand the state of stress developed in SPC disc specimen under spherical indenter.

ABI and SPC techniques have been respectively applied to investigate the effect of nitrogen content on tensile and creep properties of 316LN SS. ABI and SPC tests were conducted on four different heats of 316LN SS containing 0.07, 0.11, 0.14 and 0.22 wt.% nitrogen. The tensile properties such as yield stress and ultimate tensile strength increases with increase in nitrogen content at all the investigated temperatures. These results are consistent with the corresponding uniaxial tensile test results. The SPC rupture life increases whereas steady state deflection rate decreases with increase in nitrogen content upto 0.14 wt.%, after which the trend reverses at 0.22 wt.%. It is emphasized here that the creep behaviour can be completely understood by investigating the material under multi-axial state of stress as prevailing in SPC test, in addition to uniaxial test. The relationships among the parameters such as κ , $\dot{\epsilon}_s$ and ϕ are found to exist almost independent of nitrogen content. The first-order reaction rate theory governed the SPC deformation behaviour of all the investigated steels,

throughout the transient and tertiary stages. The master curves for transient and tertiary creep deflection obtained for various nitrogen content overlapped each other. By increasing the nitrogen content from 0.07 to 0.14 wt.%, each stage of SPC were prolonged and consequently the values parameters κ , $\dot{\delta}_s$ and ϕ decreased for the same load.

The variations of tensile and creep properties across 316LN SS fusion welded joint, comprising base metal, heat affected zone (HAZ) and weld metal, were evaluated respectively using ABI and SPC techniques. The HAZ exhibited higher tensile strength than the other regions of the steel weld joint at all investigated temperatures. The ratio of ultimate tensile strength to yield stress, which represents the work hardening behaviour, increased with an increase in temperature for the base metal and heat affected zone; whereas it remained nearly the same for the weld metal. The variations of localized creep properties across various zones of 316LN SS fusion welded joint were evaluated using SPC technique. It was observed that the weld metal showed the highest rupture life. Though the rupture curve for HAZ was lower than that for weld metal, the increase in rupture strength of HAZ was significant when compared to the base metal. This trend was also reflected in the variations of κ , $\dot{\delta}_s$ and ϕ across the weld joint.

To summarize, the capability of ABI test to sense the degradation of the strength of materials on exposure to high temperature is highlighted in this thesis. Thus ABI and SPC techniques can be utilized for structural integrity assessment studies in high temperature domain. ABI and SPC techniques are demonstrated as fast and reliable techniques for optimizing the content of alloying element in heat resistant steels under development. It is ensured that ABI and SPC techniques can be effectively utilised in studying the mechanical properties of weld joints used in high temperature applications.

7.2 Scope for future work

One of the important applications of ABI and SPC techniques is residual life assessment which can be executed in two stages. Firstly, approximately known level of damage can be imparted on a material and the degradation of its strength can be quantified by carrying out ABI and SPC tests on those specimens. Secondly, investigations can be carried out on service exposed components to estimate the residual life based on degradation in strength. The ABI and SPC studies can be extended to other fast reactor materials.

The constraint factor that is used in ABI analysis and the correlation factor used in SPC tests for finding equivalent uniaxial stress are found by empirical correlation with corresponding conventional uniaxial tests. The physical basis of such values has to be investigated so as to help to improve the applicability of both the techniques.

SPC results have a limitation that microstructural changes observed in long term uniaxial creep tests cannot be observed. SPC studies can be carried out for longer duration, by lowering the applied load, in order to find out whether the changes in microstructure in SPC tests are similar to uniaxial case. In case of weld joint, long term SPC tests can reveal the effect of precipitation of intermetallic in weld metal on the variation of strength across weld joint. It will also be interesting to carry out ABI tests on SPC tested specimens of various regions of weld joint and compare the results.

ABI and SPC testing can be utilized to study the effect of grain size, heat treatment, cold working, etc. on tensile and creep properties of various reactor materials.

The application of ABI and SPC techniques to study the effect of amount of alloying elements can be extended to other heat resistant alloys.

References

References

- [1] ASTM E8-13, Standard test methods for tension testing of metallic materials, American Society for Testing and Materials, 2013
- [2] ASTM E139-11, Standard practice for conducting creep, creep rupture and stress rupture tests on metallic materials. American Society for Testing and Materials, 2011
- [3] W.M. Sharpe Jr., D. Danley, D.A. Lavan, in: ASTM STP 1329, W.R. Conwin et al. (Eds.), ASTM, Philadelphia, PA, 1998, pp 497-512
- [4] R.L. Klueh: Nucl. Eng. Des. 2 (1985) 407-416
- [5] G.E. Lucas: J. Nucl. Mater. 117 (1983) 327-339
- [6] P.S. Kullen, H.H. Smith, D.J. Michel: J. Nucl. Mater. 158 (1988) 57-63
- [7] J.C.M. Li: Mater. Sci. Eng. A 322 (2002) 23-42
- [8] M.D. Mathew, Naveena, V.D. Vijayanand: J. Mater. Eng. Performance 22 (2013) 492
- [9] C.J. Hyde, T.H. Hyde, W. Sun, S. Nardone, E. De Bruycker: Mater. Sci. Eng. A 586 (2013) 358-366
- [10] T.H. Hyde, B.S.M. Ali, W. Sun: J.Eng. Mater. Tech. 136 (2014) 1-10
- [11] B.S.M. Ali, T.Y.P. Yuen, M. Saber: Nucl. Tech. 196 (2016) 130-140
- [12] F.K. Zhuang, S.T.Tu, G.Y. Zhou, Q.Q. Wang: Fatigue Fract. Eng. Mater. Struct. 38 (2015) 257-267
- [13] T.H. Hyde, C.J. Hyde, W. Sun: J. Pres. Ves. Tech. 136 (2014) 024502-1
- [14] F.M. Haggag, R.K. Nanstad, D.N. Braski, in: *Innovative Approaches to Irradiation Damage and Failure Analysis*, PVP Vol. 170, D.L. Marriott et al. (Eds.), American Society of Mechanical Engineers, New York, 1989, pp 101-107
- [15] F.M. Haggag, in: *Small Specimen Test Technique Applied to Nuclear Reactor Vessel Thermal Annealing and Plant Life Extension*, W.R. Corwin et al. (Eds.), ASTM STP 1204, American Society for Testing and Materials, Philadelphia, 1993, pp 27

- [16] D. Tabor: J. Inst. Of Metals 79 (1951) 1-18
- [17] F.M. Haggag, R.K. Nanstad, J.T. Hutton, D.L. Thomas, R.L. Swain, in: Applications of Automation Technology to Fatigue and Fracture Testing, A.A. Braun et al. (Eds.), ASTM 1092, American Society for Testing and Materials, Philadelphia, 1990, pp 188-208
- [18] D. Tabor: *The hardness of metals*, Oxford, Clarendon Press, 1951
- [19] H.A. Francis: J. Eng. Mater. Tech. 98 (1976) 272-281
- [20] K.L. Johnson: J. Mech. Phys. Solids 18 (1970) 115-126
- [21] X.L. Gao, X.N. Xing, G. Subash: Int. J. Solids Struct. 43 (2006) 2193-2208
- [22] X.L. Gao: Int. J. Solids Struct. 43 (2006) 6615-6629
- [23] Y. Tirupataiah, G. Sundararjan: Metall. Trans. A 22 (1991) 2375-2384
- [24] K.H. Kim, Y.C. Kim, E.C. Jeon, D. Kwon: Mater. Sci. Eng. A 528 (2011) 5259-5263
- [25] F.M. Haggag, J.A. Wang, M.A. Sokolov, K.L. Murty, in: Nontraditional methods of sensing stress, strain and damage in materials and structures, G. Lucas, D. Stubbs (Eds.), ASTM STP 1318, American Society for Testing and Materials, Philadelphia, 1997
- [26] P. Tipping, R. Cripps: Int. J. Pres. Ves. Pip. 61 (1995) 77-86
- [27] T.S. Byun, J.H. Hong, F.M. Haggag, K. Farrell, E.H. Lee: Int. J. Pres. Ves. Pip. 74 (1997) 231-238
- [28] K.L. Murty, M.D. Mathew: Int. J. Pres. Ves. Pip. 75 (1998) 831-840
- [29] K.L. Murty, P.Q. Miraglia, M.D. Mathew, V.N. Shah, F.M. Haggag: Int. J. Pres. Ves. Pip. 76 (1999) 361-369
- [30] R.O. Oviasuyi, R.J. Klassen: J. Nucl. Mater. 432 (2013) 28-34
- [31] S. Chatterjee, S. Panwar, Madhusoodanan: Nucl. Eng. Des. 288 (2015) 19-26

- [32] M.D. Mathew, K.L. Murty, K.B.S. Rao, S.L. Mannan: Mater. Sci. Eng. A 264 (1999) 159-166
- [33] M.D. Mathew, L.M. Lietzan, K.L. Murty, V.N. Shah: Mater. Sci. Eng. A 269 (1999) 186-196
- [34] G. Das, Sabita Ghosh, Sukomal Ghosh, R.N. Ghosh: Mater. Sci. Eng. A 408 (2005) 158-164
- [35] V. Karthik, K. Laha, P. Parameswaran, K.V. Kasiviswanathan, Baldev Raj: J. Test. Eval. 35 (2007) 438-448
- [36] V. Karthik, K. Laha, K.S. Chandravati, P. Parameswaran, K.V. Kasiviswanathan, Baldev Raj: Trans Indian Inst. Met. 63 (2010) 431-436
- [37] S. Ghosh, S. Yadav, G. Das: Mater. Letters 62 (2008) 2619-2622
- [38] S. Ghosh, S. Yadav, G. Das: Mater. Letters 62 (2008) 3966-3968
- [39] D.R. Barbadikar, A.R. Ballal, D.R. Peshwe, J. Ganesh Kumar, K. Laha, M.D. Mathew: Procedia Engg. 86 (2014) 910-918
- [40] D.R. Barbadikar, A.R. Ballal, D.R. Peshwe, J. Ganesh Kumar, K. Laha, M.D. Mathew: Mater. Sci. Eng. A 624 (2015) 92-101
- [41] M.D. Mathew, K.L. Murty: J. Mater. Sci. 34 (1999) 1497-1503
- [42] A.S. Hamada, F.M. Haggag, D.A. Porter: Mater. Sci. Eng. A 558 (2012) 766-770
- [43] F.M. Haggag, R.K. Nanstad, in: *Innovative Approaches to Irradiation Damage and Failure Analysis*, PVP Vol. 170, D.L. Marriott et al. (Eds.), American Society of Mechanical Engineers, New York, 1989, pp 41-46
- [44] T.S. Byun, J.W. Kim, J.H. Hong: J. Nucl. Mater. 252 (1998) 187-194
- [45] C.S. Seok, K.L. Murty: Int. J.Pr. Vessels Pip. 77 (2000) 303-311
- [46] F.M. Haggag, T.S. Byun, J.H. Hong, P.Q. Miraglia, K.L. Murty: Scripta Mater. 38 (1998) 645-651

- [47] J.F. Zarzour, P.J. Konkol, H. Dong: Mater. Charact. 37 (1996) 195-209
- [48] F.M. Khoshnaw, I.A. Hamakhan: Mater. Sci. Eng. A 426 (2006) 1-3
- [49] G. Das, M. Das, S. Sinha, K.K. Gupta, S. Chakrabarthy, A.K. Ray: Mater. Sci. Eng. A 513 (2009) 389-393
- [50] M.P. Manahan, A.S. Argon, O.K. Harling: J. Nucl. Mater. 103 (1981) 1545-1550
- [51] J.M. Baik, J. Kameda, O. Buck: Scripta Metall. 17 (1983) 1443-1447
- [52] J. Kameda, O. Buck: Mater. Sci. Eng. 83 (1986) 29-38
- [53] S.D. Norris, J.D. Parker: Mater. Sci. Tech. 12 (1996) 163-170
- [54] X. Mao, H. Takahashi: J. Nucl. Mater. 150 (1987) 42-52
- [55] J. Isselin, A. Iost, J. Golek, D. Najjar, M. Bigerelle: J. Nucl. Mater. 352 (2006) 97-106
- [56] E.N. Campitelli, P. Spatig, R. Bonade, W. Hoffelner, M. Victoris: J. Nucl. Mater. 335 (2004) 366-378
- [57] E. Fleury, J.S. Ha: Intl. J. Pr. Vessels Pip. 75 (1998) 699-706
- [58] K. Milicka, F. Dobes: Int. J. Pres. Ves. Pip. 83 (2006) 625-634
- [59] M. Suzuki, M. Eto, K. Fukaya, Y. Nishiyama, T. Kodaira, T. Oku, M. Adachi, A. Umino, I. Takahashi, T. Misawa, Y. Hamaguchi: J. Nucl. Mater. 179 (1991) 441-444
- [60] J.H. Bulloch: Int.J. Pr. Vessels Pip. 75 (1998) 791-804
- [61] T. Ishii, M. Ohmi, J. Saito, T. Hoshiya, N. Ooka, S. Jitsukawa, M. Eto: J. Nucl. Mater. 283 (2000) 1023-27
- [62] S.M. Kurtz, J.R. Foulds, C.W. Jewett, S. Srivastav, A.E. Edidin: Biomater. 18 (1997) 1659-1663
- [63] I. Serre, J.B. Vogt: Nucl. Eng. Des. 237 (2007) 677-685
- [64] B. Ule, T. Sustar: Mater. High Temp. 18 (2001) 163-170
- [65] Z. Zhou, Y. Zheng, X. Ling, R. Hu, J. Zhou: Mater. Sci. Eng. A 527(2010) 2784-89

- [66] M. Bruchhausen, K. Turba, F. de Haan, P. Hahner, T. Austin, Y. De carlan: J. Nucl. Mater. 444 (2014) 283-291
- [67] J.D. Parker, G.C. Stratford, N. Shaw, G. Spink, H. Metcalfe, in: Proc. BALTICA IV Plant Maintenance and Managing Life & Performance, Vol. 2, S. Hietanen, P. Auerkari (Eds.), Helsinki, 1998, pp 477-488
- [68] S. Tettamanti, R. Crudeli, in: Proc. BALTICA IV Plant Maintenance and Managing Life & Performance, Vol. 2, S. Hietanen, P. Auerkari (Eds.), Helsinki, 1998, pp 501-509
- [69] F. Dobes, K. Milicka: Mater. Sci. Eng. A 336 (2002) 245-248
- [70] F. Dobes, K. Milicka: Mater. Sci. Eng. A 510 (2009) 440-443
- [71] G.C. Stratford, F. Di Persio, J. Klaput, in: Proc. Eleventh Intl. Conf. on fracture, A. Carpinteri (Ed.), Italy, 2005
- [72] F. Hou, H. Xu, Y. Wang, L. Zhang: Engg. Fail. Anal. 28 (2013) 215-221
- [73] M. Lorenzo, I.I. Cuesta, J.M. Alegre: Mater. Sci. Eng. A 614 (2014) 319-325
- [74] CEN Workshop Agreement, CWA. 15627:2006E, Small Punch Test Method of Metallic Materials, CEN, Brussels, Belgium, 2006
- [75] R. Hurst, V. Bicego, J. Foulds, in: Proc. ASME Pressure Vessels and Piping Conference 2007, Vol. 9, 2008, pp 433-438
- [76] R. Hurst, K. Matocha, in: Proc. Second Intl. Conference on Small Sample Test Techniques, K. Matocha et al. (Eds.), Ostrava, 2012, pp 4-18
- [77] R. Hurst, V. Bicego, J. Foulds, in: Proc. Eighth Intl. Conference on Creep and Fatigue at Elevated Temperatures, Texas, USA, 2007
- [78] F. Dobes, K. Milicka: J. Test. Eval. 29 (2001) 31-35
- [79] M.L. Saucedo-Munoz, S. Komazaki, T. Takahashi, T. Hashida, T. Shoji: J. Mater. Res. 17 (2002) 1945-1953

- [80] R.C. Hurst, G.C. Stratford, V. Bicego, in: Proc. ECCC creep conference, London, 2005, pp 349
- [81] D.T. Blagoeva, R.C. Hurst: Mater. Sci. Eng. A 510 (2009) 219-222
- [82] K. Matocha, R. Hurst, in: Proc. First Intl. conference on Determination of mechanical properties of materials by small punch test and other miniature testing techniques, Ostrava, Czech Republic, 2010, pp 5-11
- [83] S. Tettamanti, R. Crudeli, in: Proc. of Intl. symposium on case histories on integrity and failures in industry, V. Bicego et al. (Eds.), Milan, 1999, pp 895-906
- [84] B. Ule, T. Sustar, F. Dobes, K. Milicka, V. Bicego, S. Tettamanti, K. Maile, C. Schwarzkopf, M.P. Whelan, R.H. Kozlowski, J. Klaput: Nucl. Eng. Des. 192 (1999) 1-11
- [85] S. Komazaki, T. Hashida, T. Shoji, K. Suzuki: J. Testing. Eval. 28 (2000) 249-256
- [86] F.D. Persio, G.C. Stratford, R.C. Hurst, in: Proc. BALTICA VI Life management and maintenance for power plants, Vol. 2, J. Veivo, P. Auerkari (Eds.), VTT symposium 234, Helsinki, 2004, pp 523-525
- [87] T. Izaki, T. Kobayashi, J. Kusumoto, A. Kanaya: Int. J. Pres. Ves. Pip. 86 (2009) 637-642
- [88] B. Kim, B. Lim: Acta Mechanica Solida Sinica 21 (2008) 312-317
- [89] D. Blagoeva, Y.Z. Li, R.C. Hurst: J. Nucl. Mater. 409 (2011) 124-130
- [90] S. Komazaki, T. Sugimoto, Y. Hasegawa, Y. Kohno: ISIJ Intl. 47 (2007) 1228-1233
- [91] B. Gulcimen, P. Hahner: Mater. Sci. Eng. A 588 (2013) 125-131
- [92] S. Komazaki, T. Kato, Y. Kohno, H. Tanigawa: Mater. Sci. Eng. A 510 (2009) 229-233
- [93] B.J. Kim, Y.B. Sim, J.H. Lee, M.K. Kim, B.S. Lim: Eng. Procedia. 10 (2011) 2579-2584

- [94] Z. Li, R. Sturm: *Mater. High Temp.* 23 (2006) 225-232
- [95] A.F. Padilha, D.M. Escriba, E. Materna Morris, M. Rieth, M. Klimenkov: *J. Nucl. Mater.* 362 (2007) 132-138
- [96] J.W. Simmons: *Mater. Sci. Eng. A* 207 (1996) 159-169
- [97] M.O. Spiedel, in: *High nitrogen steels, HNS88*, J. Foct, A. Hendry (Eds.), Institute of metals, London, 1989, pp 92
- [98] M.L.G. Byrnes, M. Grujicic, W.S. Owen: *Acta. Metall.* 35 (1987) 1853-1862
- [99] W.S. Ryu, D.W. Kim, W.G. Kim, I.H. Kuk, *Trans. of 15th Intl. Conf. on structural materials in reactor technology, SMiRT-15*, Korea, 1999, X275-X282
- [100] J. Sobotka, M. Liska, M. Sobotkova, M. Tomasova, V. Vodarek, V. Bina, in: *High nitrogen steels, HNS88*, J. Foct, A. Hendry (Eds.), Institute of metals, London, 1989, pp 363
- [101] D.W. Kim: *J. Nucl. Mater.* 420 (2012) 473-478
- [102] J.W. Simmons: *Scripta Metall. Mater.* 32 (1995) 265-270
- [103] M.P. Mishra, H.U. Borgstedt, M.D. Mathew, S.L. Mannan, P. Rodriguez: *Int. J. Pres. Ves. Pip.* 72 (1997) 111-118
- [104] J.J. Eckenrod, C.W. Kovach, in: *ASTM STP 679*, C.R. Brinkman, H.W. Garvin (Eds.), ASTM, Philadelphia, PA, 1979, pp 17-41
- [105] V. Shankar, T.P.S. Gill, S.L. Mannan, S. Sundaresan: *Sadhana* 28 (2003) 359-382
- [106] D.J. Kotecki, T.A. Siewert: 'WRC-1992 Constitution diagram for stainless steel weld metals: a modification of the WRC-1988 diagram', *Welding J.* 71 (1992) 171-178
- [107] V. Ganesan, M.D. Mathew, K.B. Sankara Rao: *Mater. Sci. Tech.* 25 (2009) 614-618
- [108] J. Ganesh Kumar, M. Nandagopal, P. Parameswaran, K. Laha, M.D. Mathew: *Mater. High Temp.* 31 (2014) 239-248

- [109] M.D. Mathew, G. Sasikala, K. Bhanu Sanakara Rao, S.L. Mannan: Mater. Sci. Eng. A 148 (1991) 253-260
- [110] J. Ganesh Kumar, V. Ganesan, V.D. Vijayanand, K. Laha, M.D. Mathew: Procedia Eng. 55 (2013) 534-541
- [111] M.D. Mathew, K. Laha, V. Ganesan: Mater. Sci. Eng. A 535 (2012) 76-83
- [112] J. Ganesh Kumar, M. Chowdary, V. Ganesan, R.K. Paretkar, K. Bhanu Sankara Rao, M.D. Mathew: Nucl. Eng. Des. 240 (2010) 1363-1370
- [113] V. Ganesan, M.D. Mathew, P. Parameswaran, K. Bhanu Sankara Rao: Trans. Indian Inst. Met. 63 (2010) 417-421
- [114] G. Sasikala, M.D. Mathew, K. Bhanu Sankara Rao, S. L. Mannan: J. Nucl. Mater. 273 (1999) 257-264
- [115] M.D. Mathew, S. Latha, K. Bhanu Sankara Rao: Mater. Sci. Eng. A 456 (2007) 28-34
- [116] V.D. Vijayanand, K. Laha, P. Parameswaran, V. Ganesan, M.D. Mathew: Mater. Sci. Eng. A 607 (2014) 138-144
- [117] V.D. Vijayanand, V. Ganesan, J. Ganesh Kumar, P. Parameswaran, Naveena, K. Laha: Metall. Mater. Trans. A. 46 (2015) 5456-5466
- [118] F.M. Haggag: Field indentation microprobe for structural integrity evaluation, US patent No. 4852397, published 1989, pp 1
- [119] ASTM E21-09, Standard test methods for elevated temperature tension tests of metallic materials, American Society for Testing and Materials, 2009
- [120] ABAQUS Inc., ABAQUS User's Manual. Hibbitt, Karlson, and Sorensen, Inc., Pawtucket, USA, 2010
- [121] X.Z. Zhao, J.J. Liu, B.L. Zhu, H.Z. Miao, Z.B. Luo: J. Mater. Eng. Performance 6 (1997) 203-208
- [122] H. Lee, J.H. Lee, G.M. Pharr: J. Mech. Phys. Solids 53 (2005) 2037-2069

- [123] T. Yamamoto, H. Kurishita, T. Matsushima, H. Kayano: J. Nucl. Mater. 239 (1996) 219-227
- [124] RCC-MRx, Design and construction rules for mechanical components of nuclear installations, AFCEN, Paris, 2012
- [125] K.L. Murty, M.D. Mathew, P.Q. Miraglia, V.N. Shah, F.M. Haggag, in: Non-destructive characterisation of materials in aging systems, R.L. Crane et al. (Eds.), Materials Research Society, Pennsylvania, USA, 1998, pp 327-337
- [126] D.P. Miannay: 'Time-dependent fracture mechanics', 2001, Springer-Verlag, New York
- [127] P.Q. Miraglia, Master of Science Thesis (1997)
- [128] J.M. Wheeler, J. Michler: Rev. of Scientific Instrument, 84 (2013) 101301-1
- [129] B. Taljat, T. Zacharia: Int. J. Solids Struct. 35 (1998) 4411-4426
- [130] E.S. Gonzalez, P. Miranda, F. Guiberteau, A. Pajares: J. European ceramic society 29 (2009) 2635-2641
- [131] A.Kumaraswamy, V.Vasudeva Rao: Mater. Sci. Engg. A 527 (2010) 6230-6234
- [132] A. Kumarasamy, B. Venkataraman: Scripta Mater. 54 (2006) 493-498
- [133] K.L. Murty, M.D. Mathew: Nucl. Eng. Des. 228 (2004) 81-96
- [134] ASTM E646-07, Standard test method for tensile strain hardening exponents (n-values) of metallic sheet materials, American Society for Testing and Materials, 2007
- [135] V. Ganesan, K. Laha, M. Nandagopal, P. Parameswaran, M.D. Mathew: Mater. High Temp. 31(2014) 162-170
- [136] P. Rodriguez, Bull. Mater. Sci. 6 (1984) 653-663
- [137] J. Jang, Y. Choi, Y.H. Lee, D. Kwon: Mater. Sci. Eng. A 395 (2005) 295-300
- [138] S.I. Wright, M.N. Nowell, D.P. Field: Microsc. Microanal. 17 (2011) 316-329
- [139] J. R. Rice, D. M. Tracey: J. Mech. Phys. Solids 17 (1969) 201-217

- [140] B. S. Henry, A. R. Luxmoore: Eng. Fracture Mech. 57 (1997) 375–390
- [141] G. Das, S. Ghosh, S.K. Sahyay: Mater. Letters. 59 (2005) 2246-2251
- [142] S. Komazaki, T. Nakata, T. Sugimoto, Y. Kohno, in: Advances in stainless steels, Baldev Raj, K.B.S. Rao, T. Jayakumar, P.V. Sivaprasad, Saroja Saibaba, P. Shankar (Eds.), CRC press, 2010, pp 135-146
- [143] X. Ling, Y. Zheng, Y. You, Y. Chen: Int. J. Pres. Ves. Pip. 84 (2007) 304-309
- [144] J. Chakrabarty: Int. J. Mech. Sci. 12 (1970) 315-325
- [145] Z. Yang, Z. Wang: Int. J. Pres. Ves. Pip. 80 (2003) 397-404
- [146] G.A. Webster, A.P.D. Cox, J.E. Dorn: Metal. Sci. J. 3 (1969) 221-225
- [147] F. Garofalo: Fundamentals of creep and creep rupture in metals, MacMilan, New York, 1965
- [148] W.J. Evans, B. Wilshire: Metall. Trans. 1 (1970) 2133-2139
- [149] F. Dobes, J. Cadek: Kovove Mater. 19 (1981) 31-40
- [150] B.J. Kim, I. Sohn, B.S. Lim: J. Korean Soc. Precis. Eng. 30 (2013) 809-814
- [151] W.J. Evans, B. Wilshire: Trans. Met. Soc. A.I.M.E. 242 (1968) 1303-1307
- [152] C. Phaniraj, M. Nandagopal, S.L. Mannan, P. Rodriguez: Acta Metall. Mater. 39 (1991) 1651-1656
- [153] D. Sidey, B. Wilshire: Metal Sci. J. 3 (1969) 56-60
- [154] A. Ahmadiéh, A.K. Mukherjee: Mater. Sci. Eng. 21 (1975) 115-124
- [155] A. Ahmadiéh, A.K. Mukherjee: Scripta Metall. 9 (1975) 1299-1304
- [156] B.K. Choudhary, C. Phaniraj, K. Bhanu Sankara Rao, S.L. Mannan: Key Engg. Mater. 171 (2000) 437-444
- [157] D.V.V. Satyanarayana, G. Malakondaiah, C. Phaniraj, D.S. Sarma: Mater. Sci. Tech. 25 (2009) 953-959
- [158] J. Vanaja, K. Laha, M.D. Mathew: Metall. Mater. Trans. A 45 (2014) 5076-5084

- [159] K.E. Amin, A.K. Mukherjee, J.E. Dorn: J. Mech. Phys. Solids. 18 (1970) 413-426
- [160] C. Phaniraj, M. Nandagopal, S.L. Mannan, P. Rodriguez, B.P. Kashyap: Acta Mater. 44 (1996) 4059-4069
- [161] B.K. Choudhary, C. Phaniraj, K. Bhanu Sankara Rao, S.L. Mannan: ISIJ Intl. 41 (2001) S73-S80
- [162] J. Vanaja, K. Laha: Metall. Mater. Trans. A 46 (2015) 4669-4679
- [163] P.W. Davies, W.J. Evans, K.R. Williams, and B. Wilshire: Scripta Metall., 1969, vol. 3, pp 671–674
- [164] K.I. Kobayashi, I. Kajihara, H. Koyama, G.C. Stratford: J. Solid Mech. Mater. Eng. 4 (2010) 75-86
- [165] F. Dobes, K. Milicka, P. Kratochvil: Intermetallics 12(2004) 1397-1401
- [166] A.A. Vasilyev, S.F. Sokolov, N.G. Kolbasnikov, D.F. Sokolov: Physics of Solid state, 53 (2011) 2194-2200
- [167] R. Sturm, M. Jenko, B. Ule: Materiali in Tehnologije. 36 (2002) 319-324
- [168] V. Bicego, F. Di Persio, R.C. Hurst, G.C. Stratford, in: 11th International Conference on Fracture, 2005, pp 4808–4814
- [169] F. Dobes, K. Milicka: Mater. Charact. 59 (2008) 961-964
- [170] F. Dobes, K. Milicka: Kovove Mater. 43 (2005) 66-72
- [171] G.S. Deshmukh, M.L. Prasad, D.R. Peshwe, J. Ganesh Kumar, M.D. Mathew, G. Amarendra: Trans Indian Inst. Met. 69 (2016) 907-915
- [172] J. Chen, Y.W. Ma, K.B. Yoon, J. Mech. Sci. Tech. 24 (2010) 1195-1201
- [173] L.M. Kachanov, in: The theory of creep, A.J. Kennedy (Ed.), National lending library, Boston spa, UK, 1967
- [174] T.H. Hyde, M. Stoyanov, W.Sun, C.J. Hyde: J. Strain Anal. Eng. Des. 45 (2010) 141-164

- [175] P. Dymacek, K. Milicka: Mater. Sci. Eng. A 510 (2009) 444-449
- [176] W.D. Nix: Mater. Sci. Eng. A 103 (1998) 103-110
- [177] V.J. Gavriljuk, H. Berns, in: High nitrogen steels, Springer-Verlag Berlin Heidelberg, Newyork, 1999, pp 135-183
- [178] N.I. Noskova, V.A. Pavlov, S.A. Nemnonov: Phys. Met. Metallogr. 20 (1965) 920-924
- [179] J.K.L. Lai: Mater. Sci. Eng. 61 (1983) 101-109
- [180] V. Ganesan, J. Ganesh Kumar, K. Laha, M.D. Mathew: Nucl. Eng. Des. 254 (2013) 179-184
- [181] C.F. Etienne, O.Van Rossum, F. Roode, in: Proc. Intl. conference on engineering aspects of creep, Vol. 2, Institution of mechanical engineers, London, 1980, pp 113-121
- [182] V.D. Vijayanand, K. Laha, P. Parameswaran, V. Ganesan, M.D. Mathew: Mater. Sci. Eng. A 607 (2014) 138-144
- [183] B. Lim, B. Kim, M. Park, S. Won: Intl. J. Modern. Phys. B 17 (2003) 1621-1626